Hydrodynamical Instabilities and the Trace of Dark Energy within the CMB

Veronika Junk

HYDRODYNAMICAL INSTABILITIES AND THE TRACE OF DARK ENERGY WITHIN THE CMB

Dissertation

an der Fakultät für Physik
der
Ludwig–Maximilians–Universität (LMU) München

Ph.D. Thesis

at the Faculty of Physics
of the
Ludwig–Maximilians University (LMU) Munich

submitted by

Veronika Junk

from München-Gräfelfing

Munich, October 2010

1*st* Evaluator: Prof. Dr. Andreas Burkert
2*nd* Evaluator: Prof. Dr. Jochen Weller

Date of the oral exam: 20th of December 2010

Vorwort

Die Astrophysik beinhaltet und verknüpft verschiedene Bereiche der Physik, wobei interessante Problemstellungen und fundamentale Sachverhalte (wie z.B. die Dunkle Energie) bis heute nicht eindeutig geklärt sind. Durch numerische Methoden gelingt es jedoch viele Prozesse, wie die kosmische Strukturbildung, detailliert zu studieren. Da es in diesen Bereichen sehr viele interssante Fragestellungen gibt, habe ich mich in der vorliegenden Arbeit mit zwei Themen eingehend beschäftigt.
Die numerische Beschreibung von Strömungen und den dabei auftretenden Instabilitäten bildet die Grundlage für verschiedene hydrodynamische Prozesse in der Astrophysik. Um eine möglichst genaue Darstellung der Entwicklung dieser Systeme zu erreichen, ist es wichtig an einem Testbeispiel die Genauigkeit der numerischen Algorithmen zu untersuchen. Der erste Teil meiner Dissertation befasst sich daher eingehend mit der Kelvin-Helmholtz Instabilität und deren numerische Umsetzung.
Ein weiterer wichtiger Bereich der Astrophysik behandelt die Dunkle Energie, deren Eigenschaften und Ursprung. Da mich dieses Thema schon seit Beginn meines Studiums fasziniert, widme ich mich im zweiten Teil meiner Arbeit der Quantifizierung der Dunklen Energie mit Hilfe der kosmischen Hintergrundstrahlung.
Beide Themenbereiche sind nicht direkt miteinander verknüpft. Aus diesem Grund besteht diese Dissertation aus zwei getrennten Abschnitten.

Contents

List of Figures

List of Tables

Zusammenfassung

Der erste Teil dieser Arbeit behandelt die numerische Beschreibung von Scherströmungen (grundlegend für astrophysikalische Prozesse auf verschiedensten Grössenskalen) und der dabei auftretenden Kelvin-Helmholtz Instabilität (KHI). Bezugnehmend auf die theoretische Herleitung von Chandrasekhar (1961), welche das lineare Wachstum der KHI erfasst, wird diese unter Mitberücksichtigung der physikalischen Viskosität neu berechnet und bildet die Grundlage für spätere Anwendungen und Vergleiche mit numerischen Simulationen. Der numerische Teil stützt sich auf zwei weitverbreitete Methoden in der Astrophysik, "Smooth-particle hydrodynamics" (SPH) und Gitter-Verfahren. SPH beschreibt eine Flüssigkeit durch Betrachtung von Teilchen, dessen Eigenschaften aus Nachbarteilchen innerhalb eines fest vorgegebenen Radiuses (der sogenannten Glättungs oder Smoothing Länge) bestimmt werden. Die in dieser Arbeit benutzten numerischen SPH-Algorithmen sind der VINE code (Wetzstein *et al.*, 2009; Nelson *et al.*, 2009) und der von Price (2008) (P08) beschriebene Code. Die intrinsische Viskosität in VINE wird mit Hilfe der analytischen Anwachsrate bestimmt, wobei der Effekt der sogenannten künstlichen Viskosität (wichtig in allen SPH-Anwendungen um Schock-Phänomene zu simulieren) analysiert wird. Für die üblich angesetzen Parameter ist die Entwicklung der KHI in VINE erheblich gedämpft, was aber durch Verwendung der sogannten Balsara-Viskosität korrigiert werden kann. Im Fall unterschiedlicher Dichte der Strömungsschichten wird die KHI komplett unterdrückt. Dieses Problem, von numerischer Natur und daher in vielen SPH-methoden gegenwärtig, ist Mittelpunkt aktueller Forschung. Der von P08 entwickelte Code besitzt eine Lösung implementiert in Form einer künstlichen thermischen Konduktivität. Diese sorgt dafür, dass die thermische Energie, dessen Erhaltung ein Mischen der Teilchen verhindert, beim Übergang vom dichten ins dünne Medium ausgeschmiert wird und eine Mischung ermöglicht. Das gute Übereinstimmen des Vergleichs mit der analytischen Erwartung unterstützt diese Methode.

Die Gitterverfahren unterteilen eine Flüssigkeit in Zellen, wobei die entsprechenden Gitterpunkte die gwichteten physikalischen Grössen beinhalten. Basierend auf den Gitter-codes FLASH (Fryxell *et al.*, 2000), PROTEUS (e.g. Heitsch *et al.*, 2006), PLUTO (Mignone *et al.*, 2007) und RAMSES (Teyssier, 2002) wird die Entwicklung der KHI im nicht-viskosen wie im viskosen Fall betrachtet. Im nicht-viskosen Fall gleicher Dichten stimmen FLASH und PLUTO gut mit der analytischen Erwartung überein. PROTEUS jedoch weicht stark ab und unterschätzt das Wachstum um einen Faktor von ~ 4. Um eine mögliche Überlagerung von KHI-Eigenfunktionen beim Aufsetzten der Störung auszuschliessen, wurden diese analytisch bestimmt und die Anfangsbedingungen für PROTEUS entsprechend angepasst. Die Abweichung verringert sich nur minimal, das Problem bleibt weiterhin bestehen und ist vermutlich auf die intrinsiche Viskosität innerhalb PROTEUS zurückzuführen. Dies zeigt sich auch im viskosen Fall, wo PROTEUS ebenfalls eine stark gedämpfte Entwicklung aufweist. Die viskose Entwicklung mit FLASH ist in guter Übereinstimmung mit der

analytischen Erwartung. Für unterschiedliche Dichten (mit einem Dichtekontrast von $DC = 10$) folgen FLASH, PLUTO und RAMSES der analytischen Vorhersage sehr gut. Im viskosen Fall zeigt FLASH ein leicht erhöhtes Wachstum (um ein Faktor ~ 0.12).

Der zweite Teil befasst sich mit der Thematik der Dunklen Energie (DE) und die Unterscheidung verschiedener Modelle mit Hilfe der kosmischen Hingergrundstrahlung (CMB = "cosmic microwave background"). Basierend auf den zwei weitverbreitesten Konzepten zur Charakterisierung der DE, die kosmologische Konstante $(w_{\rm DE} = -1)$ und die Quintessence (ein sich langsam veränderliches skalares Feld mit $w_{\rm DE} \neq$ *konst*.) wird das theroretische CMB L-RS Bispektrum berechnet. Es stellt eine Kreuz-Korrelation aus dem Rees-Sciama (RS) und dem Weak-lensing (L) Effekt dar. Die gravitative Ablenkung der CMB Photonen wird beschrieben durch den L-Effekt. Der RS-Effekt umfasst die späte Abnahme der Potential-Fluktuationen (Sachs & Wolfe, 1967) und das nichtlineare Wachstum kosmischer Strukturen (Rees & Sciama, 1968). Da das Wachstum beeinflusst wird von der DE geht hier direkt die Abhängigkeit vom entsprechenden DE-Modell ein. Besonderes von Interesse ist ein möglicher Beitrag zu frühen Zeiten, beschrieben durch die sogenannte "Early Dark Energy" (EDE). Um Vergleiche zu ziehen, werden zusätzlich zu EDE noch zwei weitere Quintessence-Modelle herangezogen, die Parameterisierung von Linder (2003a,b) (LIND03) und Komatsu *et al.* (2009) (KOMAT09), sowie Beispiele mit $w_{\rm DE} =$ *konst*..
Weiterhin beinhaltet der RS-Effekt das lineare- wie das nichtlineare Wachstum von Dichtefluktuationen der sich bildenden Strukturen. Daher wird ein entsprechendes Modell zur Beschreibung des nichtlinearen Regimes benötigt. Auf Grundlage der kosmologischen Störungstheorie dritter Ordnung (PT) wird das von Bernardeau *et al.* (2002) vorgestellte Konstrukt benutzt. Um eine mögliche Abhängigkeit der Resultate von diesen Modell zu quantifizieren werden (im Falle der kosmologischen Konstanten) die Beschreibungen von Ma *et al.* (1999) (MA99) und Smith *et al.* (2003) (HALOFIT) untersucht. PT und HALOFIT führen zu einer ähnlichen Entwicklung der L-RS Bispectrum-Amplitude. Der Übergang vom linearen in das nichtlineare Regime, deutlich durch den Vorzeichenwechsel der Amplitude, erreignet sich für MA99 auf grösseren Skalen im Gegensatz zu PT und HALOFIT. Dies lässt sich zurückführen auf den stärkeren nichtlinearen Beitrag von MA99 bei höhren Rotverschiebungen. Die Berechnung der Bispektrum-Amplitude für die verschiedenen Quintessence-Modelle beruht auf PT. Hierbei wird eine Abhängigkeit des Vorzeichenwechsels von dem Beitrag der DE deutlich. Je grösser die Dichte der DE, desto stärker wird das lineare Wachstum der Fluktuationen gedämpft, was ein späteres Erreichen der nichtlinearen Entwicklung zur Folge hat. Daher verschiebt sich der Übergang vom linearen in das nichtlinear Regime zu kleineren Skalen. Es ergeben sich deutliche Unterschiede der einzelnen Modellen, was sich auch in der Entwicklung des Signal-to-Noise Verhältnisses (S/N) wiederspiegelt. Das stärkste Signal folgt dem EDE-Modell mit dem grössten DE-Beitrag. Durch Vergleich der S/N Entwicklung folgt, dass PLANCK die nötige Auflösung besitzt um zwischen den unterschiedlichen Modellen zu unterscheiden.

Summary

Given the importance of shear flows for astrophysical gas dynamics, we study the evolution of the Kelvin-Helmholtz instability (KHI) analytically and numerically. We derive the dispersion relation for the two-dimensional KHI including viscous dissipation. The resulting expression for the growth rate is then used to estimate the intrinsic viscosity of four numerical schemes depending on code-specific as well as on physical parameters. Our set of numerical schemes includes the Tree-SPH code VINE, an alternative SPH formulation developed by Price (2008), and the finite-volume grid codes FLASH, PROTEUS, PLUTO and RAMSES. In the first part, we explicitly demonstrate the effect of dissipation-inhibiting mechanisms such as the Balsara viscosity on the evolution of the KHI. With VINE, increasing density contrasts lead to a continuously increasing suppression of the KHI (with complete suppression from a contrast of 6:1 or higher). The alternative SPH formulation including an artificial thermal conductivity reproduces the analytically expected growth rates up to a density contrast of 10:1. The second part addresses the shear flow evolution with FLASH, PLUTO and RAMSES. All codes result in a consistent non-viscous evolution (in the equal as well as in the different density case) in agreement with the analytical prediction. The viscous evolution studied with FLASH shows minor deviations from the analytical prediction.

Given the importance of forthcoming CMB measurements and their corresponding implications for cosmology, we re-investigate the theoretical CMB-cross correlation bispectrum (between the Rees-Sciama and weak lensing effect) and the corresponding signal-to-noise ratio assuming dark energy models with a time varying equation of state - the quintessence. Our main focus is on a special form of quintessence, the early dark energy. The theoretical predicted signals give insight if future experiments, such as PLANCK are able to distinguish between quintessence and the standard cosmological constant. Depending on the amount of dark energy density we indeed find a difference within the bispectrum evolution and thus, the signal-to-noise ratio. Furthermore, to test the dependency of our results on the model of the nonlinear power spectrum we apply (in addition to cosmological perturbation theory) two widely used approaches (MA99 and HALOFIT), both based on analytical functions. HALOFIT has a similar behavior with respect to perturbation theory, while MA99 differs considerably.

Chapter 1

Motivation

In this thesis, we study the implications of structure formation in an astrophysical context from two different perspectives. We start in the first part with the hydrodynamical evolution, where we play special attention to the occurring instabilities, in particular, the Kelvin-Helmholtz instability (KHI) and its implementation within numerical algorithms. In the second part, we analyze the effects of dark energy on forming cosmological structures (like galaxies), which leave a trace within the cosmic microwave background. 1.1 and 1.2, shortly motivate and introduce our further proceedings.

1.1 Part I : Modelling Shear Flows with SPH and Grid Based Methods

The physics of hydrodynamics are a central part in order to understand the evolution of astrophysical systems which involve any forms of gas. Therefore, structure formation at different scales can only be described sufficiently if the corresponding gas components are treated correctly. Very important in this context is the interstellar medium (ISM), which connects hydrodynamical processes on stellar-(small) and galactic-(large) scales. The ISM consists of $\sim 99\%$ gas (mostly hydrogen and helium), and $\sim 1\%$ dust made out of heavier elements (such as metals). On stellar scales, its dynamical evolution includes the turbulence of molecular clouds, which can be identified with the densest spots of the ISM. They provide the birthplaces for stars, which in turn fuel their surrounding with jets and outflows. On galactic scales, galaxy formation, where small subhalos (known as satellite galaxies) fall within the hot gaseous halo of its parent galaxy leads to an interaction between the satellites cold gas component and the ISM. Gas is stripped from the subhalo via ram pressure stripping[1] and driven towards the center of the host galaxy, where the galactic disc formation takes place.
All these scenarious display a system known as shear flows, where two gas-layers move in the opposite direction. They play a crucial part in structure formation (see Fig. 1.2) and are fundamental to understand how the universe evolved into its form today. The various complex procedures are modeled by numerical methods, where smooth particle hydrodynamics (SPH) and grid based schemes are the most commonly used. Given the importance of shear flows and the corresponding instabilities for the evolution of cosmic structures, it is essential to verify how accurate numerical algorithms describe those systems, and to determine their limitations with a test example.
The KHI (see Fig. 1.1), arising from an oscillation of the interface between two fluid layers as a result of their velocity difference is important for several astrophysical processes where shear flows emerge.

[1] In general, ram pressure arises when a body is moving through a fluid or gas. It experiences a strong drag force.

Figure 1.1: KHI in nature: KHI forming in clouds (upper left panel), in earth's atmosphere (upper right panel), and in Jupiters atmosphere (bottom panel).

It has given rise to serious discussion in the literature when numerically modeled. For example, its evolution is completely suppressed in presence of density contrasts when simulated with SPH (e.g. Agertz *et al.*, 2007; Price, 2008). In contrast to this, grid codes seem to do not suffer from such a problem. But yet, it is not clear how exact they describe the evolution of this instability. We therefore focus on the incompressible KHI applying SPH and grid based codes in order to verify their dependency on numerical parameters and to test limitations and applications.
The outline is as follows:

- Chapter 2 introduces the theoretical framework necessary for chapter 3. The basic principles of hydrodynamics are discussed in section 2.1. A short introduction concerning the main features of SPH and grid codes is given in section 2.2.

- We start with an introduction in chapter 3. The analytical treatment of the KHI in terms of linear perturbation theory is given in section 3.2. Section 3.3 outlines the numerical setup and the analysis method. Section 3.4 describes the KHI evolution with SPH, where special attention is given on the role of artificial viscosity. A serious problem is discussed when simulating shear flows with a density gradient using the SPH code VINE. A possible solution in form of an artificial thermal conductivity is tested. Section 3.5 focuses on the non-viscous and viscous KHI evolution applying the GRID-codes FLASH, PROTEUS PLUTO and RAMSES. The instability

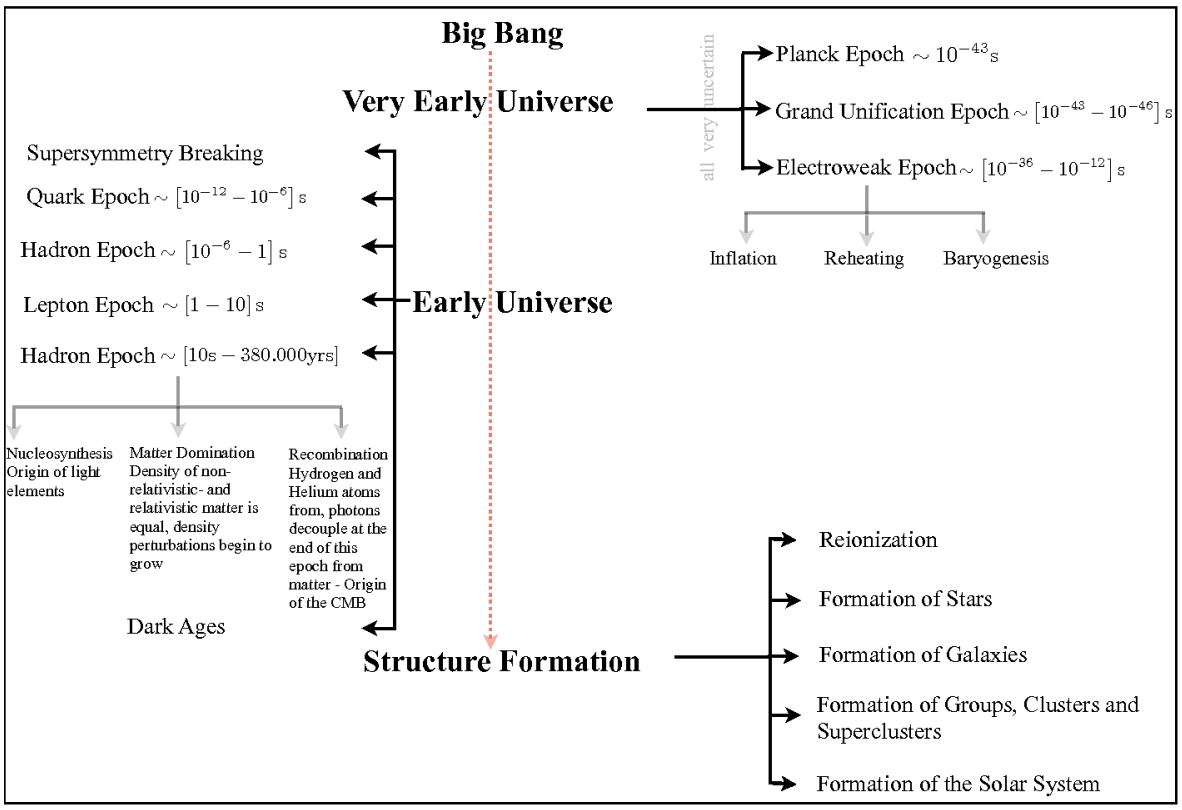

Figure 1.2: Cosmological timeline starting from the big bang until the formation of our solar system, see also Mukhanov (2005), Schneider (2006) or www.en.wikipedia.org/wiki/Timeline-of-the-Big-Bang).

growth is compared to the analytical expectation, where FLASH, PLUTO and RAMSES are in very good agreement. The summary of the results is presented in section 3.6.

1.2 Part II : The Trace of Dark Energy captured within the CMB

The surprising realization that our universe undergoes an accelerated expansion as accounted for by Supernova observations type Ia (SNIa) (Krauss & Turner, 1995; Ostriker & Steinhardt, 1995; Riess *et al.*, 1998; Perlmutter *et al.*, 1999; Netterfield *et al.*, 2002) is currently thought to originate from an unknown energy density that fills up almost our complete universe today ($\sim 70\%$). The origin and nature of this dark energy (DE) is one of the most challenging questions of astrophysics. Combined observations of SNIa, large scale structure (LSS) (Colless, 1999; Abazajian *et al.*, 2003) and the cosmic microwave background (CMB) (Spergel *et al.*, 2003; Komatsu *et al.*, 2009) point toward an equation of state[2] for DE which is close to $w_{\rm DE} \approx -1$. The standard picture invokes a cosmological constant (Λ) with the energy density of the vacuum. Yet, there exist also other possibilities like

[2] The ratio of pressure to density $w_{\rm DE} = p_{\rm DE}/\rho_{\rm DE}$.

models with a time varying $w_{\rm DE}$. A very common branch of these approaches is based on particle physics, which describe DE via a slowly changing scalar field called the quintessence. Its behavior at late times adapts that of Λ with $w_{\rm DE} = -1$, but differs from this in the past. Several attempts have been discussed, where certain parameterizations of $w_{\rm DE}$ encompass a range of models. The only possibility to distinguish between different approaches and to constrain further parameters of DE is provided by observations, where among SNIa- and LSS measurements the CMB plays an important role.
The CMB, a relict from the big bang results from the decoupling of matter and radiation at the epoch of recombination (see Fig. 1.2). It presents the most accurate measured black body radiation (Penzias & Wilson, 1965) with a temperature today about $T \sim 2.728$ K. In particular, the imprinted anisotropies (see Fig. 1.3), induced through interactions of CMB photons with their surrounding environment allow to gain insight into the physics at early times and to constrain cosmological parameters. The primary anisotropies arise before the CMB photons have decoupled and leave a Gaussian signature within their temperature distribution. However, for our study the secondary anisotropies are of more interest. These are caused as the photons travel through the universe after decoupling and interact with the forming structures. Since DE influences the growth of density fluctuations, the CMB photons carry information about DE and its equation of state $w_{\rm DE}$. This is described by the Rees-Sciama (RS) effect (see also Fig. 1.3). It leaves, along with gravitational deflection (weak lensing) a non-Gaussian signal within the CMB.
The CMB bispectrum, a tool to analyze non-Gaussianity is therefore useful to constrain properties of DE. The focus of the second part of this work is thus on the cross correlation bispectrum between the weak lensing- and RS-effect (L-RS bispectrum). We calculate the theoretical L-RS bispectrum and the corresponding signal to noise ratio using different models of DE. They aim is to obtain the limits of future CMB-observations to distinguish between Λ and quintessence. The outline is as follows:

- In Chapter 4 we concentrate on the calculation of the L-RS bispectrum and the signal-to-noise ratio (S/N). We start with an introduction followed by a short recap of cosmological basics in section 4.2, fundamental for this work. In section 4.3 we motivate the DE-models with constant $w_{\rm DE}$ and the quintessence models following Wetterich (2004) (WETT04), Linder (2003a,b) (LIND03) and Komatsu *et al.* (2009) (KOMAT09), respectively. Section 4.4 introduces the description of the nonlinear power spectrum using Bernardeau *et al.* (2002) (PT), the model of Ma *et al.* (1999) (MA99) and Smith *et al.* (2003) (HALOFIT), respectively. The basics of CMB correlation-functions are given in section 4.5. The L-RS bispectrum is discussed in detail in section 4.6, using PT, MA99 and HALOFIT, as well as the DE-models with constant $w_{\rm DE}$, WETT04, LIND03 and KOMAT09. The S/N evolution follows in section 4.7. We conclude with section 4.8

A short summary with outlook for part I and II is given in Chapter 5.

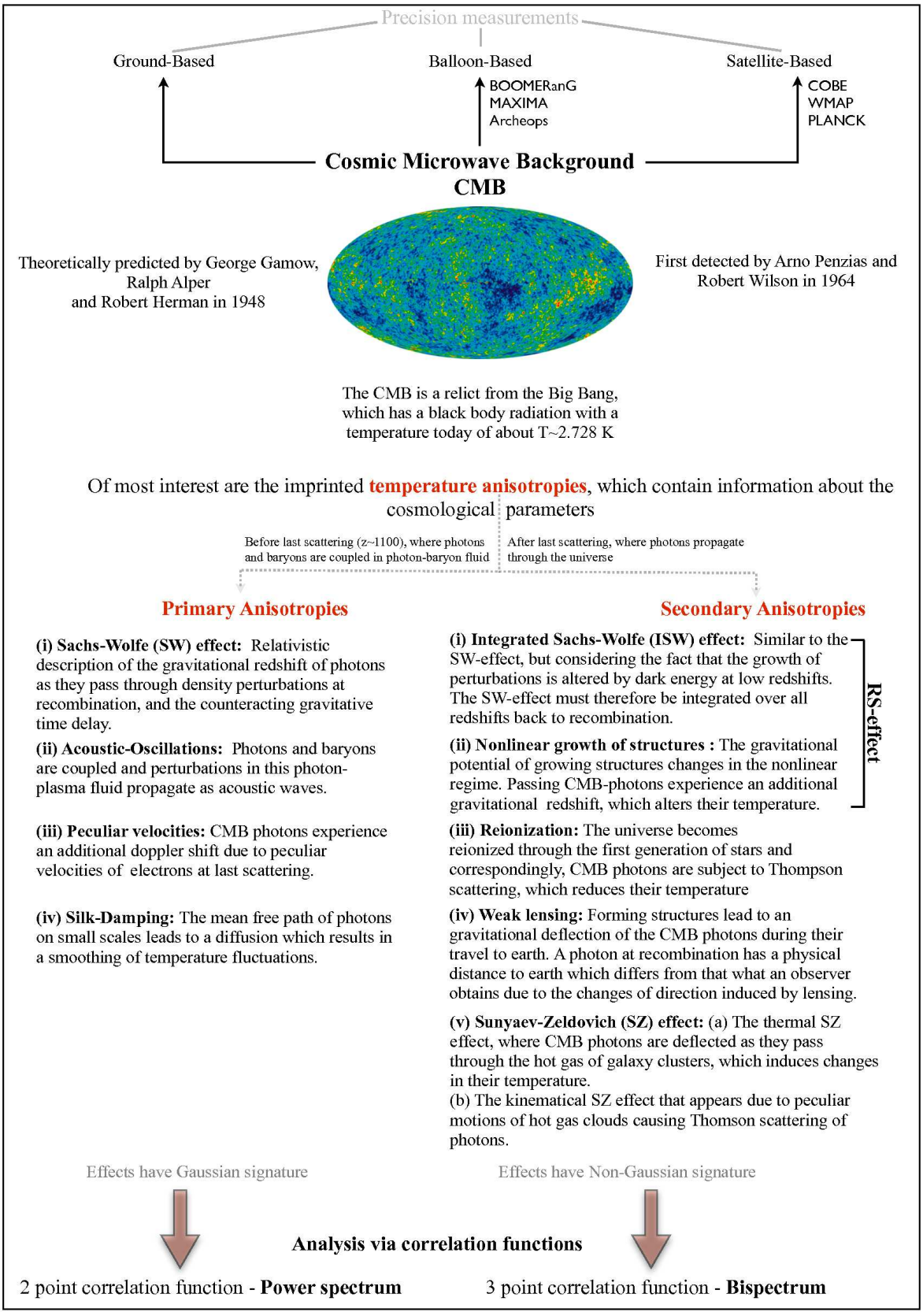

Figure 1.3: Introduction of the CMB and its most important temperature anisotropies, divided into primary- (before the decoupling of photons and baryons at the last scattering surface) and secondary anisotropies (after decoupling).

Chapter 2

Theoretical Basics

In this chapter we present the theoretical background required in chapter 3. First, the hydrodynamical principles and the linear perturbation theory are introduced. This provides the framework to derive the analytical growth rate of the Kelvin-Helmholtz instability carried out in section 3.2. Afterwards, the characteristic properties of our numerical algorithms - Smooth Particle Hydrodynamics (SPH) and grid based codes - are briefly discussed.

2.1 Basics of Hydrodynamics and Instabilities

This short overview mostly uses the convention given in Landau & Lifschitz (1991), where a complete introduction to hydrodynamics can be found.

2.1.1 Equation of Motion for the Fluid

The state of a fluid is determined by five quantities: the three velocity components (**v**), the density (ρ) and the pressure (p). It experiences additional transfer of momentum due to internal friction forces, resulting in a relative motion between the different fluid-layers. This is expressed by the momentum flux density tensor (Π), written in its components,

$$\Pi_{ik} = \rho v_i v_k - \sigma_{ik}, \tag{2.1}$$

where ρ is the density of the fluid and v_i, v_k the corresponding velocity components. The quantity σ_{ik} represents the stress tensor,

$$\sigma_{ik} = -p\delta_{ik} + \sigma'_{ik}, \tag{2.2}$$

with p being the pressure, δ_{ik} the kronecker-symbol (that equals 1 if $i = k$, and 0 otherwise), and σ'_{ik} the viscous stress tensor, which is a linear function of the first spatial velocity derivatives (Landau & Lifschitz, 1991).
The motion for this kind of fluid is fully described by the *Navier-Stokes equation*,

$$\rho \cdot \left[\frac{\partial \mathbf{v}}{\partial t} + (\mathbf{v}\cdot\nabla)\mathbf{v}\right] = -\nabla p - \rho\nabla\phi + \eta \triangle \mathbf{v} + \left(\xi + \frac{\eta}{3}\right)\nabla(\nabla\cdot\mathbf{v}), \tag{2.3}$$

with the gravitational potential ϕ, and the constant viscous coefficients η and ξ. For an incompressible fluid, which implies no sources ($\nabla \cdot \mathbf{v} = 0$), the last term in eq. (2.3) vanishes and the equation simplifies to,

$$\rho \cdot \left[\frac{\partial \mathbf{v}}{\partial t} + (\mathbf{v} \cdot \nabla)\mathbf{v} \right] = -\nabla p - \rho \nabla \phi + \rho \nu \triangle \mathbf{v}. \tag{2.4}$$

Here we introduced the kinematical viscosity ν,

$$\nu = \frac{\eta}{\rho}. \tag{2.5}$$

The mass conservation is expressed by the continuity equation,

$$\frac{\partial}{\partial t}\rho + \nabla(\rho \cdot \mathbf{v}) = 0. \tag{2.6}$$

If the fluid does not have inherent viscosity ($\nu = 0$), we obtain the familiar Euler-Jeans-equation,

$$\rho \cdot \left[\frac{\partial \mathbf{v}}{\partial t} + (\mathbf{v} \cdot \nabla)\mathbf{v} \right] = -\nabla p - \rho \nabla \phi. \tag{2.7}$$

To fully determine the fluid properties, we also need the equation of state,

$$p = p(\rho, S), \tag{2.8}$$

where S expresses the entropy. The equation of state is the link between thermodynamics and hydrodynamics. For example, the equation of state for a isothermal ideal gas is given by,

$$p = \frac{nRT}{V}, \tag{2.9}$$

where R denotes the gas constant[1], $n = N/\rho$ the particle density and T the temperature.

2.1.2 Hydrodynamical Instabilities in the Linear Regime

To mathematically describe the perturbations leading to instability effects we apply the first order perturbation theory. The perturbed values of the fluid are given by,

$$\mathbf{v} \rightarrow \mathbf{v} + \delta\mathbf{v}, \tag{2.10}$$

$$\rho \rightarrow \rho + \delta\rho, \tag{2.11}$$

$$p \rightarrow p + \delta p. \tag{2.12}$$

$\delta\mathbf{v}$ expresses the perturbation in the velocity, $\delta\rho$ and δp in the density and pressure, respectively. For the linearized Navier-Stokes- and continuity equation follows,

$$\begin{aligned} &\rho(\partial_t \delta\mathbf{v} + (\mathbf{v}\cdot\nabla)\delta\mathbf{v} + (\delta\mathbf{v}\cdot\nabla)\mathbf{v}) + \delta\rho(\partial_t\mathbf{v} + (\mathbf{v}\cdot\nabla)\mathbf{v}) = \\ &-\nabla(\delta p) + \rho\nu\triangle\delta\mathbf{v} + \delta\rho\nu\triangle\mathbf{v} + \rho\nabla(\delta\phi) + \delta\rho\nabla\phi, \end{aligned} \tag{2.13}$$

$$\partial_t\delta\rho + (\mathbf{v}\cdot\nabla)\delta\rho + (\delta\mathbf{v}\cdot\nabla)\rho = 0, \tag{2.14}$$

where we use the abbreviation $\partial/\partial t := \partial_t$. Eq. (2.13), and eq. (2.14) are crucial to derive the growth rate of the Kelvin-Helmholtz instability, which is discussed in detail in Chapter 3, section 3.2. They also provide the fundament of treating linear cosmological perturbations in the Newtonian limit discussed in Chapter 4, section 4.2.6.

[1] $R = 8.314472\,\mathrm{J}\cdot\mathrm{mol}^{-1}\mathrm{K}^{-1}$

2.2 Numerical Methods

Numerical algorithms are an important tool in modern astrophysics. Their ability to follow linear as well as nonlinear dynamics provides a detailed insight into complex physical processes. To treat hydrodynamical systems, two basic approaches are widely used: SPH and Grid-based codes.
The equations of fluid dynamics (eq. (2.4), and eq. (2.7)) have the form

$$\frac{d\mathbf{v}}{dt} = \left[\frac{\partial}{\partial t} + (\mathbf{v}\cdot\nabla)\right]\mathbf{v} = f(\mathbf{v}, \nabla\cdot\mathbf{v}, \mathbf{r}), \tag{2.15}$$

where the convectional derivative is defined by

$$\frac{d}{dt} := \left[\frac{\partial}{\partial t} + (\mathbf{v}\cdot\nabla)\right]. \tag{2.16}$$

Eq. (2.15) can be interpreted as

$$\frac{dA}{dt} = f(A, \nabla A, \mathbf{r}), \tag{2.17}$$

where A characterizes any physical quantity. To determine the rates of change of physical quantities requires their spatial derivatives. In numerical simulations, any algorithm approximates these derivatives using information from a finite number of points. In Grid-codes, the points are identified with the vertices of a mesh (see 2.2.2). For SPH, the interpolating points are the particles moving with the flow, and the interpolation of any quantity is based on a kernel estimation (see 2.2.1). In the following both approaches are introduced.

2.2.1 Basic Principles of SPH-codes

We outline shortly the basic assumptions and equations of SPH. A detailed introduction to SPH can be found in Monaghan (1992, 2005), Benz (1990) and references therein. The original idea dates back to Gingold & Monaghan (1977) and Lucy (1977).

- Interpolation and SPH equations:

  SPH follows the equations of fluid dynamics using a set of particles. It presents a kernel estimation technique, where the value of a general function $A(\mathbf{r})$ at some specific point (particle) is estimated by 'smoothing' over the values of this function at neighboring particles. The integral interpolation (A_{int}) of any function $A(\mathbf{r})$ is defined as

  $$A_{int}(\mathbf{r}) = \int A(\mathbf{r}')W(\mathbf{r}-\mathbf{r}', h)d\mathbf{r}', \tag{2.18}$$

  where h is the smoothing length that determines the region for contributing neighbors and $d\mathbf{r}'$ a differential volume element. W characterizes an interpolation kernel, which must satisfy two properties:

  $$\int W(\mathbf{r}-\mathbf{r}', h)d\mathbf{r}' := 1, \tag{2.19}$$

  $$\lim_{h\to 0} W(\mathbf{r}-\mathbf{r}', h) := \delta(\mathbf{r}-\mathbf{r}'). \tag{2.20}$$

The function A is reproduced exactly if the kernel is a delta function, while the normalization to 1 guarantees that also constants are interpolated exactly. In most numerical applications the kernel has a Gaussian form, $W(\mathbf{r}-\mathbf{r}_b,h) \sim \exp[-(\mathbf{r}-\mathbf{r}_b)^2/h^2]$. This produces a symmetric central force between pairs of particles, thereby conserving linear and angular momenta.
A more convenient choice to ensure a finite range kernel (fixed number of neighbors) is based on a cubic spline (Monaghan & Lattanzio, 1985),

$$W(\mathbf{r},h) = \frac{\tau}{h^\kappa}\cdot f\left(\frac{r}{h}\right) = \begin{cases} 1-\frac{3}{2}q^2+\frac{3}{4}q^2 & 0\le q<1, \\ \frac{1}{4}(2-q)^2 & 1\le q<2, \\ 0 & q\ge 2, \end{cases} \tag{2.21}$$

with $q = r/h$, and $\tau = [2/3; 10/(7\pi); 1/\pi]$ for the $\kappa = 1,2,3$ spatial dimensions.
For numerical studies, eq. (2.18) can be approximated by a summation interpolant,

$$A_{sum}(\mathbf{r}) = \sum_b m_b \frac{A_b}{\rho_b} W(\mathbf{r}-\mathbf{r}_b,h), \tag{2.22}$$

where the sum goes over all particles (indicated by summation index b), with the physical quantities being ρ_b, m_b, $\mathbf{v}_b$, $\mathbf{r}_b$, A_b. For example, the density is defined as,

$$\rho(\mathbf{r}) = \sum_b m_b W(\mathbf{r}-\mathbf{r}_b,h). \tag{2.23}$$

Provided that the kernel is differentiable it follows,

$$\nabla A_{sum}(\mathbf{r}) = \sum_b m_b \frac{A_b}{\rho_b} \nabla W(\mathbf{r}-\mathbf{r}_b,h). \tag{2.24}$$

However, the derivative does not vanish if A is constant. To ensure this, we have to write (Monaghan, 2005),

$$\nabla A = \frac{1}{\Phi}\left(\nabla(\Phi A) - A\nabla\Phi\right), \tag{2.25}$$

where Φ is a differentiable function. This results in,

$$\nabla A_{sum} = \frac{1}{\Phi_a}\sum m_b \frac{\Phi_b}{\rho_b}(A_b - A_a)\nabla_a W_{ab}, \tag{2.26}$$

where $\nabla_a W_{ab}$ is the gradient of $W(\mathbf{r}_a-\mathbf{r}_b,h)$ with respect to particle a. Eq. (2.26) vanishes if A is constant.
Various forms of Φ exist, resulting in different versions of derivatives. For example, using $\Phi = \rho$ we can write the continuity equation (eq (2.6)[2]) either as

$$\frac{d\rho_a}{dt} = \rho_a \sum_b \frac{m_b}{\rho_b}\mathbf{v}_{ab}\cdot\nabla_a W_{ab}, \tag{2.27}$$

or

$$\frac{d\rho_a}{dt} = \sum_b m_b \mathbf{v}_{ab}\cdot\nabla_a W_{ab}, \tag{2.28}$$

[2] Note, that we rewrite the continuity equation using the convectional derivative, eq (2.16) obtaining $d\rho/dt = -\rho\nabla\cdot\mathbf{v}$.

where $\mathbf{v}_{ab} = \mathbf{v}_a - \mathbf{v}_b$, respectively. Comparing eq. (2.27) with eq. (2.28), we see that the former involves ρ explicitly, while the latter does not. This can be crucial if systems with different (fluid) densities are involved. If this is the case, then eq. (2.27) is more accurate. Near an interface the summation for, e.g. $\nabla \cdot \mathbf{v}$ involves contributions of both fluids. Using the summation of eq. (2.27), the ratio of mass to density will be constant and $\nabla \cdot \mathbf{v}$ remains unchanged (Colagrossi, 2004). However, using that of eq. (2.28) the mass elements change and the estimate of $\nabla \cdot \mathbf{v}$ will be different, even if the fluids have the same velocity and particle positions and differ only in the density. Monaghan (2005) states that for density contrasts ≤ 2 both descriptions are valid, but for larger contrasts eq. (2.27) is preferred. We return to this important point in chapter 3 under section 3.4.
For the pressure gradient follows,

$$\frac{\nabla p}{\rho} = \nabla \left(\frac{p}{\rho} \right) + \frac{p}{\rho^2} \nabla \rho, \tag{2.29}$$

and the momentum equation[3] becomes,

$$\frac{d\mathbf{v}_a}{dt} = -\sum_b m_b \left(\frac{P_b}{\rho_b^2} + \frac{P_a}{\rho_a^2} \right) \nabla_a W_{ab}. \tag{2.30}$$

Eq. (2.30) can be derived from a discrete form of the action principle of an adiabatic fluid, it is symmetric and conserves linear and angular momentum, see Monaghan (1992).
The thermal energy per unit mass (u) is determined by the first law of thermodynamics

$$du = TdS - pdV = TdS + \frac{p}{\rho^2} d\rho, \tag{2.31}$$

with S being the entropy. For the derivative of u follows

$$\frac{du}{dt} = \frac{p}{\rho^2} \frac{d\rho}{dt} = -\frac{p}{\rho} \nabla \cdot \mathbf{v}, \tag{2.32}$$

where we use the continuity equation of the form $d\rho/dt = -\rho\,(\nabla \cdot \mathbf{v})$. Applying the different SPH descriptions (eq. (2.27), and eq. (2.28)), this expression transforms either into,

$$\frac{du}{dt} = \frac{P_a}{\rho_a^2} \sum_b m_b \mathbf{v}_{ab} \cdot \nabla_a W_{ab}, \tag{2.33}$$

or

$$\frac{du}{dt} = \frac{P_a}{\rho_a} \sum_b \frac{m_b}{\rho_b} \mathbf{v}_{ab} \cdot \nabla_a W_{ab}, \tag{2.34}$$

respectively. It can be useful to treat the energy in SPH in terms of the thermokinetic energy per unit mass,

$$e = \frac{1}{2}\mathbf{v}^2 + u, \tag{2.35}$$

[3] The Euler equation (eq. (2.7)), where gravity has been neglected, and eq. (2.16) is used such that $d\mathbf{v}/dt = -\nabla p/\rho$.

which evolves according to,

$$\frac{de}{dt} = -\frac{1}{\rho}\nabla(p\cdot\mathbf{v}) = -\sum_b m_b\left(\frac{p_a\mathbf{v}_b}{\rho_a^2}+\frac{p_b\mathbf{v}_a}{\rho_b^2}\right)\nabla_a W_{ab}, \tag{2.36}$$

and is symmetric like eq. (2.30). The description of the thermokinetic energy is often used in shock phenomena modeled with grid schemes, since it guarantees the conservation of energy.

- Artificial viscosity in SPH:

  Artificial viscosity (AV) is not a real physical viscosity. It is implemented in order to permit the treatment of shock phenomena. Eq. (2.30) does not allow for dissipation of kinetic energy into heat, and therefore cannot describe shock features. In nature, the always present intrinsic viscosity of the fluid regulates this dissipation. In SPH this is done by adding an completely artificial viscosity term and modifying the equations of momentum and energy conservation correspondingly. Monaghan & Gingold (1983) present an example for AV based on simple arguments referring to its form and relation to gas viscosity. A viscous term, Π_{ab}[4] is added to the SPH-evolution equation for the velocity (eq. (2.30)),

$$\frac{d\mathbf{v}_a}{dt} = -\sum_b m_b\left(\frac{p_b}{\rho_b^2}+\frac{p_a}{\rho_a^2}+\Pi_{ab}\right)\nabla_a W_{ab}, \tag{2.37}$$

  where,

$$\Pi_{ab} = -\nu\left(\frac{\mathbf{v}_{ab}\cdot\mathbf{r}_{ab}}{r_{ab}^2+\varepsilon h_{ab}^2}\right). \tag{2.38}$$

  The quantity $\varepsilon\sim 0.01$ prevents a singularity if $r_{ab}\to 0$, while for ν follows,

$$\nu = \frac{\alpha\bar{h}_{ab}\bar{c}_{ab}}{\bar{\rho}_{ab}}, \tag{2.39}$$

  $\bar{h}_{ab} = (h_a+h_b)/2$ and $\bar{c}_{ab} = (c_a+c_b)/2$, c denotes the sound speed. Π_{ab} is Galilean invariant and leads to a repulsive force when two particles approach each other, where it acts as an attractive force if they are receding. An improved form which prevents the so called particle streaming (i.e. particles belonging to different areas streaming between each other) leads to (Monaghan, 1992),

$$\nu = \frac{\bar{h}_{ab}}{\bar{\rho}_{ab}}\left(\alpha\bar{c}_{ab}-\beta\frac{\bar{h}_{ab}\mathbf{v}_{ab}\cdot\mathbf{r}_{ab}}{r_{ab}^2+\varepsilon h_{ab}^2}\right), \tag{2.40}$$

  $c_{ab} = c_a - c_b$ is the difference of the sound speeds. The first term $\sim \bar{h}_{ab}/\bar{\rho}_{ab}\alpha\bar{c}_{ab}$ can be interpreted as a kind of shear and bulk viscosity, where α controls its strength. The second term $\sim \bar{h}_{ab}/\bar{\rho}_{ab}\beta\left[\bar{h}_{ab}\mathbf{v}_{ab}\cdot\mathbf{r}_{ab}/\left(r_{ab}^2+\varepsilon\bar{h}_{ab}^2\right)\right]$ resembles the von Neumann-Richtmyer viscosity, controlled by β. It becomes important if compression arises. The form of eq. (2.40) has evolved further, see Lattanzio *et al.* (1985). Best results are achieved with the AV-parameters $\alpha = 1$ and $\beta = 2$, but see for a more detailed study of their effects chapter 3, section 3.4.

[4] This should not be confused with the momentum flux density tensor, eq. (2.1).

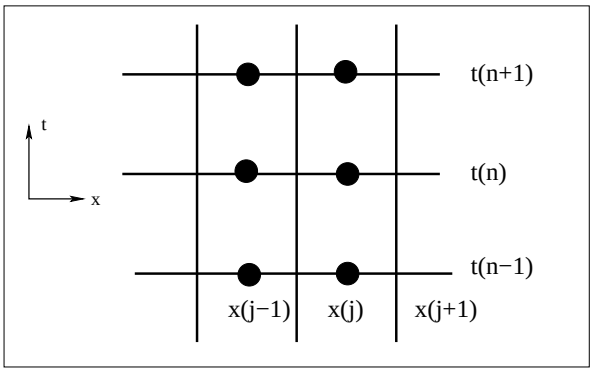

Figure 2.1: The grid discretizes the fluid in time and space (shown here by the x-direction).

Due to the AV term, energy is transformed from kinetic to thermal energy. Therefore, its contribution must also be added to the thermal energy equation (eq. (2.33)) correspondingly. The final result is given by (Monaghan & Gingold, 1983; Monaghan, 1997)

$$\frac{du}{dt} = \frac{p_a}{\Omega_a \rho_a^2} \sum_b m_b \mathbf{v}_{ab} \cdot \nabla_a W_{ab} + \frac{1}{2} \sum_a m_a \sum_b m_b \Pi_{ab} \mathbf{v}_{ab} \cdot \nabla_a W_{ab}. \tag{2.41}$$

For the thermokinetic energy (eq. (2.36)) an dissipative term of the form

$$\Upsilon_{ab} = -\frac{K \mathrm{v}_{\mathrm{sig}}(a,b) \left(e_a^* - e_b^*\right) \hat{\mathbf{r}}}{\overline{\rho}_{ab}}, \tag{2.42}$$

has to be added, where

$$e_a^* = \frac{1}{2} (\mathbf{v}_a \cdot \hat{\mathbf{r}})^2 + u_a, \tag{2.43}$$

and $\hat{\mathbf{r}} = \mathbf{r}_{ab}/|\mathbf{r}_{ab}|$. $\mathrm{v}_{\mathrm{sig}}$ is the signal velocity and K is a constant. Eq. (2.36) generalizes to,

$$\frac{de_a}{dt} = -\frac{1}{\rho} \nabla (p \cdot \mathbf{v}) = -\sum_b m_b \left(\frac{p_a \mathbf{v}_b}{\rho_a^2} + \frac{p_b \mathbf{v}_a}{\rho_b^2} + \Upsilon_{ab} \right) \nabla_a W_{ab}. \tag{2.44}$$

2.2.2 Basic Principles of GRID-codes

Another very promising and widely used approach to solve the hydrodynamical equations is presented by the Grid-codes. In this framework, various methods to solve the differential equations in terms of grid points have been proposed.
All grid-methods divide the fluid into separate cells called the mesh. An example is shown in Fig. 2.1. A common scenario to solve partial differential equations, in particular the fluid equations (eq. 2.15) is known as discretization, while a further improvement is provided by the Riemann-Solvers. We motivate both approaches below:

- DISCRETIZATION METHODS: A very simple method is to transform the regarded equations into an discretized form. For example, consider the one-dimensional scalar equation

$$\frac{\partial A}{\partial t} + b \frac{\partial A}{\partial x} = 0, \tag{2.45}$$

where b is a positive constant. We seek the solution $A(x,t)$, with the following initial conditions,

$$A(x,0) = \Psi(x). \tag{2.46}$$

Assuming that the mesh spacing Δx, and the time step Δt are constant, the solution $A(x,t)$ can be expressed by the analogous discretized solution at the mesh cell j and time level n as A_j^n, which is located at the center of the cell in physical space (see also Fig. 2.1). By replacing the derivatives of eq. (2.45) with one-sided finite difference approximations the equation becomes,

$$\frac{A_j^{n+1} - A_j^n}{\Delta t} + O(\Delta t) + b\frac{A_j^n - A_{j-1}^n}{\Delta x} + O(\Delta x) = 0 \text{ for } b > 0 \tag{2.47}$$

$$\frac{A_j^{n+1} - A_j^n}{\Delta t} + O(\Delta t) + b\frac{A_{j+1}^n - A_j^n}{\Delta x} + O(\Delta x) = 0 \text{ for } b < 0. \tag{2.48}$$

This scenario applies the one-sided forward differencing in time. Depending on whether b is positive or negative, the left side of the grid point j is called upwind side for $b > 0$ (downwind side for $b < 0$), while the right is called downwind side for $b > 0$, (upwind side for $b < 0$). If the error terms are dropped, the discrete evolution equation for A_j^n follows as,

$$A_j^{n+1} = A_j^n + \frac{b\Delta t}{\Delta x}\left(A_{j-1}^n - A_j^n\right) \text{ for } b > 0, \tag{2.49}$$

$$A_j^{n+1} = A_j^n + \frac{b\Delta t}{\Delta x}\left(A_j^n - A_{j+1}^n\right) \text{ for } b < 0, \tag{2.50}$$

where the term $\frac{b\Delta t}{\Delta x}$ determines the stability of the scheme, and is called CFL (Courant, Friedrichs, and Lewy) number. The scheme is stable, if

$$\left|\frac{b\Delta t}{\Delta x}\right| \leq 1. \tag{2.51}$$

There exist various simple finite difference schemes, e.g. downwind differencing or centered differencing.

- RIEMANN SOLVERS: These schemes are used to solve Riemann problems (RP), such as the hydrodynamical fluid equations. The RP's are fundamental to study the interaction between waves, and allow to analyze the micro-wave structure of the flows. Properties like shocks and rare-fraction waves appear as characteristics in the solution. RP's consist of conservation laws together with piecewise constant data including a single discontinuity. Thus, they appear naturally in grid codes, which solve conservation laws on discrete grids.
  For example, a simple, one dimensional RP has the initial state of,

$$A(x,0) = \begin{cases} A_L & \text{for } x \leq 0, \\ A_R & \text{for } x > 0, \end{cases} \tag{2.52}$$

which is constant for $x \leq 0$ and $x > 0$, but differs between left and right. Such a system can be identified with a one dimensional hydrodynamic problem, where initially gas with a certain temperature and density is confined at the left side of a removable barrier, and another gas of different temperature and density at the right side. The barrier is removed at $t = 0$ and the

system begins to evolve[5].
For the Euler equations (eq. (2.7)), the RP is defined as:

$$\rho, \mathrm{v}, P = \begin{cases} \rho_L, \mathrm{v}_L, P_L & \text{for } x \leq 0, \\ \rho_R, \mathrm{v}_R, P_R & \text{for } x > 0, \end{cases} \tag{2.53}$$

It is much more complex due to the nonlinear nature of eq. (2.7). Analytical solutions can be obtained only for special cases. The majority of RP's are solved numerically.
The first exact numerical solver was introduced by Godunov (1959). It is an extension to the discretization method (as discussed above) for solving nonlinear-systems of hyperbolic conservation laws. Consider Fig. 2.1 with the numerical solution at t_n given by A_j^n, which is located at the cell-center x_j. The interface between two cells resides at $x_{j+1/2}$. At each time step the state within each cell is constant (piecewise constant). Yet, at the interfaces the state variables describe a jump. This construct resembles the definition of a RP, here within two adjacent cells. The solution at each interface characterizes the subgrid analytic evolution of the hydrodynamic system.
Based on *Godunovs-Theorem* (Godunov, 1954), which states that linear numerical schemes that are used to solve partial differential equations are first-order accurate, various methods of approximate solvers have been proposed, e.g. Roe solver (Roe, 1981), HLLC solver (Harten *et al.*, 1983), HLLE solver (Harten *et al.*, 1983; Einfeld, 1988), and Rotated-hybrid Riemann solvers (Nishikawa & Kitamura, 2008).

[5] These so called shock tube tests are very common to test the accuracy of numerical hydrodynamical schemes (e.g. Sod, 1978)

Chapter 3

Modelling Shear Flows with SPH and Grid Based Methods

3.1 Introduction

3.1.1 Definitions:

In general, shear flows express two fluid- or gas-layers, which are moving in the opposite direction. They are an integral part of many astrophysical processes, from jets, the formation of cold streams, to outflows of protostars (Dekel *et al.*, 2009; Agertz *et al.*, 2009; Diemand *et al.*, 2008; Walch *et al.*, 2010), and cold gas clouds falling through the diffuse hot gas in dark matter halos (Bland-Hawthorn *et al.*, 2007; Burkert *et al.*, 2008). Jets and outflows of young stars can entrain ambient material, leading to mixing and possibly the generation of turbulence in e.g. molecular clouds (Burkert, 2006; Banerjee *et al.*, 2007; Gritschneder *et al.*, 2009b; Carroll *et al.*, 2009), while the dynamical interaction of cold gas clouds with the background galactic halo medium can lead to gas stripping of e.g. dwarf spheroidals (e.g. Grcevich *et al.*, 2010), and the disruption of high-velocity clouds (Quilis & Moore, 2001; Heitsch & Putman, 2009). The KHI, arising from an oscillation of the interface between two fluid layers as a result of their velocity difference is believed to significantly influence the gas dynamics in all of these different scenarios.
Moreover, viscous flows play a crucial role in e.g. gas accretion onto galactic discs (Das & Chattopadhyay, 2008; Park, 2009; Heinzeller *et al.*, 2009), as well as in dissipative processes like the turbulent cascade. Typically, the gas viscosity seems to be rather low in the interstellar medium, with typical flow Reynolds numbers of 10^5.
To describe these complex processes in detail, numerical schemes are applied to follow the hydrodynamical evolution. Numerous simulations use smoothed-particle hydrodynamics (SPH), (Gingold & Monaghan, 1977; Lucy, 1977; Benz, 1990; Monaghan, 1992, 2005), because its Lagrangian approach allows us to follow the evolution to high densities and small spatial scales. In combination with N-body codes, it is a perfect tool for cosmological simulations (e.g. Hernquist & Katz, 1989; Couchman *et al.*, 1995; Springel & Hernquist, 2002; Marri & White, 2003; Serna *et al.*, 2003) and galaxy formation and evolution (Katz *et al.*, 1992; Evrard *et al.*, 1994; Navarro *et al.*, 1995; Steinmetz & Navarro, 1999; Thacker & Couchman, 2000; Steinmetz & Navarro, 2002; Naab *et al.*, 2006). SPH describes the physical properties of a fluid by smoothing over a representative set of particles. However, this can lead to several problems. It can fail to correctly model sharp density gradients such as

contact discontinuities, or velocity gradients occurring in e.g. shear flows (see Agertz *et al.*, 2007), thus suppressing shear instabilities such as the KHI.

3.1.2 Earlier Studies:

An interesting problem to test the limitations of SPH as well as grid codes is the passage of a cold dense gas cloud moving through a hot and less dense ambient medium (Murray *et al.*, 1993; Vietri *et al.*, 1997; Agertz *et al.*, 2007). Such a configuration would be typical for gas clouds raining onto galactic protodisks, for High-Velocity Clouds in the Milky Way and for cold HI clouds in the Galactic disk. Murray *et al.* (1993) demonstrated using a grid code that in the absence of thermal instabilities and/or gravity clouds moving through a diffuse gas should be disrupted by hydrodynamical shear flow instabilities within the time they need to travel through their own mass. Agertz et al. (2007) have shown that the KHI, and therefore the disintegration of such clouds is suppressed in SPH simulations. This problem, in particular the suppression of the KHI, has been subject to recent discussion in the literature. Several solutions have been proposed, e.g. Price (2008) discusses a mechanism, which involves a special diffusion term (see also Wadsley *et al.*, 2008).
Furthermore, Read *et al.* (2010) identify two effects occurring in the SPH formalism, each one separately contributing to the instability suppression. The first problem is related to the leading order error in the momentum equation, which should decrease with increasing neighbor number. However, numerical instabilities prevent its decline. By introducing appropriate kernels, Read *et al.* (2010) showed that this problem can be cured. The second problem arises due to the entropy conservation. Entropy conservation inhibits particle mixing and leads to a pressure discontinuity. This can be avoided by using a temperature weighted density following Ritchie & Thomas (2001). Recently, Abel (2010) has shown to reduce the leading error problem by using a novel discretization of the pressure equation, which smoothes the force on the kernel scale and improves the stability.
Another characteristic of SPH is the implementation of an artificial viscosity (AV) term (Monaghan & Gingold, 1983), which is necessary in order to treat shock phenomena and to prevent particle interpenetration. AV can produce an artificial viscous dissipation in a flow corresponding to a decrease of the Reynolds-number and therefore a suppression of the KHI (Monaghan, 2005). To confine this effect, a reduction of viscous dissipation was proposed by Balsara (1995) and improved by Colagrossi (2004). Thacker *et al.* (2000) studied different AV-implementations in SPH and pointed out that the actual choice of the AV-implementation is the primary factor in determining code performance. An extension of SPH which includes physical fluid viscosities was discussed by e.g. Takeda *et al.* (1994), Flebbe *et al.* (1994), Español & Revenga (2003), Sijacki & Springel (2006) and Lanzafame *et al.* (2006).
An alternative to conventional numerical schemes may arise from a new class of hybrid schemes based on unstructured grids and combining the strengths of SPH and grid codes (Springel, 2010). Some of the problems listed above might be solved with this type of implementation.

3.1.3 Outline:

In this chapter we determine how accurate shear flows and the corresponding incompressible KHI are described in common numerical schemes. Therefore, in section 3.2, we analytically derive the growth rates of the KHI including viscosity. In section 3.3 we briefly describe the numerical schemes and outline how the simulations have been analyzed. We then discuss our results. At first, we concentrate

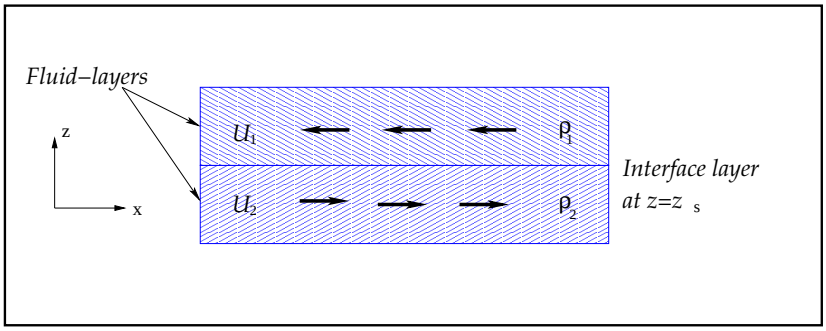

Figure 3.1: Sketch of the initial conditions considered: Two fluid layers with constant densities ρ_1 and ρ_2 flowing in opposite directions with uniform velocities U_1 and U_2.

on the standard SPH implementation, which does not contain a physical viscosity but instead uses AV. However, as mentioned above, AV does influence the evolution of the flow. In section 3.4, we discuss the ability of two numerical SPH-schemes to model the incompressible KHI, namely the Tree-SPH method VINE (Wetzstein *et al.*, 2009; Nelson *et al.*, 2009), and the SPH code of Price (2008).
By comparing to the derived analytical solution, we asses the effects of AV in VINE and estimate the intrinsic physical viscosity caused by AV (3.4.1). We then study the development of the KHI for different density contrasts (3.4.2). We show that the instability is suppressed for density contrasts equal to or larger than 6 : 1. We also discuss the remedy suggested by Price (2008), hereafter P08.
In section 3.5 we then study the same problem with the grid codes, FLASH (Fryxell *et al.*, 2000), PROTEUS (e.g. Heitsch *et al.*, 2006), PLUTO (Mignone *et al.*, 2007) and RAMSES (Teyssier, 2002). We study the non-viscous as well as the viscous evolution of the KHI for equal (3.5.1) as well as non-equal (3.5.2) density layers. We summarize our findings in section 3.6.

3.2 KHI – analytical description

The Kelvin Helmholtz instability is a very common phenomena. It might be found either for fluid-layers with a sufficient difference in the velocity across their interfaces, or in a continuous fluid, if a form of velocity shear is present. Considering two incompressible fluid layers (Fig. 3.1) with constant densities (ρ_1, ρ_2), and flow velocities (U_1, U_2) an external perturbation results in an oscillation of the interface, where the amplitude grows due to a pressure difference between concavities and convexities of the oscillation. This leads to a rolling up of the boundary layer. An example is the flow of air over water, responsible for the buildup of waves.
To derive the growth rate of the KHI including viscosity, we follow the analysis of Chandrasekhar (1961) (see also Funada & Joseph (2001) and Kaiser *et al.* (2005)). The fluid system is assumed to be viscous and incompressible. We use Cartesian coordinates in x, y, and z with two fluids at densities ρ_1, ρ_2, and velocities U_1, U_2 moving antiparallel along the x-axis, separated by an interface layer at $z = z_s$, see Fig. 3.1. We neglect the effect of self-gravity. The hydrodynamical equations for such a system are then given by the continuity equation (eq. 2.6) and momentum equation (eq. 2.7) with the flow density ρ, velocity $\mathbf{v}$, the thermal pressure p and the kinematic viscosity ν.

3.2.1 Linear Perturbations

This analysis is an extension of the work done by Chandrasekhar (1961), where we rederive the linear KHI growth including a constant viscosity. The linearized Navier-Stokes- (eq. (2.3)) and continuity-equation (eq. (2.6)) are determined by eq. (2.13) and eq. (2.14). The perturbed quantities are given by,

$$\mathbf{v} \rightarrow \mathbf{v}+\delta\mathbf{v}, \tag{3.1}$$
$$\rho \rightarrow \rho+\delta\rho, \tag{3.2}$$
$$p \rightarrow p+\delta p, \tag{3.3}$$

where $\mathbf{v} = (U(z)+\mathrm{u},\mathrm{v},\mathrm{w})$ with $\mathrm{u},\mathrm{v},\mathrm{w}$ expressing the perturbation in the velocity and $\delta\rho$, δp in the density and pressure, respectively. The goal of this calculation is the dispersion-relation, which contains the time evolution of the modes and allows to constrain the linear KHI growth rate.
Inserting these perturbed values into eq. (2.13) and eq. (2.14) yields the system of linearized equations as

$$\rho\partial_t\mathrm{u}+\rho U\partial_x\mathrm{u}+\rho\mathrm{w}\partial_z U = -\partial_x\delta p+\nu(\rho+\delta\rho)\partial_z^2 U+\rho\nu(\partial_x^2+\partial_y^2+\partial_z^2)\mathrm{u}, \tag{3.4}$$
$$\rho\partial_t\mathrm{v}+\rho U\partial_x\mathrm{v} = -\partial_y\delta p+\rho\nu(\partial_x^2+\partial_y^2+\partial_z^2)\mathrm{v}, \tag{3.5}$$
$$\rho\partial_t\mathrm{w}+\rho U\partial_x\mathrm{w} = -\partial_z\delta p+\rho\nu(\partial_x^2+\partial_y^2+\partial_z^2)\mathrm{w}+\sum_s T_s\left[(\partial_x^2+\partial_y^2)\delta z_s\right]\cdot\delta(z-z_s), \tag{3.6}$$
$$\partial_t\delta\rho+U\partial_x\delta\rho = -\mathrm{w}\partial_z\rho, \tag{3.7}$$
$$\partial_t\delta z_s+U_s\partial_x\delta z_s = -\mathrm{w}(z_s), \tag{3.8}$$
$$\partial_x\mathrm{u}+\partial_y\mathrm{v}+\partial_z\mathrm{w} = 0. \tag{3.9}$$

Eqs. (3.4), (3.5) and (3.6) represent the linearized Navier-Stokes equation, where in eq. (3.6) the effect of surface tension has been incorporated, and the density may change discontinuously at the interface positions denoted by z_s. The derivatives $\partial/\partial_{t,x,y,z}$ are abbreviated by $\partial_{t,x,y,z}$. T_s is introduced as an advanced parameter who describes the surface tension at the shear layer. It does not play a role for our analysis, yet to be complete we include it in the calculation. Eq. (3.7) is the linearized continuity equation. In eq. (3.8) the subscript s distinguishes the value of the quantity at $z = z_s$ (the interface layer). The last equation, eq. (3.9) expresses the incompressibility of the fluid. With perturbations of the form

$$\mathrm{u},\mathrm{v},\mathrm{w},\delta\rho,\delta p,\delta z_s \sim \exp\left[i(k_x x+k_y y+nt)\right], \tag{3.10}$$

where $D \equiv d/dz$ and $k^2 = k_x^2+k_y^2$, we arrive at

$$i\rho(n+k_x U)\mathrm{u}+\rho(DU)\mathrm{w} = -ik_x\delta p-\rho\nu k^2\mathrm{u}+\nu(\rho+\delta\rho)(D^2U)+\rho\nu(D^2\mathrm{u}), \tag{3.11}$$
$$i\rho(n+k_x U)\mathrm{v} = -ik_y\delta p-\rho\nu k^2\mathrm{v}+\rho\nu(D^2\mathrm{v}), \tag{3.12}$$
$$i\rho(n+k_x U)\mathrm{w} = -(D\delta p)-k^2\sum_s T_s\delta z_s\cdot\delta(z-z_s)-\rho\nu k^2\mathrm{w}+\rho\nu(D^2\mathrm{w}), \tag{3.13}$$
$$i(n+k_x U)\delta\rho = -\mathrm{w}(D\rho), \tag{3.14}$$
$$i(n+k_x U)\delta z_s = \mathrm{w}(z_s), \tag{3.15}$$
$$i(k_x\mathrm{u}+k_y\mathrm{v}) = -(D\mathrm{w}), \tag{3.16}$$

Note that the linear growth of the KHI with time is determined by n, which is the quantity we are solving for. To do so, we need first the dispersion relation, which quantifies the time evolution of the different modes. Combining these equations and assuming that the flow is aligned with the perturbation vector, i.e. $k = k_x$, we obtain the dispersion-relation as,

$$\begin{aligned} &D\{\rho(n+kU)(D\mathrm{w}) - k\rho(DU)\mathrm{w}\} - \rho k^2(n+kU)\mathrm{w} = iD\left\{\rho\nu k^2(D\mathrm{w})\right\} - \\ &iD\left\{\rho\nu(D^3\mathrm{w})\right\} - D\left\{k\nu(\rho+\delta\rho)(D^2U)\right\} + i\rho\nu k^2(D^2\mathrm{w}) - i\rho\nu k^4\mathrm{w} - \\ &k^4\left(\sum_s Ts\cdot\delta(z-z_s)\right)\left(\frac{\mathrm{w}}{n+kU}\right)_s. \end{aligned} \tag{3.17}$$

The term, $i\rho\nu k^2(D^2\mathrm{w})$ in eq. (3.17) can be replaced with

$$i\rho\nu k^2(D^2\mathrm{w}) = ik^2D(\rho\nu(D\mathrm{w})) - ik^2(D\mathrm{w})(D(\rho\nu)). \tag{3.18}$$

Eq. (3.17) describes the interrelation of the modes. Most important for the KHI is their evolution at the interface $z = z_s$. Let us consider the boundary condition at z_s, which is determined by an integration over an infinitesimal element ($z_s - \varepsilon$ to $z_s + \varepsilon$), for the limit $\varepsilon \to 0$. Please note, that with eq. (3.14) it follows for $\delta\rho$,

$$\delta\rho = i\frac{\mathrm{w}}{(n+k_xU)}(D\rho). \tag{3.19}$$

After integration the boundary condition becomes,

$$\begin{aligned} &\Delta_s\{\rho(n+kU)(D\mathrm{w}) - \rho k(DU)\mathrm{w}\} = -k^4T_s\left(\frac{\mathrm{w}}{n+kU}\right)_s + \\ &ik^2\Delta_s\{\nu\rho(D\mathrm{w})\} - i\Delta_s\left\{\nu\rho(D^3\mathrm{w})\right\} - k\Delta_s\left\{\nu\rho(D^2U)\right\} + ik^2\Delta_s\{\nu\rho(D\mathrm{w})\} - \\ &ik\Delta_s\left\{\nu\frac{\mathrm{w}}{(n+kU)}(D\rho)(D^2U)\right\} - ik^2\lim_{\varepsilon\to0}\int_{z_s-\varepsilon}^{z_s+\varepsilon}(D\mathrm{w})D(\nu\rho)\,dz \end{aligned} \tag{3.20}$$

where Δ_s is specifying the jump of any continuous quantity f at $z = z_s$,

$$\Delta_s(f) = f_{(z=z_s+0)} - f_{(z=z_s-0)}. \tag{3.21}$$

(For $\nu \equiv 0$ we retrieve the corresponding expression as given by Chandrasekhar (1961).) Using eq. (3.20) we seek the solution for n, which characterizes the linear KHI evolution with time. This is the main issue in the following subsection.

3.2.2 Special case: constant velocities and densities

To simplify the derivation of the growth rate n further, we consider the case of two fluid layers with constant densities ρ_1 and ρ_2, respectively, and constant flow velocities U_1 and $U_2 = -U_1$. In each region of constant $\rho_{1,2}$ and $U_{1,2}$, eq. (3.17) reduces to,

$$\left[(n+kU_{1,2})\rho_{1,2} - 2i\nu k^2\right](D^2\mathrm{w}) + i\nu(D^4\mathrm{w}) - k^2\left[(n+kU_{1,2}) - i\nu k^2\right]\mathrm{w} = 0 \tag{3.22}$$

The layers are separated at $z = z_s = 0$, and $\mathrm{w}/(n+kU)$ must be continuous at the interface. Also, w must be finite for $z \to \infty$, so that the solution of eq. (3.22) has the following form,

$$\mathrm{w} = A(n+kU_1)e^{+kz}\ (z<0) \tag{3.23}$$

$$\mathrm{w} = A(n+kU_2)e^{-kz}\ (z>0). \tag{3.24}$$

Inserting this in the eq. (3.20) the characteristic equation yields,

$$n^2 + 2\left[k(\alpha_2 U_2 + \alpha_1 U_1) - \frac{ik^2}{2}(\alpha_2 \nu_2 + \alpha_1 \nu_1)\right] n + k^2(\alpha_2 U_2^2 + \alpha_1 U_1^2) - k^3 \frac{T_S}{\rho_1 + \rho_2} - ik^3(\alpha_2 \nu_2 U_2 + \alpha_1 \nu_1 U_1) = 0. \quad (3.25)$$

The parameters α_1, α_2 are defined by,

$$\alpha_1 = \frac{\rho_1}{\rho_1 + \rho_2},\ \alpha_2 = \frac{\rho_2}{\rho_1 + \rho_2}. \quad (3.26)$$

Solving for n, we get the expression for the mode of the linear KHI:

$$n = -\left[k(\alpha_2 U_2 + \alpha_1 U_1) - \frac{ik^2}{2}(\alpha_2 \nu_2 + \alpha_1 \nu_1)\right] \pm \left\{k^2 \alpha_1 \alpha_2 \left(ik[\nu_1 - \nu_2] - (U_1 - U_2)\right) \cdot (U_1 - U_2) + \frac{k^3 T_s}{(\rho_1 + \rho_2)} - \frac{k^4}{4}(\alpha_2 \nu_2 + \alpha_1 \nu_1)^2\right\}^{1/2} \quad (3.27)$$

We assume that $\nu_1 = \nu_2 = \nu$ (which is the case if we consider a medium consisting of the same material), and $U_2 = -U_1 = U$. This leads to

$$n = \left[k^2 U^2(\alpha_2 - \alpha_1) + \frac{i\nu k^2}{2}\right] \pm \sqrt{-4k^2 \alpha_1 \alpha_2 U^2 + \frac{k^3 T_s}{(\rho_1 + \rho_2)} - \frac{k^4 \nu^2}{4}}. \quad (3.28)$$

The mode is exponentially growing/decaying with time, if the square root of n becomes imaginary,

$$n = \left[k^2 U^2(\alpha_2 - \alpha_1)\right] + i\left[\frac{\nu k^2}{2} \pm \sqrt{4k^2 U^2 \alpha_1 \alpha_2 - \frac{k^3 T_s}{\rho_1 + \rho_2} + \frac{\nu^2 k^4}{4}}\right]. \quad (3.29)$$

The first term describes oscillations (which is not of interest for the growth), the second term the growth/decay, with a damping due to the viscosity. Dropping the first term, eq. (3.29) results in

$$n = i\left[\frac{\nu k^2}{2} \pm \sqrt{4k^2 U^2 \alpha_1 \alpha_2 - \frac{k^3 T_s}{\rho_1 + \rho_2} + \frac{\nu^2 k^4}{4}}\right]. \quad (3.30)$$

We use eq. (3.30) for the comparison with our numerical studies in the case of different density shearing layers. The surface tension term $k^3 T_s/(\rho_1 + \rho_2)$ is counteracting the instability. As mentioned before, we do not consider T_s and skip it from now on. For equal density shearing layers $\rho_1 = \rho_2 = \rho$, eq. (3.30) leads to

$$n = i\left[\frac{\nu k^2}{2} \pm \sqrt{k^2 U^2 + \frac{\nu^2 k^4}{4}}\right]. \quad (3.31)$$

In section 3.4 and section 3.5 we use the velocity in direction of the perturbation, which in the above analysis refers to the z-direction and therefore, to the v_z-velocity component (w). Our simulation setup (see section 3.3) only uses two dimensions (x and y), where the perturbation will be in the y-direction. Hence, we have to identify the v_y-velocity component with w. The exponential term in eq. (3.10) $\sim \exp(int)$ describes the time evolution of the KHI. In the following, we therefore compare $\ln(v_y)$ with the analytical expectation $\ln(w) \sim int$.

3.2.2 presents a short discussion on the dependence of $[i \cdot n]$ with viscosity (ν) and density contrast ($DC = \rho_2/\rho_1$).

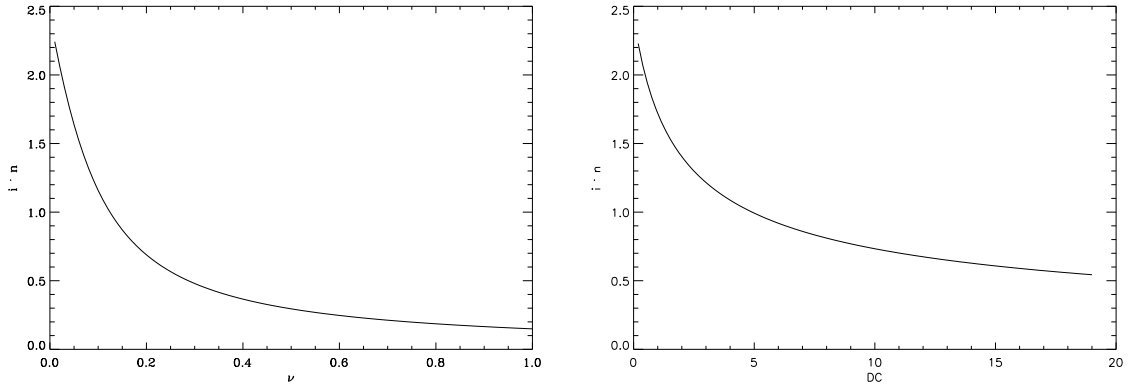

Figure 3.2: Left side: Evolution of the linear analytical KHI growth (eq. (3.31)) with ν, for equal density layers. Right side: The same, but with DC (eq. (3.30)) assuming $\nu = 0$.

physical parameters	dimensionless	in cgs units
Box size	2	2 cm
Mass	4	2780.81 g
velocity	0.387	0.40 km/s
time	1	$9.8 \cdot 10^{-6}$s

Table 3.1: Initial conditions in dimensionless units (first column) and in cgs units (second column). In the text we always refer to dimensionless units.

Analytical growth of the KHI

We briefly analyze the dependence of the linear KHI-growth on the various parameters such as the viscosity (ν) and the density contrast (DC). The parameters are in code units, for conversion to physical units refer to table 3.1.
Fig. 3.2 shows the behavior of $[i \cdot n]$ with ν (left panel) and DC (right panel), important for the comparison with simulations. The flow-velocity has been set to $U = 0.387$, $k = 2\pi$ (see also 3.3.3). The left panel of Fig. 3.2 assumes equal density layers with the KHI growth determined by eq. (3.31). The right panel shows the variation with DC, where the growth is described through eq. (3.30). In this case we use $\rho_1 = 1$, $\nu = 0$, the other parameters are as before. As can be seen in Fig. 3.2, increasing ν and DC suppresses the linear growth and dampens the KHI evolution. We return to this issue in the sections 3.4 and 3.5, when simulating the KHI using different values of DC and ν.

3.3 KHI - numerical description

In the previous section we have derived an analytical framework for the evolution of the KHI. The predictions can now be directly compared to numerical simulations of the formation and evolution of a KHI in two dimensional shear flows. For this we use two independent numerical approaches - particle based and grid based - to follow the hydrodynamics of the system. All physical parameters

are given in code units, see table 3.1 for conversion to physical units.

3.3.1 SPH models - VINE & P08

The parallel Tree-SPH code VINE (Wetzstein *et al.*, 2009; Nelson *et al.*, 2009) has been successfully applied to a number of astrophysical problems on various scales (Naab *et al.*, 2006; Jesseit *et al.*, 2007; Gritschneder *et al.*, 2009a; Walch *et al.*, 2010; Kotarba *et al.*, 2009). In VINE the implementation of AV is based on the description by Monaghan & Gingold (1983), and it includes the modifications by Lattanzio *et al.* (1986). AV is not a real physical viscosity, but implemented to allow the treatment of shock phenomena. A viscous term, Π

$$\Pi = -\nu \left(\frac{\mathbf{v} \cdot \mathbf{r}}{r^2 + \varepsilon h^2} \right), \tag{3.32}$$

is added to the SPH momentum equations. The quantity $\varepsilon \sim 0.01$ prevents a singularity if $r \to 0$, while $\bar{h}$ present the mean smoothing length between two particles. For ν follows,

$$\nu = \frac{\bar{h}}{\bar{\rho}} \left(\alpha \bar{c} - \beta \frac{\bar{h} \mathbf{v} \cdot \mathbf{r}}{r^2 + \varepsilon h^2} \right), \tag{3.33}$$

$\bar{\rho}$, and $\bar{c}$ are the mean density and the mean sound speed, respectively. The AV-parameter α controls the shear and the bulk viscosity, whereas the β parameter regulates the shock-capturing mechanism (see also section 2.2.1). In the following we set $\alpha = 0.1$, and $\beta = 0.2$ if not otherwise specified. AV reduces the Reynolds-number of the flow, resulting in the damping of the KHI (Monaghan, 2005). Balsara (1995) proposed a corrective term

$$\frac{|\nabla \cdot v|}{|\nabla \cdot v| + |\nabla \times v|}, \tag{3.34}$$

improving the behavior of the AV in shear flows. Further improvements are discussed in Monaghan (2005) and references therein. VINE can be run with and without the 'Balsara-viscosity'.

To prevent the so-called 'artificial pairing' in SPH (e.g. Schuessler & Schmitt, 1981), we implement a correction developed by Thomas & Couchman (1992). This artificial clumping occurs due to an inappropriate choice of the smoothing function. The general disadvantage of using any Gaussian type kernels is the vanishing gradient at decreasing particle separation which leads to a decreasing pressure gradient - at small distances SPH particles tend to stick together. To overcome this problem a cusp-like kernel with a finite gradient has to be used or an additional force must be added to account for a monotonic gradient of the smoothing function.

Thomas & Couchman (1992) introduced the following formula for this additional force:

$$\frac{dW(u)}{du} = \begin{cases} 4 & u \leq \frac{2}{3}, \\ 3u(4-3u) & \frac{2}{3} < u \leq 1 \\ 3(2-u)^2 & 1 < x \leq 2 \\ 0 & otherwise \end{cases}, \tag{3.35}$$

with $u = r/h$, where r is the particle separation and h the smoothing length. We incorporate this formula in our SPH-algorithm.

The SPH code presented in P08 uses a different implementation of AV as explained in Morris (1997) to prevent the side effects of artificial dissipation. Additionally, a diffusion term called 'artificial thermal conductivity' is implemented (see § 3.4.2), which has been shown to prevent the KHI suppression in shear flows with large density contrasts (Price, 2008).

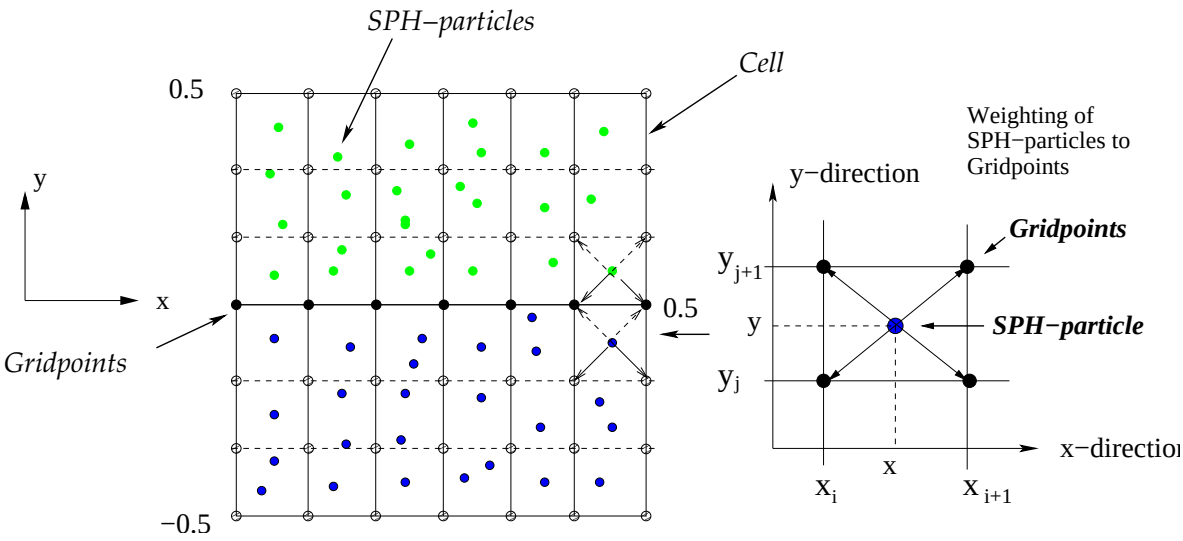

Figure 3.3: The SPH-particles are divided in the corresponding bins of a superimposed grid with fixed cell-sizes.

3.3.2 Grid-based models - FLASH, PROTEUS, PLUTO & RAMSES

We choose the publicly available, MPI-parallel FLASH code version 2.5 (Fryxell *et al.*, 2000). FLASH is based on the block-structured AMR technique implemented in the PARAMESH library (MacNeice *et al.*, 2000). However, we do not make use of the AMR refinement technique, but use uniform grids throughout this paper. In FLASH's hydrodynamic module the Navier-Stokes equations are solved using the piecewise parabolic method (Colella & Woodward, 1984), which incorporates a Riemann solver to compute fluxes between individual cells. We use a Riemann tolerance value of 10^{-7} and a CFL of 0.5. Due to FLASH's hydrodynamic scheme, the intrinsic numerical viscosity is reduced to a minimum. This allows us to study the influence of a physical viscosity on the growth of the KHI. We therefore modify the hydrodynamical equations based on the FLASH module 'diffuse' to explicitly include a viscous term, which scales with a given kinematic viscosity (see 3.5.1 and 3.5.2). As an additional test, we apply the Godunov-type high resolution shock capturing scheme PROTEUS (e.g. Heitsch *et al.*, 2006), PLUTO (Mignone *et al.*, 2007) and RAMSES (Teyssier, 2002). All are multiphysics, multialgorithm modular codes, especially designed for the treatment of discontinuities. For the simulations described in this paper, we employ different Riemann-solvers such as the Lax-Friedrichs scheme together with a second order Runge-Kutta solver, a two-shock Riemann solver with linear reconstruction embedded in a second order Runge-Kutta scheme, and a two-shock Riemann solver, but with parabolic reconstruction embedded in a third order Runge-Kutta scheme on a uniform, static grid.

3.3.3 Initial conditions and analysis method

Our numerical ICs are identical to the ones used for the derivation of the analytical growth rates (see section 3.2, Fig. 3.1 and table 3.1). To excite the instability, we apply a velocity perturbation in *y*

direction:

$$\mathrm{v}_y = \mathrm{v}_0 \sin(k \cdot x) \cdot \exp\left[-\left(\frac{y}{\sigma_0}\right)^2\right], \tag{3.36}$$

where k is the wavenumber and v_0 is the perturbation amplitude of the y-velocity triggering the instability. The parameter σ_0 controls how quickly the perturbation decreases with y (see discussion appendix A.3). It is set to $\sigma_0 = 0.1$ if not otherwise specified. Initial pressure and density are set to $p_0 \equiv 1$ and $\rho_0 \equiv 1$, resulting in a sound speed of $c_{s,0} = \sqrt{5/3}$ with an adiabatic exponent of $\gamma = 5/3$. Since the analysis of section 3.2 is only valid for an incompressible fluid, the flow speed U must be subsonic. We chose $U \equiv 0.3 \times c_{s,0} \approx 0.387$, and the initial perturbation is $\mathrm{v}_0 = 0.1 \times U$. We tested the assumption of incompressibility by calculating $\nabla \cdot \mathrm{v}$, which vanishes for incompressible flows. This is satisfied in the linear regime, the primary focus of our work. The wavenumber k is equal to $4\pi/L$, where L is the box length. The simulated box ranges from $[-1,1]$ in both directions. We use periodic boundary conditions. If not otherwise specified the AV parameters are set to $\alpha = 0.1$ and $\beta = 0.2$.

To analyze the two dimensional SPH and grid simulations consistently, we bin the SPH particles on a 64^2 grid, using the cloud-in-cell method (Hockney & Eastwood, 1988), see Fig. 3.3. Additional details are given in appendix A.1. For the grid codes, the same initial conditions are used. A resolution of 512^2 is adopted during the calculation, but we rebin to a 64^2 grid for the analysis. We measure the fastest-growing mode, which is the $k = 4\pi/L$ mode of the velocity perturbation in y direction (i.e. the mode at which the initial perturbation resides) via a Fourier analysis. The relevant modes are selected in Fourier space, and then are transformed back into real space. For more details see appendix A.2.

Our SPH-simulations (see section 3.4) always use equal mass particles if not otherwise specified. As an additional test (see 3.4.2) we apply for a density contrast of $10:1$ different mass particles to analyze the effect on the KHI-growth.

3.4 SPH-Simulations of the KHI

In the following, we model the evolution of the KHI in systems with $\rho_1 = \rho_2$ (3.4.1) and $\rho_1 \neq \rho_2$ (3.4.2). We apply VINE, if not otherwise specified and use the analytical growth rates (eqs. (3.30), (3.31)) derived in section 3.2.1 to determine the effect of AV.

3.4.1 Fluid layers with equal densities:

In the case of $\rho_1 = \rho_2$ we vary the following parameters: the resolution, which can be either enhanced by using more particles, or decreasing the smoothing length h, and the AV-parameters α and β. We vary one parameter at a time, while the other ones are set to the fiducial values (see 3.3.1). In the context of AV we discuss the importance of the Balsara-viscosity. In appendix A.3 we also discuss the influence of different σ_0, which determines the strength of the initial v_y-perturbation (eq. (3.36)).

- DEPENDENCE ON RESOLUTION:
  According to the smoothing procedure in the SPH scheme, each particle requires a certain number of neighboring particles for the calculation of its physical quantities. In VINE, these range

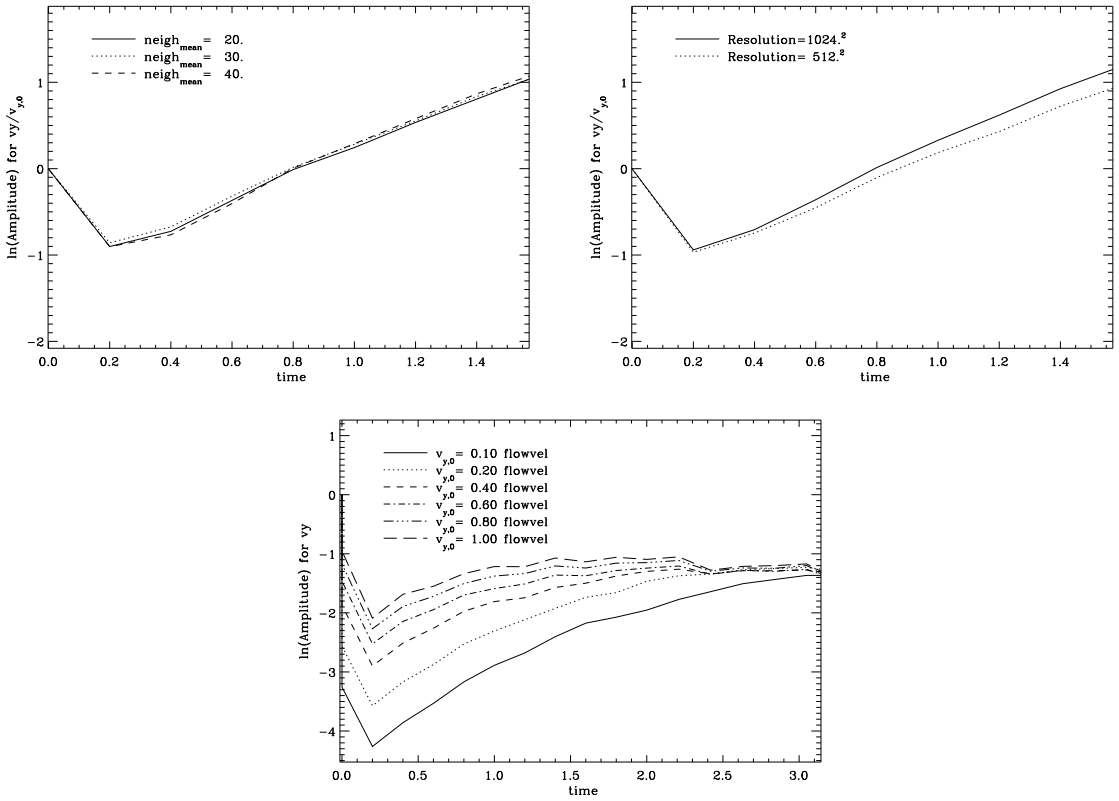

Figure 3.4: Time evolution of the v_y-amplitude using VINE for different numbers of mean neighbors, $\bar{n}_{neigh}$ (left panel), for different particle number (right panel), and for different $v_{y,0}$ (bottom panel).

from $n_{neigh,min}$ to $n_{neigh,max}$. The corresponding mean value of neighbors, $\bar{n}_{neigh}$, determines the smoothing length h. For a constant particle number, increasing $\bar{n}_{neigh}$ leads to a larger smoothing length, while at the same time the effective resolution is decreased.
In Fig. 3.4 we show the time evolution of the v_y-amplitude, which describes the growth of the KHI. For $t \leq 0.2$ the amplitudes decrease since the SPH particles lose kinetic energy by moving along the y-direction into the area of the opposite stream (see appendix A.3). Therefore we only consider $t > 0.2$ when fitting the growth rates of the KHI. The left panel of Fig. 3.4 shows the amplitude growth for $\bar{n}_{neigh} = 20$, 30, and 40, respectively. (The commonly used value in two dimensions is $\bar{n}_{neigh} = 30$). All three cases appear to be similar. Thus, different $\bar{n}_{neigh}$ do not have a substantial impact on the KHI-amplitude growth.
The right panel of Fig. 3.4 shows the dependence on particle number, for the fiducial case of 512^2 (dotted line) and for an increased resolution of 1024^2 (solid line). The difference for the fitted viscosity is small ($\leq 1\%$).

- DEPENDENCE OF THE KHI ON $v_{y,0}$:
  The bottom panel in Fig. 3.4 shows the time evolution of the KHI-amplitudes with increasing initial perturbation $v_{y,0}$ ranging from 0.1 to 1. (Note, that in this case we do not normalize the

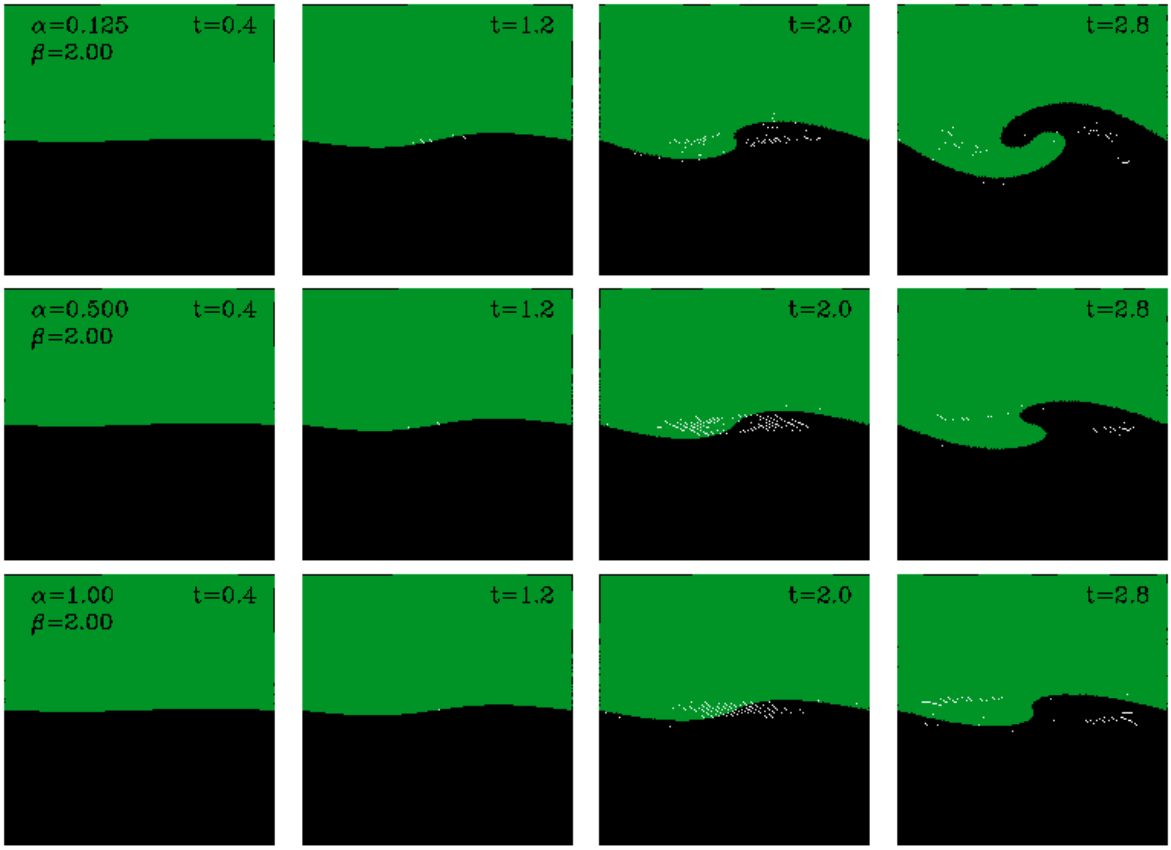

Figure 3.5: Time evolution of the KHI using VINE for increasing AV parameter α (top to bottom) and constant $\beta = 2$ The panels show the central region of each simulation box, ranging from $[-0.5, 0.5]$. The upper layer (green area) is moving to the left, the lower layer (black area) to the right. Noticeable damping occurs for $\alpha > 0.125$ (see left panel of Fig. 3.7).

v_y-amplitude and let it evolve towards larger times.) For $v_{y,0} \geq 1$ the subsonic- passes over to the supersonic-regime and the instability grows and saturates faster. At later times ($t > 3$) all examples converge. Our analysis (section 3.2) is only valid for small perturbations (i.e. in the subsonic regime) and assumes incompressibility. Therefore, we have to restrict our initial $v_{y,0}$, for which we set 0.1 to satisfy both conditions.

- DEPENDENCE OF KHI ON α, β:
  In Fig. 3.5, Fig. 3.6 and Fig. 3.7 we show the KHI-evolution for different values of α and β without the Balsara-viscosity. Increasing the AV-parameter α or β results in a successive suppression of the KHI. Values of $\alpha > 2$ and $\beta > 1$ lead to a decay of the initial perturbation. However, β does not affect the growth as much as α. Therefore, we first concentrate on α as the operating term on the KHI.
  Can we assign an equivalent physical viscosity ν_{SPH} to the SPH scheme, i.e. can we determine how ”viscous” the fluid described by SPH is intrinsically? To quantify its value, the analytical

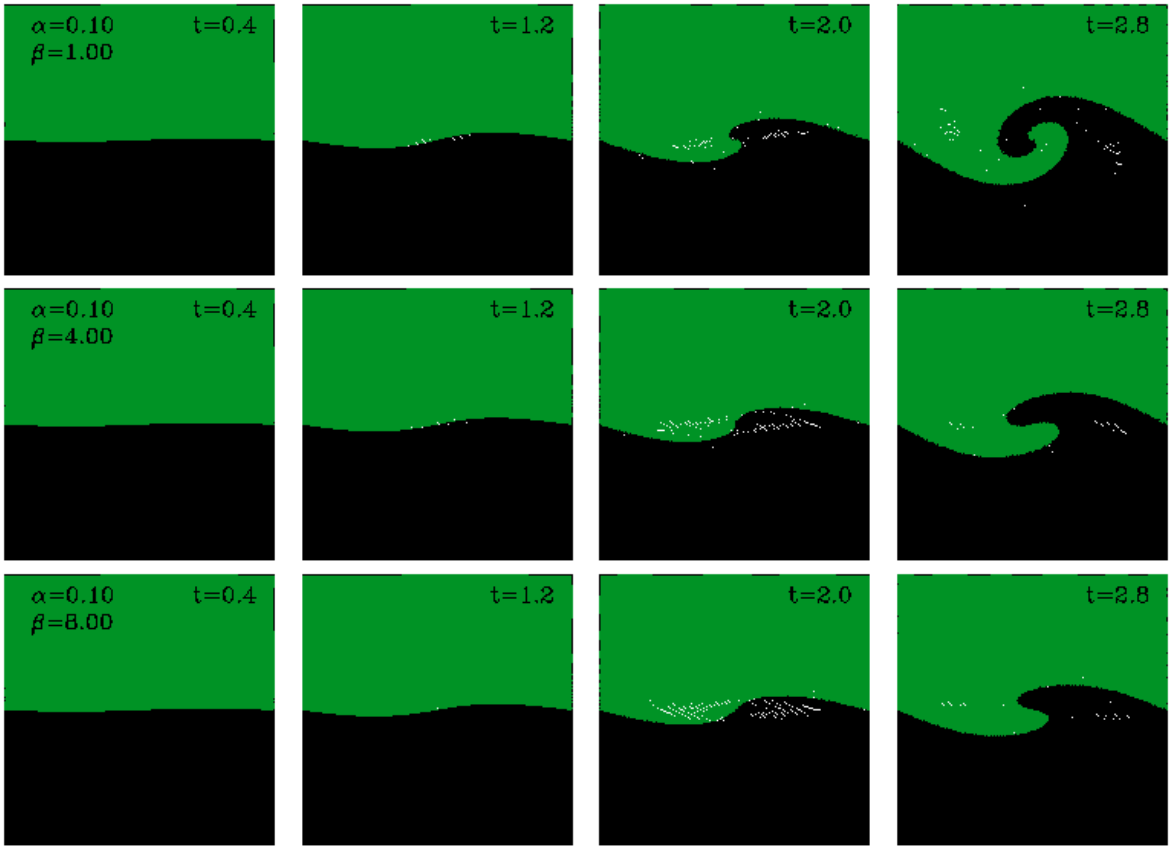

Figure 3.6: Like Fig. 3.5 but for increasing values of the AV-parameter β ($\alpha = 0.1$). A noticeable damping occurs for of $\beta > 1$ (see right panel of Fig. 3.7).

slope (eq. (3.31)), with the viscosity being the free parameter, is fitted to the simulated growing amplitudes. We show the best fits for $\alpha = 0.125$ and $\alpha = 2$ in the left panel of Fig. 3.7 (thick dashed dotted lines), for which we find the intrinsic viscosity of $\nu_{\rm SPH} = 0.07$ and $\nu_{\rm SPH} = 0.1$. Here we assumed the time range of $[0.2, 1]$, for which we determine the fits, to be well in the linear regime.

In the upper panel of Fig. 3.9 we present the derived values of $\nu_{\rm SPH}$ as a function of α. In summary, $\nu_{\rm SPH}$ increases linearly with increasing α, and the corresponding slope is 0.039. We also derive an offset of 0.065, which is the remaining intrinsic viscosity for $\alpha = 0$. For each simulation, we also show the effective Re number of the flow (see bottom panel of Fig. 3.9), which was computed from $Re = l \cdot U / \nu_{\rm SPH}$. The parameter l describes the characteristic scale of the perturbation, in our case the wavelength and U is the velocity of the flow. Clearly, the Reynolds-numbers we reach with our models are well below the commonly expected numbers for turbulent flows ($Re > 10^5$). If we interpret $\nu_{\rm SPH}$ as a real physical viscosity, then VINE is not able to describe viscous turbulence.

The effective viscosity of the flow is also influenced by different values of β. Changing β by a factor of two (e.g. from $\beta = 0.5$ to $\beta = 1$) results in an increase in effective viscosity by a

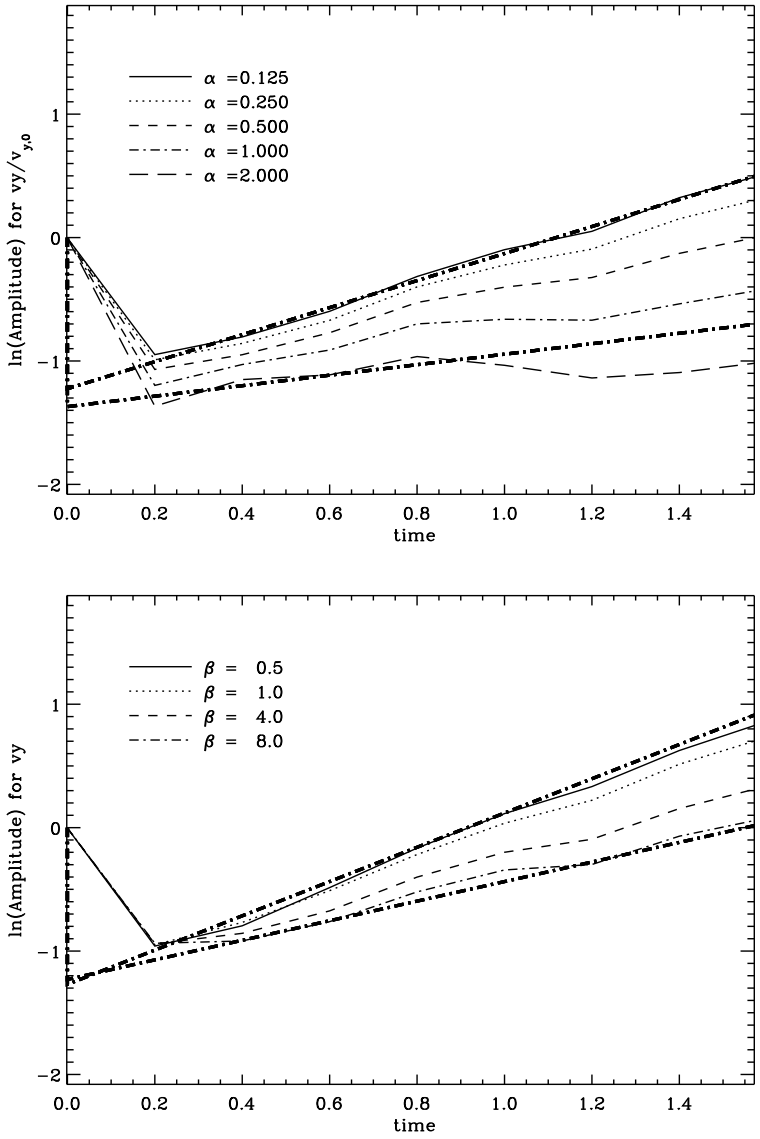

Figure 3.7: Upper panel: Time evolution of the VINE v_y-amplitude for different values of the AV-parameter α, where β has been fixed to $\beta = 2$. The thick dashed-dotted lines correspond to the analytical fit, shown for $\alpha = 0.125$ and $\alpha = 2$ (which corresponds to $\nu_{\rm SPH} = 0.07$ and $\nu_{\rm SPH} = 0.1$). Bottom panel: Like before, but for different values of the AV-parameter β, where α has been fixed to $\alpha = 0.1$.

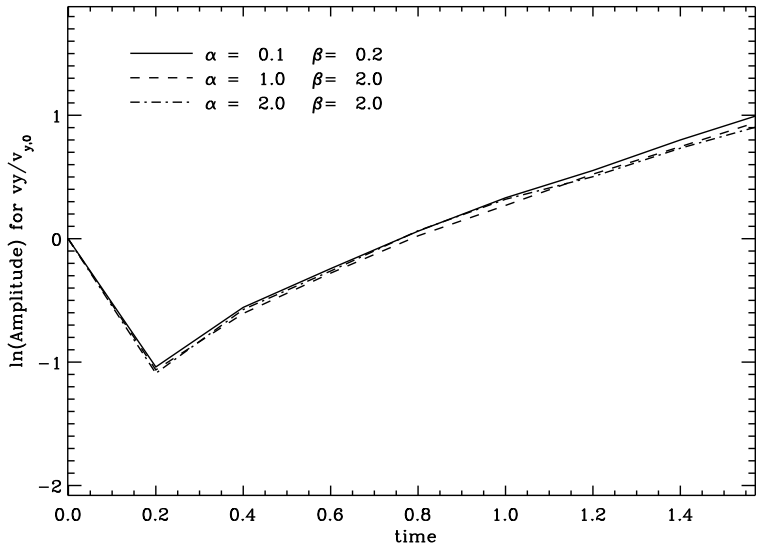

Figure 3.8: Time evolution of the VINE v_y-amplitude for different values of the AV-parameters α and β, where the Balsara-viscosity has been used. The damping of the amplitudes is completely prohibited by the Balsara switch.

factor of 0.01 (see bottom panel of Fig. 3.7).

- DEPENDENCE ON THE BALSARA-VISCOSITY:
  We showed that AV leads to artificial viscous dissipation, resulting in the damping of the KHI. To prevent this, we use the Balsara-viscosity, see also section 3.3.1. In Fig. 3.8 we show the corresponding amplitudes for three examples of AVs: ($\alpha = 0.1$, $\beta = 0.2$), ($\alpha = 1$, $\beta = 2$) and ($\alpha = 2$, $\beta = 2$). Clearly, the Balsara viscosity reduces the damping of the KHI, rendering $\nu_{\rm SPH}$ almost independently of α and β (see also Fig. 3.9).

3.4.2 Fluid layers with variable densities:

While the previously addressed case of equal densities helped us to understand the detailed evolution of the KHI as modeled with SPH, the astrophysically more interesting case are shear flows with different densities. The resolution of the diffuse region is lower by a factor of $\sqrt{DC}$, where DC is the ratio of the densities in dense and diffuse medium (e.g. $DC = 10$ corresponds to a density contrast of $10:1$). We return to our standard set of parameters, in which case $\alpha = 0.1$ and $\beta = 0.2$. For these low AV parameters we do not need the Balsara-viscosity (see 3.4.1). Nonetheless, we did run test simulations with the Balsara switch, which we found to confirm our former finding, since the growth of the KHI was not affected (see also bottom panel of Fig. 3.10). In the following, we (i) analyze the growth of the KHI for different values of DC (with equal mass particles) and address the problem of KHI suppression, while in (ii) we test the influence of equal mass or spatial resolution.

(i) KHI GROWTH AS A FUNCTION OF DC:

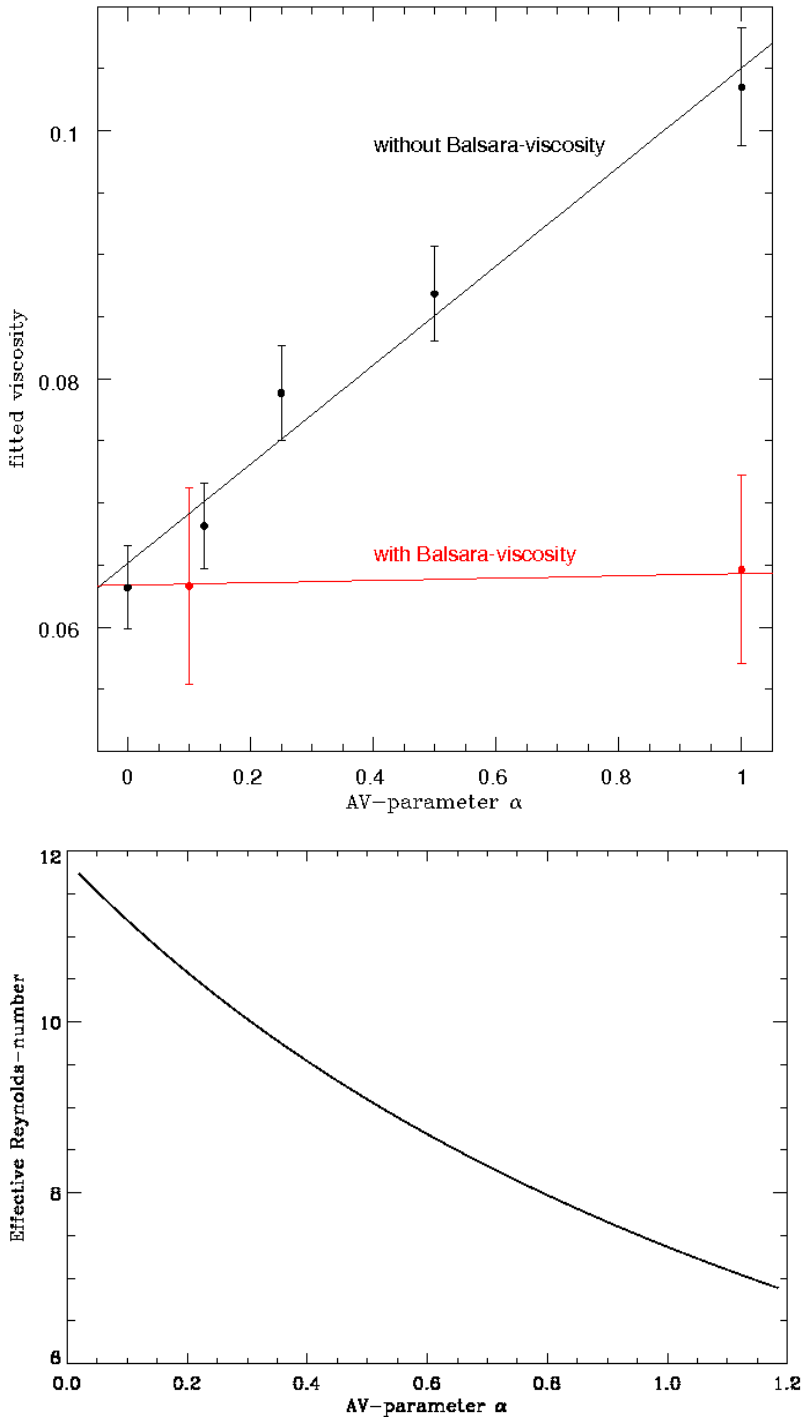

Figure 3.9: Upper panel: Derived physical viscosities ($\nu_{\rm SPH}$) corresponding to different AV parameters α with (open red points) and without (filled black points) Balsara-viscosity. Bottom panel: the effective Reynolds-number with respect to α. Since each α corresponds to an ν_{SPH}, we can compute the appropriate *Re*.

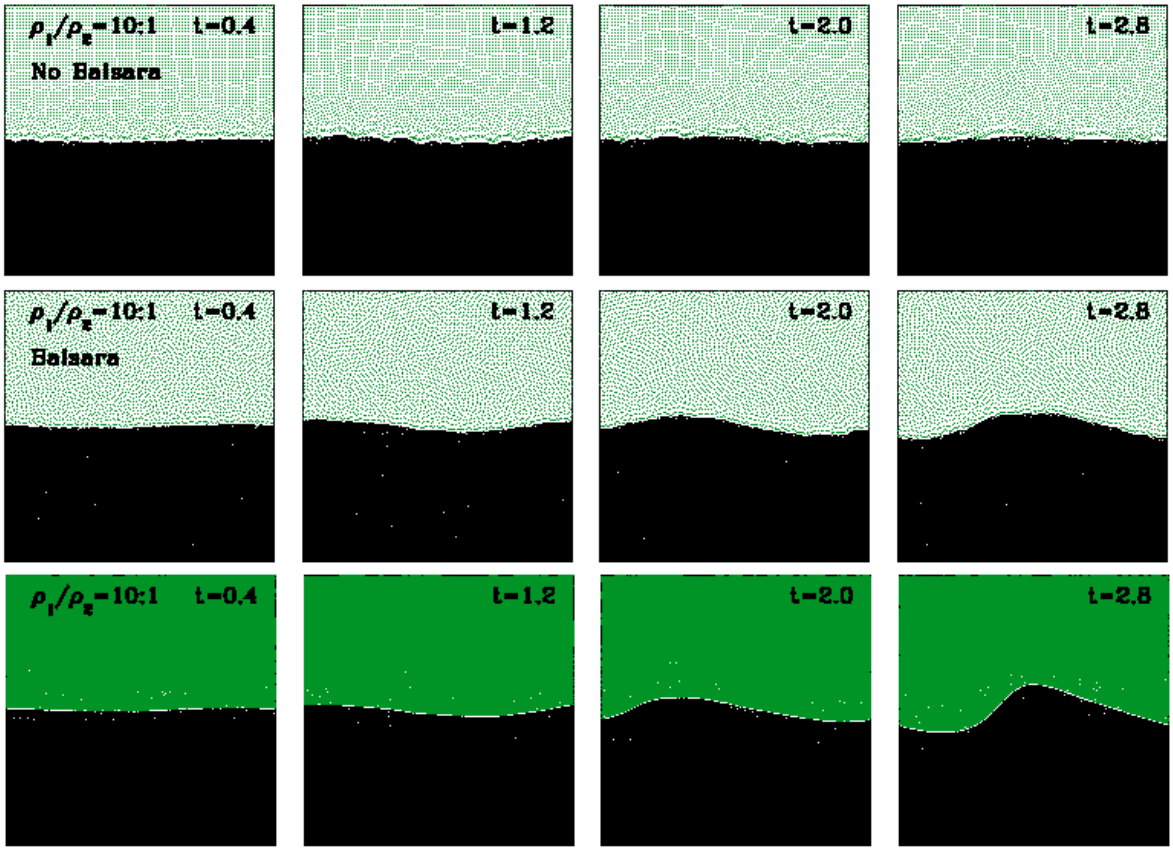

Figure 3.10: KHI with VINE for $DC = 10$. Top panel: Case of equal particle masses. Middle panel: Case of equal particle masses using the Balsara switch. Bottom panel: Case of unequal particle masses and therefore equal particle numbers in both layers. The KHI is suppressed in all cases.

We show the KHI evolution for increasing DC in Fig. 3.11 and the corresponding amplitudes in Fig 3.12. The analytical prediction (eq. (3.30)) using $v_{\rm int}$ (see 3.4.1) is indicated by the thick dashed dotted lines for $DC = 1.5$ and $DC = 2$ (left panel) and agrees with the simulated growth. However, for $DC \geq 6$ the KHI does not develop anymore (therefore we do not compare it with the analytical expectation). This SPH problem of KHI suppression has been studied in great detail (e.g. Agertz *et al.*, 2007; Price, 2008; Wadsley *et al.*, 2008; Read *et al.*, 2010; Abel, 2010). SPH particles located at the interface have neighbors at both sides of the boundary (i.e. from the dense- and less dense region). Therefore, the density at the boundary is smoothed during the evolution. However, the corresponding entropy (or, depending on the specific code, the thermal energy) is artificially fixed in these (isothermal) setups which results in an artificial contribution to the SPH pressure force term, due to which the two layers are driven apart. One possible solution is to either adjust the density (Ritchie & Thomas, 2001; Read *et al.*, 2010), or to smooth the entropy (thermal energy) (Price, 2008; Wadsley *et al.*, 2008; Abel, 2010).
A remedy has been discussed by Price (2008), who proposed to add a diffusion term, which is called artificial thermal conductivity (ATC), to adjust the thermal energy. Price (2008) states that these

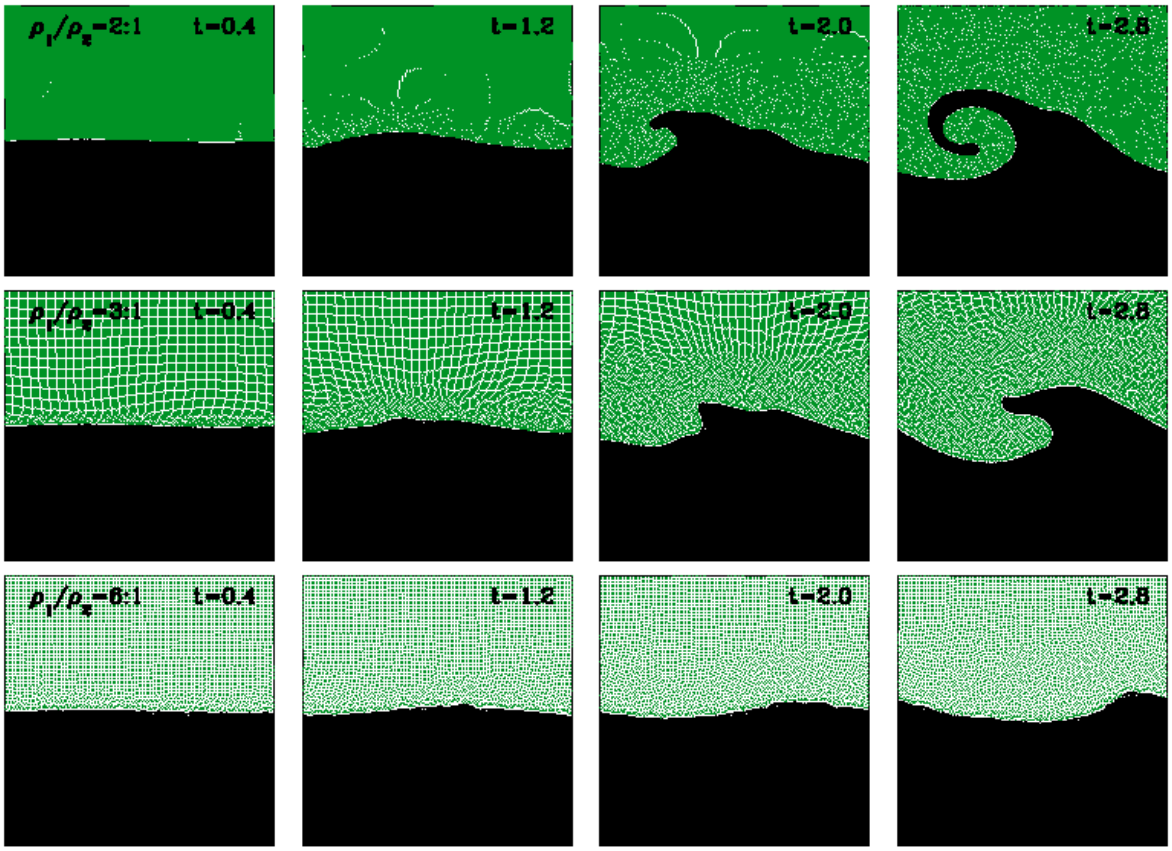

Figure 3.11: Like Fig. 3.10 top panel, but for different density contrasts. From top to bottom we show $DC = 2, 3, 6$. For $DC \geq 6$ the KHI does not develop anymore.

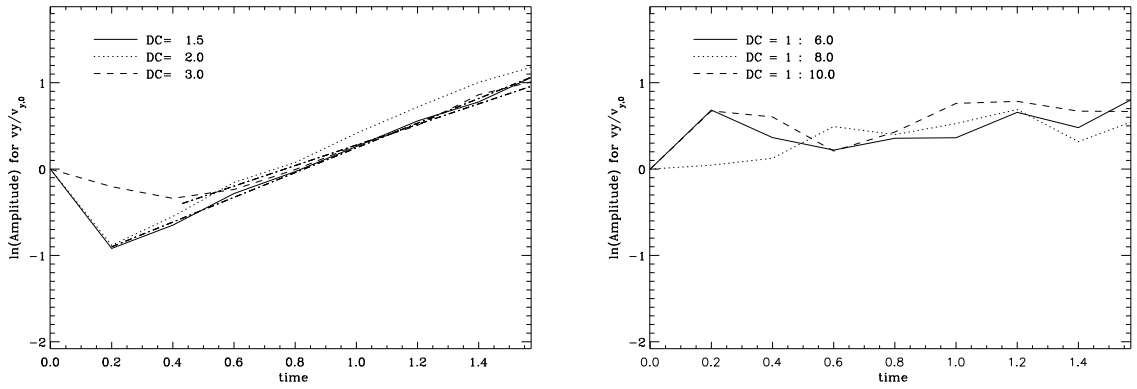

Figure 3.12: Time evolution of the VINE v_y-amplitude using different values of DC. Left panel: the KHI does develop up until to $DC = 3$. Right panel: The KHI is suppressed in all cases for $DC > 6$. The thick dashed-dotted lines on the left panel correspond to the analytical growth (using v_{int}) shown for $DC = 1.5$ and $DC = 3$. For further details the discussion in the text.

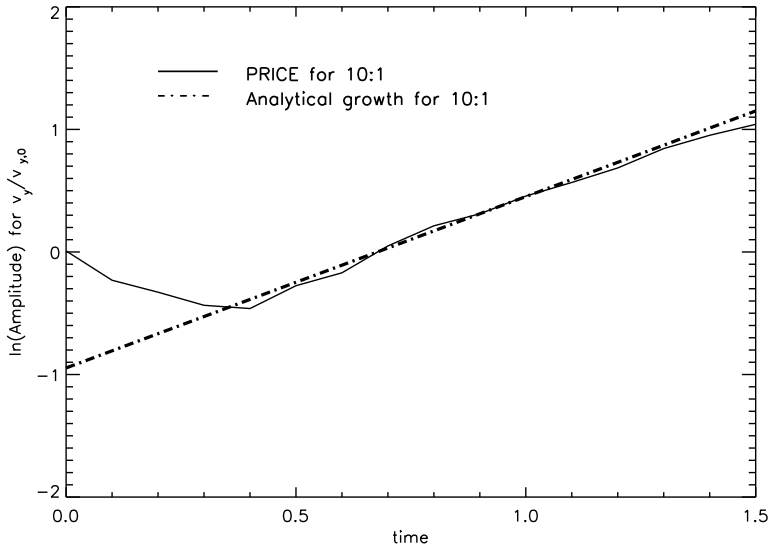

Figure 3.13: Time evolution of the KHI modeled with P08 for the $DC = 10$. The dashed-dotted line corresponds to the analytical prediction, eq. (3.68), which is in good agreement with the simulation.

discontinuities correspond to missing surface integrals in the SPH equation, which are a direct result due to the assumption of differentiability of the SPH evolution equations. By demonstrating the difference between the integral and differential density evolution, Price (2008) shows that in the latter case the surface integral terms vanish. As long as boundaries are not involved, the two interpretations are equivalent. This changes once the fluid has boundaries or discontinuities – such as in shear flows. Many SPH implementations chose the differential form of the evolution equations, and thus fail to account for the surface terms. Price (2008) proposes to add dissipation terms to recover these missing discontinuities. For example, the integral form of the continuity equation can be written as,

$$\int \left[\frac{\partial \rho'}{\partial t} + \nabla' \cdot \left(\rho' \mathbf{v}' \right) \right] W(\mathbf{r} - \mathbf{r}', h) = 0, \tag{3.37}$$

which results in

$$\frac{\partial}{\partial t} \int \rho' W dV' - \int \rho' \mathbf{v}' \cdot \nabla' W dV' + \int \nabla' \cdot \left[\rho' \mathbf{v}' W \right] dV = 0. \tag{3.38}$$

See also chapter 2, section 2.2.1 for the basic equations. Using $\nabla' W = -\nabla W$ and the convective derivative (eq. (2.16)) together with the Stokes[1] theorem, we can recast the last part into a surface integral,

$$\frac{d}{dt} \int \rho' W dV' - \int \rho' (\mathbf{v} - \mathbf{v}') \cdot \nabla W dV' + \int \left[\rho' \mathbf{v}' W \right] \cdot d\mathbf{S} = 0. \tag{3.39}$$

[1] $\int_V \nabla \cdot \mathbf{F} dV = \int \mathbf{F} \cdot d\mathbf{S}$

Converting the integral into a sum we get,

$$\sum_b m_b W_{ab} = \sum_b (\mathbf{v_a} - \mathbf{v_b}) \cdot \nabla W_{ab} - \int \left[\rho' \mathbf{v}' W\right] \cdot d\mathbf{S}. \tag{3.40}$$

This equation contains an additional term involving the surface-integral. In most cases it vanishes except at boundaries or flow discontinuities. This means, that treating SPH equations either using the integral form or the differential form has important consequences. Differential SPH equations like the velocity evolution, eq. (2.30) assume that the surface-integral term vanishes, which is not the case if boundaries are present. Therefore, contributions of an surface term to the sum are not accounted for. Price (2008) proposes to add dissipation terms to the SPH equations in order to recover the missing discontinuities. These dissipation parts diffuse the discontinuities on the smoothing scale. A general form for the *discontinuity capturing terms* (Monaghan, 1997) is given by,

$$\left(\frac{dA}{dt}\right)_{diss} = \sum_j m_j \frac{\alpha_A \mathrm{v_{sig}}}{\bar{\rho}_{ij}} (A_i - A_j) \hat{\mathbf{r}}_{\mathbf{ij}} \cdot \nabla \mathbf{W_{ij}}, \tag{3.41}$$

for a scalar parameter A, with α_A describing its amount of diffusion of order unity and $\mathrm{v_{sig}}$ being the estimation for the signal velocity between particle pairs. For example, if the SPH code conserves the energy a diffusion term can be added to the thermal energy equation,

$$\frac{du}{dt} = \frac{de}{dt} - \mathbf{v}\frac{d\mathbf{v}}{dt}, \tag{3.42}$$

which is the ATC as mentioned before. This results in,

$$\left(\frac{du}{dt}\right)_{diss} = -\sum_b \frac{m_b}{\bar{\rho}_{ab}} \left[\frac{1}{2}\alpha \mathrm{v_{sig}} \left(\mathbf{v_{ab}} \cdot \hat{\mathbf{r}}_{\mathbf{ab}}\right)^2 + \alpha_u \mathrm{v}^u_{\mathrm{sig}} \left(u_a - u_b\right)\right] \cdot \hat{\mathbf{r}}_{\mathbf{ab}} \cdot \nabla_a W_{ab}. \tag{3.43}$$

$\mathrm{v}^u_{\mathrm{sig}}$ is the signal velocity for the energy. With this method, the KHI should develop according to the test cases of P08.
In Fig. 3.13 we test whether the P08 approach is indeed in agreement with our analytical prediction. Note that P08 has a method implemented to account for the artificial viscous dissipation caused by AV (similar to the Balsara-viscosity). Thus, the viscous effects of AV are strongly reduced. For $DC = 10$ and using 512^2 particles in the dense layer we indeed find good agreement between measured and analytical growth rates. If the standard SPH scheme is used, a correction term like ATC has to be included to obtain a KHI in shear flows with different densities, which is consistent with the analytical prediction.

(ii) KHI GROWTH USING EQUAL AND DIFFERENT PARTICLE MASSES:
First, we investigate the development of the KHI for the standard SPH case of equal mass resolution throughout the computational domain, and therefore fewer particles in the low density fluid layer (see top panel of Fig. 3.10 for $DC = 10$, where the dense medium is resolved with 512^2 particles). This results in a varying spatial resolution, due to the fact that SPH derives the hydrodynamic quantities within a smoothing length h set by a fixed number of nearest neighbors. This construct – as has been discussed in detail earlier in e.g. Agertz *et al.* (2007) – specifically lowers the Reynolds-number of the shear flow across density discontinuities, thus affecting the evolution of the KHI. As can be seen in the top panel of Fig. 3.10, the KHI is completely suppressed.

Second, we test the case of equal spatial resolution in both fluid layers, and therefore unequal particle masses within the computational domain (Fig. 3.10, lower panel). Again, we find the KHI to grow too slowly with respect to the analytical estimate. However, the suppression is less effective in the latter case.

3.5 GRID-Simulations of the KHI

For comparison to the SPH treatment of Kelvin-Helmholtz instabilities, we study an identical setup of fluid layers with the grid-based codes FLASH, PROTEUS, PLUTO and RAMSES (see 3.3.2). We reuse the previously specified initial conditions with a grid resolution of 512^2 cells in the standard case. For FLASH and PROTEUS, we additionally include physical viscosity of various strength in some of the simulations (see 3.3.2). Note, that for the following examples we use $\sigma_0 = 1$ if not otherwise specified, which does not affect the growth of the amplitudes in the linear regime (for further information see discussion in the appendix A.3).

3.5.1 Fluid layers with equal densities

Non-viscous evolution

The upper panel of Fig. 3.14 shows the non-viscous KHI-evolution, using FLASH (solid line), PLUTO (dotted line), and for comparison VINE (dashed line). In the VINE example, the AV has been set to zero ($\alpha = \beta = 0$). The expected analytical growth (eq. (3.31)) reduces with $\nu = 0$ to $n \sim k \cdot U = 2.43$ (indicated by the thick dashed dotted line). The FLASH and PLUTO amplitudes develop in a similar pattern and are almost undistinguishable. Their fitted slopes within the linear regime (which lies roughly between $t = 0.3 - 0.6$) results in $n_{\mathrm{fit}} = 2.49$. FLASH and PLUTO show a consistent growth in agreement with the analytical prediction. VINE on the other hand exhibits a slightly slower growth. This deviation is due to the intrinsic viscosity ($\nu_{\mathrm{int}} = 0.065$) that was estimated in 3.4.1.
The upper panel of Fig. 3.15 shows the non-viscous KHI-evolution with PROTEUS (solid line) compared to its high resolution amplitude (dashed line) using 1024^2 particles. Note that for these examples we set $\sigma_0 = 0.1$, but this does not influence the KHI growth (see also appendix A.3).
The PROTEUS amplitude is damped by a factor of ~ 1.3 as compared to the analytical prediction (indicated by the thick dashed dotted line). Using a higher resolution does not change the amplitude growth. Thus, the resolution is not a contributing factor to solve the disagreement. PROTEUS underpredicts the linear KHI growth, see also the viscous evolution discussed in the following.

Viscous evolution

The bottom panel of Fig. 3.14 shows the viscous KHI-amplitudes using FLASH. The corresponding analytical predictions (eq. (3.31)) are shown by the thick dashed-dotted lines for the examples with $\nu = 0.00003$ and $\nu = 0.03$. To quantify the growth of the KHI in the FLASH simulations, we again fit the slopes of the KHI-amplitude in the linear regime (between $t = 0.3 - 0.6$). The result (diamond symbols) along with the corresponding error is plotted in Fig. 3.16. For small viscosities ($\nu < 0.003$), we find the growth rates of the KHI in FLASH to be in good agreement with the analytical prediction. In this viscosity range, the dominant term in the analytical prediction (eq. (3.31)) is $\sim kU$. Therefore, any influence of ν is marginal, and the amplitudes do not change considerably. FLASH treats the fluid

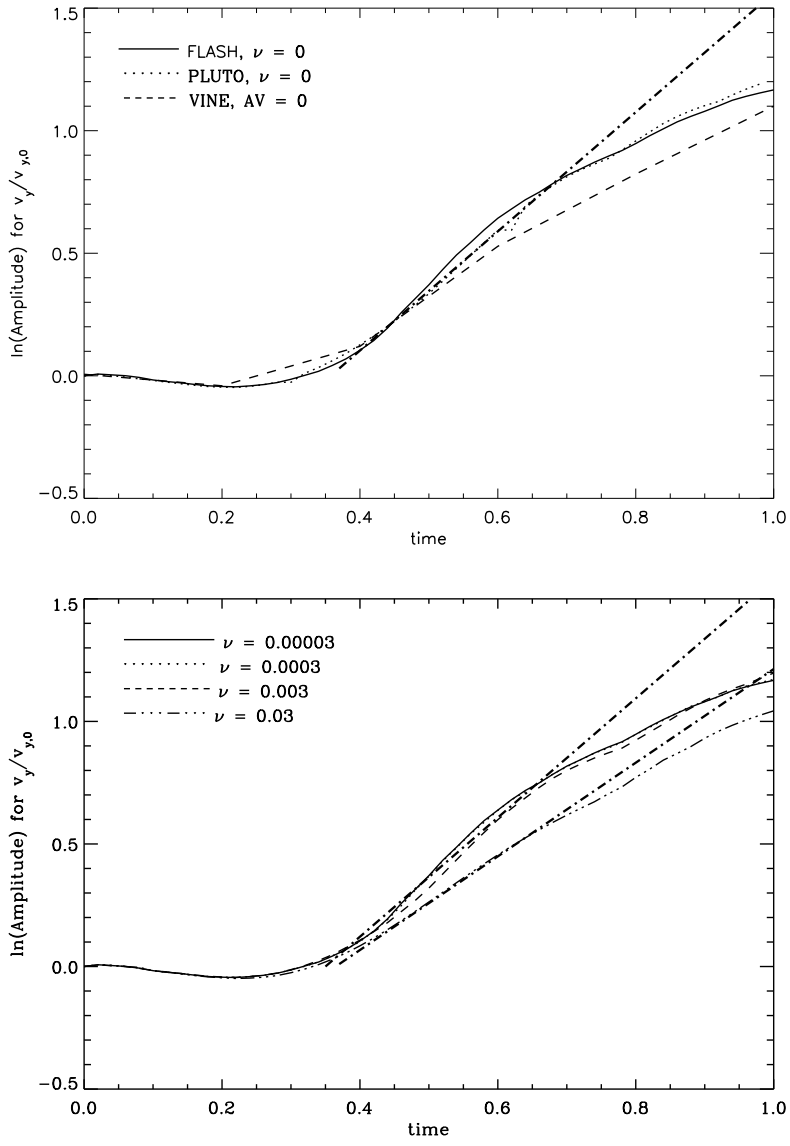

Figure 3.14: Evolution of KHI amplitudes for equal density layers. Upper panel: Non-viscous evolution for FLASH (solid line), and PLUTO (dotted line). Additionally, we show the example with VINE (dashed line), where the AV has been set to zero ($\alpha = \beta = 0$). Bottom panel: Viscous KHI evolution using FLASH. The thick dashed-dotted lines correspond to the analytical prediction, eq. (3.31).

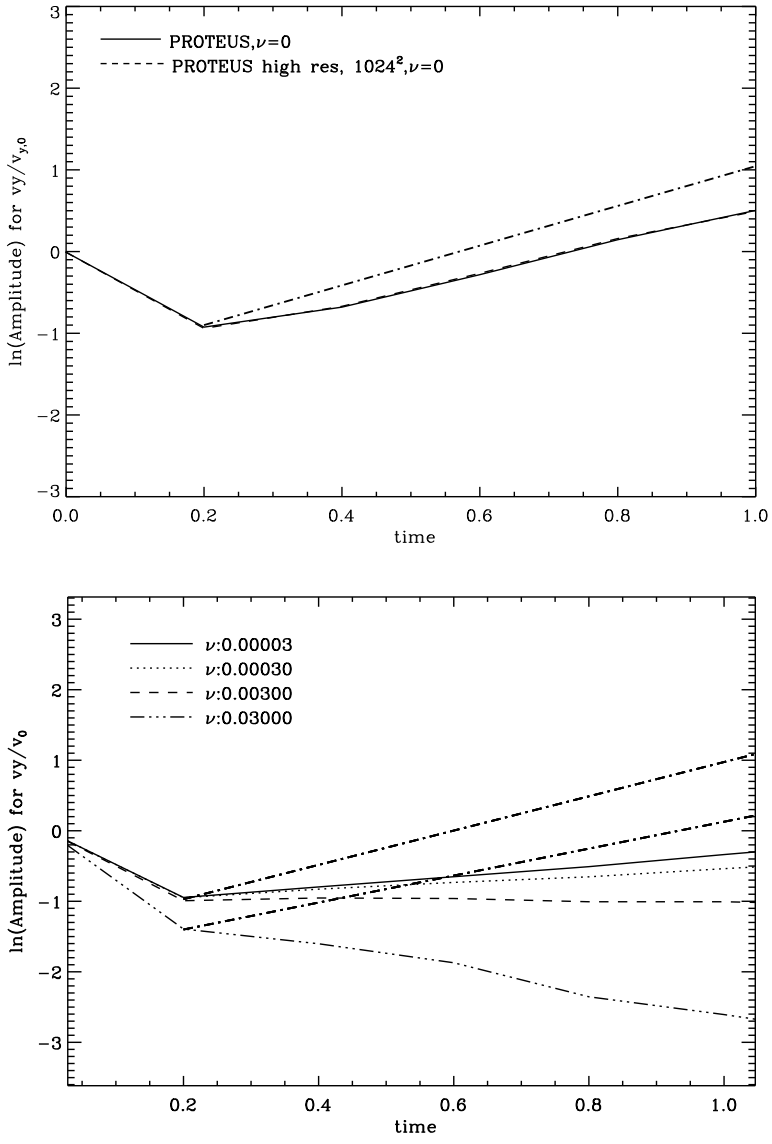

Figure 3.15: Evolution of KHI amplitudes using PROTEUS for equal density layers. Upper panel: Non-viscous evolution (solid line) compared to the high-resolution amplitude (dashed line). Bottom panel: Viscous KHI evolution. The thick dashed-dotted lines correspond to the analytical prediction, eq. (3.31). Note, that these examples use $\sigma_0 = 0.1$.

as if $\nu \approx 0$.
However, with increasing viscosity, the amplitudes should be damped. This behavior is in fact visible at the bottom panel of Fig. 3.14 (as well as in Fig. 3.16). The growth rates of the KHI agree very well with the analytical prediction.
The bottom panel of Fig. 3.15 presents the viscous KHI evolution using PROTEUS. The corresponding analytical predictions (eq. (3.31)) are shown by the thick dashed-dotted lines again for the examples with $\nu = 0.00003$ and $\nu = 0.03$. The fitted slopes underpredict the analytical expectation roughly by a factor of ~ 4 (see also the red diamond symbols in Fig. 3.16). Increasing ν leads to a decrease of the amplitudes as expected. However, already at a viscosity of $\nu \geq 0.003$ the KHI becomes completely suppressed.
Why does PROTEUS differ so dramatically? A possible explanation could be that we deal with a mixture of Eigenfunctions, when initiating the initial perturbation in PROTEUS. This might lead to a domination of decreasing modes over the increasing mode and thus, to a damped KHI evolution. To verify this possibility, we derive analytically the Eigenfunctions of the KHI and adjust our initial conditions correspondingly to eqs. (3.60)-(3.67) (see below). The Eigenfunctions excite only the growing mode of the KHI, the linear growth should therefore agree with the analytical expectation if the problem of PROTEUS is caused by decreasing modes.

PROTEUS with the KHI-Eigenmodes

We derive the Eigenmodes of the KHI for the case of equal fluid layers, i.e. where $\rho_1 = \rho_2 = \rho$, $U_1 = -U, U_2 = U$. The focus is on the direction of the perturbation (i.e. we consider the velocities u (x-direction) and w (z-direction), see also 3.2.2). In this case the perturbed equations (see section 3.2) reduce to,

$$
\begin{aligned}
i\rho(n+kU)\mathrm{u} + \rho(DU)\mathrm{w} &= -ik\delta p - \rho\nu k^2\mathrm{u} + \nu\rho(D^2U), && (3.44)\\
i\rho(n+kU)\mathrm{w} &= -(D\delta p) - \rho\nu k^2\mathrm{w} + \rho\nu(D^2\mathrm{w}), && (3.45)\\
i(n+kU)\delta\rho &= -\mathrm{w}(D\rho), && (3.46)\\
i(n+kU)\delta z_s &= \mathrm{w}(z_s), && (3.47)\\
i(k\mathrm{u}) &= -(D\mathrm{w}). && (3.48)
\end{aligned}
$$

Since $\rho = const.$, we have $D\rho = 0$, and therefore $\delta\rho = 0$. The Eigenfunctions are obtained referring to the following recipe:

- Chose one of the perturbed variables (u, w, δz_s, $\delta\rho$, δp)
- Recast the residual variables after the chosen quantity, for example, by chosing w we have to rewrite $u = u(\mathrm{w})$, $\delta z_s = \delta z_s(\mathrm{w})$, $\delta\rho = \delta\rho(\mathrm{w})$
- Replace the frequency n with the solution of the dispersion-relation for the growing modes

We chose the perturbed z-velocity (w) as the depending quantity, which has the following form (including the time as well as the spatial dependence),

$$
\begin{aligned}
\mathrm{w}_< &= A_<(n+kU_1)e^{+kz}e^{i(nt+kx)}\ (z<0) && (3.49)\\
\mathrm{w}_> &= A_>(n+kU_2)e^{-kz}e^{i(nt+kx)}\ (z>0). && (3.50)
\end{aligned}
$$

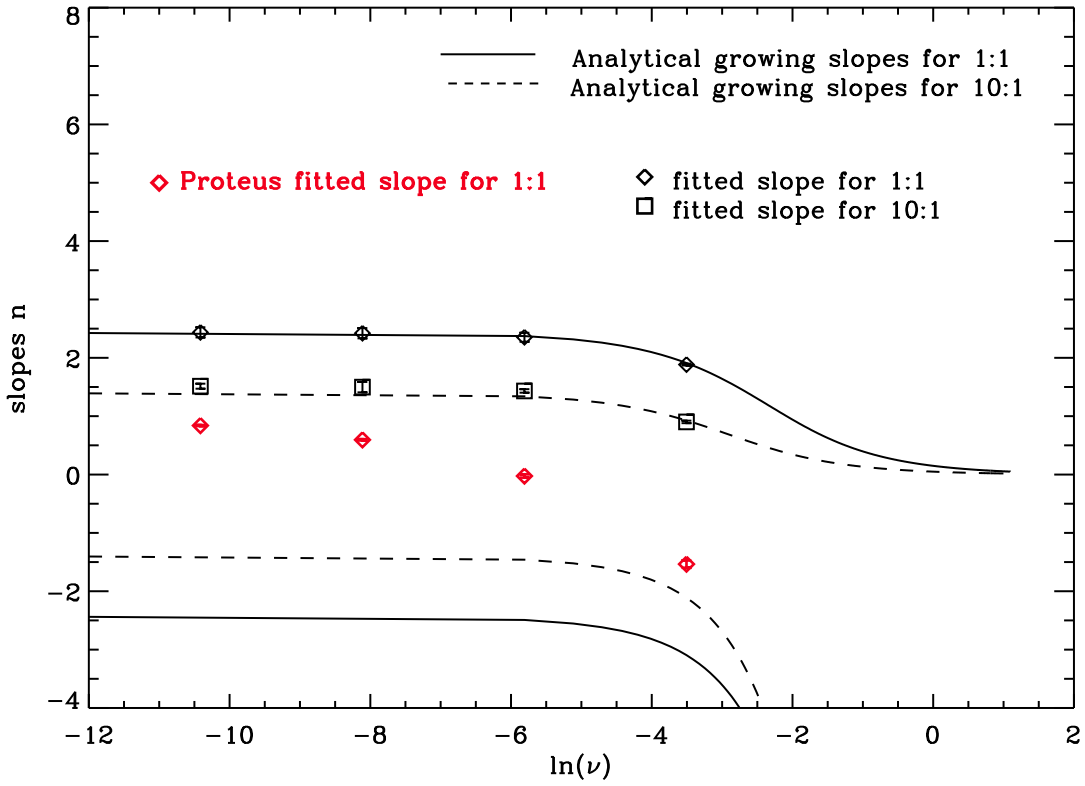

Figure 3.16: Comparison of the analytical expectation and the models for DC=1 (diamond shaped symbols, black for FLASH and red for PROTEUS) and $DC = 10$ (square symbols, only FLASH). The slopes derived for FLASH and PROTEUS correspond to the analytical fits. The lines represent the analytic prediction, for $DC = 1$ (solid line, see eq. (3.31)) and $DC = 10$ (dashed line, see eq. (3.30)).

At the interface ($z = z_s = 0$) the term $\frac{\mathrm{w}}{(n+kU)}$ must be continuous, which means

$$\left|\frac{\mathrm{w}_<}{(n+kU)}\right| = \left|\frac{\mathrm{w}_>}{(n-kU)}\right|,$$

using $U_1 = -U_2, U_2 = U$. Inserting $\mathrm{w}_{<,>}$ it follows from eq. (3.47),

$$\delta z_{s,<} = -iA_< e^{i(nt+kx)}, \tag{3.51}$$
$$\delta z_{s,>} = -iA_> e^{i(nt+kx)}, \tag{3.52}$$

while eq. (3.48) results in,

$$\mathrm{u}_< = iA_<(n+kU)e^{kz}e^{i(nt+kx)}, \tag{3.53}$$
$$\mathrm{u}_> = -iA_>(n-kU)e^{-kz}e^{i(nt+kx)}. \tag{3.54}$$

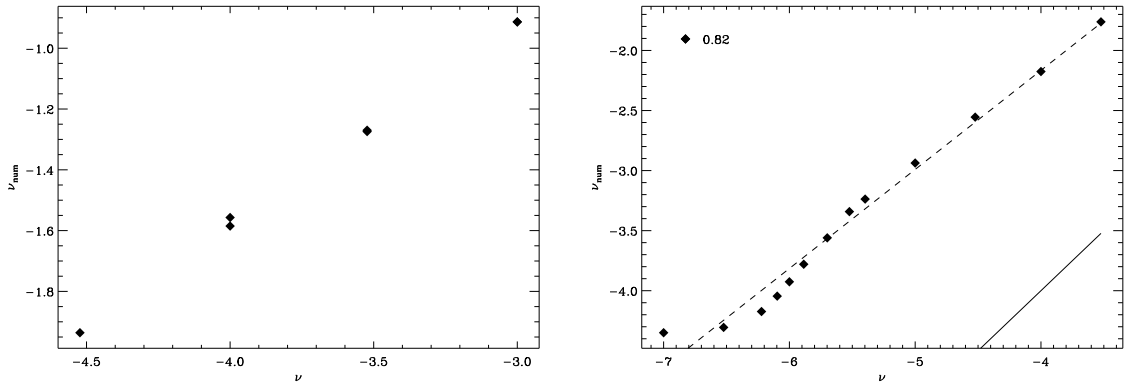

Figure 3.17: PROTEUS: Fitted viscosity ($\nu_{\rm num}$) against physical viscosity (ν) without using the KHI-Eigenfunctions (left side) and with the Eigenfunctions (right side). Note, that the x,y-axis is logarithmic. The solid line in the right plot denotes $\nu_{\rm num} = \nu$.

And for $\delta p_{<,>}$ using eq. (3.45) we have,

$$\delta p_{<} = -\frac{i}{k} A_{<} \rho (n + kU)^2 e^{kz} e^{i(nt+kx)}, \tag{3.55}$$

$$\delta p_{>} = \frac{i}{k} A_{>} \rho (n - kU)^2 e^{-kz} e^{i(nt+kx)}. \tag{3.56}$$

The solution of the dispersion-relation for the growing modes is determined by eq. (3.31),

$$n = i \left[\frac{\nu k^2}{2} - \sqrt{\frac{\nu^2 k^4}{4} + k^2 U^2} \right] = in', \tag{3.57}$$

where we introduced the abbreviation n'.
It follows at $t = 0$, $\mathrm{w}_{<}(t=0) = A_{<}(in' + kU) = \mathrm{w}_0$. Furthermore, the amplitude can be split into a real-part and a imaginary-part $(A_{<,>} = Re(A_{<,>}) + i \cdot Im(A_{<,>}))$,

$$A_{<} = \frac{\mathrm{w}_0 kU}{(n'^2 + k^2U^2)} - in' \frac{\mathrm{w}_0}{(n'^2 + k^2U^2)}, \tag{3.58}$$

$$A_{>} = -\frac{\mathrm{w}_0 kU}{(n'^2 + k^2U^2)} - in' \frac{\mathrm{w}_0}{(n'^2 + k^2U^2)}. \tag{3.59}$$

The absolute value of $w_{<,>}$ is given by $|w_{<,>}| = \sqrt{Re(w_{<,>})^2 + Im(w_{<,>})^2}$, the square-root of the real and imaginary part of $w_{<,>}$. Calculating the absolute values for our quantities,

$$|w_>| = w_0 \cdot \exp(-k \cdot z) \cdot \exp(-n' \cdot t), \tag{3.60}$$
$$|w_<| = w_0 \cdot \exp(k \cdot z) \cdot \exp(-n' \cdot t), \tag{3.61}$$
$$|u_>| = w_0 \cdot \exp(-k \cdot z) \cdot \exp(-n' \cdot t), \tag{3.62}$$
$$|u_<| = w_0 \cdot \exp(k \cdot z) \cdot \exp(-n' \cdot t), \tag{3.63}$$
$$|\delta z_{s,>}| = \frac{w_0}{\sqrt{n'^2 + k^2 U^2}} \cdot \exp(-n' \cdot t), \tag{3.64}$$
$$|\delta z_{s,<}| = \frac{w_0}{\sqrt{n'^2 + k^2 U^2}} \cdot \exp(-n' \cdot t), \tag{3.65}$$
$$|\delta p_>| = \frac{\rho}{k} \sqrt{n'^2 + k^2 U^2} w_0 \exp(-k \cdot z) \cdot \exp(-n' \cdot t), \tag{3.66}$$
$$|\delta p_<| = \frac{\rho}{k} \sqrt{n'^2 + k^2 U^2} w_0 \exp(k \cdot z) \cdot \exp(-n' \cdot t), \tag{3.67}$$

gives us the Eigenfunctions of the KHI.
For our simulations, w corresponds to v_y-velocity component with $w_0 = v_{y,0}$, respectively. The perturbed velocity-component in x-direction, u corresponds to $v_x = U + u$.

Applying the Eigenfunction improves the situation slightly, see Fig. 3.17 which presents the fitted viscosities (denoted here as $\nu_{num,}$) against the physical viscosities (ν) (left side without-, right side with Eigenfunctions). Note, that the x and y-axes are logarithmic. Despite this small enhancement, the fitted slopes are still too low. A mixture of Eigenfunctions is not the source of the problem.
Another possible scenario could be that the artificial intrinsic viscosity (ν_{int}) dominates. This effect appears in any numerical algorithm describing fluid dynamics, and is related to numerical noise. ν_{int} should be very small in most applications, but if not, it could dominate over the physical viscosity. If this is the case, then any viscous evolution using PROTEUS has to be regarded with caution. We therefore do not use PROTEUS for our further studies.

3.5.2 Fluid layers with different densities

Non-viscous evolution

Finally, we investigate a density contrast of 10 : 1, similar to the example studied with VINE (see 3.4.2). Fig. 3.18 shows the non-viscous evolution of the KHI for the $DC = 10$ case (upper line for FLASH, bottom line for PLUTO). It can be seen that for both codes the interface layer starts to roll-up and the instability is developed. This is in disagreement with the previously discussed case using SPH, where the KHI is completely suppressed for $DC > 6$ (see 3.4.2).
The upper panel of Fig. 3.19 presents the corresponding amplitudes for FLASH (solid line), PLUTO (dotted line) and RAMSES (three dotted dashed line) compared to the analytical prediction (thick dashed-dotted line), which in this case reduces to

$$n = \pm i \sqrt{4k^2 U^2 \alpha_1 \alpha_2}. \tag{3.68}$$

For FLASH we show two different resolutions (512^2 and 1024^2). The amplitudes resulting in the case of low and high resolution are effectively indistinguishable. This is an important result, as it

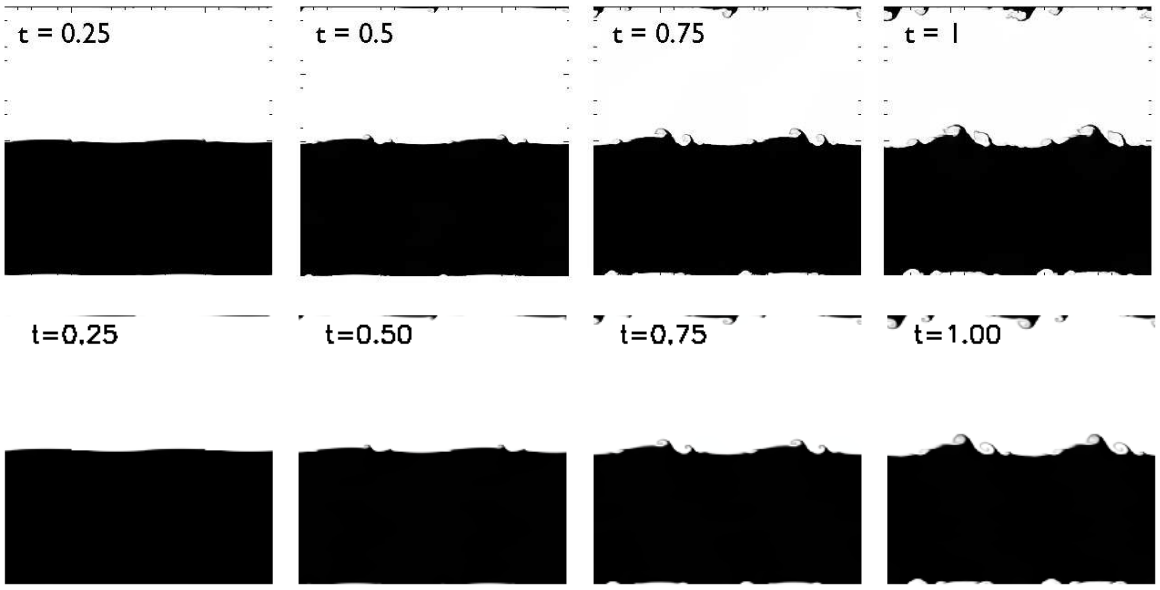

Figure 3.18: Time evolution of the KHI density in a simulation with $v = 0$ and $DC = 10$ for FLASH (top row) and PLUTO (bottom row). The plotted box size is from $[-1,1]$ in both directions, the resolution is 512^2. The KHI develops, which is in contrast to the example simulated with VINE.

demonstrates that small scale perturbations, which arise due to numerical noise and which could violate the linear analysis (as we then might follow the growth of higher order modes rather than the initial perturbation) are not important. Therefore, we have shown that our simulations are converged as we would otherwise expect the growth of the KHI to be slightly dependent on the grid resolution (see 3.5.3 and the recent findings of Robertson *et al.* (2009), who had to smooth the density gradient between the two fluid layers in order to achieve convergence in terms of grid resolution). Moreover, both FLASH and PLUTO evolve similarly. RAMSES begins to grow a bit later (at $t \sim 0.2$), which is due to the use of an diffusive solver (see also the discussion in the following paragraph). For all four examples the slope of the amplitude evolution can be approximated to 1.4, which is in good agreement with the analytical expectation. Note that we do not show the comparison with the VINE amplitude since the KHI does not evolve for $DC = 10$ (see 3.4.2).

Many grid codes offer a variety of hydrodynamical solvers. We therefore tested the influence of different numerical schemes on the growth of the KHI using PLUTO (see bottom panel of Fig. 3.19). We show three different examples; 'sim000' is a Lax-Friedrichs scheme together with a second order Runge-Kutta solver (tvdlf); 'sim001' implements a two-shock Riemann solver with linear reconstruction embedded in a second order Runge-Kutta scheme; 'sim002' also implements a two-shock Riemann solver, but with parabolic reconstruction, and embedded in a third order Runge-Kutta scheme. Both, 'sim001' and 'sim002' show a similar growth of the KHI in agreement with the analytical prediction (see Fig. 3.19, top right panel). The more diffusive scheme used in 'sim000' causes a small delay in the growth of the KHI, but results in a similar slope within the linear regime (up to $t = 0.6$).

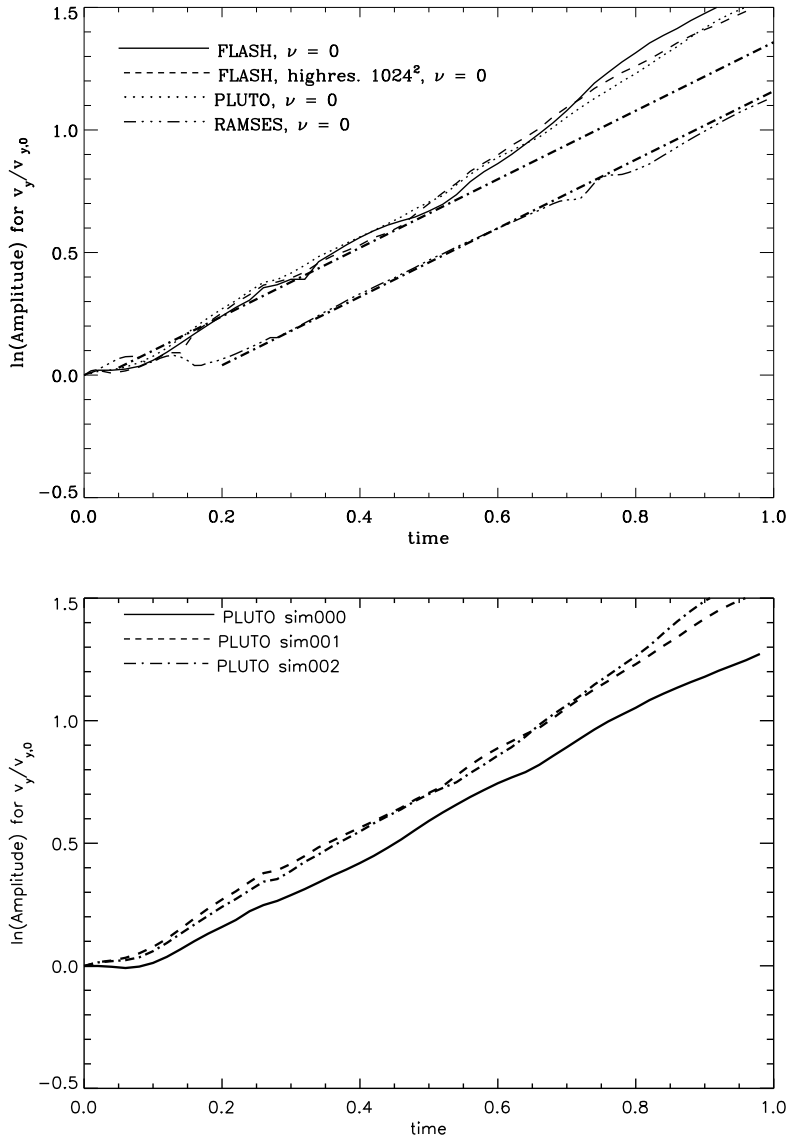

Figure 3.19: The same as in Fig. 3.14 but for a $DC = 10$. Upper panel: Non-viscous evolution for FLASH (solid line), PLUTO (dotted line), RAMSES (three dotted dashed line), and the high-resolution (1024^2) amplitude for FLASH (dashed line). Bottom panel: Non-viscous evolution using PLUTO, with different solvers, see text for more details.

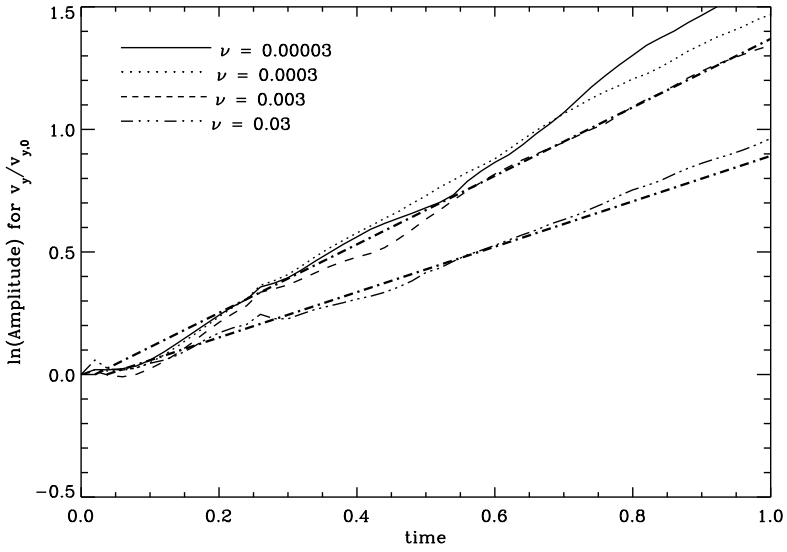

Figure 3.20: Viscous time evolution of KHI amplitudes using FLASH. The thick dashed-dotted lines correspond to the analytical prediction, eq. (3.30).

Viscous evolution

Fig. 3.20 shows the viscous KHI-amplitudes using FLASH, which are increasingly suppressed with increasing ν. The corresponding analytical prediction (eq. (3.30)) is shown for $\nu = 0.0003$, and $\nu = 0.03$ (thick dashed-dotted lines). For $\nu < 0.03$ the simulated growth rate is slightly enhanced by a factor of ~ 0.12 as compared to the analytical prediction (see also Fig. 3.16). However, for higher viscosities ($\nu \geq 0.03$) we find good agreement between simulation and analytical prediction.

3.5.3 FLASH with Smoothing

Robertson *et al.* (2009) introduced a ramp-function to suppress artificial small scale perturbations (see Fig. 3.18) in order to achieve convergence in grid simulations. To test this approach and its influence on the KHI-evolution, we implement a similar function which for our initial conditions takes the form

$$R(y) = \frac{1}{1+\exp\left[2y/\Delta_y\right]}. \tag{3.69}$$

Δ_y describes the smoothing over the cells in the y-direction, and the new density distribution follows as (Robertson *et al.*, 2009)

$$\rho(y) = \rho_1 + R(y)\left[\rho_2 - \rho_1\right]. \tag{3.70}$$

The flow-velocity U is given by

$$U(y) = U_1 + R(y)\cdot(U_2 - U_1), \tag{3.71}$$

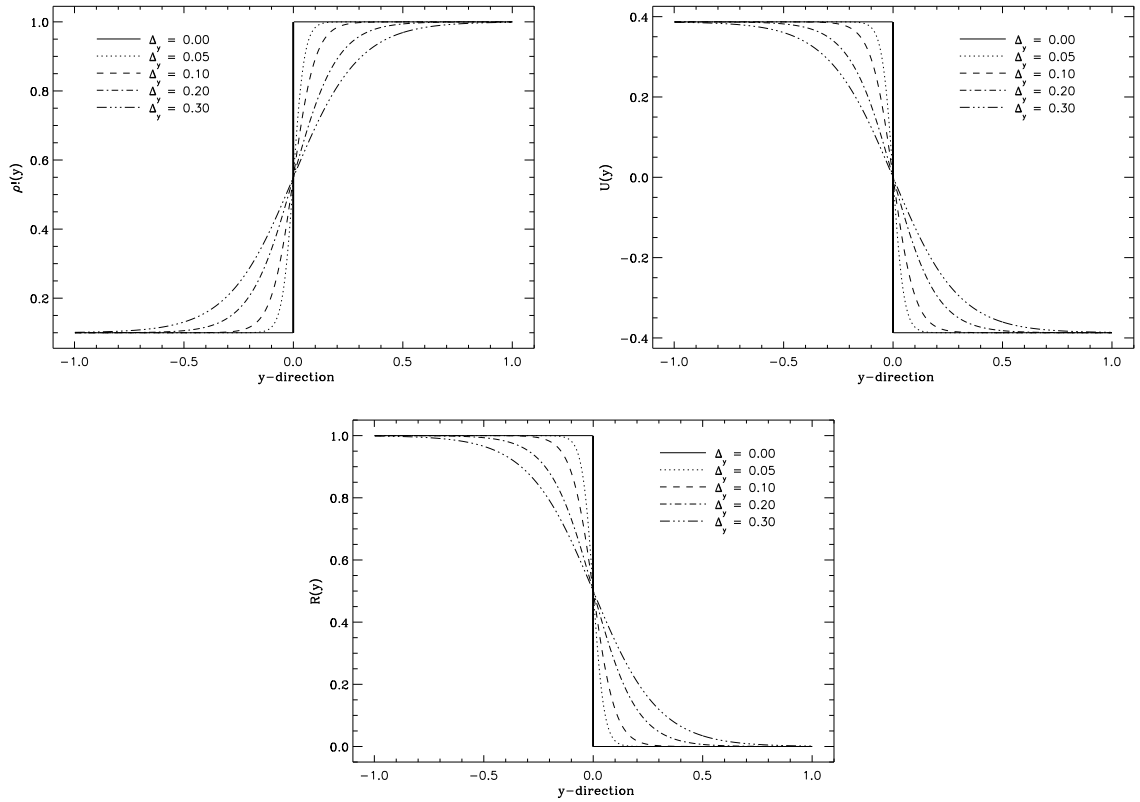

Figure 3.21: Top left panel: Initial density configuration varying with y, using different smoothing parameters, $\Delta_y = 0$ (no smoothing), $\Delta_y = 0.05$ (value used by Robertson *et al.* (2009)), $\Delta_y = 0.1$, 0.2, and 0.3, respectively. Top right panel: The same but for the flow-velocity U. Bottom panel: Corresponding ramp-functions (eq. (3.69)) varying with y.

with $U_2 = -U_1$. Fig. 3.21 shows the initial conditions using eq. (3.69): upper left panel the initial density (eq. (3.70)), upper right panel the initial flow-velocity (eq. (3.71)), and at the bottom panel the corresponding ramp-function (eq. (3.69)) for the smoothing parameters $\Delta_y = 0$ (no smoothing), $\Delta_y = 0.05$ (value used by Robertson *et al.*, 2009), $\Delta_y = 0.1$, and $\Delta_y = 0.2$.
Taking these initial settings we performed simulations using FLASH ($DC = 10$ and $\nu = 0$). Fig. 3.22 presents the KHI-evolution for $\Delta_y = 0.05$, 0.1, and 0.2 (the boxsize is from $[-0.5, 0.5]$). For $\Delta_y = 0.05$, as proposed by Robertson *et al.* (2009) the artificial perturbations completely vanish. The corresponding amplitude growth is shown in Fig. 3.23. Increasing Δ_y increases the diffusion at the interface and shifts the growth to later times. However, the slopes do not change (see Fig. 3.23). Using the ramp function to suppress artificial small scale perturbations does not alter the KHI-evolution, but delays the onset of the growth.

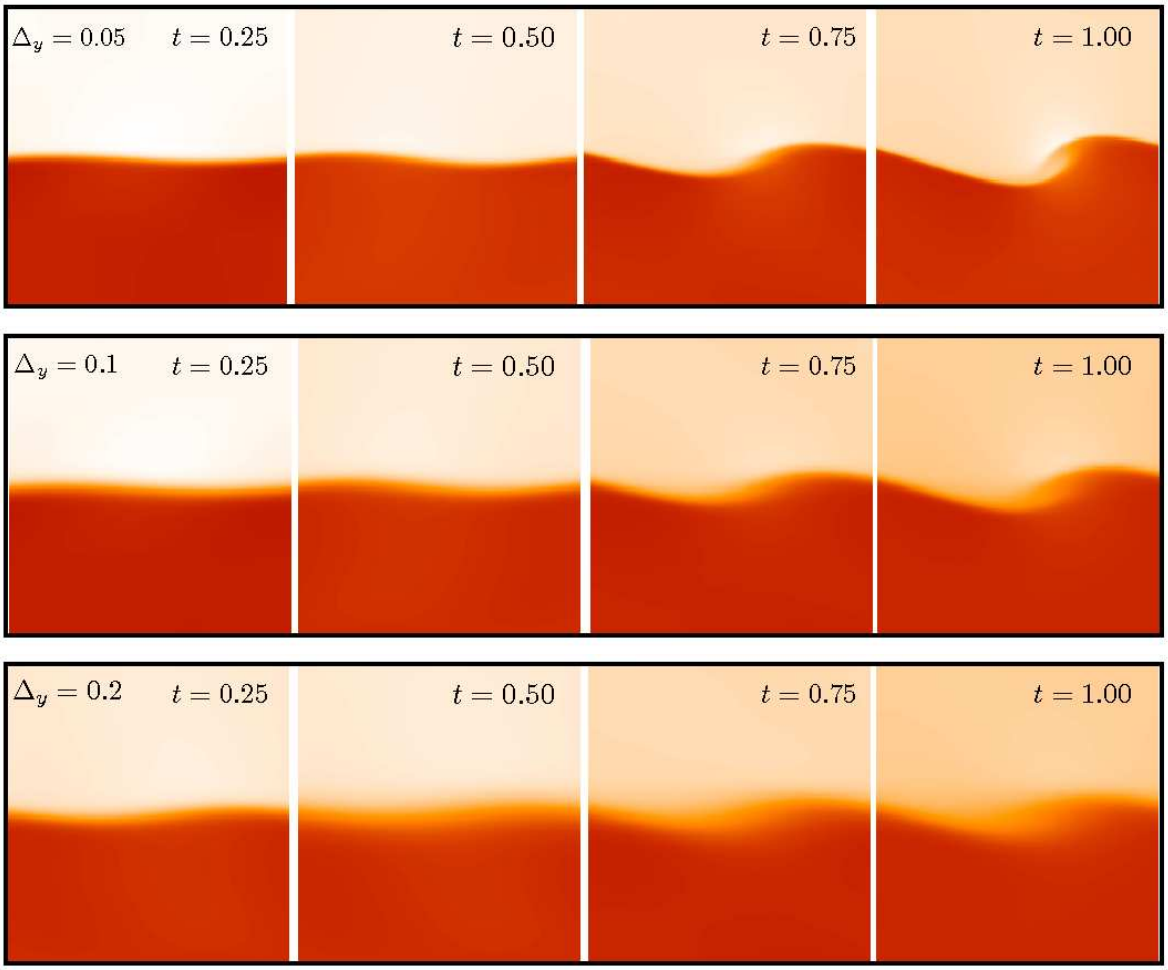

Figure 3.22: Time evolution of the KHI using FLASH, for increasing Δ_y (top to bottom) with $DC = 10$ and $\nu = 0$. The plotted box size is from $[-0.5, 0.5]$ in both directions.

3.6 Conclusions

We have studied the Kelvin-Helmholtz instability applying different numerical schemes. We use two methods for our SPH models, namely the Tree-SPH code VINE (Wetzstein *et al.*, 2009; Nelson *et al.*, 2009), and the code developed by Price (2008). The grid based simulations of the KHI rely on FLASH (Fryxell *et al.*, 2000), while as a test for the non-viscous evolution we also apply PLUTO (Mignone *et al.*, 2007).

We first extended the analytical prescription of the KHI by Chandrasekhar (1961) to include a constant viscosity. With this improvement we were able to measure the intrinsic viscosity of our subsequently performed numerical simulations. We test both SPH as well as grid codes with this method.

We then concentrated on the KHI-evolution with SPH. We performed a resolution study to measure the dependence of the KHI growth on the mean number of SPH neighbors ($\bar{n}_{SPH}$) and the total num-

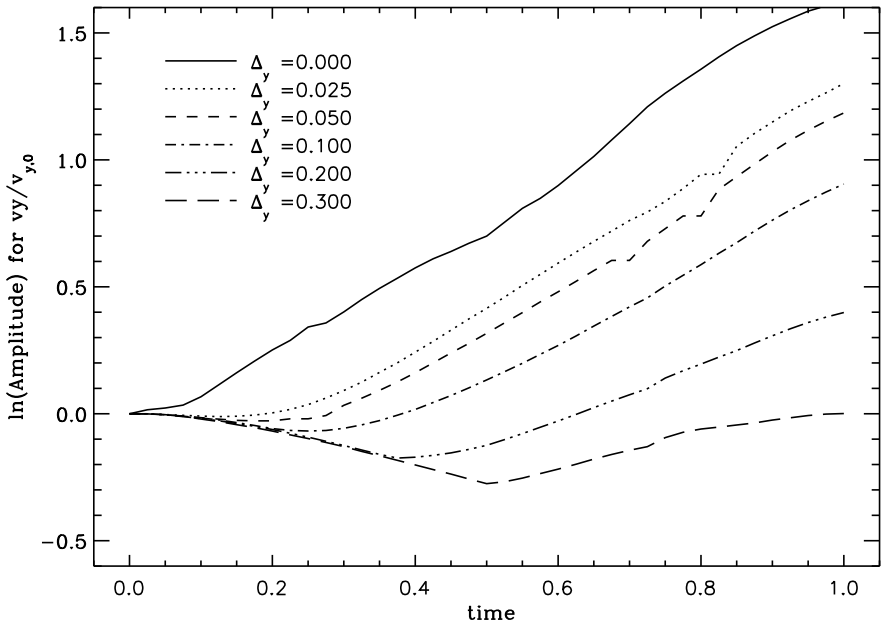

Figure 3.23: The same as Fig. 3.19 (upper panel) using FLASH but for different Δ_y's. From top to bottom increasing as $\Delta_y = 0, 0.025, 0.05, 0.1, 0.2,$ and 0.3, respectively.

ber of particles, respectively. We found that our simulations were well resolved and that a different number of $\bar{n}_{SPH}$ did not significantly influence the KHI growth rate.

In case of equal density shearing layers we then measured the intrinsic viscosity in VINE by evaluating our simulations against the analytical prediction in the linear regime. Without using the Balsara viscosity the AV parameters α and β effectively lead to a damping of the KHI. The commonly suggested and used settings of $\alpha = 1$, and $\beta = 2$ result in a strong suppression of the KHI. More quantitatively, we derive values of $0.065 < \nu_{\rm SPH} < 0.1$ for $0 < \alpha < 1$. Different values of β do not have a strong impact on $\nu_{\rm SPH}$. By introducing the Balsara-viscosity the dissipative effects of the AV can be reduced significantly, effectively rendering the results to be independent of α and β. However, the constant floor viscosity of $\nu_{\rm SPH} = 0.065$ prevails. Furthermore for a given α, we estimated the effective Reynolds-number (*Re*) of the flow. For the minimum SPH viscosity of $\nu_{\rm SPH} = 0.065$ we derive a maximum Reynolds number of 12. This is very small compared to typical Reynolds numbers of real turbulent flows ($Re > 10^5$). For different density shearing layers we confirmed the results discussed in Agertz *et al.* (2007), i.e. the KHI is completely suppressed for shear flows with different densities (in the case of VINE for $DC \geq 6$). Here, using the Balsara switch does not solve the problem. This indicates that other changes to the SPH formalism are required in order to correctly model shearing layers of different densities. To demonstrate this we applied the solution of Price (2008) to our initial conditions for DC=10. In this case the KHI was suppressed in VINE. However, we found good agreement between the analytically predicted amplitude evolution and the simulation of Price (2008) for $DC = 10$.

The second part of this chapter addresses the non-viscous- and viscous KHI evolution using grid

codes. In the case of equal density shearing layers, we found the non-viscous growth rates for shear flows with FLASH, PLUTO and RAMSES to be in good agreement with the analytical prediction. In the viscous case, the FLASH-amplitudes show only a minor dependency on the viscosity if $\nu < 0.03$. Increasing the viscosity leads to a damped evolution, with the simulated growth coinciding with the analytical prediction. However, PROTEUS disagrees and underpredicts the analytical growth by factor of ~ 1.3 in the non-viscous case, as well as in the viscous case where a complete suppression occurs at $\nu \geq 0.003$. Using the KHI-eigenfunctions as initial setup to prevent a possible dominance of decreasing modes does not solve the problem.
For non-viscous shear flows (with a density contrast of $DC = 10$) the KHI does develop for FLASH, PLUTO and RAMSES in agreement with the analytical prediction. In the viscous case FLASH (also analyzed with $DC = 10$) slightly overpredicts the corresponding growth rates for $\nu < 0.03$, it coincides with the analytical prediction when the slopes are multiplied by a constant factor of ~ 0.12. Finally, we use the ramp-function to smooth the contrast as proposed by Robertson *et al.* (2009) and test its influence on the non-viscous growth, which we find to be unaltered.
The comparison between VINE, FLASH and PLUTO in the equal density case, where $AV = 0$ and $\nu = 0$, demonstrated that VINE does have an intrinsic viscosity (which we estimated to $\nu_{\text{int}} \sim 0.065$). For simulations in three dimensions, we expect a similar problem for SPH when modelling the KHI with density contrasts, as already discussed by Agertz *et al.* (2007). This problem, due to the fixed entropy (or thermal energy) in the SPH formalism arises independently on the dimension, but is prevented using ATC .

Chapter 4

The Trace of Dark Energy captured within the CMB

4.1 Introduction

4.1.1 Definitions:

One of the most puzzling mysteries in cosmology is the recently detected accelerated expansion of the universe (Krauss & Turner, 1995; Ostriker & Steinhardt, 1995; Riess *et al.*, 1998; Perlmutter *et al.*, 1999; Netterfield *et al.*, 2002). It remains an unresolved question what mechanism causes this special behavior. Several different solutions have been proposed, the most popular one is the concept of dark energy (DE) which contributes about $\sim 70\%$ to the total energy density of the universe today,

$$\Omega^0_{\rm tot} = \Omega^0_{\rm M} + \Omega^0_{\rm DE}, \tag{4.1}$$

where the subscripts denote the values of total-, (dark and baryonic) matter- and DE- contributions at the present, indicated by the index 0 (see also Fig. 4.1). Widely accepted DE models are the cosmological constant (Λ) and quintessence.
The cosmological constant, first introduced by Einstein (1917) to obtain a static non-evolving universe is identified with the vacuum energy that fills the empty space and exhibits a negative pressure resulting in an acceleration of the expansion. A detailed summary is given in e.g. Padmanabhan (2003), see also in Peebles (1984) the constraint of inflation on cosmological models including Λ. However, this concept gives rise to a serious problem known as the *Cosmological-Constant-Problem* (Weinberg, 1989; Carroll, 2001; Padmanabhan, 2003). The observed magnitude of Λ is of order $\sim 10^{-123}$ smaller than the predicted value obtained from quantum-field theory. This results in a very fine-tuned value for Λ, the so-called fine-tuning problem. Another unresolved question refers to the point where it started to dominate over matter, known as the coincidence problem. If this would have happened early in the universe, the repulsive nature of Λ would have prohibited any formation of structures. On the other hand, if this event occurs at later epochs, no evidence for Λ would have been observed yet. Why this event happens exactly at the 'right moment' (about redshift ~ 0.7) is not understood.
The second proposed form for DE, the quintessence has its roots in particle physics and alleviates some of the problems involved with Λ. The idea to identify DE with an evolving dynamical scalar field including a non constant equation of state (i.e. the ratio of pressure to density expressed through $w_{\rm DE}$) was first introduced and discussed in detail by Wetterich (1988), Peebles & Ratra (1988), Ratra

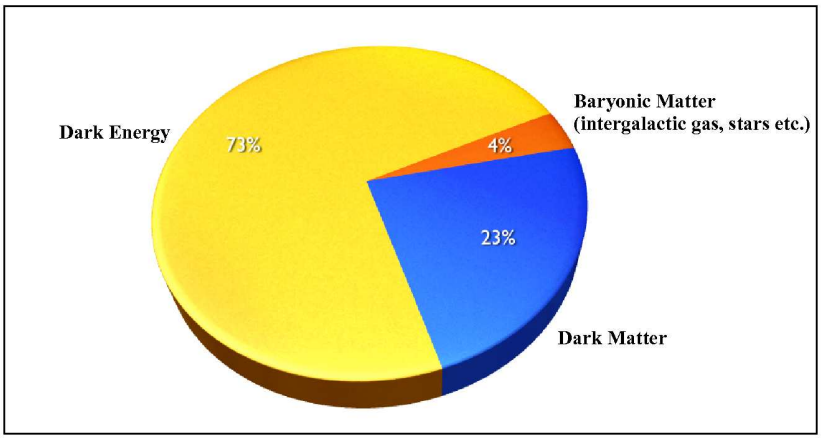

Figure 4.1: Contribution of energy densities in our universe today.

& Peebles (1988), and Caldwell *et al.* (1998). The Quintessence allows a form of DE which behaves like Λ at late times, but starts from a different value at earlier times. This soothes somewhat the fine-tuning problem (Liddle & Scherrer, 1999; Steinhardt *et al.*, 1999). The application of quintessence is wide, ranging from particle physics (e.g. Masiero *et al.*, 2000) to cosmology (e.g. Coble *et al.*, 1997; Ferreira & Joyce, 1998).

4.1.2 Earlier Studies:

The question, which form of DE our universe possesses can only be answered by astrophysical observations. DE, and thus, the acceleration is parameterized through $w_{\rm DE}$, whose determination (the exact value or functional form) is the central point in order to distinguish between different models. Beside the important measurements of supernovae type Ia (SNIa) (Krauss & Turner, 1995; Ostriker & Steinhardt, 1995; Riess *et al.*, 1998; Perlmutter *et al.*, 1999; Netterfield *et al.*, 2002) and large scale structures (LSS) (e.g. Dodelson *et al.*, 2002) is the cosmic microwave background (CMB), detected in the 1960th by Penzias & Wilson (1965) measured to high accuracy by several still ongoing experiments, e.g. balloon based like BOOMERanG (de Bernardis *et al.*, 2000), MAXIMA (Hanany *et al.*, 2000; Balbi *et al.*, 2000, 2001), Archeops (Benoît *et al.*, 2003a,b), or satellite based experiments, like COBE (Bennett *et al.*, 1996), WMAP (Spergel *et al.*, 2003, 2007; Komatsu *et al.*, 2009) and PLANCK[1]. The interaction of CMB photons with their surrounding environment results in anisotropies, which are imprinted as fluctuations in their temperature (see also Fig. 1.3). The primordial anisotropies contain information about the universe before the photons have decoupled from the baryons and leave a Gaussian signal within the CMB temperature. The secondary anisotropies arise after the decoupling, as the photons travel freely through the universe and interact with forming structures. Since DE influences the growth of cosmic structures, they contain information about DE in form of non-Gaussian contributions. In particular, the *Rees-Sciama* (RS)-effect, a combination of the *Integrated-Sachs-Wolfe* (ISW)-effect (the late time decay of the potential fluctuations) and the nonlinear growth of density fluctuations (Rees & Sciama, 1968) induces, in addition to gravitational deflection of photons these

[1] see http://www.sciops.esa.int

secondary anisotropies in the CMB (e.g. Goldberg & Spergel, 1999; Zaldarriaga, 2000). Therefore, comparisons of measured and theoretical calculated angular distributions of temperature fluctuations (in terms of correlation functions, i.e. power- and bispectrum) allow to set important constraints on cosmological parameters.
The three-point-correlation function (bispectrum), most sensitive to non-Gaussian contributions is very useful to trace the imprint of nonlinear growth in order to set limits on $w_{\rm DE}$. This has been the main issue of previous studies (e.g. Spergel & Goldberg, 1999; Goldberg & Spergel, 1999; Komatsu, 2002; Verde & Spergel, 2002; Cooray & Hu, 2001; Serra & Cooray, 2008; Hanson *et al.*, 2009). Including the lensing contribution, we analyze the theoretical cross correlation bispectrum between the primordial-, lensing-, and RS-effect (L-RS bispectrum). A similar analysis considering a cosmological constant has been done by Verde & Spergel (2002). For further studies see also Giovi *et al.* (2003), and Giovi *et al.* (2005). We extend this study in allowing a time-varying equation of state for the DE-component. Our main focus is on *early quintessence* (Wetterich, 2004), a special form of DE, which does exhibit non-negligible contributions at earlier epochs (unlike the cosmological constant, that becomes dominant at late times). Several studies in this context have been done e.g. Caldwell *et al.* (2003), Barreiro *et al.* (2003), Caldwell & Doran (2004), Wang & Tegmark (2004), Bartelmann *et al.* (2006) and Grossi & Springel (2009).

4.1.3 Outline:

In this chapter we calculate the theoretical L-RS bispectrum and the corresponding signal-to-noise (S/N) ratio for different quintessence models. The (S/N) ratio is used to approximate how accurate future experiments, like PLANCK can distinguish between these models.
We start by giving a short introduction of the cosmological basics necessary for our study in section 4.2. In section 4.3, we introduce in detail the quintessence models following Wetterich (2004) (WETT04), Linder (2003a,b) (LIND03) and Komatsu *et al.* (2009) (KOMAT09), where we also discuss DE models with constant equation of states. Since the RS-effect depends on the linear as well as on the nonlinear evolution of density fluctuations, we need a description for the linear- and the nonlinear regime. In section 4.4 we therefore introduce this in form of the nonlinear power spectrum. To test the dependency of our results on the used model, we compare three different approaches, cosmological perturbation theory based on Bernardeau *et al.* (2002) (PT) and the fitting formulae following Ma *et al.* (1999) (MA99), and Smith *et al.* (2003) (HALOFIT), respectively. For a related study of power spectra in this context see Mangilli & Verde (2009). The analysis of the L-RS bispectrum and the (S/N) ratio is carried out in section 4.6 and section 4.7. Finally, we summarize our results in the section 4.8.

4.2 Cosmological Basics

This section outlines the basic principles of cosmology, which are fundamental to study the evolution of the universe and its dependence on the various kinds of energy density, in particular dark energy. Important quantities, which are needed in the following sections are defined.
We begin in 4.2.1 with reviewing Einsteins gravitational theory, the most crucial fundament for cosmology. The cosmological principles, explained in 4.2.2 set the basic assumptions to describe the kinematical and the dynamical evolution of our universe. The Hubble-law, the cosmological redshift and the conformal distance are introduced in 4.2.3, while the Robertson-Walker metric (which

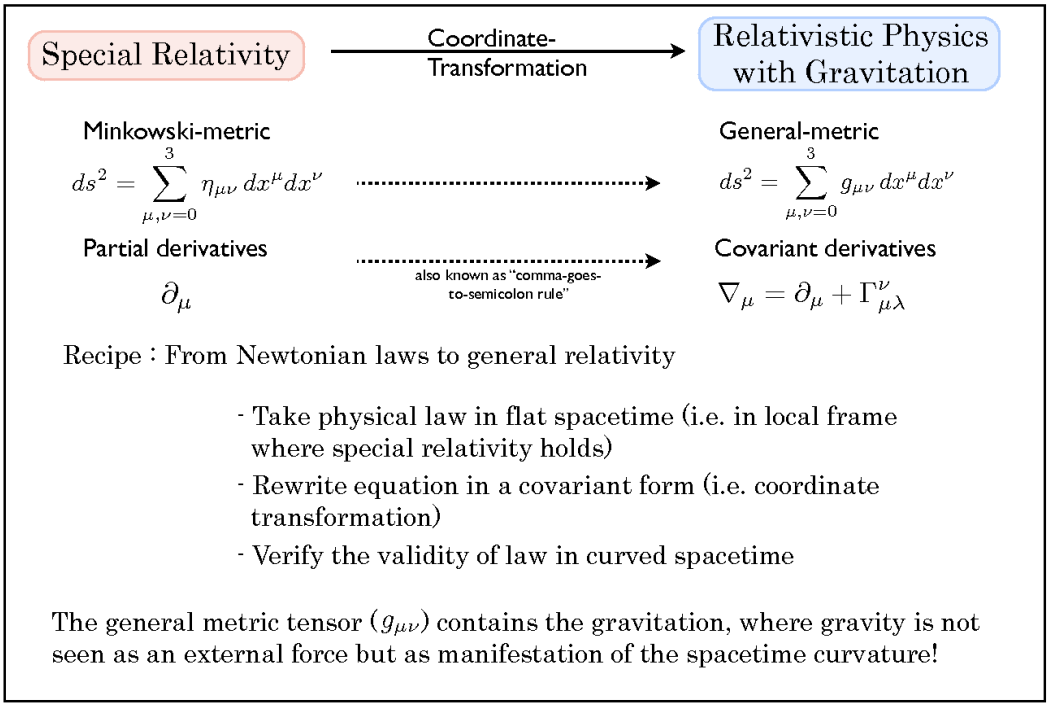

Figure 4.2: Recipe: From Newtonian to general relativistic physics.

expresses the basic assumptions of isotropy and homogeneity) is defined in 4.2.4. The Friedmann-equations, given in 4.2.5 quantify the evolution of the scalefactor and the corresponding energy densities. The growth factor, motivated in 4.2.6 characterizes the linear growth of structures. 4.2.7 describes the special case of a universe containing dark matter and dark energy, which is our frame of reference. Finally, we outline the statistical description of perturbation theory in 4.2.8.
A more detailed introduction can be found in e.g. Padmanabhan (1993), Padmanabhan (2003), Dodelson (2003), Mukhanov (2005) and Schneider (2006).

4.2.1 General Relativity

General relativity (GR) is a complete and consistent theory of gravity describing relativistic matter with a general equation of state valid on all scales. Gravity itself is not identified as an external force but as a consequence of the spacetime curvature. GR is based on the so-called equivalence principle:

- The inertial- and gravitational mass are indistinguishable (weak equivalence principle). Let us consider an observer confined in a capsule without any connection to the outside world. He cannot distinguish by experiment (like studying the motion of test objects) if he is in an accelerating frame (rocket) or sitting on earth surface in its gravitational field.

- In small enough regions of spacetime (local inertial systems) the theory of special relativity (SRT) without gravitation is valid (strong equivalence principle).

The weak equivalence principle emphasizes the universality of gravity, which couples to all masses in the same way. The strong equivalence principle states that in small regions the spacetime metric reduces locally to the Euclidean metric

$$ds^2 = \eta_{\mu\nu} dx^\mu dx^\nu, \tag{4.2}$$

where $\eta_{\mu\nu}$ is given by

$$\eta_{\mu\nu} = \begin{pmatrix} 1 & 0 & 0 & 0 \\ 0 & -1 & 0 & 0 \\ 0 & 0 & -1 & 0 \\ 0 & 0 & 0 & -1 \end{pmatrix} \tag{4.3}$$

and the indices μ, ν run over $0,1,2,3$ using Einsteins summing convention (the units are set so that $c = 1$). Starting from these principles, it is possible to obtain relativistic relations including gravity by transforming physical laws from a locally flat spacetime (e.g. the rocket) into a covariant form with the general spacetime metric

$$ds^2 = g_{\mu\nu} dx^\mu dx^\nu, \tag{4.4}$$

where $g_{\mu\nu}$ is the metric tensor whose components describe gravitation (see also Fig. 4.2). The metric tensor determines the properties of the space, in particular, its curvature. The form of $g_{\mu\nu}$ depends on the choice of coordinates.
The field equations, which describe the reaction of the metric towards energy and momentum are the well known Einstein-equations, which we motivate below.
The Einstein equations follow from the variation of the Hilbert-Einstein action, (see e.g. Padmanabhan, 2003)

$$S = \frac{1}{16\pi G} \int R\sqrt{-g} d^4x + \int L_{\mathrm{M}}(\phi, \partial\phi)\sqrt{-g} d^4x, \tag{4.5}$$

where L_{M} characterizes the matter-Lagrangian, which depends for example on the dynamical variable ϕ with g being the determinant of $g_{\mu\nu}$ and R the *Ricci-scalar* characterizing the trace of the *Ricci-tensor* $R_{\mu\nu}$

$$R_{\mu\nu} = \frac{\partial \Gamma^\alpha_{\mu\nu}}{\partial x^\alpha} - \frac{\partial \Gamma^\alpha_{\mu\alpha}}{\partial x^\nu} + \Gamma^\alpha_{\beta\alpha}\Gamma^\beta_{\mu\nu} - \Gamma^\alpha_{\beta\nu}\Gamma^\beta_{\mu\alpha}. \tag{4.6}$$

The *Christoffel-symbols* $\Gamma^\alpha_{\mu\nu}$ are defined as

$$\Gamma^\alpha_{\mu\nu} = \frac{1}{2} g^{\alpha\delta} \left(\frac{\partial g_{\mu\delta}}{\partial x^\nu} + \frac{\partial g_{\delta\nu}}{\partial x^\mu} - \frac{\partial g_{\mu\nu}}{\partial x^\delta} \right). \tag{4.7}$$

Variation of S with respect to the metric tensor $g_{\mu\nu}$ results in,

$$\frac{1}{\sqrt{-g}} \frac{\delta S}{\delta g^{\mu\nu}} = \frac{1}{16\pi G} \left(R_{\mu\nu} - \frac{1}{2} g_{\mu\nu} R \right) - \frac{1}{\sqrt{-g}} \frac{\delta(\sqrt{-g} L_{\mathrm{M}})}{\delta g^{\mu\nu}} = 0. \tag{4.8}$$

Identifying

$$T_{\mu\nu} = -2 \frac{1}{\sqrt{-g}} \frac{\delta(\sqrt{-g} L_{\mathrm{M}})}{\delta g^{\mu\nu}} \tag{4.9}$$

with the energy-momentum tensor that accounts for the matter contribution and acts as source we obtain the Einstein equations,

$$R_{\mu\nu} - \frac{1}{2} g_{\mu\nu} R = 8\pi G T_{\mu\nu}. \tag{4.10}$$

A characteristic feature arises from the fact that the source is the entire energy-momentum tensor. Unlike in non-gravitational physics, where only changes in energy from one state to another can be measured and the normalization of the energy is arbitrary, in gravitational physics the actual value of energy matters. A constant shift in the energy (equal to a different normalization) allows an additional contribution to the action (eq. (4.5)). Let us consider a matter Lagrangian with an additional constant term, i.e.

$$L'_{\mathrm{M}} = L_{\mathrm{M}} - \left(\frac{\Lambda}{8\pi G} \right), \tag{4.11}$$

($\Lambda = const.$). The equations of motion for matter ($\delta L_{\mathrm{M}} / \delta \phi = 0$) do not change, but the action can be interpreted differently (see e.g. Padmanabhan, 2003), more precisely by

$$S = \frac{1}{16\pi G} \int R \sqrt{-g} d^4x + \int \left(L_{\mathrm{M}} - \frac{\Lambda}{8\pi G} \right) \sqrt{-g} d^4x \tag{4.12}$$

or

$$S = \frac{1}{16\pi G} \int (R - 2\Lambda) \sqrt{-g} d^4x + \int L_{\mathrm{M}} \sqrt{-g} d^4x. \tag{4.13}$$

In the first case, eq. (4.12) characterizes Λ as a shift in L_{M}, which is equal to a shift in the matter Hamiltonian and therefore, a shift in the null point energy. The dynamic of matter remains unchanged, yet Gravitation gets an additional contribution,

$$R_{\mu\nu} - \frac{1}{2} g_{\mu\nu} R = 8\pi G \left(T_{\mu\nu} + \frac{\Lambda}{8\pi G} g_{\mu\nu} \right). \tag{4.14}$$

This additional term can be identified as $\Lambda / (8\pi G) g_{\mu\nu} \equiv \rho_{\mathrm{vac}}\, g_{\mu\nu}$, with ρ_{vac} the vacuum energy density which we discuss in detail in 4.3.1.
In the second case, eq. (4.13) describes Gravitation through two constants, Newtons gravitational constant G and Λ. The Einstein equations can be written as

$$R_{\mu\nu} - \frac{1}{2} g_{\mu\nu} R - g_{\mu\nu} \Lambda = 8\pi G T_{\mu\nu}. \tag{4.15}$$

The space-time is curved even in absence of matter ($T_{\mu\nu} = 0$). This is an unusual situation, for more details see Padmanabhan (2003).
A mixture between both effects is also possible. Interaction with matter is determined by $(R - 2\Lambda)$, which implies an intrinsic cosmological constant. L_{M} can have constant shifts if the energy densities change during the dynamical evolution. Let us assume the matter-Lagrangian of a classical scalar field ϕ with the potential $V(\phi)$,

$$L_{\mathrm{M}} = -\frac{1}{2} g^{\mu\nu} \nabla_\mu \phi \nabla_\nu \phi - V(\phi), \tag{4.16}$$

and the energy momentum tensor,

$$T_{\mu\nu}^{(\phi)} = \nabla_\mu\phi\nabla_\nu\phi - \frac{1}{2}g_{\mu\nu}g^{\rho\sigma}\nabla_\rho\phi\nabla_\sigma\phi - g_{\mu\nu}V(\phi), \tag{4.17}$$

where we introduced the covariant derivative

$$\nabla_\mu = \partial_\mu + \Gamma^\nu_{\mu\lambda}. \tag{4.18}$$

If the field configuration is constant, e.g. at the minimum of the potential $V(\phi)$ the energy impulse tensor takes the form of a cosmological constant,

$$T_{\mu\nu}^{\text{eff}} = \left[V(\phi_{\text{min}}) + \frac{\Lambda}{8\pi G}\right] g_{\mu\nu}, \tag{4.19}$$

with,

$$\Lambda_{\text{eff}} = \Lambda + 8\pi G V(\phi_{\text{min}}). \tag{4.20}$$

If ϕ_{min} and $V(\phi_{\text{min}})$ change during the dynamical evolution, so does Λ_{eff}. Any field configuration that varies slowly with time will result in a slowly varying Λ_{eff}. This scalar field description - the quintessence - is important since it allows to characterize alternative forms for DE, which are discussed in 4.3.2.

4.2.2 Cosmological Principles

Our standard cosmology is based on two basic assumptions:

- The distribution of matter in the universe is homogeneous and isotropic at sufficiently large scales (> 100 Mpc[2]).
- Gravitational interaction determines the large scale structure, which is described by GR. The geometry follows from the Einstein-equations with the tensor $T_{\mu\nu}$ acting as source.

The first principle sets the kinematical evolution of the universe as a time ordered number of three dimensional hypersurfaces of constant time (each one homogeneous and isotropic). The universe is expanding (see 4.2.3) and thus, to conserve isotropy and homogeneity the curvature scale has to be time dependent. Furthermore, this gives rise to a special metric, see 4.2.4.
The second principle sets the dynamical evolution of the universe with GR as fundament. The gravitational interaction with matter follows from the solution of eq. (4.10) with the corresponding $T_{\mu\nu}$. First order perturbation theory allows to study the linear evolution of density fluctuations, which we discuss in the Newtonian limit in 4.2.6. In the following we define the most fundamental quantities in cosmology.

[2] The unit parsec [pc] is an astrophysical measure of distance and defined as the distance an astronomical unit (1 AU: mean distance between earth and sun) would appear under an angle of 1 arc-second ($1" = 1/3600^\circ$). 1 Parsec = 3.0856802510^{16} meters.

4.2.3 Hubble-Law, Cosmological Redshift and Conformal Distance

An important discovery was the expansion of the universe, first observed by Edwin Hubble in 1929 and therefore known as the Hubble law,

$$\mathbf{v_0} = H(t) \cdot \mathbf{x} \text{ or, } \dot{\mathbf{x}}_0 = H(t)\mathbf{x}. \tag{4.21}$$

Eq. (4.21) connects the relative velocity $\mathbf{v_0}$ of two observers having the relative distance $\mathbf{x}$ in an expanding, homogeneous and isotropic universe. The dot denotes the derivative with respect to time ($\dot{\mathbf{x}} = d\mathbf{x}/dt$). The parameter $H(t)$ is the time dependent *Hubble-constant*. (In this context, the meaning of "constant" refers to its independence on spatial coordinates.) Integrating eq. (4.21) leads to,

$$\mathbf{x} = a(t)\mathbf{r}, \tag{4.22}$$

with the scalefactor $a(t)$,

$$a(t) = \exp\left(\int H(t)dt\right), \tag{4.23}$$

and $\mathbf{r}$ the conformal or comoving distance between the two observers. The scalefactor is normalized to its value today at $t = t_0$, such that $a(t_0) = 1$. It then describes the distance as a function of time. The Hubble-constant can be rewritten as,

$$H(t) = \frac{\dot{a}(t)}{a(t)}, \tag{4.24}$$

defining the expansion rate of the universe. Todays value is often denoted by $H(t = t_0) \equiv H_0$, and a common convention is:

$$H_0 = h \cdot 100\,\mathrm{km\,s^{-1}\,Mpc^{-1}}, \tag{4.25}$$

where we use $h = 0.702$ obtained from Komatsu *et al.* (2009) (see also table 4.1 for the other cosmological values).
The absolute value of the comoving distance can then be expressed through the scalefactor $a(t)$,

$$r(a) = \int_a^1 \frac{da'}{a'^2 H(a')}. \tag{4.26}$$

Another very important parameter is the cosmological redshift characterized by z. Because of the continuous creation of space, objects like galaxies are drifting away form us. The wavelength of an emitted photon λ_{emit}, which reaches us at the present time with a wavelength λ_{obs}, has been stretched by the factor the Universe has expanded,

$$z = \frac{\lambda_{\mathrm{obs}} - \lambda_{\mathrm{emit}}}{\lambda_{\mathrm{emit}}}. \tag{4.27}$$

In terms of the scalefactor a it follows,

$$1 + z = \frac{1}{a(t_{\mathrm{emit}})}. \tag{4.28}$$

To describe the time-dependence of cosmological quantities, it can be helpful to either use the cosmological redshift z or the scalefactor a, connected via eq. (4.28). The explicit time-dependence follows from $a(t)$ determined by the solution of the Friedmann equations (eqs. (4.56), (4.57)). For example, the comoving distance (eq. (4.26)) expressed through z results in (see also eq. (4.41))

$$r(z) = \frac{1}{H_0}\int_0^z \frac{dz'}{H(z')} = \frac{1}{H_0^2}\int_0^z dz' \left((1-\Omega_0)(1+z')^2 + \Omega_0 \frac{\rho(z')}{\rho_0}\right)^{-1/2}. \tag{4.29}$$

4.2.4 Roberston-Walker Metric

The underlying metric satisfying the fundamental principles of isotropy and homogeneity is known as the *Robertson-Walker-metric* (RWM),

$$ds^2 = c^2dt^2 - a^2(t)\left[\frac{dr^2}{1-kr^2} + r^2 \cdot d\Omega^2\right] \equiv g_{\mu\nu}dx^\mu dx^\nu, \tag{4.30}$$

with $d\Omega^2 = (d\Theta^2 + \sin^2\Theta d\phi^2)$ and the coordinates given by $x^\mu = x(t,r,\Theta,\phi)$. The curvature of the spatial part of the metric is characterized through k, and becomes Euclidean if $k = 0$. The corresponding density is called *critical density*:

$$\rho_c(t) = \frac{3H^2(t)}{8\pi G}. \tag{4.31}$$

If the universe has a density higher than $\rho_c(t)$, $\rho(t) > \rho_c(t)$ then $k = +1$ (closed universe), whereas a lower value $\rho(t) < \rho_c(t)$ results in $k = -1$ (open universe), and for $\rho(t) = \rho_c(t)$ follows $k = 0$ (flat universe). A very often used definition is the *density parameter*, i.e. the ratio between density to critical density:

$$\Omega(t) = \frac{\rho(t)}{\rho_c(t)} = \frac{8\pi G\rho(t)}{3H^2(t)}. \tag{4.32}$$

The time dependence of the scalefactor $a(t)$ ensures that the universe remains homogeneous and isotropic, while the components of the metric tensor $g_{\mu\nu}$ define the gravitational field. The RWM is an important ingredient, when inserted into the Einstein equations (eq. 4.10) it results in the time evolution equations for the scalefactor and the energy density, which we discuss in the following.

4.2.5 The Friedmann Equations

The Friedmann equations quantify the time evolution of the scalefactor and the density, and are obtained by inserting the underlying Robertson-Walker-metric (eq. (4.30)) into the Einstein equations (eq (4.10)). This results in

$$\dot{\rho}(t) = -3H(t)\left[\rho(t) + p(t)\right], \tag{4.33}$$

$$\ddot{a}(t) = -\frac{4\pi G}{3}\left[\rho(t) + 3p(t)\right]a(t). \tag{4.34}$$

Eq. (4.33) expresses the energy conservation, while eq. (4.34) determines the time evolution of $a(t)$. The energy-density,

$$\rho(t) = \rho_{\rm Rad}(t) + \rho_{\rm M}(t) + \rho_{\rm DE}(t), \tag{4.35}$$

or equivalently, the density parameter (eq. (4.32))

$$\Omega(t) = \Omega_{\rm Rad}(t) + \Omega_{\rm M}(t) + \Omega_{\rm DE}(t) \tag{4.36}$$

contains contributions of radiation (Rad), dark- and baryonic matter (M), and dark energy (DE), respectively. The pressure $p(t)$ is given through the equation of state (w) for all contributions,

$$p(t) = w(t) \cdot \rho(t) = w_{\rm Rad}(t) \cdot \rho_{\rm Rad}(t) + w_{\rm M}(t) \cdot \rho_{\rm M}(t) + w_{\rm DE}(t) \cdot \rho_{\rm DE}(t). \tag{4.37}$$

Note that in case of matter the pressure vanishes, i.e. $p_{\rm M} = 0$.
By multiplying eq. (4.34) with $\dot{a}$ and using eq. (4.33) we obtain after integration

$$H^2(t) = \frac{8\pi G}{3}\rho(t) - \frac{k}{a^2(t)}. \tag{4.38}$$

With eqs. (4.33)-(4.38) the overall time evolution of $\rho(t)$ and $a(t)$ are defined.
For some problems it is more convenient to express eq. (4.38) in terms of the redshift z. To do so we use eq. (4.32) to write

$$H^2(z) + k(1+z)^2 = \Omega_0 H_0^2 \frac{\rho(z)}{\rho_0}, \tag{4.39}$$

considering the fact that $a(t = t_0) = 1$, and $\Omega(t = t_0) = \Omega_0$, $\rho(t = t_0) = \rho_0$ denoting the values today. Note that for ρ (eq. (4.35)) we also take z instead of t to parameterize the time evolution. Identifying

$$k = (1 - \Omega_0) H_0^2, \tag{4.40}$$

it follows for $H(z)$

$$H(z) = H_0 \left((1 - \Omega_0)(1+z)^2 + \Omega_0 \frac{\rho(z)}{\rho_0} \right)^{1/2}. \tag{4.41}$$

The cosmological parameters that we are going to use are given in table 4.1 and follow from WMAP (Komatsu *et al.*, 2009).

4.2.6 Structure Formation in the Universe

One of the most important issues of cosmology is how the Universe went from its initial homogeneous state into the complex form seen today. Initial small density fluctuations, attributed to zero point quantum fluctuations that arise during the epoch of inflation, are responsible for the formation of structures like the observed galaxies and galaxy clusters. The growth of density fluctuations is often described using the density contrast,

$$\delta(t, \mathbf{x}) = \frac{\rho(t, \mathbf{x}) - \rho_{\rm bg}(t)}{\rho_{\rm bg}(t)} \tag{4.42}$$

where $\rho_{\rm bg}(t)$ refers to the homogeneous background density and $\rho(t, \mathbf{x})$ describes the local density enhancement,

$$\rho(t, \mathbf{x}) = \rho_{\rm bg}(t) + \delta\rho(t, \mathbf{x}). \tag{4.43}$$

The linear regime is characterized by $\delta \ll 1$, for which the universe can be treated as an ideal fluid described in the Newtonian limit by the Euler-Jeans equation (eq. (2.7)). This has to be linearized in addition to the continuity equation (eq. (2.6)), and the Poisson equation

$$\Delta\Phi(t,\mathbf{x}) = 4\pi G\rho(t,\mathbf{x}), \tag{4.44}$$

which determines the peculiar gravitational field of the density fluctuations. The potential $\Phi(t,\mathbf{x})$ can be decomposed into

$$\Phi(t,\mathbf{x}) = \Phi_0(t) + \delta\Phi(t,\mathbf{x}), \tag{4.45}$$

with $\Phi_0(t)$ being the background potential and $\delta\Phi(t,\mathbf{x})$ the contribution from the fluctuations. The velocity $\mathbf{v}(t,\mathbf{x})$ consists of the Hubble velocity $\mathbf{v_0}(t)$ (eq. 4.21) and corresponding to the peculiar gravitational field, the peculiar velocity $\mathbf{u}(t,\mathbf{x})$,

$$\mathbf{v}(t,\mathbf{x}) = H(t)\cdot\mathbf{r}(t) + \mathbf{u}(t,\mathbf{x}) = \mathbf{v_0}(t) + \mathbf{u}(t,\mathbf{x}), \tag{4.46}$$

where $\mathbf{u}(t,\mathbf{x})$ can be identified with the perturbed velocity $\delta\mathbf{v}(t,\mathbf{x})$ and

$$\mathbf{v}(t,\mathbf{x}) = \mathbf{v_0}(t) + \delta\mathbf{v}(t,\mathbf{x}). \tag{4.47}$$

To incorporate the expansion of the universe, it is helpful to make use of the comoving coordinate $\mathbf{r}$ (eq. (4.26)), and the corresponding derivatives[3]. In these coordinates the linearized equations for eq. (2.6), eq. (2.7) and eq. (4.44) transform with the help of eq. (4.33), and eq. (4.34) into,

$$\left(\frac{\partial\delta}{\partial t}\right) + \frac{1}{a}\nabla\delta\mathbf{v} = 0, \tag{4.48}$$

$$\left(\frac{\partial\delta\mathbf{v}}{\partial t}\right) + \frac{c_s^2}{a}\nabla\delta + \left(\frac{\dot{a}}{a}\right)\delta\mathbf{v} = -\frac{1}{a}\nabla\delta\Phi, \tag{4.49}$$

$$\Delta\delta\Phi = 4\pi G a^2\rho_{\mathrm{bg}}\delta, \tag{4.50}$$

where the entropy perturbations have been neglected and we used the fact that the pressure vanishes for matter. After some conversions it follows,

$$\ddot{\delta} + 2\frac{\dot{a}}{a}\dot{\delta} - \frac{c_s^2}{a^2}\Delta\delta - 4\pi G\rho\delta = 0. \tag{4.51}$$

The parameter c_s is the sound speed connected with the linearized pressure, $p = p(\rho)$ via $\delta p = c_\mathrm{s}^2\delta\rho$. Eq. (4.51) describes the growth of structures in the universe on scales smaller than the horizon-scale[4]. Applying a Fourier transformation

$$\delta(t,\mathbf{r}) = \sum\delta_\mathbf{k}(t)\cos(\mathbf{r}\cdot\mathbf{k}), \tag{4.52}$$

with the comoving wave vector $\mathbf{k}$ and $\delta_\mathbf{k}$ the amplitude, the spatial part $c_s^2/a^2\Delta\delta$ can be separated where each mode $\delta_\mathbf{k}(t)$ develops independently. The evolution of the density contrast is determined

[3] For the corresponding derivatives follows, $\left(\frac{\partial}{\partial t}\right)_\mathbf{x} = \left(\frac{\partial}{\partial t}\right)_\mathbf{r} - (\mathbf{v_0}\cdot\nabla_\mathbf{x})$ and $\nabla_\mathbf{x} = \frac{1}{a}\nabla_\mathbf{r}$. The subscript $\mathbf{r}$ is omitted in the further equations.

[4] The horizon-scale (or -length) describes the range for physical interaction, i.e. the range a photon can travel at a given time. Its comoving length is calculated as $r_{\mathrm{horizon}} = \int a d\eta$, with $d\eta = dt/a$ denoting the conformal time.

by $\delta_{\mathbf{k}} = D(t) \cdot \delta_{\rm norm}$, normalized at $t = t_{\rm norm}$ and $\delta_{\mathbf{k}}(t = t_{\rm norm}) \equiv \delta_{\rm norm}$. (We drop in the following the subscript **k**). $D(t)$ represents the *linear growth factor*,

$$D(t) = \frac{\delta(t)}{\delta_{\rm norm}}, \tag{4.53}$$

while the *linear growth suppression factor* $g(t)$ is defined as the growth relative to that in a flat, matter only dominated universe (i.e. $\Omega(t) = \Omega_{\rm M}(t)$, and $D(t) \sim a(t)$),

$$g(t) = \frac{D(t)}{a(t)}. \tag{4.54}$$

$g(t)$ characterizes the reduced growth due to the presence of an additional energy density to the matter component. Assuming a universe containing matter and dark energy with negligible pressure fluctuations, an integral form of $g(t)$ can be derived and is given in e.g. Heath (1977), Eisenstein *et al.* (1999), and Hamilton (2001). However, for our purposes the differential form of $g(t)$ is needed, which is derived in the Newtonian limit in the following subsection, where we also introduce the cosmological framework for our study.

4.2.7 Special Case: Universe containing Dark Matter and Dark Energy

For our studies, we concentrate on contributions of dark matter and dark energy assuming a flat universe, thus $\rho(t) = \rho_{\rm M}(t) + \rho_{\rm DE}(t)$ or $\Omega(t) = \Omega_{\rm M}(t) + \Omega_{\rm DE}(t)$, and $k = 0$. The density is determined through

$$\rho(a) = \Omega_{\rm M}^0 \cdot (a)^{-3} + \Omega_{\rm DE}^0 \cdot \exp\left\{-3\int (1 + w_{\rm DE}(a'))\frac{da'}{a'}\right\}, \tag{4.55}$$

$\Omega_{\rm M}^0 \equiv \Omega_{\rm M}(t = t_0)$ and $\Omega_{\rm DE}^o \equiv \Omega_{\rm DE}(t = t_0)$ correspond to their values today (see also table 4.1). The equation of state for DE is $p_{\rm DE} = w_{\rm DE} \cdot \rho_{\rm DE}$, while for matter it vanishes. The Friedmann-equations have the form

$$\left(\frac{\dot{a}(t)}{a(t)}\right)^2 = \frac{8\pi G}{3}\left(\rho_{\rm M}(t) + \rho_{\rm DE}(t)\right), \tag{4.56}$$

$$\ddot{a}(t) = -\frac{4\pi G}{3}\left[\rho_{\rm M}(t) + \rho_{\rm DE}(t)(1 + w_{\rm DE}(t))\right] a(t). \tag{4.57}$$

The first order perturbation of the Jeans equations applied on a expanding background (eq. (4.51)) can be recast for the dark matter component into

$$\ddot{\delta}_{\rm M} + 2\frac{\dot{a}}{a}\dot{\delta}_{\rm M} - 4\pi G\rho_{\rm M}\delta_{\rm M} = 0. \tag{4.58}$$

We concentrate on the growth of dark matter perturbations only, where a smooth dark energy component is assumed and fluctuations in DE are neglected. This assumption is valid as long as the scales are not too small. DE reduces the growth rate of perturbations in the linear regime (large scales). To express eq. (4.58) in terms of the growth-suppression factor with $a(t)$ as the evolution variable we set eq. (4.63) into (4.54), and rewrite

$$\delta(t) = a(t) \cdot \delta_{\rm norm} \cdot g(t), \tag{4.59}$$

Spectral Index n_s	0.962
Hubble Constant H_0	$70.2\text{kms}^{-1}/\text{Mpc}^{-1}$
Matter Density/Critical Density Ω_M	0.277
Dark Energy Density/Critical Density Ω_Λ	0.723
Fluctuation amplitude at 8h^{-1}Mpc σ_8	0.817
Age of the Universe t_0	13.69 Gyr

Table 4.1: Cosmological parameters following WMAP (Komatsu *et al.*, 2009): Ω_M and Ω_Λ are the density parameters (eq. (4.32)) of matter and DE, H_0 is the hubble constant today (eq. (4.25)), which gives $h = 0.702$. The spectral index n_s expresses the exponential behavior of the linear power spectrum and σ_8 its normalization, see 4.2.8.

whose time-derivatives are plugged into eq. (4.58). With the Friedmann equations, eq. (4.56) and eq. (4.57) the evolution equation for the growth suppression factor follows as,

$$\frac{d^2g}{d\ln a^2} + \frac{1}{2}\left[6 - (1+3w_\text{DE}(a)\Omega_\text{DE}(a))\cdot\left(1 - \frac{3}{8\pi G}\cdot\frac{k}{a^2}\right)^{-1}\right]\frac{dg}{d\ln a} + \left[-\frac{1}{2}\left(1 - \frac{3}{8\pi G}\cdot\frac{k}{a^2}\right)^{-1}\cdot(4 - 3\Omega_\text{DE}(a)\cdot(1-w_\text{DE}(a))) + 2\right]g = 0, \tag{4.60}$$

implying a dark matter dominated universe with a dark energy and matter contribution of $\Omega_\text{DE}(a)$ and $\Omega_\text{M}(a)$.
For the most interesting case of a flat universe ($k = 0$ and $\Omega_\text{M}(a) + \Omega_\text{DE}(a) = 1$) we obtain

$$2\frac{d^2g}{d\ln a^2} + [5 - 3w_\text{DE}(a)\Omega_\text{DE}(a)]\frac{dg}{d\ln a} + 3[1 - w_\text{DE}(a)]\Omega_\text{DE}(a)g = 0, \tag{4.61}$$

see also Wang & Steinhardt (1998), Linder & Jenkins (2003), Padmanabhan (2003) and Cooray *et al.* (2004). For constant values of w_DE, the solution is given by a combination of hypergeometric functions. For a non constant $w_\text{DE}(t) = w_\text{DE}(a(t))$, this equation can be solved numerically, which is our approach. We obtain solutions for $g(a)$, which also determines $D(a)$ respectively $D(z)$ via,

$$D(a) = g(z)\cdot a, \text{ or} \tag{4.62}$$

$$D(z) = \frac{g(z)}{(1+z)}. \tag{4.63}$$

Some details about the numerical procedure are discussed in B.1.

4.2.8 Statistical description of cosmological perturbations

To statistically characterize the structure of the matter-distribution of the universe, we define the so called *two-point-correlation-function*, ξ. This function describes the correlation of matter (e.g. galaxies) at different positions. It is given by,

$$\xi = \langle\delta(\mathbf{x})\delta(\mathbf{y})\rangle\,. \tag{4.64}$$

The homogeneity and the isotropy of the universe implies that ξ only depends on the absolute value of the distance $|\mathbf{x}-\mathbf{y}|$, thus $\xi \to \xi(r)$.
An alternative description is provided by the *power spectrum*, $P(k)$, the Fourier-Transform of the correlation-function. $P(k)$ describes the amplitude distribution of $\delta(t,\mathbf{x}) = \sum \delta_{\mathbf{k}}(t)\cos(\mathbf{x}\cdot\mathbf{k})$ at $k = |\mathbf{k}|$. (Note that $\mathbf{k}$ is the comoving wave vector, see 4.2.6.) The connection between $P(k)$ and ξ emerges from,

$$P(k) = 2\pi \int r^2 \frac{\sin(kr)}{kr}\xi(r)dr, \tag{4.65}$$

or vice versa,

$$\xi(r) = 2\pi \int k^2 \frac{\sin(kr)}{kr}P(k)dk = 4\pi^3 \int \Delta(k)\frac{\sin(kr)}{kr}\frac{dk}{k}, \tag{4.66}$$

where the dimensionless power spectrum $\Delta(k)$ has been introduced,

$$\Delta(k) = \frac{k^3}{2\pi^2}\cdot P(k). \tag{4.67}$$

Both, $P(k)$ and ξ, depend on the cosmological time or rather the redshift. If we assume that linear perturbation theory holds, i.e. $\delta(t) = D(t)\cdot\delta_0$ (normalized to its value today, $t_{\text{norm}} = t_0$ and omitting again the subscript $\mathbf{k}$), we can write,

$$\xi(t,r) = D^2(t)\cdot\xi(t_0,r) = D^2(t)\cdot\xi_0(r), \tag{4.68}$$

and

$$P(t,k) = D^2(t)\cdot P(t_0,k) = D^2(t)\cdot P_0(k). \tag{4.69}$$

In the case that the power spectrum P_0 is known, the power spectrum for all time follows via eq. (4.69). However, the evolution of fluctuations depends on the particular epoch (matter or radiation), as well as on the scale of the perturbations with respect to the horizon-length. This leads to the introduction of an correction term, characterized by the so called *transfer function*, $T(k)$. The transfer function can be calculated for several cosmological models if the matter content is specified, see for example Bardeen *et al.* (1986), explained in more detail in the appendix B.2. The linear power spectrum follows as

$$P(t,k) = D^2(t)\cdot A\cdot k^{n_s}\cdot T^2(k), \tag{4.70}$$

and transforms for $n_s = 1$ into the well known Harrison-Zeldovich spectrum. The factor A is a normalization constant that has to be deduced from observations. An important parameterization for this normalization is given by the parameter σ_8, which is simply correlated to the so called *linear bias factor b*.
The linear bias factor characterizes the relation between dark matter and galaxies (which are expected to follow the distribution of dark matter), and is defined via

$$\delta_g \equiv \frac{\Delta n}{\bar{n}} = b\cdot\frac{\Delta\rho}{\rho_{\text{bg}}} = b\cdot\delta. \tag{4.71}$$

$\bar{n}$ is the mean density of the considered galaxy-population and $\Delta n = n - \bar{n}$ the corresponding derivation of the local number-density n from the mean. $\Delta\rho/\rho_{\text{bg}} = (\rho-\rho_{\text{bg}})/\rho_{\text{bg}}$ (eq. (4.42)) expresses the dark

matter overdensity. From eq. (4.71) we see that b is the ratio of the relative overdensity of galaxies to the dark matter.
Observations of optical selected galaxies indicate that on scales of about $\sim 8h^{-1}$ Mpc their fluctuation-amplitude is close to 1, i.e.

$$\sigma_{8,g}^2 \equiv \left\langle \left(\frac{\Delta n}{\overline{n}} \right)^2 \right\rangle \approx 1, \tag{4.72}$$

with the corresponding dispersion of dark matter being

$$\sigma_8^2 = \left\langle \delta^2 \right\rangle_8 . \tag{4.73}$$

Using eq. (4.71) yields

$$\sigma_8 = \frac{\sigma_{8,g}}{b} \approx \frac{1}{b}. \tag{4.74}$$

Due to the simplicity of eq. (4.74) the parameter σ_8 generally serves as normalization constant, usually for P_0. A more detailed description can be found in Schneider (2006), and Mukhanov (2005).
A description to model the nonlinear power spectrum (required in section 4.5) is discussed in detail in section 4.4. In the following we introduce the different forms of DE.

4.3 Approaches to describe dark energy

After defining the most crucial quantities in cosmology, we can now delve into the mysterious nature of DE and its influence on structure formation. This is important in the following sections, as these effects lead to a non-Gaussian signal in the temperature distribution of CMB photons. About $\sim 70\%$ of today's energy density is attributed to this dark component (see Fig. 4.1), which still lacks any scientific explanation. Observations of SNIa (Krauss & Turner, 1995; Ostriker & Steinhardt, 1995; Riess *et al.*, 1998; Perlmutter *et al.*, 1999; Netterfield *et al.*, 2002), LSS measurements like 2dFGRS[5] (e.g. Colless, 1999) or SDSS[6] (e.g. Abazajian *et al.*, 2003) in combination with CMB measurements (e.g. Spergel *et al.*, 2003; Komatsu *et al.*, 2009) indicate that its equation of state today is very close to $w_{\rm DE} \approx -1$. The standard scenario, in good agreement with these observational findings points toward a cosmological constant (Λ) which is identified with the vacuum energy density ($\rho_{\rm vac}$), see 4.3.1. This model with the concordance set of cosmological parameters (see table 4.1) is known as the ΛCDM-model, where cold dark matter (CDM) has considerable success in reproducing observational results on cluster scales. However, a constant Λ rises two serious questions: (i) the fine-tuning problem and (ii) the coincidence problem. The first expresses the large discrepancy of ~ 123 orders of magnitude between the small observed value of $\rho_{\rm vac} \sim (10^{-3}{\rm GeV})^4$ in contrast to the prediction of quantum field theory $\rho_{\rm vac} \sim 10^{76}{\rm GeV}^4$. This very fine tuned $\rho_{\rm vac}$ results in $\rho_{\rm vac} \sim \rho_{\rm M}$ today and invokes the second problem, which refers to the point in time when DE begins to dominate over matter. If this would happen already at early times, then the acceleration of the expansion would prohibit any gravitational collapse, and thus prevent the formation of structures like our galaxy. On the other hand, if it starts to

[5] The Anglo Australian Telescope two degree field Galaxy Redshift Survey - 2dFGRS, see also http://www.mso.anu.edu.au/2dFGRS/.
[6] Sloan Digital Sky Survey, see also http://www.sdss.org/publications/.

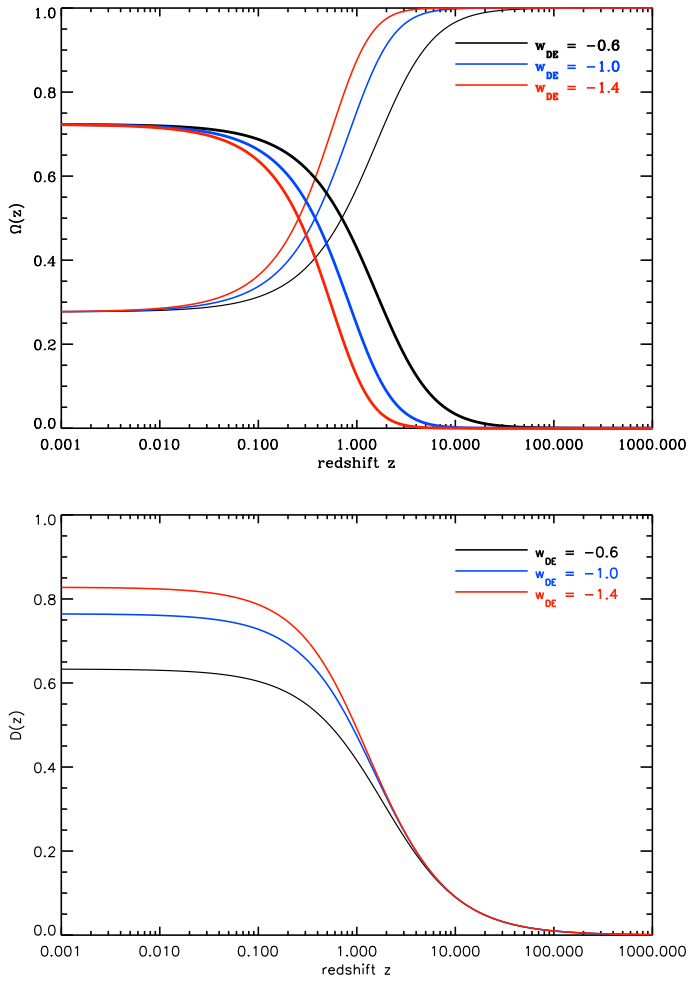

Figure 4.3: Upper panel: Evolution of the density parameters $\Omega_{\rm DE}$ (eq. (4.79)) (thick lines) and $\Omega_{\rm M}$ (eq. (4.78)) (thin lines) with redshift z, using $w_{\rm DE} = -0.6$ (blue lines) $w_{\rm DE} = -1$ (black lines) and $w_{\rm DE} = -1.4$ (red lines). Bottom panel: Evolution of the corresponding growth factor $D(z)$ (eq. (4.63)).

dominate at late times we would not have found any evidence of DE yet.
These problems, combined into the cosmological constant problem open the room for other models regarding DE such as the quintessence, see 4.3.2. The quintessence, a slowly rolling scalar field with a time varying equation of state alleviates the coincidence problem that comes with Λ. It allows forms of DE that result in $w_{\rm DE} = -1$ today, but which start from a different value at earlier times. This somewhat circumvents the question why DE begins to dominate at the 'right time'. Various models have been proposed, see e.g. Linder (2008) for a review. A very simple parameterization in form of a taylor expansion for $w_{\rm DE}$, which can be interpreted as a generalization of the behavior of physically motivated sets of models has been introduced by Chevallier & Polarski (2001); Linder (2003a,b) (LIND03) and revised by Komatsu *et al.* (2009) (KOMAT09). In addition, Wetterich (2004) (WETT04) defined a new form called early quintessence, which has a non-negligible contribution at

early times and is based on a bending form using $\Omega_{\rm M}^0$ (the matter content today) and $w_0 = -1$. This model is very attractive, since observations set physical limits on the amount of this early dark energy (EDE) (Xia & Viel, 2009).
In the following we introduce these different forms, in particular, EDE which are used to calculate the theoretical L-RS bispectrum signal and the corresponding signal to noise ratio (see sections 4.6 and 4.7). We start with the familiar idea of a cosmological constant (4.3.1) before concentrating on models with a variable equation of state - the quintessence (4.3.2).

4.3.1 Cosmological constant - Λ

The concept of a cosmological constant was first introduced by Einstein (1917) in order to describe a static, finite and non-evolving universe. However, after the discovery of the expansion of the universe by Edwin Hubble it was not considered for a long time. Very recently, it has been reestablished in order to encompass the until then unknown acceleration of the expansion within the Einstein-equations. The cosmological constant is often denoted as Λ and the corresponding energy density is identified as the vacuum energy density

$$\rho_{\rm vac} = \frac{\Lambda}{8\pi G}. \tag{4.75}$$

The evolution of this density is parameterized by the second term of eq. (4.55) with an equation of state given by $p_{\rm DE} = w_{\rm DE} \cdot \rho_{\rm DE}$, where $w_{\rm DE} = const$. The accepted standard value of $w_{\rm DE} = -1$ implies a negative pressure[7], which results in an accelerated expansion. The matter- and dark energy-density contributions are given by (cf. eq. (4.55) with the redshift z instead of the scalefactor a as evolution parameter),

$$\rho_{\rm M}(z) = \rho_{\rm M}^0 \cdot (1+z)^3, \tag{4.76}$$
$$\rho_{\rm DE}(z) = \rho_{\rm DE}^0 \cdot (1+z)^{3(1+w_{\rm DE})}, \tag{4.77}$$

along with the corresponding density parameters,

$$\Omega_{\rm M}(z) = \frac{\Omega_{\rm M}^0}{\Omega_{\rm M}^0 + \Omega_{\rm DE}^0 \cdot (1+z)^{3w_{\rm DE}}}, \tag{4.78}$$
$$\Omega_{\rm DE}(z) = \frac{\Omega_{\rm DE}^0 (1+z)^{3w_{\rm DE}}}{\Omega_{\rm M}^0 + \Omega_{\rm DE}^0 \cdot (1+z)^{3w_{\rm DE}}}. \tag{4.79}$$

Observations indicate that $w_{\rm DE}$ is very close to -1. For comparison, we use two additional values ($w_{\rm DE} = -0.6$, and $w_{\rm DE} = -1.4$) to discuss the implications.
The upper panel of Fig. 4.3 shows the evolution of $\Omega_{\rm DE}$ (thick lines) and $\Omega_{\rm M}$ (thin lines) with z, using $w_{\rm DE} = -0.6$ (blue curves), $w_{\rm DE} = -1.0$ (black curves) and $w_{\rm DE} = -1.4$ (red curves). The passing from the matter to the dark energy dominated epoch happens at $\rho_{\rm M} = \rho_{\rm DE}$, where

$$z_{\rm eq} = \left[\frac{\Omega_{\rm M}^0}{\Omega_{\rm DE}^0}\right]^{1/(3w_{\rm DE})} - 1, \tag{4.80}$$

[7] This can be understood by thermodynamical arguments: Consider an increasing volume V that contains vacuum with an inner energy of $U \sim V$. The first principle of hydrodynamics for increasing volumes implies $dU = -pdV > 0$, therefore the pressure must be negative to satisfy $dU > 0$.

which results in $z_{\rm eq} = 0.7, 0.4, 0.2$ for the examples above. Decreasing the value of $w_{\rm DE}$ shifts $z_{\rm eq}$ towards smaller redshifts, i.e. the crossing from matter to dark energy domination is delayed. The acceleration of the universe is reduced and the damping effect of DE on forming structures less significant. This is also indicated by the increasing growth factors $D(z)$ (with decreasing $w_{\rm DE}$) at the bottom panel of Fig. 4.3. The growth factors follow from eq. 4.63, where $g(z)$ is obtained integrating eq. (4.61). Note that we always normalize $g(z)$ to 1 at $z = 100$, for which the normalization for $D(z)$ follows to be 0.01. The corresponding comoving distances (eq. (4.29)) are given in appendix B.3.
However, as discussed above the standard picture of $w_{\rm DE} = -1$ implies the cosmological constant problem, which gives rise to study quintessence models with a time dependent equation of state, which will be the focus in the following.

4.3.2 Quintessence

As mentioned before, quintessence is based on the idea of a scalar field ϕ with a variable equation of state. It interacts only gravitational with a self-interaction described by the scalar field potential $V(\phi)$, see also e.g. Padmanabhan (2003), and Linder (2008). The simple approach of a canonical Lagrangian (eq. (4.16)), leads to the equation of motion, the *Klein-Gordon-equation*,

$$\Box\phi - \frac{dV}{d\phi} = 0, \tag{4.81}$$

with

$$\Box = \nabla^\mu \nabla_\mu = g^{\mu\nu}\nabla_\mu\nabla_\nu. \tag{4.82}$$

The energy density and pressure are identified by comparing the energy-momentum tensor (eq. (4.17)) with that of a perfect fluid[8], for what follows,

$$u_\mu = \frac{\nabla_\mu\phi}{\sqrt{\nabla^\nu\phi\nabla_\nu\phi}}, \tag{4.83}$$

$$\rho_\phi = \frac{V(\phi)}{\sqrt{1-\nabla^\nu\phi\nabla_\nu\phi}}, \tag{4.84}$$

$$p_\phi = -V(\phi)\sqrt{1-\nabla^\nu\phi\nabla_\nu\phi}. \tag{4.85}$$

Note that the covariant derivatives reduce to partial derivatives when acting on a scalar. It follows for p_ϕ and ρ_ϕ,

$$\rho_\phi = \frac{1}{2}\dot\phi^2 + V(\phi) + \frac{1}{2}(\nabla\phi)^2 \tag{4.86}$$

$$p_\Phi = \frac{1}{2}\dot\phi^2 - V(\phi) - \frac{1}{6}(\nabla\phi)^2. \tag{4.87}$$

The spatial derivations in eq. (4.86) and eq. (4.87) are neglected since the field is expected to be smooth within the Hubble scale and to zeroth order. The equation of state ($w_{\rm DE}$) is given by,

$$w_{\rm DE} = \frac{p_\phi}{\rho_\phi} = \frac{1-(2V/\dot\phi^2)}{1+(2V/\dot\phi^2)}. \tag{4.88}$$

[8] The energy-momentum tensor in case of a perfect fluid is $T^{\mu\nu} = (\rho + p)u^\mu u^\nu - g^{\mu\nu}p$.

Using eq. (4.86), and eq. (4.87) it follows,

$$V(\phi) = \rho_\phi - \frac{1}{2}\dot{\phi}^2, \tag{4.89}$$

$$\dot{\phi} = \rho(1+w_{\rm DE}). \tag{4.90}$$

Furthermore, multiplying eq. (4.81) with $\dot{\phi}$ leads to,

$$\frac{d}{dt}\left[\frac{\dot{\phi}}{2}\right] + 6H\left[\frac{\dot{\phi}}{2}\right] = -\dot{V}(\phi), \tag{4.91}$$

$$\dot{\rho_\phi} - \dot{V}(\phi) + 3H(\rho_\phi + p_\phi) = -\dot{V}(\phi), \tag{4.92}$$

$$\frac{d\rho_\phi}{d\ln a} = -3\rho_\phi(1+w_{\rm DE}), \tag{4.93}$$

which allows to change between the field description and fluid description (Linder, 2008). Since many different forms for the potential $V(\phi)$ exist, it is convenient to introduce a certain parameterization for $w_{\rm DE}$ to cover a range of models. We concentrate on the approaches listed below, where we start with the parameterization of Chevallier & Polarski (2001), and Linder (2003a,b), which describes the dynamics in form of a taylor expansion. This model is useful at low-redshifts, since it parameterizes the present value of $w_{\rm DE}(z)$ and the first derivative. However, using CMB data it can be difficult to extrapolate to high redshifts, because $w_{\rm DE}(z)$ expresses the leading order term of the expansion which can become unreasonably small or large. An revised version of this model has therefore been proposed by Komatsu *et al.* (2009), which is discussed afterwards. Finally, we turn our attention to the EDE model from Wetterich (2004), which covers the physics back to the last scattering surface (i.e. where the CMB photons decouple from the baryons around $z \sim 1100$). The CMB anisotropies are very sensitive to contributions of EDE at last scattering (Doran *et al.*, 2001a), while also structure formation depends on the mean fraction of EDE (Ferreira & Joyce, 1998; Doran *et al.*, 2001b). Observations are able to set constrains on these contributions (Xia & Viel, 2009). This makes it an very interesting model to study.

- PARAMETERIZATION OF LIND03:
  A very simple form for $w_{\rm DE}$ has been proposed by Chevallier & Polarski (2001), and Linder (2003a,b). It identifies the equation of state for DE as a taylor expansion in a,

  $$w_{\rm DE}(a) = w_0 + w_a \cdot (1-a), \tag{4.94}$$

  or in z,

  $$w_{\rm DE}(z) = w_0 + w_a \cdot \left(\frac{z}{1+z}\right), \tag{4.95}$$

  with $w_0 = -1$, and the fit parameter w_a (Linder, 2003a)

  $$w_a \equiv \left[-w'/a\right]_{|z=1} = -2w'(z=1), \tag{4.96}$$

  that describes the time variation of $w' \equiv dw_{\rm DE}/dz$. This parameterization is widely used in the literature. Linder (2003a,b) state that this model gives a good approximation to the exact field equations for different scalar field potentials. It behaves reasonable at low redshifts, and the

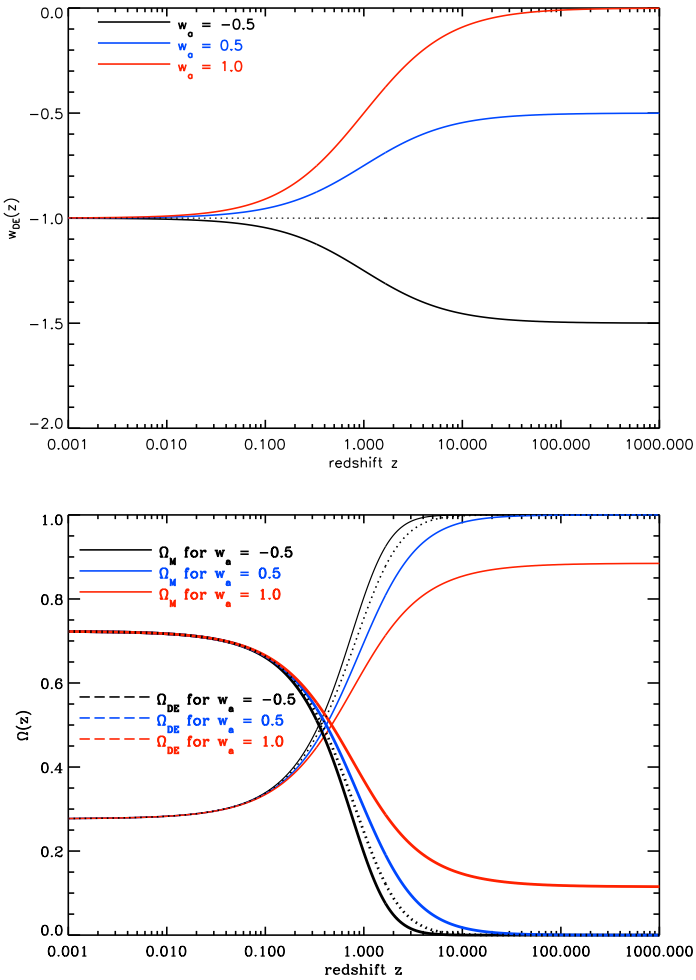

Figure 4.4: Upper panel: Evolution of $w_{\rm DE}$ (eq. (4.95)) with redshift using the LIND03 parameterization for $w_a = -0.5$ (black line), $w_a = 0.5$ (blue line) and $w_a = 1$ (red line), respectively. Bottom panel: Evolution of $\Omega_{\rm DE}$ (eq. (4.98)) (thick lines) and $\Omega_{\rm M}$ (eq. (4.78)) (thin lines). The black dotted line expresses the standard case with $w_{\rm DE} = -1$.

parameters w_0 and w_a are not strongly affected if the form of $w_{\rm DE}$ is extended. Supergravity[9] (SUGRA) indicates $w_a \sim 0.58$ (Linder, 2003a). To test the implications of w_a, we use two additional values.

The upper panel of Fig. 4.4 shows the evolution of $w_{\rm DE}$ (eq. (4.95)) with z, using $w_a = -0.5$ (black line), $w_a = 0.5$ (blue line) and $w_a = 1$ (red line). The standard case with $w_{\rm DE} = -1$ is indicated by the black dotted line. All examples approach $w_{\rm DE} = -1$ at small redshifts as expected. Increasing w_a from -0.5 (where $w_{\rm DE}$ drops below the standard value) to 0.5 and 1 increases the amount of DE. The corresponding energy density (cf. second term of eq. (4.55))

[9] Supergravity is a field theory connecting GR and supersymmetry.

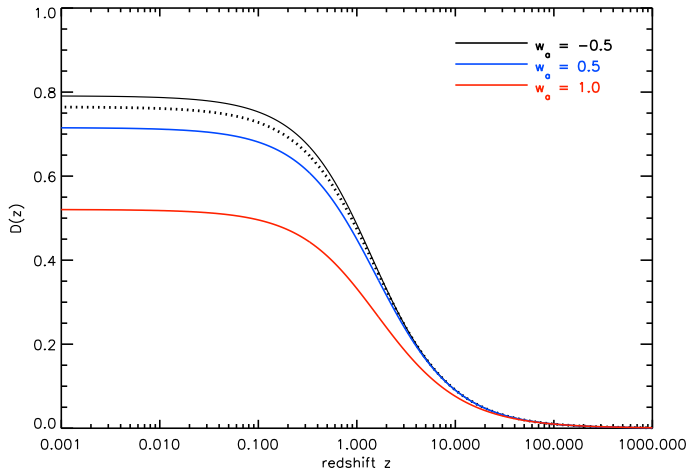

Figure 4.5: Evolution of the growth factor $D(z)$ (eq. (4.63)) with redshift using the LIND03 parameterization for $w_a = -0.5$ (black line), $w_a = 0.5$ (blue line) and $w_a = 1$ (red line), respectively. The black dotted line expresses the standard case with $w_{\rm DE} = -1$.

follows as,

$$\rho_{\rm DE}(z) = \Omega^0_{\rm DE} \cdot (1+z)^{3[w_0+w_a+1]} \cdot \exp\left\{-3w_a\left(\frac{z}{1+z}\right)\right\}, \tag{4.97}$$

(for $\rho_{\rm M}$ see eq. (4.76)), while the density parameter of DE is given by

$$\Omega_{\rm DE}(z) = \frac{\Omega^0_{\rm DE}(1+z)^{3[w_0+w_a]} \cdot \exp\left\{-3w_a\left(\frac{z}{1+z}\right)\right\}}{\Omega^0_{\rm M} + \Omega^0_{\rm DE}(1+z)^{3[w_0+w_a]} \cdot \exp\left\{-3w_a\left(\frac{z}{1+z}\right)\right\}}. \tag{4.98}$$

$\Omega_{\rm M}$ is determined through eq. (4.78). The evolution for $\Omega_{\rm DE}$ and $\Omega_{\rm M}$ with z is presented at the bottom panel of Fig. 4.4. $\Omega_{\rm DE}$ increases accordingly to an increasing w_a, which shifts $z_{\rm eq}$ ($\rho_{\rm M} = \rho_{\rm DE}$) toward higher redshifts and thus to earlier times. Therefore, the linear growth of structures, expressed by $D(z)$ (eq. 4.63) decreases, see Fig. 4.5. The comoving distances (eq. 4.26) are given in the appendix B.3. The redshift $z_{\rm eq}$ results in an implicit equation, therefore we do not show it here.

- PARAMETERIZATION OF KOMAT09:
  Another example for a parameterized equation of state is presented in Komatsu *et al.* (2009), which assume at low redshifts an equation of state defined in a similar manner as in Linder (2003a,b), but with a different behavior at high redshifts. This is distinguished through a fixed transition redshift, denoted as $z_{\rm trans}$. For $z < z_{\rm trans}$ the equation of state $w_{\rm DE}(z)$ follows eq. (4.95). For redshifts $z > z_{\rm trans}$ it approaches $w_{\rm DE}(z) \approx -1$. This prevents that $w_{\rm DE}(z)$ can become unreasonable small or large when extrapolated to high z. The equation of state is given by,

$$w_{\rm DE}(z) = \frac{\tilde{w}(z)}{1+(1+z)/(1+z_{\rm trans})} - \frac{1}{1+(1+z_{\rm trans})/(1+z)}, \tag{4.99}$$

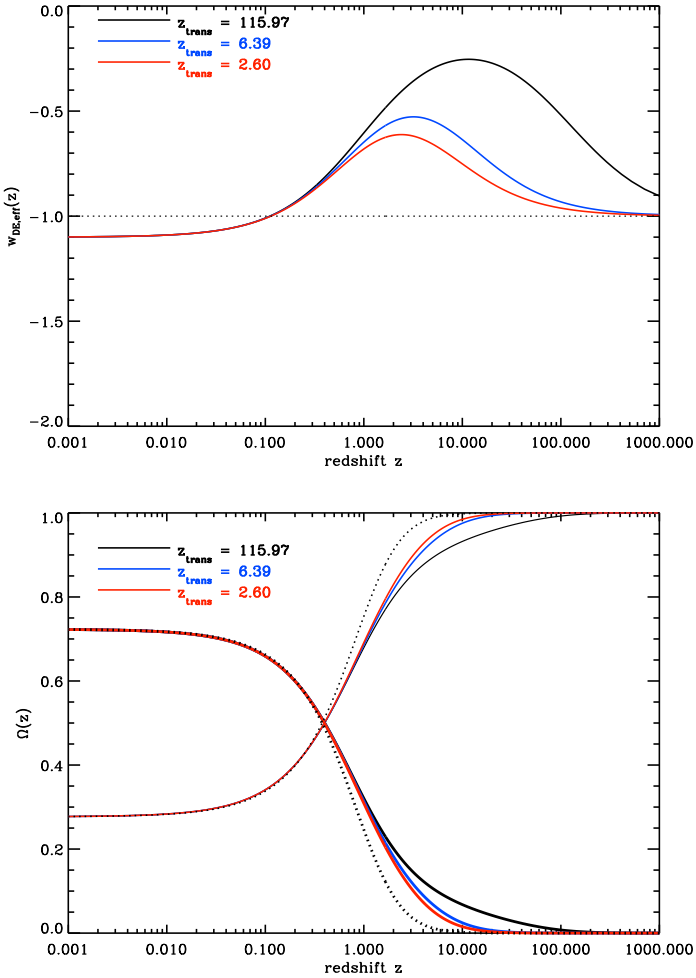

Figure 4.6: Upper panel: Evolution of $w_{\rm DE,eff}$ (eq. (4.99)) with redshift using the KOMAT09 parameterization for $z_{\rm trans} = 115.97$ (black line), $z_{\rm trans} = 6.39$ (blue line) and $z_{\rm trans} = 2.60$ (red line). Bottom panel: Evolution of $\Omega_{\rm DE}$ (eq. (4.107)) (thick lines) and $\Omega_{\rm M}$ (eq. (4.78)) (thin lines) with redshift. The black dotted line denotes the standard case with $w_{\rm DE} = -1$.

with

$$\tilde{w}(z) = \tilde{w}_0 + \left(\frac{z}{1+z}\right)\tilde{w}_a. \tag{4.100}$$

The evolution of the effective equation of state (Komatsu *et al.*, 2009),

$$w_{\rm DE,eff} = \frac{1}{\ln(1+z)}\int_0^{\ln(1+z)^{-1}} d\ln(1+z')w_{\rm DE}(z') = -1 - \frac{z\cdot\ln(1+z)}{(1+z)}\cdot\tilde{w}_a + \frac{1+\tilde{w}_0+(2+z_{\rm trans})\tilde{w}_a}{\ln(1+z)}\cdot\ln\frac{(1+z)+(1+z_{\rm trans})}{(1+z)(1+z_{\rm trans})}, \tag{4.101}$$

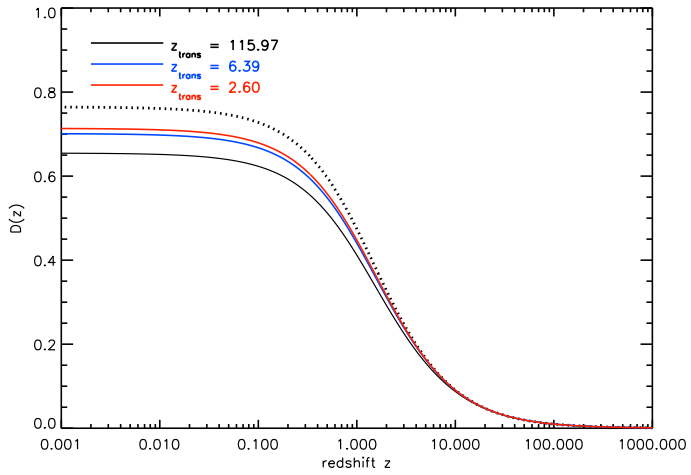

Figure 4.7: Evolution of the growth factor $D(z)$ (eq. (4.63)) with redshift using the KOMAT09 parameterization for $z_{\rm trans} = 115.97$ (black line), $z_{\rm trans} = 6.39$ (blue line) and $z_{\rm trans} = 2.60$ (red line).

is shown at the upper panel of Fig. 4.6 with z, using $z_{\rm trans} = 115.97$ (black line), 6.39 (blue line) and 2.60 (red line). We took these values in order to include constraints on early quintessence (see also table 4.2). The standard case ($w_{\rm DE} = -1$) is indicated again by the black dotted line. The present day value w_0 and the first derivative $w' \equiv dw/dz|_{z=0}$ are used as free parameters, for which Komatsu *et al.* (2009) obtained $w_0 = -1.1$, and $w' = 1$. They are not sensitive to the choice of the transition redshift. Their relation to $\tilde{w}_0$ and $\tilde{w}_a$ follows as,

$$1 + w_0 = \frac{1 + \tilde{w}_0}{(2 + z_{\rm trans})/(1 + z_{\rm trans})}, \tag{4.102}$$

$$w' = \frac{\tilde{w}_a}{(2 + z_{\rm trans})/(1 + z_{\rm trans})} - \frac{1 + \tilde{w}_0}{(2 + z_{\rm trans})^2}, \tag{4.103}$$

with the inverse relations being,

$$1 + \tilde{w}_0 = \frac{(2 + z_{\rm trans})}{(1 + z_{\rm trans})} \cdot (1 + w_0), \tag{4.104}$$

$$\tilde{w}_a = \frac{(2 + z_{\rm trans})}{(1 + z_{\rm trans})} \cdot w' + \frac{1 + w_0}{1 + z_{\rm trans}}. \tag{4.105}$$

$w_{\rm DE,eff}$ decreases for decreasing $z_{\rm trans}$, which reduces the amount of DE. The corresponding DE density contribution (cf. second term of eq. (4.55)) follows as,

$$\rho_{\rm DE}(z) = \Omega^0_{\rm DE} \cdot (1 + z)^{3(1 + w_{\rm eff})}. \tag{4.106}$$

(for $\rho_{\rm M}$ see eq. (4.76)), with the DE density parameter

$$\Omega_{\rm DE} = \frac{\Omega^0_{\rm DE}(1 + z)^{3w_{\rm DE,eff}}}{\Omega^0_{\rm M} + \Omega^0_{\rm DE}(1 + z)^{3w_{\rm DE,eff}}}, \tag{4.107}$$

Best fit to data	$\Omega_{\rm EDE}$ at $z_{\rm lss}$	$z_{\rm trans}$	$z_{\rm eq}$	$\Omega_{\rm EDE}$ at $z_{\rm sf}$	$z_{\rm trans}$	$z_{\rm eq}$
WMAP5+BAO+SN	0.0064	6.39	0.28	0.0672	2.29	0.26
WMAP5+BAO+SN+GRB+Lyα	$1.77 \cdot 10^{-6}$	115.97	0.31	0.0529	2.60	0.26
WMAP5+BAO+SN+GRB+GFLyα	$1.71 \cdot 10^{-9}$	1264.04	0.31	0.0543	2.55	0.26

Table 4.2: Early dark energy constrains form observations, see Xia & Viel (2009). The first row states the observations, WMAP in combination with baryonic acoustic oscillations (BAC), supernovae (SN), gamma ray bursts (GRB) and Lyman alpha (Lyα) measurments. $z_{\rm trans}$ marks the redshift where an constant $w_{\rm DE}$ turns to a different behavior and $z_{\rm eq}$ gives the redshift where $\rho_{\rm DE} = \rho_M$. The constraints on EDE are denoted by $\Omega_{\rm EDE}$ at $z_{\rm lss}$ respectively $z_{\rm sf}$.

and the corresponding matter component $\Omega_{\rm M}$ (eq. (4.78)). The evolution of $\Omega_{\rm DE}$ (thick lines) and $\Omega_{\rm M}$ (thin lines) is presented at the bottom panel of Fig. 4.6. The passing from matter to DE dominance is shifted towar smaller z (i.e. later times). It results in an implicit equation and is therefore not shown here. Decreasing $z_{\rm trans}$ from 115.97 to 6.39 and 2.60 decreases $\Omega_{\rm DE}$, which implies increasing growth factors $D(z)$ (eq. (4.63), as indicated in Fig. 4.7. The corresponding comoving distances (eq. 4.26) are shown in the appendix B.3.

- EARLY DARK ENERGY - PARAMETERIZATION OF WETT04:
  This model includes early quintessence, where a non-vanishing scalar field component with a non-negligible energy density near the redshift of last scattering (denoted as $z_{\rm lss} \sim 1100$) and structure formation (identified with $z_{\rm sf}$) is assumed. The last scattering surface marks the time when photons decouple from the baryons soon after recombination. The era of structure formation encompasses the growth of matter fluctuations (see also Fig. 1.2). The general idea is to parameterize $\Omega_{\rm DE}(z)$ based on two parameters,

$$\Omega_{\rm M}^0 = 1 - \Omega_{\rm DE}^0, \tag{4.108}$$

$$w_0 = -1, \tag{4.109}$$

  ($\Omega_{\rm M}^0 = \Omega_{\rm M}(z=0)$, and $\Omega_{\rm DE}^0 = \Omega_{\rm DE}(z=0)$). Using the relation between $\Omega_{\rm DE}$ and $w_{\rm DE}$, which is valid if the energy density next to DE is only dark matter,

$$\frac{d\Omega_{\rm DE}}{dy} = 3\Omega_{\rm DE}\,(1-\Omega_{\rm DE})\,w_{\rm DE}, \tag{4.110}$$

  and

$$y = \ln(1+z) = -\ln a. \tag{4.111}$$

  Wetterich (2004) proposes to parameterize the function

$$R(y) = \ln\left(\frac{\Omega_{\rm DE}(z)}{1-\Omega_{\rm DE}(z)}\right), \tag{4.112}$$

  which obeys (in absence of radiation)

$$\frac{\partial R(y)}{\partial y} = 3w_{\rm DE}(y) \tag{4.113}$$

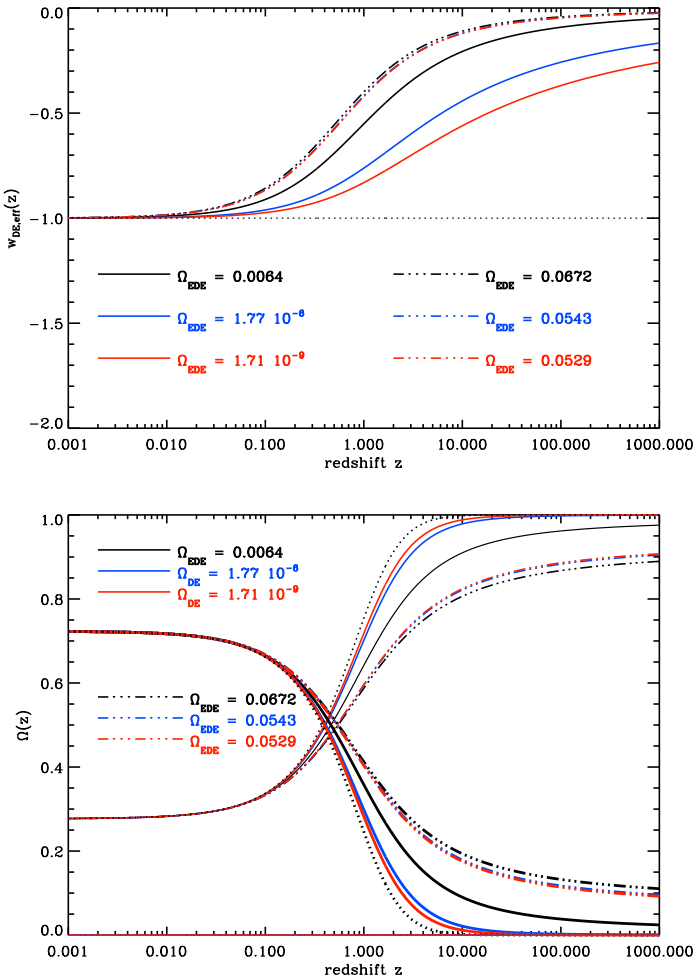

Figure 4.8: Upper panel: Evolution of $w_{\mathrm{DE,eff}}$ with redshift using the WETT04 parameterization, for Ω_{EDE} contributions at z_{lss} (solid lines) and z_{sf} (dashed triple dotted lines), see also table 4.2. Bottom panel: Evolution of the density parameters Ω_{DE} (eq. (4.121)) (thick lines) and Ω_{M} (eq. (4.78)) (thin lines).

through

$$R(y) = R_0 + 3\frac{3w_0 y}{1+by}. \tag{4.114}$$

R_0 is determined via,

$$R_0 = \ln\left(\frac{1-\Omega_{\mathrm{M}}^0}{\Omega_{\mathrm{M}}^0}\right). \tag{4.115}$$

and $b = 1/y_{\mathrm{trans}} = 1/\ln(1+z_{\mathrm{trans}})$ characterizes the bending parameter, where an constant equation of state turns into a different behavior (i.e. for $z > z_{\mathrm{trans}}$). A positive b implies the presence

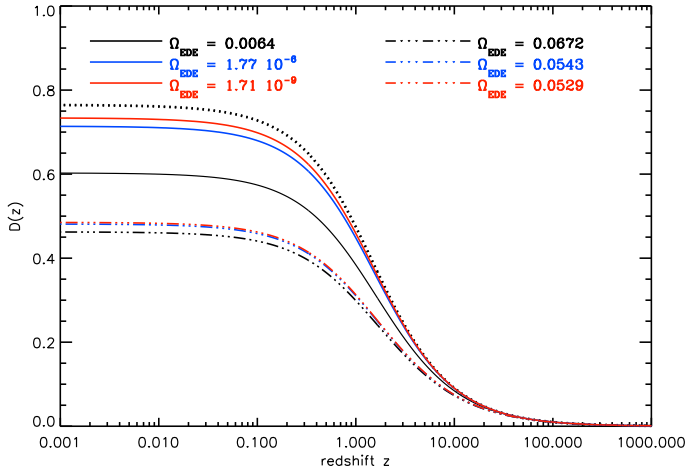

Figure 4.9: Evolution of the corresponding growth factors $D(z)$ (eq. (4.63)) using WETT04.

of EDE,

$$\Omega_{\rm EDE} = \Omega_{\rm DE}(y \to \infty) = \frac{\exp\left(R_0 + 3w_0/b\right)}{1 + \exp\left(R_0 + 3w_0/b\right)}, \tag{4.116}$$

which equals $\Omega_{\rm DE}$ at $z_{\rm lss}$ and $\bar{\Omega}_{\rm DE}$ at $z_{\rm sf}$ (Wetterich, 2004) and enters therefore the CMB anisotropies or structure formation, which we want to analyze with the bispectrum. Using eq. (4.116) it follows for b

$$b = \frac{3w_0}{\ln\left(\frac{1-\Omega_{\rm EDE}}{\Omega_{\rm EDE}}\right) + \ln\left(\frac{1-\Omega_{\rm M}^0}{\Omega_{\rm M}^0}\right)}. \tag{4.117}$$

Xia & Viel (2009) discuss observational constraints on $\Omega_{\rm EDE}$ for contributions at $z_{\rm lss}$ and $z_{\rm sf}$ using WMAP, acoustic baryonic oscillations (BAC), supernovae (SN), gamma ray bursts (GRB) and Lyman alpha (Lyα) measurements. Table 4.2 shows their best fit parameters for $\Omega_{\rm EDE}$, which we apply. The equation of state is given by (Wetterich, 2004),

$$w_{\rm DE}(z) = \frac{w_0}{[1 + b\ln(1+z)]^2}, \tag{4.118}$$

with the effective equation of state being,

$$w_{\rm DE,eff}(z) = 3\int_0^z w_{\rm DE}(z')\frac{dz'}{(1+z')} = \frac{w_0}{(1 + b\ln(1+z))}. \tag{4.119}$$

The upper panel of Fig. 4.8 shows the evolution of $w_{\rm DE,eff}$ with z (solid lines for $\Omega_{\rm EDE}$- contributions at $z_{\rm lss}$, and dashed triple dotted lines for contributions at $z_{\rm sf}$). Decreasing the amount of $\Omega_{\rm EDE}$ at $z_{\rm lss}$ from 0.0064 (black line), to $1.77 \cdot 10^{-6}$ (blue line) and $1.71 \cdot 10^{-9}$ (red line) reduces $w_{\rm DE,eff}$. The same happens for $\Omega_{\rm EDE}$- contributions at $z_{\rm sf}$, decreasing from 0.0672 (black line)

to 0.0543 (blue line) and 0.0529 (red line). The case of a standard cosmological constant, with $w_{\rm DE} = -1$ is indicated by the black dotted line. It lies below the discussed EDE examples for redshifts larger than $z > 0.01$.
The energy density results in (cf. second term of eq. (4.55)),

$$\rho_{\rm DE}(z) = \Omega^0_{\rm DE} \cdot (1+z)^{3\left(1+w_{\rm DE,eff}\right)}, \tag{4.120}$$

(for $\rho_{\rm M}$ see eq. (4.76)). The evolution of the DE density parameter,

$$\Omega_{\rm DE}(z) = \frac{\Omega^0_{\rm DE}(1+z)^{3w_{\rm DE,eff}}}{\Omega^0_{\rm M} + \Omega^0_{\rm DE}(1+z)^{3w_{\rm DE,eff}}}, \tag{4.121}$$

and the corresponding matter component $\Omega_{\rm M}$ (eq. (4.78)) is presented at the bottom panel of Fig. 4.8 (thick lines for $\Omega_{\rm DE}$, thin lines for $\Omega_{\rm M}$, the same line-styles and colors as before). Again, the standard case of $w_{\rm DE} = -1$ is shown by the black dotted line. The passing from the matter- to the DE- dominated epoch ($\rho_{\rm M} = \rho_{\rm DE}$) happens at

$$z_{\rm eq} \quad = \quad \left(\frac{\Omega^0_{\rm M}}{\Omega^0_{\rm DE}}\right)^{\left[3w_0 - b\ln\left(\frac{\Omega^0_{\rm M}}{\Omega^0_{\rm DE}}\right)\right]^{-1}} - 1, \tag{4.122}$$

see also table 4.2. Decreasing the amount of $\Omega_{\rm EDE}$ (at $z_{\rm lss}$ or $z_{\rm sf}$) shifts $z_{\rm eq}$ to later times, since the influence of DE at early times is weaker and the acceleration of the expansion reduced. The growth of structures is stronger, see evolution of the growth factor (eq. 4.63) in Fig. 4.9, which increases for decreasing $\Omega_{\rm EDE}$ but is always less than that of the standard cosmological constant (black dotted line). The corresponding comoving distances (eq. 4.26) are shown in the appendix B.3.

Further approaches for parameterizations of $w_{\rm DE}$ exist. We restrict our study to the examples introduced above, where a comparison of the different $D(z)$ is given in the appendix B.4.
These models of DE and their corresponding growth factors are important for the calculation of the bispectrum (see section 4.5), which depends on the power spectrum of matter fluctuations (eq. (4.70)) and thus, on $D(z)$. However, the analysis in 4.2.8 is restricted only to the linear regime, yet the bispectrum also receives contributions from nonlinear scales. Therefore, we address in the next section the challenging part to model the nonlinear power spectrum.

4.4 The Nonlinear Power Spectrum of Matter Fluctuations

After introducing the DE models, we focus in this section on the nonlinear evolution of cosmic structures in the terms of the matter power spectrum.
CMB photons experience gravitational interactions with forming objects (e.g. galaxies) as they pass through the universe after decoupling. This results in anisotropies (see section 4.5), which depend on the linear as well as on the nonlinear evolution of fluctuations that directly enter into the CMB bispectrum (see section 4.6). Those fluctuations are statistically described by the power spectrum. Different methods to model the nonlinear regime have been proposed. Mangilli & Verde (2009) discuss two models in combination with the bispectrum and point out that an accurate description is required to

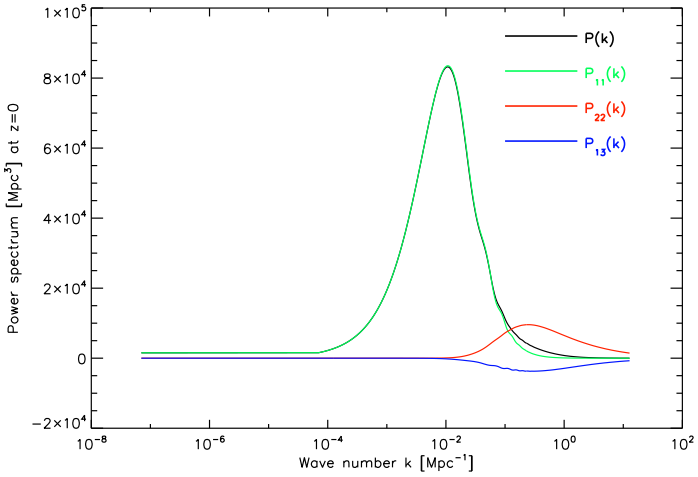

Figure 4.10: Power spectrum components at $z = 0$ following PT, complete $P(k)$ eq. (4.143) (black line), linear part $P_{11}(k)$ eq. (4.69) (green line), nonlinear parts $P_{22}(k)$ eq. (4.144) (red line) and $P_{13}(k)$ eq. (4.145) (blue line).

obtain unbiased estimates on DE- and other cosmological parameters such as Ω_M and σ_8. Our calculations are based on the non-linear cosmological perturbation theory (PT). PT provides an exact solution for the nonlinear matter power spectrum as long as the perturbative expansion is valid. It has been shown by Jeong & Komatsu (2006) that it agrees with power spectra obtained from numerical simulations. To test the dependency of our results on the exact model, we use two additional approaches (in the case of a standard cosmological constant with $w_{\rm DE} = -1$). Very common and established models are provided by Ma *et al.* (1999) (MA99) and Smith *et al.* (2003) (HALOFIT), which are based on analytical functions. We start with a short overview in 4.4.1, and discuss the comparison in 4.4.2.

4.4.1 Descriptions of Nonlinear Power Spectra

The evolution for $\delta \gtrsim 1$ takes place in the nonlinear regime. In order to study the properties of fluctuations the use of approximations or numerical schemes is required, since the evolution includes higher order perturbations and cannot be expressed definitely in terms of analytic functions. Various attempts to model the nonlinear power spectrum have been proposed and discussed, see appendix B.5 or e.g. Smith *et al.* (2003) for a detailed review. We motivate our approaches below:

- NONLINEAR COSMOLOGICAL PERTURBATION THEORY - PT:
  This method concentrates on the so-called 'weakly non-linear regime', where perturbation theory suffices to quantify the evolution of fluctuations. It includes the next-to-leading order correction to the linear power spectrum by using third-order perturbation theory (Vishniac, 1983; Fry, 1984; Goroff *et al.*, 1986; Suto & Sasaki, 1991; Makino *et al.*, 1992; Jain & Bertschinger, 1994; Scoccimarro & Frieman, 1996). A self-contained review is given in Bernardeau *et al.* (2002). We motivate the idea below.
  In the Newtonian limit, the basic equations that characterize the universe as an ideal fluid

are given by eqs.(2.6), (2.7), and (4.44). In comoving coordinates (using the conformal time, $d\eta = dt/a$ and eq. (4.42)) they transform into

$$\delta'(\mathbf{r},\eta) + \nabla\cdot[(1+\delta(\mathbf{r},\eta))\mathbf{v}(\mathbf{r},\eta)] = 0, \tag{4.123}$$

$$\mathbf{v}'(\mathbf{r},\eta) + (\mathbf{v}(\mathbf{r},\eta)\cdot\nabla)\mathbf{v}(\mathbf{r},\eta) = -\frac{a'}{a}\mathbf{v}(\mathbf{r},\eta) - \nabla\Phi(\mathbf{r},\eta), \tag{4.124}$$

$$\Delta\Phi(\mathbf{r},\eta) = 4\pi G a^2 \rho_{\rm bg}\delta(\mathbf{r},\eta), \tag{4.125}$$

where $\mathbf{v}(\mathbf{r},\eta) = d\mathbf{r}/d\eta$ and derivatives with respect to η are characterized by a dash (e.g. $a' = da/d\eta$). Assuming a curl free velocity field we set $\Theta(\mathbf{r},\eta) \equiv \nabla\cdot\mathbf{v}(\mathbf{r},\eta)$ and linearize the eqs. (4.123), (4.124) with the help of eq. (4.125),

$$\delta'(\mathbf{r},\eta) + \Theta(\mathbf{r},\eta) = 0, \tag{4.126}$$

$$\mathbf{v}'(\mathbf{r},\eta) + \frac{a'}{a}\mathbf{v}(\mathbf{r},\eta) = -\nabla\Phi(\mathbf{r},\eta). \tag{4.127}$$

The velocity field $\mathbf{v}(\mathbf{r},\eta)$ is completely described by its divergence $\Theta(\mathbf{r},\eta)$ and vorticity $\nabla\times\mathbf{v}(\mathbf{r},\eta)$, whose evolution equations follow from eq. (4.127),

$$\frac{\partial\Theta(\mathbf{r},\eta)}{\partial\eta} + \frac{a'}{a}\Theta(\mathbf{r},\eta) + \frac{3}{2}\Omega_{\rm M}\left(\frac{a'}{a}\right)^2\delta(\mathbf{r},\eta) = 0, \tag{4.128}$$

$$\frac{\partial}{\partial\eta}(\nabla\times\mathbf{v}(\mathbf{r},\eta)) + \frac{a'}{a}(\nabla\times\mathbf{v}(\mathbf{r},\eta)) = 0. \tag{4.129}$$

The vorticity evolution, determined by eq. (4.129) is proportional to $\propto a^{-1}$. In the linear regime its evolution is suppressed due to the expansion of the universe and thus, not of interest for our purposes.

The main idea of PT is to expand the density and velocity fields about the linear solutions of eq. (4.126) and eq. (4.128), which correspond to time dependent scalings of the initial density field,

$$\delta(\mathbf{r},\eta) = \sum_{n=1}^{\infty}\delta^n(\mathbf{r},\eta), \tag{4.130}$$

$$\Theta(\mathbf{r},\eta) = \sum_{n=1}^{\infty}\Theta^n(\mathbf{r},\eta), \tag{4.131}$$

where $\delta^{(1)}$ and $\Theta^{(1)}$ are linear in the initial density field, $\delta^{(2)}$, $\Theta^{(2)}$ quadratic, etc. Applying a Fourier-Transformation,

$$\tilde{A}(\mathbf{k},\eta) = \int\frac{d^3\mathbf{r}}{(2\pi)^3}\exp(-i\mathbf{k}\cdot\mathbf{r})A(\mathbf{r},\eta), \tag{4.132}$$

to eq. (4.130) and eq. (4.131) results in

$$\tilde{\delta}(\mathbf{k},\eta) = \sum_{n=1}^{\infty}a^n(\eta)\delta_n(\mathbf{k}), \tag{4.133}$$

$$\tilde{\Theta}(\mathbf{k},\eta) = -\frac{a'(\eta)}{a(\eta)}\sum_{n=1}^{\infty}a^n(\eta)\delta_n(\mathbf{k}), \tag{4.134}$$

which present the perturbative expansion in Fourier space. Taking the divergence of eq. (4.124) and using the Fourier transformation for eq. (4.126) and eq. (4.128) leads to the linear evolution equations in Fourier space,

$$\begin{aligned}\tilde{\delta}'_{\mathbf{k}}(\eta)+\tilde{\Theta}_{\mathbf{k}}(\eta) &= -\int\frac{d^3k_1}{(2\pi)^3}\int d^3k_2\,\delta_D(\mathbf{k}_1+\mathbf{k}_2-\mathbf{k})\frac{\mathbf{k}\cdot\mathbf{k}_1}{k_1^2}\cdot \\ &\quad \tilde{\delta}_{\mathbf{k}_2}(\eta)\tilde{\Theta}_{\mathbf{k}_1}(\eta), \qquad (4.135)\\ \tilde{\Theta}'_{\mathbf{k}}(\eta)+\frac{a'}{a}\tilde{\Theta}_{\mathbf{k}}(\eta)+\frac{3a'^2}{2a^2}\Omega_{\mathrm{M}}(\eta)\tilde{\delta}_{\mathbf{k}}(\eta) &= -\int\frac{d^3k_1}{(2\pi)^3}\int d^3k_2\,\delta_D(\mathbf{k}_1+\mathbf{k}_2-\mathbf{k})\cdot \\ &\quad \frac{k^2(\mathbf{k}_1\cdot\mathbf{k}_2)}{2k_1^2k_2^2}\tilde{\Theta}_{\mathbf{k}_1}(\eta)\tilde{\Theta}_{\mathbf{k}_2}(\eta). \qquad (4.136)\end{aligned}$$

We further assume that the universe is matter dominated $\Omega_{\mathrm{M}}(\eta)=1$ and $a(\eta)=\eta^2$, which brings eq. (4.135) and eq. (4.136) into a homogeneous form in η, respectively $a(\eta)$. This assumption is not entirely fulfilled, since at low redshifts DE begins to dominate. Yet, the next-to-leading order correction to $P(k)$ is insensitive of the background cosmology if the corresponding growth factor for $\delta_{\mathbf{k}}$ is used (Bernardeau *et al.*, 2002). The system can now be solved with eq. (4.133) and eq. (4.133). Expanding $\tilde{\delta}_{\mathbf{k}}(\eta)$ and $\tilde{\Theta}_{\mathbf{k}}(\eta)$ in powers of the linear solution with $\delta_1(\mathbf{k})$ as basis leads to,

$$\begin{aligned}\tilde{\delta}(\mathbf{k},\eta) &= \sum_{n=1}^{\infty}a^n(\eta)\int\frac{d^3q_1}{(2\pi)^3}\cdots\frac{d^3q_{n-1}}{(2\pi)^3}\cdot\int d^3q_n\,\delta_D\left(\sum_{i=1}^{n}\mathbf{q}_i-\mathbf{k}\right)\cdot \\ &\quad F_n(\mathbf{q}_1,\mathbf{q}_2,...,\mathbf{q}_n)\delta_1(\mathbf{q}_1)...\delta_1(\mathbf{q}_n), \qquad (4.137)\\ \tilde{\Theta}(\mathbf{k},\eta) &= -\sum_{n=1}^{\infty}a'(\eta)a^{n-1}(\eta)\int\frac{d^3q_1}{(2\pi)^3}\cdots\frac{d^3q_{n-1}}{(2\pi)^3}\cdot\int d^3q_n\,\delta_D\left(\sum_{i=1}^{n}\mathbf{q}_i-\mathbf{k}\right)\cdot \\ &\quad G_n(\mathbf{q}_1,\mathbf{q}_2,...,\mathbf{q}_n)\delta_1(\mathbf{q}_1)...\delta_1(\mathbf{q}_n), \qquad (4.138)\end{aligned}$$

where δ_D is the three-dimensional Dirac delta distribution, and the functions F_n and G_n are determined by (Jain & Bertschinger, 1994),

$$\begin{aligned}F_n(\mathbf{q}_1,...,\mathbf{q}_n) &= \sum_{m=1}^{n-1}\frac{G_m(\mathbf{q}_1,...,\mathbf{q}_m)}{(2n+3)(n-1)}\cdot \qquad (4.139)\\ &\quad \left[(1+2n)\frac{\mathbf{k}\cdot\mathbf{k_1}}{k_1^2}F_{n-m}(\mathbf{q}_{m+1},...,\mathbf{q}_n)+\frac{k^2(\mathbf{k_1}\cdot\mathbf{k_2})}{k_1^2k_2^2}G_{n-m}(\mathbf{q}_{m+1},...,\mathbf{q}_n)\right],\\ G_n(\mathbf{q}_1,\mathbf{q}_2,...,\mathbf{q}_n) &= \sum_{m=1}^{n-1}\frac{G_m(\mathbf{q}_1,...,\mathbf{q}_m)}{(2n+3)(n-1)}\cdot \qquad (4.140)\\ &\quad \left[3\frac{\mathbf{k}\cdot\mathbf{k_1}}{k_1^2}F_{n-m}(\mathbf{q}_{m+1},...,\mathbf{q}_n)+n\frac{k^2(\mathbf{k_1}\cdot\mathbf{k_2})}{k_1^2k_2^2}G_{n-m}(\mathbf{q}_{m+1},...,\mathbf{q}_n)\right],\end{aligned}$$

($\mathbf{k}_1\equiv\mathbf{q}_1+...+\mathbf{q}_m$, $\mathbf{k}_2\equiv\mathbf{q}_{m+1}+...+\mathbf{q}_n$, $\mathbf{k}\equiv\mathbf{k}_1+\mathbf{k}_2$ and $F_1=G_1=1$). Using eq. (4.139) and eq. (4.140) with their corresponding recursion relations, the power spectrum at any order in perturbation can be calculated.

The linear density field δ_1 is a Gaussian random field for which the ensemble average of odd powers in δ_1 vanishes. For the next order $n = 2$ the kernels F_2 and G_2 are given by

$$F_2(\mathbf{q}_1,\mathbf{q}_2) = \frac{5}{7} + \frac{1}{2}\frac{\mathbf{q}_1\cdot\mathbf{q}_2}{q_1 q_2}\left(\frac{q_1}{q_2}+\frac{q_2}{q_1}\right) + \frac{2}{7}\cdot\frac{(\mathbf{q}_1\cdot\mathbf{q}_2)^2}{q_1^2 q_2^2}, \tag{4.141}$$

$$G_2(\mathbf{q}_1,\mathbf{q}_2) = \frac{3}{7} + \frac{1}{2}\frac{\mathbf{q}_1\cdot\mathbf{q}_2}{q_1 q_2}\left(\frac{q_1}{q_2}+\frac{q_2}{q_1}\right) + \frac{4}{7}\cdot\frac{(\mathbf{q}_1\cdot\mathbf{q}_2)^2}{q_1^2 q_2^2}. \tag{4.142}$$

Jain & Bertschinger (1994) obtained the next-to-leading order correction to $P(k,z)$ (see also Jeong & Komatsu, 2006) as,

$$P(k,z) = D(z)^2 P_{11}(k) + D(z)^4[2P_{13}(k) + P_{22}(k)] \tag{4.143}$$

where $D(z)^2\cdot P_{11}(k)$ expresses the linear power spectrum (eq. (4.69)), and $P_{22}(k)$ and $P_{13}(k)$ are determined through

$$P_{22}(k) = 2\int \frac{d^3q_1}{(2\pi)^3} P_{11}(q) P_{11}(|\mathbf{k}-\mathbf{q}|)\left[F_2^{(s)}(\mathbf{q},\mathbf{k}-\mathbf{q})\right]^2, \tag{4.144}$$

$$F_2^{(s)}(\mathbf{k}_1,\mathbf{k}_2) = \frac{5}{2} + \frac{2}{7}\frac{(\mathbf{k}_1\cdot\mathbf{k}_2)^2}{k_1^2 k_2^2} + \frac{\mathbf{k}_1\cdot\mathbf{k}_2}{2}\left(\frac{1}{k_1^2}+\frac{1}{k_2^2}\right), \tag{4.145}$$

$$2P_{13}(k) = \frac{2\pi k^2}{252} P_{11}(k)\int_0^\infty \frac{d^3q_1}{(2\pi)^3} P_{11}(q)\cdot \left[100\frac{q^2}{k^2} - 158 + 12\frac{k^2}{q^2} - 42\frac{q^4}{k^4} + \frac{3}{k^5 q^3}(q^2-k^2)^3(2k^2+7q^2)\ln\left(\frac{k+q}{|k-q|}\right)\right]. \tag{4.146}$$

$F_2^{(S)}$ denotes the symmetrized kernel obtained by summing over all possible permutations of the variables. The growth factor $D(z)$ contains the cosmological framework. It increases with decreasing redshifts (see also section 4.3), thus, the nonlinear part scaled with the forth power in $D(z)$ gets stronger. Fig. 4.10 displays the several contributions at $z = 0$: The complete power spectrum is presented by the black curve, which coincides for wavenumbers below $k \leq 0.1$ Mpc^{-1} with the linear part (i.e. $D^2(z)P_{11}(k)$), indicated by the green curve. The nonlinear part of eq. (4.143) is given by $D^4(z)[2P_{13}(k) + P_{22}(k)]$, where $P_{13}(k)$ is shown by the blue curve, while $P_{22}(k)$ is presented by the red curve. They begin to influence $P(k)$ at $k > 0.1$ Mpc^{-1}.
We use eq. (4.143) - eq.(4.146) to calculate $P(k,z)$.

- NONLINEAR POWER SPECTRUM OF MA *et al.* (1999) - MA99:
This model presents a simple analytic approximation for the linear and nonlinear mass power spectrum, assuming spatially flat cold dark matter (CDM) cosmologies and a time varying dark energy component - the quintessence. It has been widely used in the literature and is easy to implement. Its description is an extension of the work by Ma (1998), where the functional form of the power spectrum is based on analytic solutions and the coefficients are determined by fits to numerical simulated power spectra. The basic idea to map the linear to the nonlinear regime was introduced by Hamilton *et al.* (1991). The function $\Delta_{nl}(k_{nl},z) = f[\Delta_l(k_l,z)]$ relates the

linear to the nonlinear power spectrum, with $\Delta(k,z) = k^3/(2\pi^2)\cdot P(k,z)$. Note that Δ_{nl} and Δ_l are calculated at different wave numbers, connected via

$$k_l = \frac{k_{nl}}{(1+\Delta_{nl})^{-1/3}}. \tag{4.147}$$

The resulting power spectrum has the form,

$$\Delta_{nl}(k_{nl},z) \quad = \quad G\left(\frac{\Delta_l(k_l,z)}{g_0^{3/2}\sigma_8^{\beta}}\right)\cdot\Delta_l(k_l,z), \tag{4.148}$$

using the abbreviation

$$x = \frac{\Delta_l(k_l,z)}{g_0^{3/2}\sigma_8^{\beta}}, \tag{4.149}$$

the function $G(x)$ is given by

$$G(x) \quad = \quad [1+\ln(1+0.5x)]\cdot\frac{1+0.02x^4+c_1x^8/g^3}{1+c_2x^{7.5}}, \tag{4.150}$$

where

$$g_0 \quad = \quad |w_{\rm DE}|^{1.3|w_{\rm DE}|-0.76}\cdot g(z=0), \tag{4.151}$$

$$\sigma_8 \quad = \quad \sigma_8(z=0)\cdot\frac{g}{g(z=0)}(1+z), \tag{4.152}$$

with the parameters $c_1 = 1.08\cdot10^{-4}$, $c_2 = 2.10\cdot10^{-5}$, $\beta = 0.83$ and σ_8 the rms linear mass fluctuation on a $8h^{-1}$Mpc scale. g is the growth suppression factor (eq. (4.54)) for which exists in the case of quintessence an approximation (Ma, 1998)

$$g \quad = \quad (-w_{\rm DE})^t\cdot g_\Lambda, \tag{4.153}$$

$$t \quad = \quad -(0.255+0.30w_{\rm DE}+0.0027/w_{\rm DE})\,[1-\Omega_{\rm M}(z)]- \\ (0.366+0.266w_{\rm DE}-0.07/w_{\rm DE})\ln\Omega_{\rm M}(z). \tag{4.154}$$

(g_Λ denotes the growth suppression factor for a universe with the standard cosmological constant, $w_{\rm DE} = -1$.) However, we use the exact solution for g, determined by eq. (4.61).
The functional form of $G(x)$ resembles the appropriate asymptotic behavior in the linear- ($\Delta_{nl}\rightarrow\Delta_l, x\ll1$) and the stable clustering regime ($\Delta_{nl}\propto\Delta_l^{3/2}, x\gg1$). The factor $[1+\ln(1+0.5x)]$ accounts for the non-vanishing positive slope of Δ_{nl}/Δ_l in the mildly nonlinear regime ($-1<\Delta_l<1$). This arises due to the fact that Δ_{nl} and Δ_l are evaluated at the wave numbers k_{nl} and k_l, where k_l is always smaller than k_{nl}. Therefore, $\Delta_l(k_l,z)$ is smaller and the fraction $\Delta_{nl}(k_{nl},z)/\Delta_l(k_l,z)$ larger than unity.

- HALO MODEL - HALOFIT:
  In this approach the density field is identified as a distribution of matter clumps described through their individual density profiles. The original idea dates back to Neyman & Scott (1952) and was adapted by Scherrer & Bertschinger (1991). The correlation between different halos is responsible for the large scale clustering of mass, while for small scales they arise form the clustering of dark matter particles within the same halo (Peebles, 1974b; McClelland & Silk, 1977; Sheth & Jain, 1997). Further developments were made by Seljak (2000) and Smith *et al.* (2003), respectively. For a more detailed review refer to Smith *et al.* (2003), and Cooray & Sheth (2002).
  The halo model consists of two contributions (remember that $\Delta(k,z) = k^3/(2\pi^2)\cdot P(k,z)$)

$$P(k) = P_Q(k) + P_H(k), \text{ or } \Delta(k) = \Delta_Q(k) + \Delta_H(k), \tag{4.155}$$

  where $P_Q(k)$ characterizes the quasi-linear term that presents the power generated by the large scale placement of halos, and $P_H(k)$ the halo term that determines the power resulting from their self correlation. Smith *et al.* (2003) proposed an empirical approach, where

$$\Delta_Q(k) \quad = \quad \Delta_l(k)\left\{\frac{[1+\Delta_l(k)]^{\beta_n}}{1+\alpha_n\Delta_l(k)}\right\}\exp\left[-f(y)\right], \tag{4.156}$$

  with $y = k/k_\sigma$, $f(y) = y/4 + y^2/8$ and $\Delta_l(k)$ being the linear power spectrum. k_σ expresses the nonlinear scale, $f(y)$ the decay rate and α_n, β_n are spectral dependent coefficients. The halo term is given by (Peacock & Smith, 2000; Ma & Fry, 2000; Seljak, 2000; Scoccimarro *et al.*, 2001)

$$\Delta_H = \frac{\Delta'_H(k)}{1+\mu_n y^{-1} + \nu_n y^{-2}}, \tag{4.157}$$

  with $\Delta'_H(k)$ being,

$$\Delta'_H(k) = \frac{a_n y^{3f_1(\Omega)}}{1+b_n y^{f_2(\Omega)} + [c_n f_3(\Omega) y]^{3-\gamma_n}}. \tag{4.158}$$

  a_n, b_n, c_n, γ_n, μ_n, ν_n are again dimensionless parameters that depend on the spectrum. The nonlinear scale k_σ arises from the condition that

$$\sigma(k_\sigma^{-1}, z) \equiv 1, \tag{4.159}$$

  where $\sigma(R,z)$ expresses the variance of the linear density field,

$$\sigma^2(R,z) = \int \Delta_l(k,z)|W(kR)|^2 \frac{d\ln k}{k}, \tag{4.160}$$

  with the filter function W and the effective filter radius R. Assuming an Gaussian filter it follows,

$$\sigma^2(R_G,z) \equiv \int \Delta_l(k,z)\exp\left(-k^2R_G^2\right)d\ln k. \tag{4.161}$$

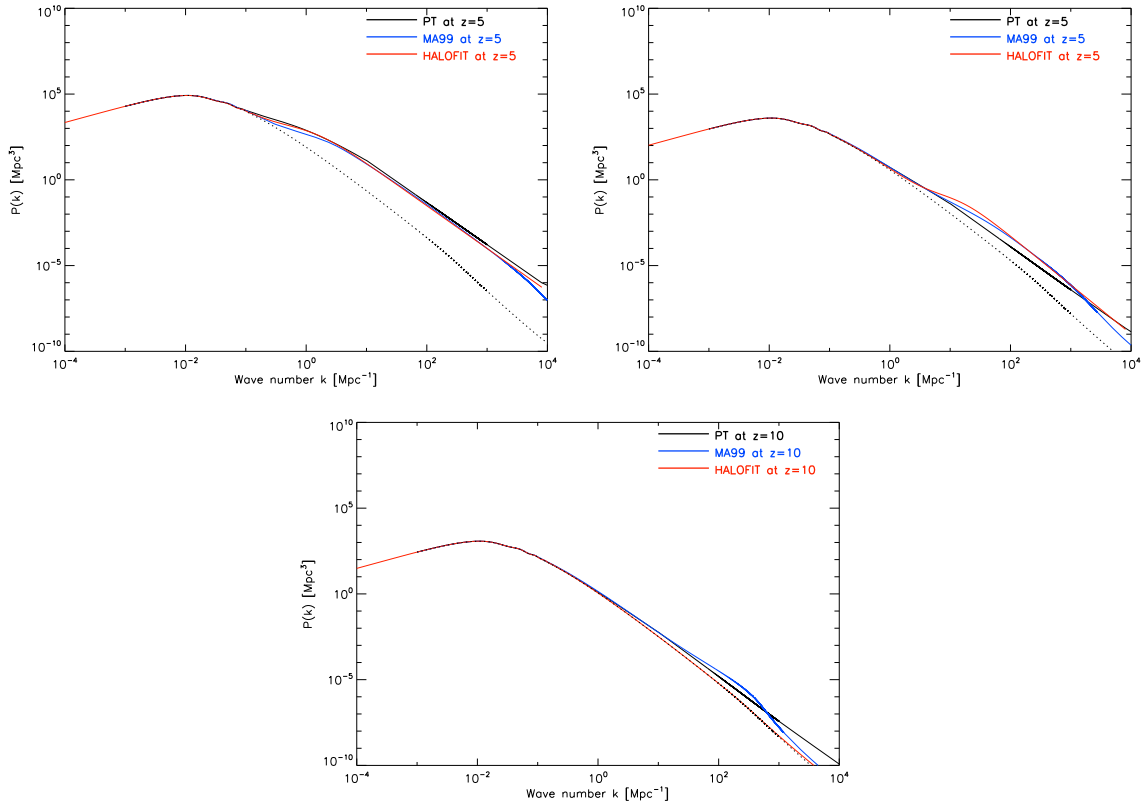

Figure 4.11: Comparison of the power spectra using PT (black line), MA99 (blue line) and HALOFIT (red line). Upper left panel: At $z = 0$. Upper right panel: At $z = 5$. Bottom panel: At $z = 10$. The linear power spectrum is indicated by the black dotted line.

To model curved spectra Smith *et al.* (2003) define the effective index

$$3 + n_{\rm eff} \equiv -\frac{d^2 \ln \sigma^2(R,z)}{d \ln R}|_{\sigma=1}, \tag{4.162}$$

with the spectral curvature being,

$$C \equiv -\frac{d^2 \ln \sigma^2(R,z)}{d \ln R}|_{\sigma=1}. \tag{4.163}$$

The coefficients they obtained by fitting the parameters to simulations are given in the appendix B.6

4.4.2 Evolution of Power Spectra for PT, MA99 & HALOFIT

Fig. 4.11 and Fig. 4.12 show the evolution of $P(k,z)$ and the ratio of linear- to nonlinear power spectrum $R(k)$ with wave number k, using PT (black line), MA99 (blue line) and HALOFIT (red line) at

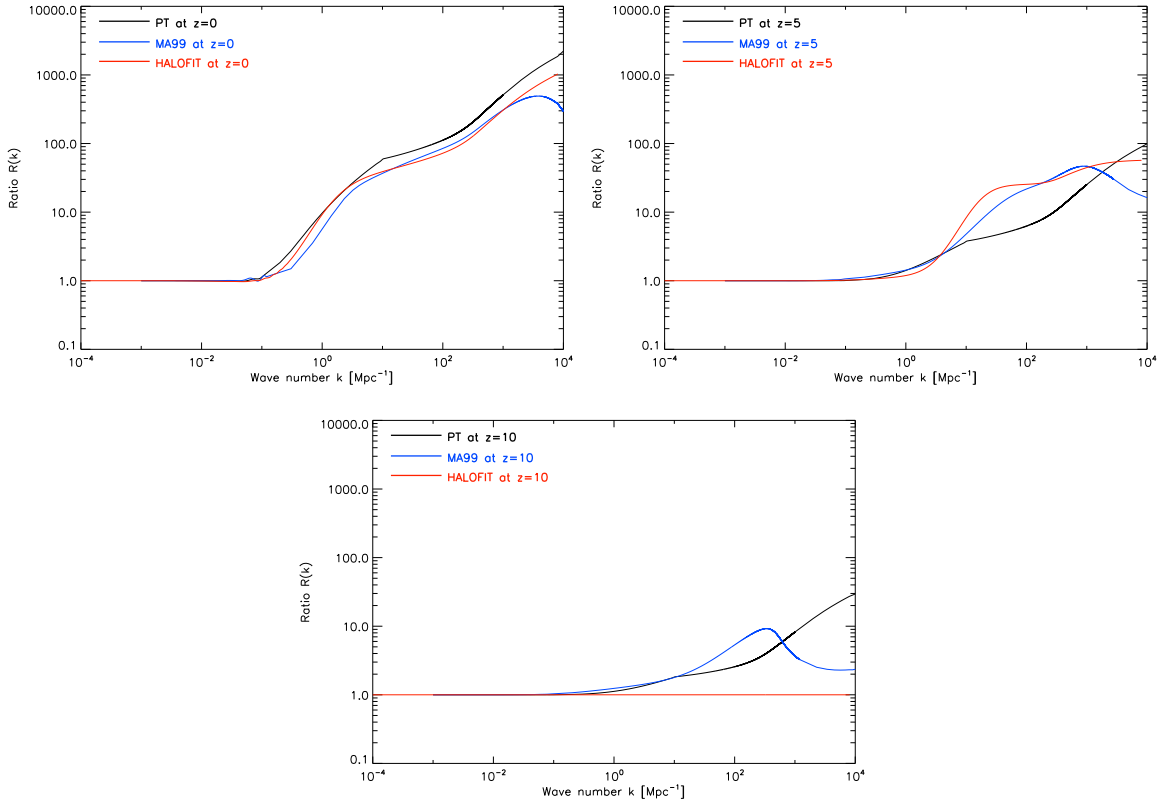

Figure 4.12: The same as Fig. 4.11 but for the ratios of nonlinear to linear power spectra.

$z = 0$ (upper left panels), $z = 5$ (upper right panels) and $z = 10$ (bottom panels). The black dotted line in Fig. 4.11 expresses the linear power spectrum. We take as DE model the standard cosmological constant ($w_{\rm DE} = -1$).

At small wave numbers (large scales) the fluctuations grow linearly, hence all power spectra are in the linear regime and do not differ. The $R(k)$ are constant and equal to one. Going to larger k (smaller scales) nonlinear effects arise. At $z = 0$ (see upper left panel of Fig. 4.11), PT exhibits the strongest nonlinear contribution for $k > 0.1$ Mpc^{-1}, HALOFIT follows closely while MA99 is slightly lower but coincides with HALOFIT at ~ 100 Mpc^{-1} before it begins to drop around ~ 1000 Mpc^{-1}. This behavior is also reflected in the evolution of $R(k)$ (see upper left panel of Fig. 4.12). The PT-ratio begins to rise at $k > 0.1$ Mpc^{-1}, indicating the dominating nonlinear power at small scales. The MA99- and HALOFIT-$R(k)$ lie slightly below, where MA99 decreases rapidly at ~ 1000 Mpc^{-1}.

At $z = 5$ (upper right panels of Fig. 4.11 and Fig. 4.12), all examples evolve similar for $k < 4$ Mpc^{-1}. In the range $k \sim [4 - 1000]$ Mpc^{-1}, HALOFIT and MA99 have stronger nonlinear contributions in contrast to PT, which result in a stronger $R(k)$. The MA99- and HALOFIT-ratios rise above PT and evolve similar at ~ 100 Mpc^{-1}. However, soon afterwards MA99 begins to decrease, while PT begins to dominate around ~ 1000 Mpc^{-1}.

For increasing redshifts the nonlinear effects become less dominant and therefore, the power spectra should comply with the linear spectrum. This is indeed the case (see the bottom panels of Fig. 4.11

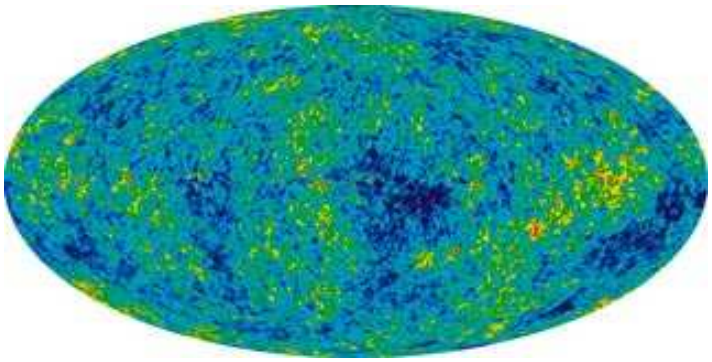

Figure 4.13: The WMAP sky map obtained from www.map.gsfc.nasa.gov.

and Fig. 4.12). HALOFIT does not exhibit any nonlinear contribution, yet PT and MA99 have a slightly increased nonlinear power at larger k. MA99 lies above PT, but decreases at $k \sim 600$ Mpc^{-1}. In general, PT dominates at very large scales ($k > 1000$ Mpc^{-1}) and small redshifts, while MA99 and HALOFIT possess more nonlinear power for $k \sim [4-1000]$ Mpc^{-1} at intermediate redshifts. We return to this issue when discussing the amplitude of the bispectrum, see section 4.6. Note that in the literature MA99 is very often used, but assuming an implicit dependence on k_{nl}, e.g. Giovi *et al.* (2003),

$$\Delta_{nl}(k_{nl},z) = G\left(\frac{\Delta(k_{nl},z)}{g_0^{3/2}\sigma_8^{\beta}}\right)\cdot\Delta_l(k_l,z), \tag{4.164}$$

but see the discussion in the appendix B.7.

4.5 Correlation Functions of the CMB

Now we come to an very important part of this chapter, the correlation functions of the CMB, in particular its bispectrum.
CMB photons carry information about the primordial state of the universe in form of primary anisotropies, while gravitational interaction after decoupling induces secondary anisotropies, see also 4.5.1. Since DE influences forming objects that interact with CMB photons during the epoch of structure formation, these temperature fluctuations encompass information about DE and its equation of state. The CMB power- and bispectrum are thus useful tools to constrain DE and other cosmological parameters. In 4.5.2 and 4.5.3 we introduce the basic framework of CMB statistics in form of these correlation functions. The CMB two- and three-point-correlation-function along with their corresponding power- and bispectrum are described. They build the background to study anisotropies in the CMB. For more details see also e.g. Luo (1994), Spergel & Goldberg (1999), and Goldberg & Spergel (1999). The definitions are used to calculate the L-RS-bispectrum in 4.6, and the corresponding signal-to-noise ratio in section 4.7.

4.5.1 CMB-Anisotropies

Measuring the temperature of CMB photons at a spot in the sky from different incoming directions reflects the inhomogeneities (e.g. Kogut *et al.*, 1993; Miller *et al.*, 2000; Spergel *et al.*, 2003, 2007; Komatsu *et al.*, 2009) and results in sky maps, see Fig. 4.13. As mentioned before, of most interest are the imprinted fluctuations divided into primary and secondary anisotropies (see also Fig. 1.3). We shortly introduce them below. For more details see e.g. Hu *et al.* (1997), Hu & Dodelson (2002), or Schneider (2006).

Primary Anisotropies

The primary (or primordial) anisotropies arise in the very early stages of the Universe when it still was dominated by radiation and the baryons and photons coupled via Thomson-scattering, called baryon-photon-plasma (see also Fig. 1.2). Density inhomogeneities, induced by quantum fluctuations during the epoch of inflation are responsible for the gravitational redshift of the photons. Photons located in higher density regions experience a gravitational redshift due to the larger potential which results in the loss of energy (temperature). Yet, the effect of gravitational induced time-dilation is counteracting. The relativistic description of both processes by Sachs & Wolfe (1967) is known as the *Sachs-Wolfe-Effect*. Another contribution follows from peculiar velocities (see 4.2.6). During the last interaction between photons and electrons (before decoupling) this additional velocity leads to a further Doppler-shift of the photons. Furthermore, regions with higher baryonic density have a higher baryon-photon pressure, the baryons are adiabatically compressed and begin to oscillate. This rises the temperature of both components, adding to the anisotropies. Finally, the *Silk-Damping* describes the smoothing of temperature fluctuations on small scales as a result of photon diffusion.
The primordial anisotropies can be analyzed by the two-point-correlation function (power spectrum) due to their Gaussian nature, see 4.5.2. By comparing theoretical models to the measured angular distribution of the CMB it is possible to obtain constrains on various cosmological parameters, see e.g. Schneider (2006) for a summary.

Secondary Anisotropies

The secondary anisotropies are caused during the propagation of the CMB photons through the Universe after decoupling. Reionization (see also Fig. 1.2), resulting from the first generation of stars leads to Thomson-Scattering of photons with free electrons, decreasing the photon temperature. Additionally, ongoing structure formation implies a time-varying gravitational potential where the late time decay of the potential, known as the Integrated-Sachs-Wolfe effect, and the nonlinear growth of structures (Rees & Sciama, 1968) are combined into the Rees-Sciama effect. Gravitational deflection (weak lensing) of photons as they pass through intervening large scale structure is yet another source. The *Sunyaev-Zeldovich* (SZ)-effect describes temperature variations due to scattering of photons while traveling through the hot gas within galaxy-clusters. Since the measured intensity is lower for lower frequencies and larger for higher frequencies, this effect can be detected in the CMB-data and corrected for.
The secondary anisotropies arise from nonlinear effects and introduce non-Gaussianity, which can be analyzed using higher order correlation functions e.g., the three-point-correlation function (bispectrum), see 4.5.3. The dependence of the RS- and weak lensing-effect on structure formation and thus, on DE allows to study theoretically calculated cross correlation bispectra using different DE-models.

This can be used to estimate how forthcoming CMB observations can constrain DE (see sections 4.6 and 4.7).

4.5.2 2-Point Correlation Function - Power spectrum of the CMB

Inflation predicts the spectrum of the fluctuations to be Gaussian, therefore, only even order correlation functions are nonzero. They are all expressed through the two-point correlation function (or temperature autocorrelation function),

$$C(\Theta) = \left\langle \frac{\Delta T}{T}(\mathbf{l_1}) \frac{\Delta T}{T}(\mathbf{l_2}) \right\rangle, \tag{4.165}$$

averaged over all unit vectors (**l**) in the direction 1, 2, with $\mathbf{l_1} \cdot \mathbf{l_2} = \cos(\Theta)$, and Θ being the fixed angular separation. Furthermore, $\frac{\Delta T}{T}(\mathbf{l}) = \frac{T(\mathbf{l})-T_0}{T_0}$, where T_0 is the mean Temperature of the CMB.
To analyze the continuous spectrum of temperature fluctuations, $\Delta T/T$ is expanded in terms of spherical harmonics,

$$Y_{lm}(\mathbf{l}) = \left[\frac{2l+1}{4\pi}\frac{(l-|m|)!}{(l+|m|)!}\right]^{1/2} P_{lm}(\cos\Theta) e^{im\phi} \begin{cases} (-1)^m & m \geq 0, \\ 1 & m < 0 \end{cases} \tag{4.166}$$

where $0 \leq \Theta \leq \pi$, $0 \leq \phi \leq 2\pi$, $l = [0,..,\infty]$, $-l \leq m \leq l$ and $P_{lm}(\cos\Theta)$ is an associated Legendre function,

$$P_{lm}(x) = \frac{(-1)^m}{2^l l!}(1-x^2)^{m/2}\frac{d^{l+m}}{dx^{l+m}}(x^2-1)^l, \tag{4.167}$$

with $x = cos\Theta$. The expansion results in

$$\frac{\Delta T}{T}(\mathbf{l}) = \sum_{l,m} a_{lm} Y_{lm}(\mathbf{l}), \tag{4.168}$$

and can be interpreted as a kind of generalized Fourier-Transformation, since for the surface of a sphere the orthonormal functions are the spherical harmonics. Using the orthogonality condition for Y_{lm},

$$\int Y^*_{lm} Y_{l'm'} d\Omega = \delta_{ll'}\delta_{mm'}, \tag{4.169}$$

it follows for the coefficients a_{lm},

$$a_{lm} = \int \frac{\Delta T}{T}(\mathbf{l}) Y^*_{lm}(\mathbf{l}) d^2 l. \tag{4.170}$$

The distribution of the a_{lm}'s is determined through the quantum fluctuations laid down during inflation. Each of the $(2l+1)$ coefficients to a_{lm} gives an independent estimate of the amplitude of temperature fluctuations related to the multipole l. For example, for $l = 2$ we have five independent contributions, while for $l = 1000$ we get 2001. From this arises an important aspect, for large scales (small l's) we have only a few independent estimates. Thus, the precision to which the amplitudes can be measured is limited. This effect is called *cosmic variance*,

$$\left(\frac{\Delta C_l}{C_l}\right)_{\text{cosmic variance}} = \sqrt{\frac{2}{2l+1}} \tag{4.171}$$

and presents a fundamental barrier that cannot be improved by enhancing the accuracy of the measurements.
The mean value of a_{lm} vanishes, i.e. $\langle a_{lm}\rangle = 0$, while the variance provides an estimate of the power at l,

$$C_l = \langle a_{lm}\, a^*_{l'm'}\rangle = \left\langle |a_{lm}|^2 \right\rangle = \frac{1}{2l+1}\sum_m a_{lm} a^*_{lm}. \tag{4.172}$$

C_l denotes the power spectrum. Using eq. (4.168) and

$$\sum_{lm} Y^*_{lm}(\mathbf{l_1}) Y_{lm}(\mathbf{l_2}) = \sum_l \frac{2l+1}{4\pi} P_l(\cos\Theta), \tag{4.173}$$

we can rewrite the two-point correlation function (eq. (4.165)),

$$C(\Theta) = \frac{1}{4\pi}\sum_l (2l+1) C_l P_l(\cos\Theta). \tag{4.174}$$

4.5.3 3-Point Correlation Function - Bispectrum of the CMB

An indicator of non Gaussianity in the CMB temperature fluctuations is presented by the three-point function or analogous the *bispectrum*, since it vanishes in the Gaussian limit. The three point correlation function measures and correlates the temperature of the background radiation at three different positions ($\mathbf{l_1}$, $\mathbf{l_2}$, $\mathbf{l_2}$) in the sky. It is given as,

$$B(\mathbf{l_1},\mathbf{l_2},\mathbf{l_3}) = \left\langle \frac{\delta T}{T}(\mathbf{l_1}) \frac{\delta T}{T}(\mathbf{l_2}) \cdot \frac{\delta T}{T}(\mathbf{l_3}). \right\rangle \tag{4.175}$$

For the corresponding angular bispectrum follows,

$$B^{m_1 m_2 m_3}_{l_1 l_2 l_3} = \langle a_{l_1 m_1} a_{l_2 m_2} a_{l_3 m_3}\rangle, \tag{4.176}$$

where the a_{lm} are determined by eq. (4.170). The multipole moments satisfy the triangle condition and the parity invariance: $m_1+m_2+m_3 = 0$, $l_1+l_2+l_3 =$ even, and $|l_i - l_j| \le l_k \le l_i + l_j$. The universe is assumed to be rotationally invariant, which requires the bispectrum to be independent from orientation and the triangle-configuration. The *angular averaged bispectrum* is defined as,

$$B_{l_1,l_2,l_3} = \sum_{m_1,m_2,m_3} \begin{pmatrix} l_1 & l_2 & l_3 \\ m_1 & m_2 & m_3 \end{pmatrix} B^{m_1 m_2 m_3}_{l_1 l_2 l_3}. \tag{4.177}$$

It contains the *Wigner*-3 *j symbol*, which transforms the m's under rotation and preserves the triangle configuration. The Wigner-3 j symbol describes the bispectrum azimuthal angle dependence, and satisfying the orthogonality properties,

$$\sum_m \begin{pmatrix} l_1 & l_2 & l_3 \\ m_1 & m_2 & m_3 \end{pmatrix}^2 = 1, \tag{4.178}$$

$$\sum_{m'_1 m'_2} \begin{pmatrix} l_1 & l_2 & l_3 \\ m'_1 & m'_2 & m'_3 \end{pmatrix} \begin{pmatrix} l_1 & l_2 & L \\ m'_1 & m'_2 & M' \end{pmatrix} = \frac{\delta_{l_3 L}\delta_{m'_3, M}}{2L+1}. \tag{4.179}$$

Using the rotational invariance and the symmetry properties (eq. (4.178), and eq. (4.179)) it follows,

$$B_{l_1 l_2 l_3}^{m_1 m_2 m_3} = \zeta_{l_1 l_2 l_3}^{m_1 m_2 m_3} \cdot b_{l_1 l_2 l_3}, \tag{4.180}$$

where $\zeta_{l_1 l_2 l_3}^{m_1 m_2 m_3}$ is the so called *Gaunt integral*,

$$\begin{aligned} \zeta_{l_1 l_2 l_3}^{m_1 m_2 m_3} &= \int d^2\mathbf{l} Y_{l_1 m_1}(\mathbf{l}) Y_{l_2 m_2}(\mathbf{l}) Y_{l_3 m_3}(\mathbf{l}) \\ &= \sqrt{\frac{(2l_1+1)(2l_2+1)(2l_3+1)}{4\pi}} \cdot \begin{pmatrix} l_1 & l_2 & l_3 \\ 0 & 0 & 0 \end{pmatrix} \cdot \begin{pmatrix} l_1 & l_2 & l_3 \\ m_1 & m_2 & m_3 \end{pmatrix}, \end{aligned} \tag{4.181}$$

which includes the angle dependence and the triangle constraint via the Wigner-3 j symbol. $b_{l_1 l_2 l_3}$ denotes the *reduced bispectrum* that comprises all physical information (Komatsu & Spergel, 2001). Eq. (4.180) is valid as long as the universe is isotropic, thus $b_{l_1 l_2 l_3}$ only depends on the spatial separation between the points. As the reduced bispectrum does not include the Wigner-3 symbol, it is easier to be calculated and furthermore, it quantifies the physical properties of $B_{l_1 l_2 l_3}^{m_1 m_2 m_3}$.
In terms of $b_{l_1 l_2 l_3}$, together with

$$\sum_m \begin{pmatrix} l_1 & l_2 & l_3 \\ m_1 & m_2 & m_3 \end{pmatrix} \zeta_{l_1 l_2 l_3}^{m_1 m_2 m_3} = \sqrt{\frac{(2l_1+1)(2l_2+1)(2l_3+1)}{4\pi}} \cdot \begin{pmatrix} l_1 & l_2 & l_3 \\ 0 & 0 & 0 \end{pmatrix}, \tag{4.182}$$

the angle-averaged-bispectrum is given by,

$$B_{l_1, l_2, l_3} = \sqrt{\frac{(2l_1+1)(2l_2+1)(2l_3+1)}{4\pi}} \begin{pmatrix} l_1 & l_2 & l_3 \\ 0 & 0 & 0 \end{pmatrix} b_{l_1 l_2 l_3}. \tag{4.183}$$

The bispectrum consists of several sources (primary- as well as secondary sources). In section 4.6, the primordial-lensing-RS bispectrum will be discussed in detail.

4.6 Cross-Correlation Bispectrum

The Lensing-Rees-Sciama (L-RS) bispectrum (Verde & Spergel, 2002), describes the coupling between the Rees-Sciama and weak lensing effect. The RS-effect combines the late-time decay of gravitational potential fluctuations in a non-Einstein-de Sitter Universe - the ISW-effect (Sachs & Wolfe, 1967), and the non-linear growth of density fluctuations along the photon path (Rees & Sciama, 1968). The CMB temperature at any position (**l**) in the sky can be expanded as,

$$\begin{aligned} \frac{\Delta T(\mathbf{l})}{T} &= \frac{\Delta T(\mathbf{l} + \nabla\Theta)}{T} \\ &\approx \frac{\Delta T^{\mathrm{P}}(\mathbf{l})}{T} + \nabla \frac{\Delta T^{\mathrm{P}}(\mathbf{l})}{T} \cdot \nabla\Theta(\mathbf{l}) + \frac{\Delta T^{\mathrm{NL}}(\mathbf{l})}{T} + \frac{\Delta T^{\mathrm{SZ}}(\mathbf{l})}{T}. \end{aligned} \tag{4.184}$$

The first term $\Delta T^{\mathrm{P}}/T$ indicates the primordial contribution, the second the gravitational lensing effect, the third term the RS-contribution and the last the Sunyaev-Zeldovich effect (Zeldovich & Sunyaev, 1969). The SZ-effect will be neglected, since it can be singled out of the CMB signal due to its frequency dependence (see also 4.5.1). Other effects, like the Ostriker-Vishniac (OV) effect (Ostriker & Vishniac, 1986), which arises due to additional velocity perturbations during reionization are neglected. The OV effect appears at very small angular scales (i.e. large l) and does not affect our analysis. The considered terms are listed below.

- PRIMORDIAL-CONTRIBUTION:
  As discussed in section 4.5, the primordial anisotropies reflect the state of the universe at the last scattering surface. On large scales the SW-effect (Sachs & Wolfe, 1967) takes place, which increases the temperature of the CMB photons as they pass through density fluctuations and entails additional gravitational redshifts. However, due to the gravitative time delay (which is counteracting), the photons are scattered towards earlier times where the temperature was higher. The net effect leads, in the Newtonian limit to an contribution of $\Delta T^{\mathrm{P}}/T \sim 1/3\Delta\Phi$. Furthermore, hydrodynamical effects at intermediate scales imply variations in the photon temperature and result in acoustic oscillations. Verde & Spergel (2002) express these primordial effects through,

$$\frac{\Delta T^{\mathrm{P}}(\mathbf{l})}{T(\mathbf{l})} = \int \frac{d^3k}{(2\pi)^3} \exp(i\mathbf{k}\cdot\mathbf{l}r_*)\tilde{\Phi}(k)g(k), \tag{4.185}$$

  where g denotes the radiation transfer functional, $\tilde{\Phi}$ is the Fourier transform of the gravitational potential perturbation Φ[10], and r_* is the comoving distance to the last scattering surface. For the exact calculation see also e.g. Spergel & Goldberg (1999) and Goldberg & Spergel (1999).

- LENSING-CONTRIBUTION:
  In general, gravitational lensing elongates and stretches the images of background galaxies, which lie behind a source (e.g. another galaxy known as source galaxy). It can be interpreted as a lens that distorts the light. Lensing directly probes the distribution of the source mass, and is therefore very important for many astrophysical measurements. Gravitational lensing of CMB photons causes secondary anisotropies as they travel through the universe after decoupling. The forming structures deflect the photons, thus they contain information about the potential and the cosmological framework. The lensing potential $\Theta(\mathbf{l})$,

$$\Theta(\mathbf{l}) = -2\int_0^{r_*} dr \frac{r_* - r}{r r_*}\Phi(r, \mathbf{l}\cdot r), \tag{4.186}$$

  is the projection of the gravitational potential along the line of sight. For more details see Bartelmann & Schneider (2001) and Komatsu & Spergel (2001). The lensing effect leads to an additional change of the temperature distribution of CMB photons which is of non-Gaussian nature and can be traced with the bispectrum.

- RS-CONTRIBUTION:
  The RS-effect is a unique probe of time variation of the gravitational potential. It encompasses the ISW-effect (which is similar to the SW-effect) and takes into account the nonlinear growth of density fluctuations. CMB photons experience an gravitational redshift as they pass through perturbations. However, at low redshifts DE dominates and influences the growth. To take this into account the SW-effect must be integrated back to recombination which explains the denotation as integrated SW-effect. The temperature change is described by,

$$\frac{\Delta T^{\mathrm{NL}}(\mathbf{l})}{T(\mathbf{l})} = 2\int dr \frac{\partial}{\partial\eta}\Phi(\eta, \mathbf{l}\cdot r), \tag{4.187}$$

[10] Φ is identified as the fluctuation in the metric, see also Hu & White (1997), Hu (2000).

where again Φ is the Newtonian potential of the perturbation, r the comoving distance (eq. (4.26)) and $\partial/\partial\eta$ the partial derivative with respect to the conformal time. Eq. (4.187) includes the linear as well as the nonlinear evolution of density fluctuations. In the case of a matter only dominated universe the potential Φ remains constant in the linear regime and its derivative vanishes. However, if DE is taken into account its behavior changes depending on the particular scale, i.e.

- Linear Regime: Φ decays with time and $\partial\Phi/\partial\eta > 0$.
- Nonlinear Regime: Φ grows with time and $\partial\Phi/\partial\eta < 0$.

This results in a sign change when crossing from the linear- to the nonlinear scales, which is reflected correspondingly in the bispectrum.

All three effects are coupled via the potential Φ, and are thus correlated. The L- and RS-effect lead to a non Gaussian contribution to the CMB anisotropies which can be analyzed with the cross correlation bispectrum, which will be calculated in the following.
Setting eq. (4.184) into eq. (4.170) it follows for the a_{lm}, (Verde & Spergel, 2002)

$$a_{lm} = a_{lm}^{\mathrm{P}} + \int d^2\mathbf{l}\nabla\frac{\Delta T^{\mathrm{P}}(\mathbf{l})}{T(\mathbf{l})}\cdot\nabla\Theta(\mathbf{l})\cdot Y_{lm}^*(\mathbf{l}) + a_{lm}^{\mathrm{NL}}. \tag{4.188}$$

Applying the following expansions,

$$\Theta(\mathbf{l}) = \sum_{l,m}\Theta_{lm}Y_{lm}(\mathbf{l}), \tag{4.189}$$

$$\frac{\Delta T^{\mathrm{P}}(\mathbf{l})}{T(\mathbf{l})} = \sum_{l,m}a_{lm}Y_{lm}(\mathbf{l}), \tag{4.190}$$

eq. (4.188) results in,

$$a_{lm} = a_{lm}^{\mathrm{P}} + \sum_{l'm'}\sum_{l''m''}a_{l'm'}\Theta_{l''m''}\int d^2\mathbf{l}Y_{lm}^*(\mathbf{l})\nabla Y_{l'm'}(\mathbf{l})\nabla Y_{l''m''}(\mathbf{l}) + a_{lm}^{\mathrm{NL}}. \tag{4.191}$$

Using the relation, (Hu, 2000)

$$\begin{aligned}\int d^2\mathbf{l}Y_{lm}^*(\mathbf{l})\nabla Y_{l'm'}(\mathbf{l})\nabla Y_{l''m''}(\mathbf{l}) &= \frac{1}{2}\left[l'(l'+1)+l''(l''+1)-l(l+1)\right]\cdot \\ &\quad \int d^2\mathbf{l}Y_{lm}^*(\mathbf{l})Y_{l'm'}(\mathbf{l})Y_{l''m''}(\mathbf{l}),\end{aligned} \tag{4.192}$$

with the Gaunt-integral (eq. (4.181)) and $Y_{lm}^*(\mathbf{l}) = (-1)^m Y_{l-m}(\mathbf{l})$, we arrive at,

$$\begin{aligned}a_{lm} &= a_{lm}^{\mathrm{P}} + \frac{1}{2}\sum_{l'm'}\sum_{l''m''}(-1)^{(m+m'+m'')}\zeta_{ll'l''}^{-mm'm''}\cdot \\ &\quad \left[l'(l'+1)+l''(l''+1)-l(l+1)\right]a_{l'm'}^{\mathrm{P}*}\Theta_{l''-m''}^* + a_{lm}^{\mathrm{NL}}.\end{aligned} \tag{4.193}$$

From this follows the bispectrum,

$$\begin{aligned}B_{l_1l_2l_3}^{m_1m_2m_3} &= \zeta_{l_1l_2l_3}^{m_1m_2m_3}\cdot\frac{1}{2}\left[l_1(l_1+1)-l_2(l_2+1)+l_3(l_3+1)\right]\cdot \\ &\quad C_{l_1}^{\mathrm{P}}\langle\Theta_{l_3m_3}^* a_{l_3m_3}^{\mathrm{NL}}\rangle + 5\,perm.\end{aligned} \tag{4.194}$$

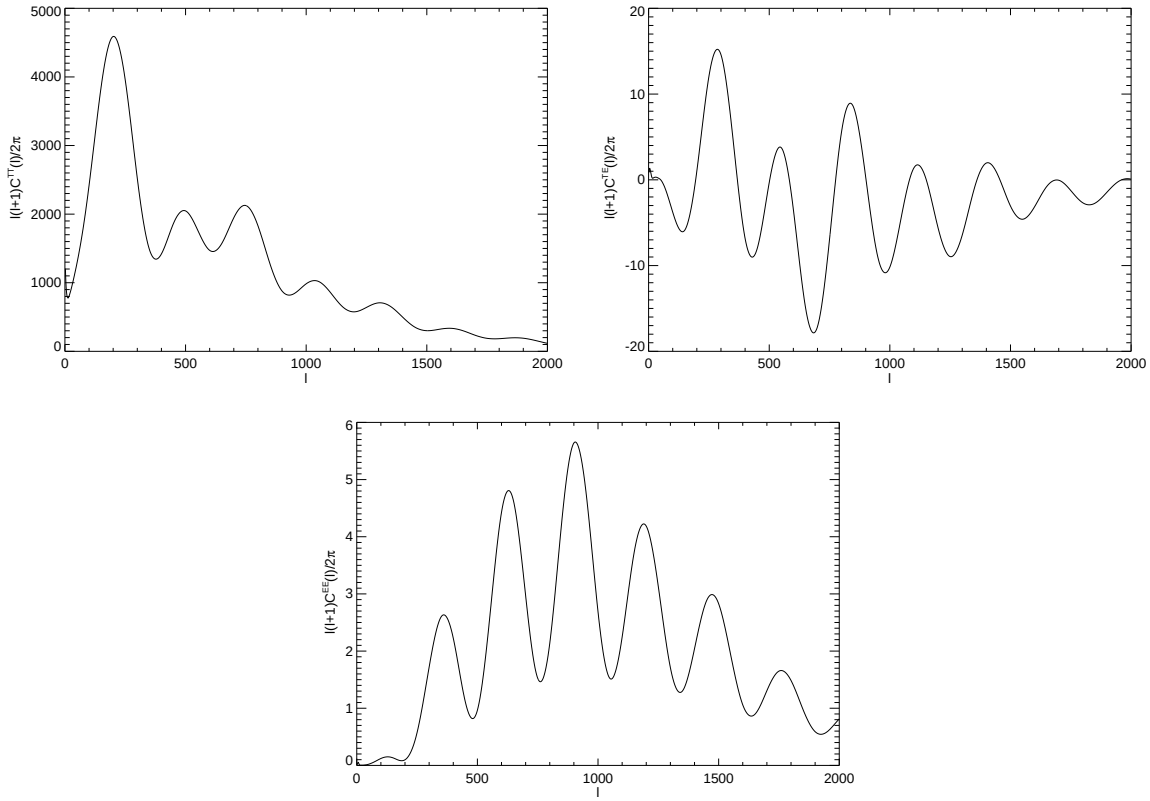

Figure 4.14: Evolution of the the primordial CMB temperature and polarization with multipole-moment l, obtained from CMBFAST. Upper left panel: $C^{TT}(l)$, which corresponds to eq. (4.196). Upper right panel: Polarization $C^{TE}(l)$. Bottom panel: Polarization $C^{EE}(l)$.

with the reduced bispectrum being

$$b_{l_1 l_2 l_3} = \frac{1}{2}\left[l_1(l_1+1) - l_2(l_2+1) + l_3(l_3+1)\right] \cdot C_{l_1}^{\mathrm{P}} \langle \Theta_{l_3 m_3}^{*} a_{l_3 m_3}^{\mathrm{NL}} \rangle + 5\, perm. \tag{4.195}$$

The primordial power spectrum C_l^{P} (eq. (4.172)) is obtained using CMBFAST (Seljak & Zaldarriaga, 1996), see also Fig. 4.14. Additionally, we include the detector noise

$$C_l = C_l^{\mathrm{P}} + C_l^{\mathrm{N}}, \tag{4.196}$$

where C_l^{N} is given by (Knox, 1995)

$$C_l^N \quad = \quad \exp\left(l^2 \sigma_b^2\right) S, \tag{4.197}$$

with S being the instrument sensitivity and $\sigma_b \sim \Theta_{FWHM}/2.3$, assuming that the experimental beam is Gaussian. We take PLANCK limited parameters (the case for WMAP limited parameters is discussed in the appendix B.10).

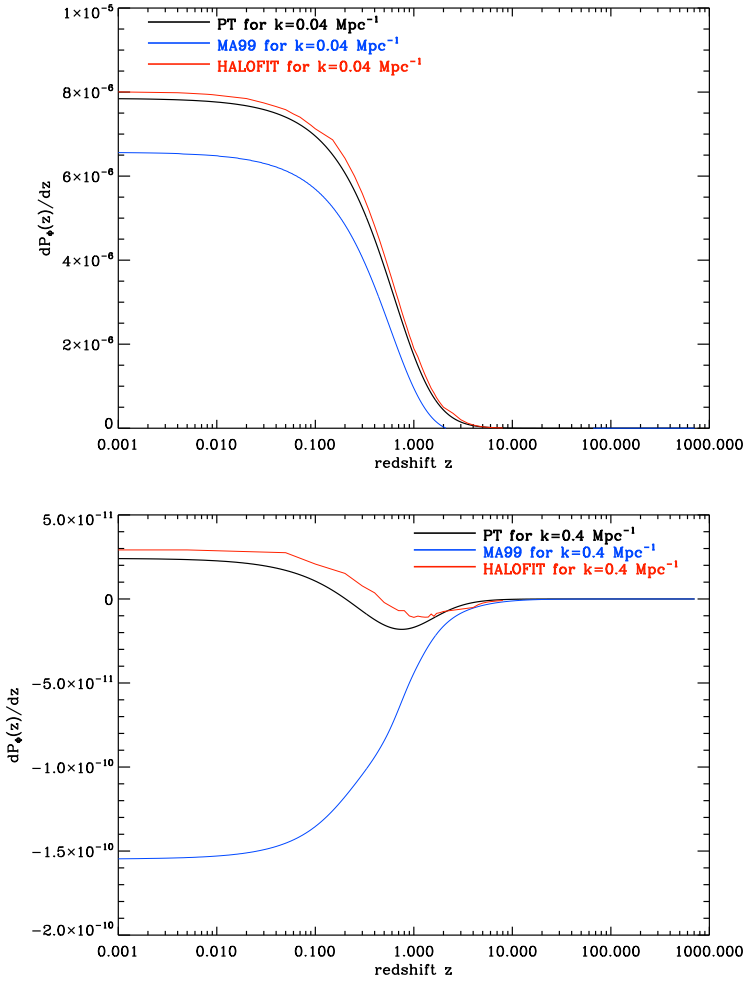

Figure 4.15: Evolution of $\partial P_\Phi(k,z)/\partial z$ (eq. (4.200) the derivative of $P_\Phi(k,z)$ with z, which is most sensitive to the onset of the nonlinear regime. We use PT (black line), MA99 (blue line) and HALOFIT (red line) keeping the wave number constant. Upper panel: $k = 0.04$ Mpc^{-1}. Bottom panel: $k = 0.4$ Mpc^{-1}.

The bispectrum amplitude is determined through $Q(l) \equiv \left\langle \Theta^*_{lm} a^{\rm NL}_{lm} \right\rangle$ and was derived by Verde & Spergel (2002),

$$\begin{aligned} Q(l) &= -4\left\langle \int d\mathbf{l_1} d\mathbf{l_2} dr \frac{r_* - r}{r_* r} \Phi(\eta, \mathbf{l_1} r) \cdot \int d\eta \frac{\partial \Phi(\eta, \mathbf{l_2} r)}{\partial \eta} Y^{*m_1}_{l_1}(\mathbf{l_1}) Y^{*m_2}_{l_2}(\mathbf{l_2}) \right\rangle, \\ &\backsimeq 2\int_0^{z_*} \frac{r(z_*) - r(z)}{r(z_*) r(z)^3} \frac{\partial}{\partial z} P_\Phi(k,z)|_{k=l/r(z)} dz. \end{aligned} \tag{4.198}$$

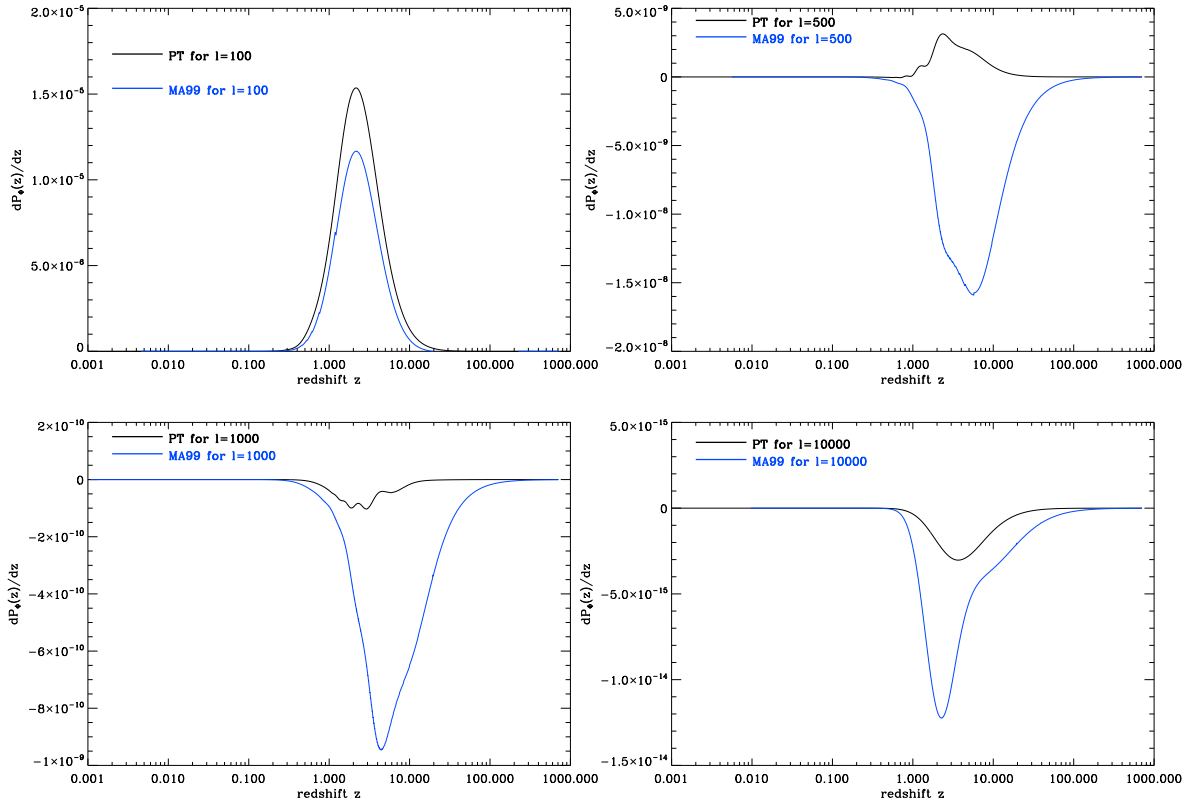

Figure 4.16: The same as Fig. 4.15 using PT (black line) and MA99 (blue line) for constant multipole-moments l. Upper left panel: $l = 100$. Upper right panel: $l = 500$. Bottom left panel: $l = 1000$. Bottom right panel: $l = 10000$.

z_* is the redshift of the last scattering surface and P_Φ the power spectrum of the gravitational potential fluctuations

$$P_\Phi(k,z) = \left(\frac{3}{2}\Omega_0\right)^2 \left(\frac{H_0}{k}\right)^4 P(k,z)(1+z)^2, \tag{4.199}$$

evaluated at $k = l/r(z)$ and then derived afterwards with respect to z. $P_\Phi(k,z)$ and correspondingly its derivative reflect the behavior of the potential Φ, which changes sign when the fluctuations leave the linear regime and enter the nonlinear evolution. This change marks the crossing point and appears, according to eq.(4.198) also in the behavior $Q(l)$. $P_\Phi(k,z)$ depends on the power spectrum of matter fluctuations $(P(k,z))$. We use PT-theory to characterize the nonlinear regime (eq. (4.143)), see also section 4.4. As comparison, we use MA99 (eq. (4.148)) and HALOFIT for a standard cosmological constant with $w_{\rm DE} = -1$. The derivative of P_Φ follows as

$$\frac{\partial}{\partial z} P_\Phi(k,z) = P_\Phi(k,z) \cdot \left[\frac{1}{P(k,z)} \frac{\partial P(k,z)}{\partial z} + \frac{1}{(1+z)}\right], \tag{4.200}$$

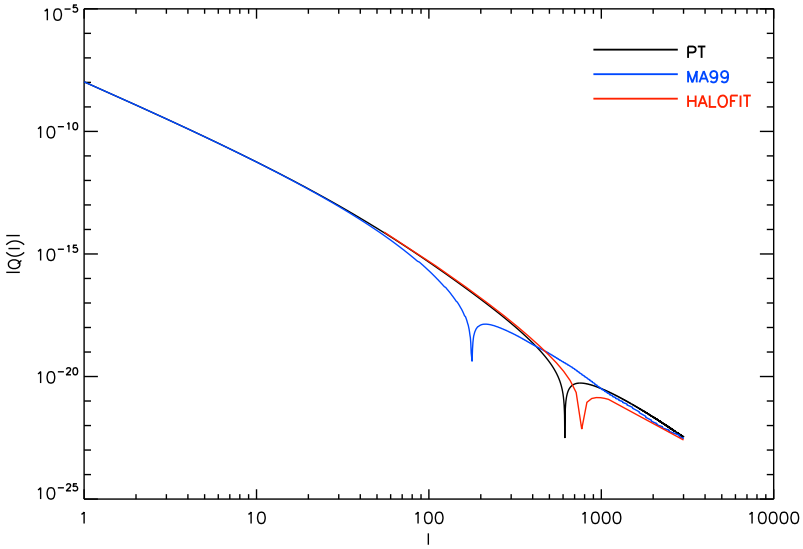

Figure 4.17: Evolution of the bispectrum amplitude $|Q(l)|$ (eq. (4.198)) with the multipole-moment l for PT (black line), MA99 (blue line) and HALOFIT (red line) using $w_{\rm DE} = -1$. The sign change denotes the onset of nonlinear effects: left side linear-, right side nonlinear regime.

and results for PT in

$$\frac{\partial P_\Phi(k,z)}{\partial z} = 2g^2(z)c(k)\cdot\left\{\left(\frac{g'(z)}{g(z)}\right)P^{\rm lin}(k) + D^2(z)\left[\frac{g'(z)}{g(z)} + \frac{D'(z)}{D(z)}\right]P^{\rm nonlin}(k)\right\}. \qquad (4.201)$$

$P^{\rm lin}(k)$ denotes the linear part, i.e. $P_{11}(k)$ and $P^{\rm nonlin}(k)$ the nonlinear contribution, $[2P_{13}(k)+P_{22}(k)]$. $c(k)$ is the pre-factor $c(k) = (1.5\cdot\Omega_0)^2(H_0/k)^4$. (The derivatives characterized by a dash are with respect to redshift, e.g. $g'(z) = dg/dz$, not to be confused with the conformal derivative). See appendices B.8 for further derivatives using MA99.
In the following we are going to discuss the evolution of $\partial P_\Phi/\partial z$ (eq. (4.200)) and $Q(l)$ (eq. (4.198)) for PT, MA99 and HALOFIT (see 4.6.1) and the DE models using $w_{\rm DE} = const.$, LIND03, KOMAT09 and WETT04 (see 4.6.2), respectively.

4.6.1 Bispectrum Evolution for PT, MA99 & HALOFIT

Behavior of $\partial P_\Phi(k,z)/\partial z$:

Fig. 4.15 and Fig. 4.16 show the evolution of $\partial P_\Phi(k,z)/\partial z$ (eq. (4.200)) with redshift, most sensitive to the onset of nonlinearity for the constant wave numbers $k = 0.04$ Mpc^{-1} and $k = 0.4$ Mpc^{-1}, and constant multipole-moments $l = 100$, $l = 500$, $l = 1000$ and $l = 10000$, respectively.
In Fig. 4.15 we present PT (black line), MA99 (blue line) and HALOFIT (red line). At $k = 0.04$ Mpc^{-1} (upper panel) every contributing fluctuation evolves linear. At high redshifts the universe is matter dominated, where the potential (Φ) of the density perturbations along with the corresponding power spectrum $(P_\Phi(k.z))$ remains constant and $\partial P_\Phi/\partial z = 0$. Approaching smaller redshifts DE

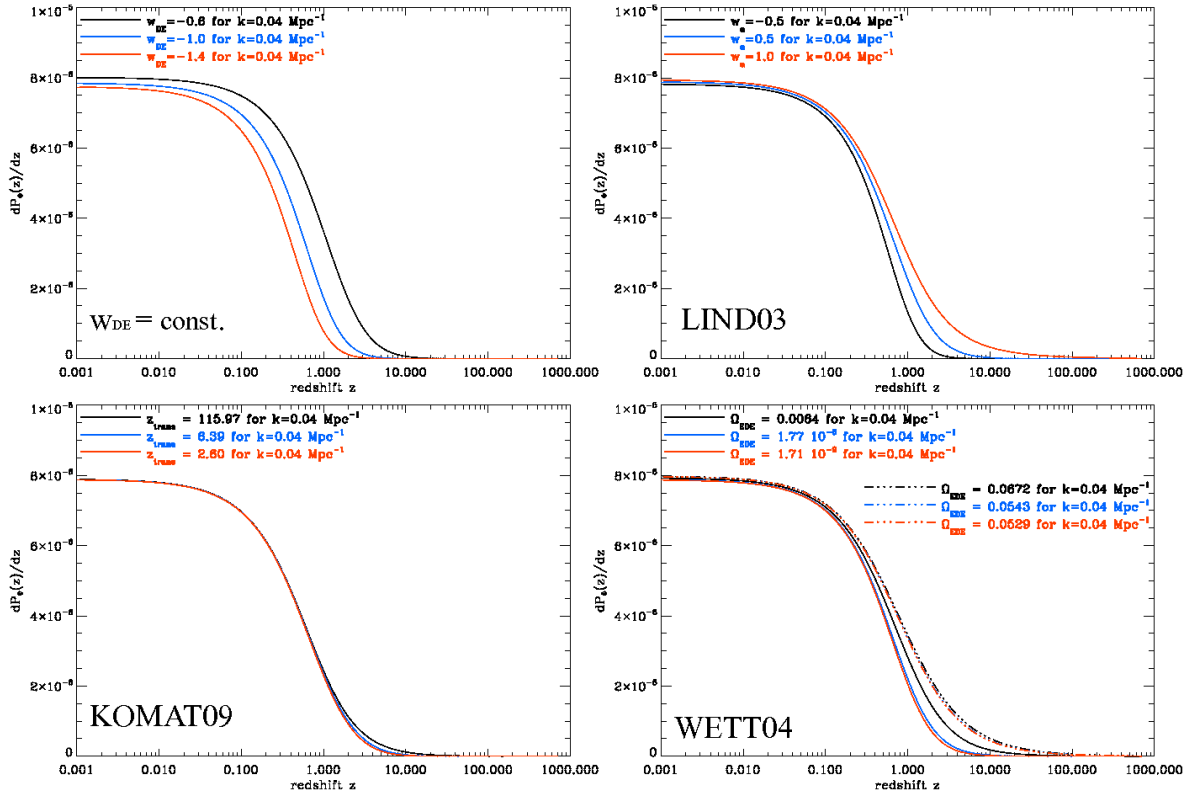

Figure 4.18: Evolution of $\partial P_\Phi/\partial z$ with redshift for $k = 0.04\,\mathrm{Mpc}^{-1}$. Upper left panel: Constant equation of states using $w_{\mathrm{DE}} = -0.6$ (black line), -1 (blue line) and -1.4 (red line). Upper right panel: LIND03 for $w_a = -0.5$ (black line), 0.5 (blue line) and 1 (red line). Bottom left panel: KOMAT09 with $z_{\mathrm{trans}} = 115.97$ (black line), 6.39 (blue line) and 2.69 (red line). Bottom right panel: WETT04 for Ω_{EDE} contributions at z_{lss} (solid lines) and z_{sf} (dashed triple dotted lines), see also table 4.2.

begins to dominate entailing an reduced growth of structures. Accordingly, Φ and $P_\Phi(k,z)$ decrease with decreasing z, while $\partial P_\Phi(k,z)/\partial z$ begins to rise. For PT the dominating term in eq. (4.201) corresponds to $\sim (g'(z)/g(z))\,P^{\mathrm{lin}}(k)$. It evolves similar to HALOFIT, while MA99 is slightly lower. For $k = 0.4\,\mathrm{Mpc}^{-1}$ (right panel) we enter the nonlinear regime, where the fluctuations have decoupled from the Hubble flow. This is indicated by the drop of $\partial P_\Phi(k,z)/\partial z$ around $z \sim 1$. Like before, the derivative of $P_\Phi(k,z)$ vanishes at high z. At small redshifts Φ and $P_\Phi(k,z)$ increase as the fluctuations begin to collapse. This results in an decrease of $\partial P_\Phi(k,z)/\partial z$ until it reaches equilibrium and saturates. The dominating term for PT corresponds now to $\sim D^2(z)\,[g'(z)/g(z) + D'(z)/D(z)]\,P^{\mathrm{nonlin}}(k)$. PT and HALOFIT are again both quite similar. However, MA99 drops dramatically at low z which seems to be unphysical compared to the other descriptions and indicates that all fluctuations are already in the nonlinear regime. This strange behavior of MA99 is also reflected in Fig. 4.16 (here we show only PT and MA99 as HALOFIT resembles PT). For $l = 100$ (upper left panel) the contributing wave numbers $(k = l/r(z))$ are small and the regime is linear, where $\partial P_\Phi(k,z)/\partial z > 0$ for both models. PT is slightly stronger than MA99. However, when increasing to $l = 500$ (upper right panel), MA99 has

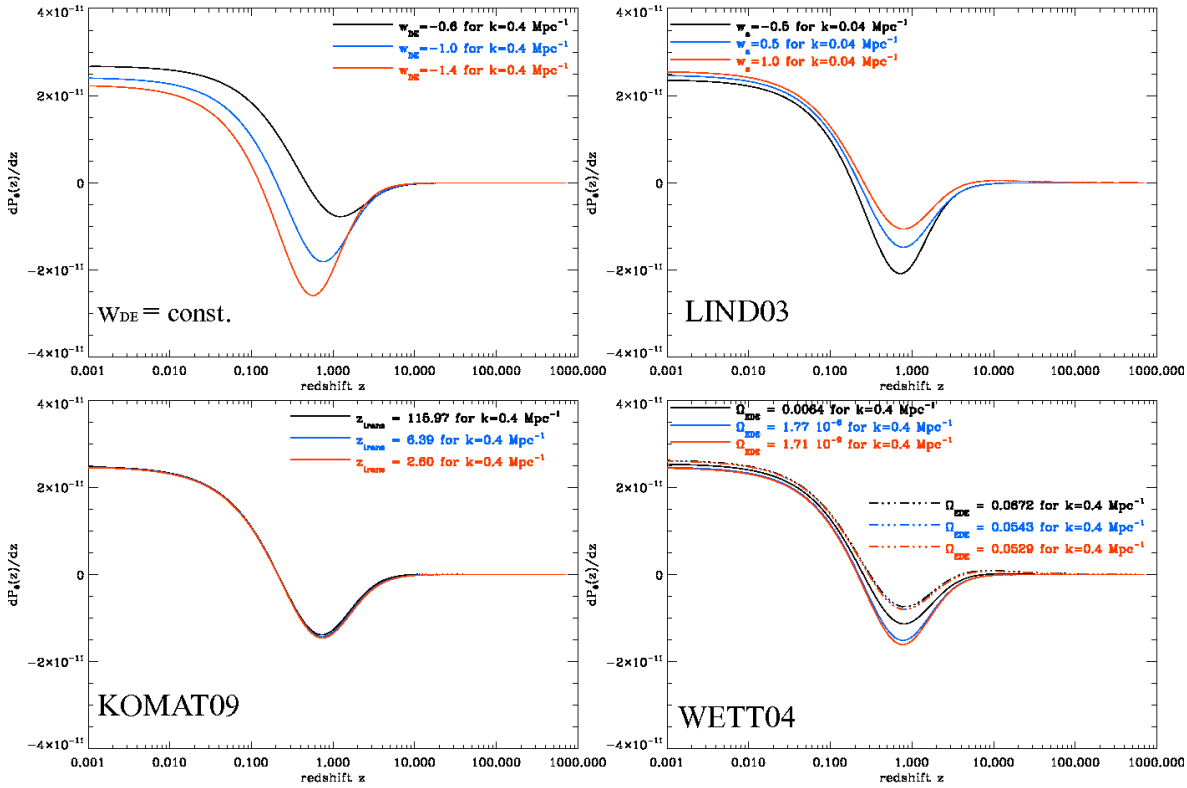

Figure 4.19: The same as in Fig. 4.18 but for the constant wave number $k = 0.4$ Mpc^{-1}.

already become nonlinear for which $\partial P_\Phi(k,z)/\partial z < 0$ in contrast to PT. As mentioned in 4.4.2, MA99 exhibits more nonlinear power at intermediate k and z. Therefore, for increasing l (i.e. k) the crossing from the linear to the nonlinear scales happens before PT (and HALOFIT). For $l = 1000$ (bottom left panel) and $l = 10000$ (bottom right panel) the corresponding k's are large and PT and MA99 are both in the nonlinear domain.

Behavior of $Q(l)$:

The largest contribution to the bispectrum amplitude (eq. (4.198)) comes from intermediate redshifts. As already discussed, at large z (where the universe is matter dominated) $\partial P_\Phi(k,z)/\partial z$ vanishes, while for smaller redshifts it decreases or increases depending on the scale (determined through $k = l/r(z)$). The integand of $Q(l)$ follows the behavior of $\partial P_\Phi(k,z)/\partial z$ and changes sign when crossing from the linear to the nonlinear scale. This is reflected in the bispectrum evolution shown by Fig. 4.17, for which we also include HALOFIT (red line). The sign change for MA99 appears between $l \sim [200-300]$ (which corresponds to smaller k's, i.e. larger scales), while for PT and HALOFIT the crossing happens around $l \sim [700-900]$ (smaller scales). Since PT has in the mean more nonlinear power with respect to HALOFIT (see Fig. 4.12), its sign change is slightly shifted towards smaller l.

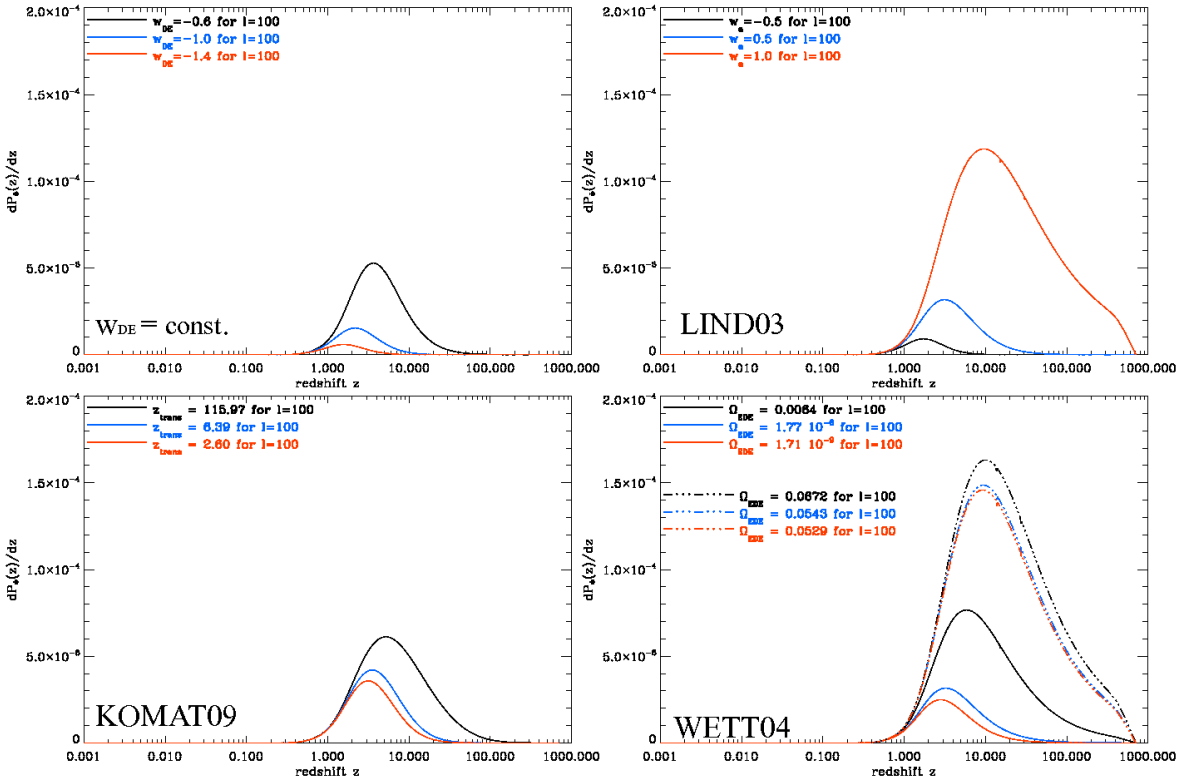

Figure 4.20: The same as Fig. 4.18 but for the constant multipole moment $l = 100$.

To conclude, it is important to note that different approaches of nonlinear power spectra result in different scales on which nonlinear effects become dominant, hence altering any comparison with observed bispectra. Jeong & Komatsu (2006) showed that PT provides a significantly better fit to numerical simulations than the conventional approaches of MA99 and HALOFIT. Thus from now on, we use PT (eq. (4.143)). Its direct dependence on the growth factor makes it easy to incorporate different DE models. Attempts to describe the linear- and the nonlinear evolution of the bispectrum analytically have been done by e.g. Boubekeur *et al.* (2009) and Pitrou *et al.* (2010).

4.6.2 Bispectrum Evolution using $w_{\rm DE} = const.$, LIND03, KOMAT09 & WETT04

Behavior of $\partial P_\Phi(k,z)/\partial z$:

The Figures 4.18, 4.19, 4.20, 4.21, and 4.22 show the evolution of $\partial P_\Phi(k,z)/\partial z$ with redshift for the constant wave numbers $k = 0.04$ Mpc^{-1} and $k = 0.4$ Mpc^{-1}, and constant multipole-moments $l = 100$, $l = 1000$ and $l = 10000$, respectively. We skip the example with $l = 500$, since most of the quintessence models do not reach the nonlinear stage before $l \sim 1000$ and the evolution of $\partial P_\Phi(k,z)/\partial z$ for $l < 1000$ is similar to $l = 100$. (See also appendix B.9 for $\partial P_\Phi(k,z)/\partial z$ with $k = 4$ Mpc^{-1}.) The upper left panels correspond to constant equation of states with $w_{\rm DE} = -0.6$ (black line), -1 (blue line) and -1.4 (red line). The upper right panels show LIND03 using $w_a = -0.5$ (black line),

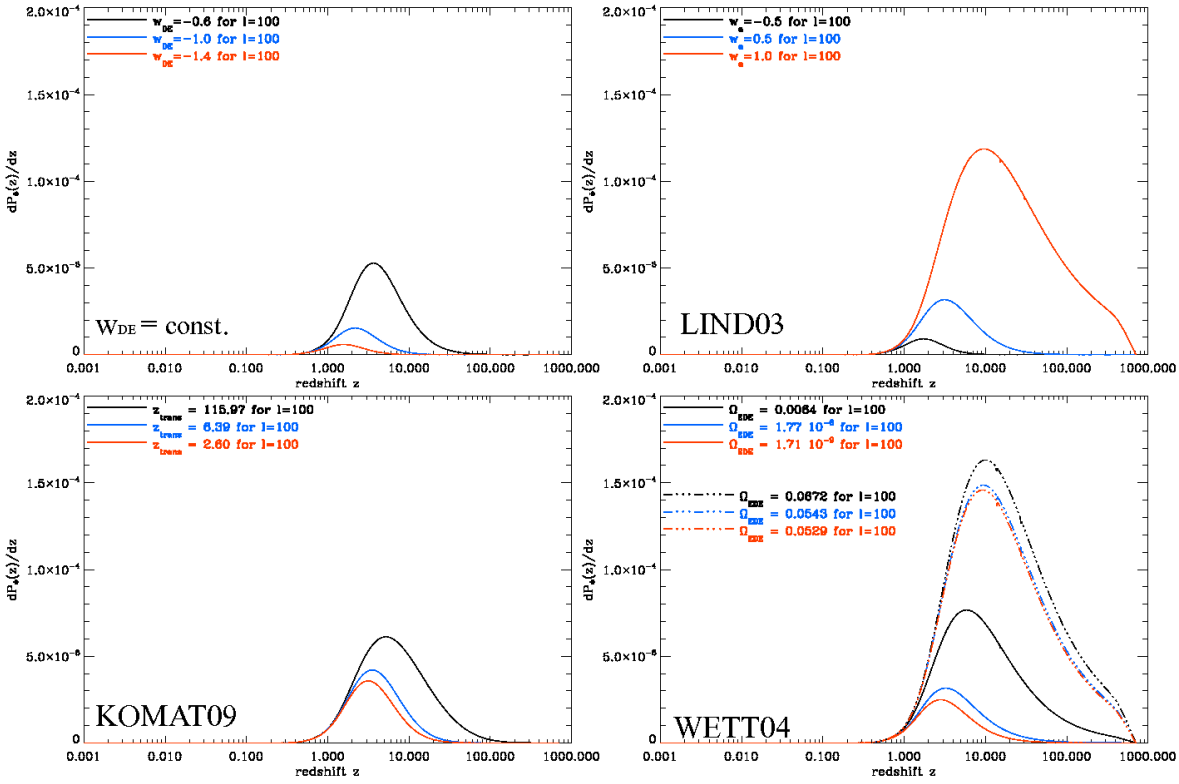

Figure 4.21: The same as in Fig 4.18 but for the constant multipole moment $l = 1000$.

0.5 (blue line) and 1 (red line), while the bottom left panels show KOMAT09 for $z_{\rm trans} = 115.97$ (black line), 6.39 (blue line) and 2.60 (red line). The bottom right panels display WETT04 for $\Omega_{\rm EDE}$ contributions at $z_{\rm lss}$ (solid lines) and $z_{\rm sf}$ (dashed triple dotted lines), see also table 4.2.

For $k = 0.04$ Mpc^{-1} the regime is linear and the dominating term in eq. (4.201) corresponds to $\sim (g'(z)/g(z))\,P^{\rm lin}(k)$, where $\partial P_\Phi(k,z)/\partial z > 0$ at low redshifts (see 4.6.1). In the case of constant $w_{\rm DE}$ (upper left panel of Fig. 4.18), $\partial P_\Phi(k,z)/\partial z$ increases with increasing $w_{\rm DE}$. The strongest evolution follows for $w_{\rm DE} = -0.6$, which has also the highest contribution of $\Omega_{\rm DE}$. The same holds for WETT04 (bottom right panel of Fig. 4.18), where $\partial P_\Phi(k,z)/\partial z$ exhibits the strongest evolution for contributions of $\Omega_{\rm EDE} = 0.0064$ at $z_{\rm lss}$ and $\Omega_{\rm EDE} = 0.0627$ at $z_{\rm sf}$. In the case of LIND03 (upper right panel of Fig. 4.18) and KOMAT09 (bottom left panel of Fig. 4.18) this is the case using $w_a = 1$ and $z_{\rm trans} = 115.97$, respectively.

At $k = 0.4$ Mpc^{-1}, presented in Fig. 4.19 we enter the nonlinear stage and contributions from $\sim D^2(z)\,[g'(z)/g(z) + D'(z)/D(z)]\,P^{\rm nonlin}(k)$ lead to the drop of $\partial P_\Phi(k,z)/\partial z$ around $z = 0.6$ (see 4.6.1). The behavior of $\partial P_\Phi(k,z)/\partial z$ remains the same, using $w_{\rm DE}$ (upper left panel), $\Omega_{\rm EDE}$ (upper right panel), w_a (bottom left panel) and $z_{\rm trans}$ (bottom right panel).

In general, $\partial P_\Phi(k,z)/\partial z$ increases with increasing $\Omega_{\rm DE}$. As discussed in section 4.3, the linear growth of structures (characterized through $D(z)$) is suppressed if $\Omega_{\rm DE}$ increases. Since $g(z) \sim D(z)$ (eq. (4.54)), the terms $(g'(z)/g(z))$ (at $k = 0.04$ Mpc^{-1}) and $(g'(z)/g(z) + D'(z)/D(z))$ (at $k = 0.4$ Mpc^{-1}) increase with $\Omega_{\rm DE}$. This results in the enhancement of $\partial P_\Phi(k,z)/\partial z$, as seen in Fig. 4.18 and

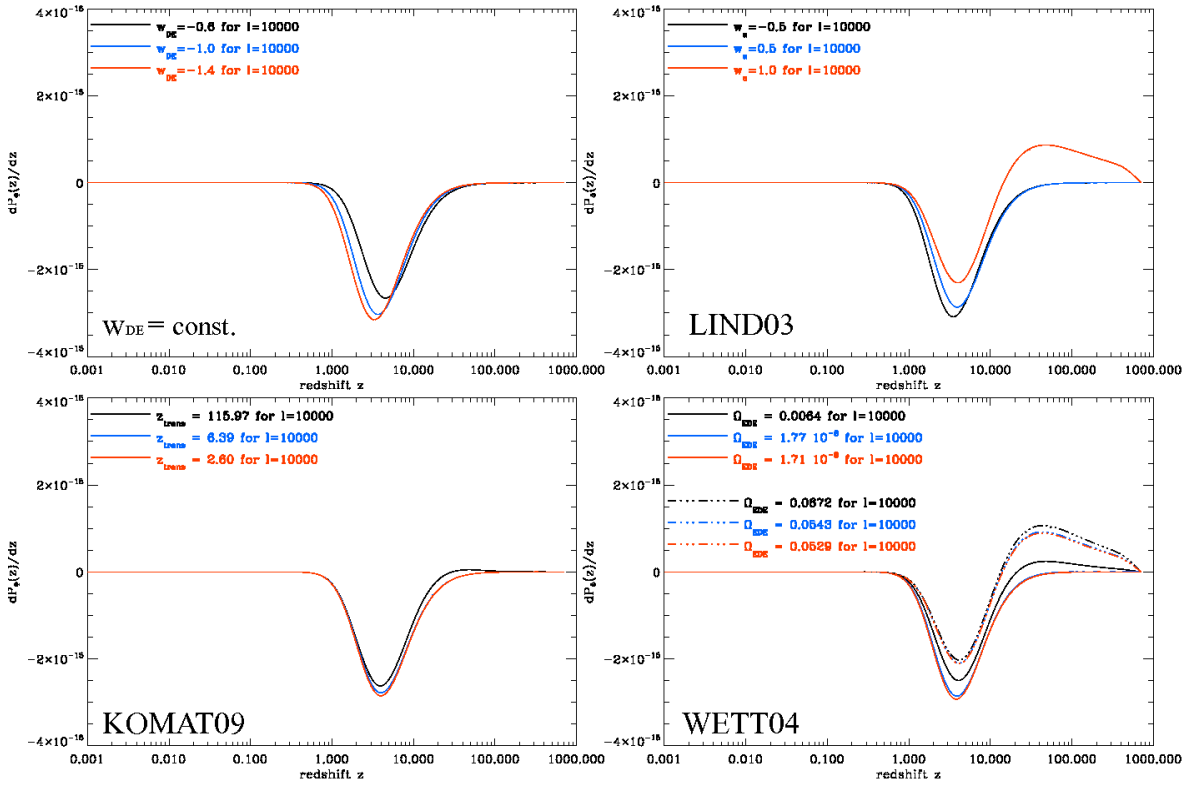

Figure 4.22: The same as in Fig 4.18 but for the constant multipole moment $l = 10000$.

Fig. 4.19.
For the multipole $l = 100$, shown in Fig. 4.20 the contributing k's are small and the regime is linear, where $\partial P_\Phi/\partial z > 0$. As before, the examples with the largest $\Omega_{\rm DE}$ exhibit the strongest $\partial P_\Phi/\partial z$. Increasing to $l = 1000$, presented in Fig. 4.21 implies $\partial P_\Phi/\partial z < 0$ for $w_{\rm DE} \leq -1$ (upper left panel), $\Omega_{\rm EDE} \leq 1.77 \cdot 10^{-6}$ (upper right panel), $w_a \leq 0.5$ (bottom left panel) and $z_{\rm trans} \leq 2.60$ (bottom right panel). These examples have crossed from the linear to the nonlinear evolution, indicated by the small drops around $z = 2$ (see also Fig. 4.23 for the At $l = 10000$, shown in Fig. 4.22 all examples are well within the nonlinear domain, for which $\partial P_\Phi/\partial z < 0$. The main contribution to the integral (eq. 4.198) follows from intermediate redshifts, $z \sim [1-20]$.

Behavior of $Q(l)$:

The strength of $\Omega_{\rm DE}$ is strongly correlated to the onset of nonlinearity. For increasing values the growth of structures is more damped and the crossing from the linear to the nonlinear stage becomes delayed. The scales where the fluctuations reach $\delta \sim 1$ are therefore much smaller, see Fig. 4.23 which shows the evolution of the corresponding bispectrum amplitude $|Q(l)|$ (eq. (4.198)). Increasing $w_{\rm DE}$ from -1.4 to -0.6 (upper left panel) shifts the onset of the nonlinear regime towards larger l (smaller scales). The same happens for LIND03 (upper right panel), and KOMAT09 (bottom left panel), respectively. Increasing $w_a = -0.5$ to 1, and $z_{\rm trans}$ from 2.60 to 115.97 dampens the growth

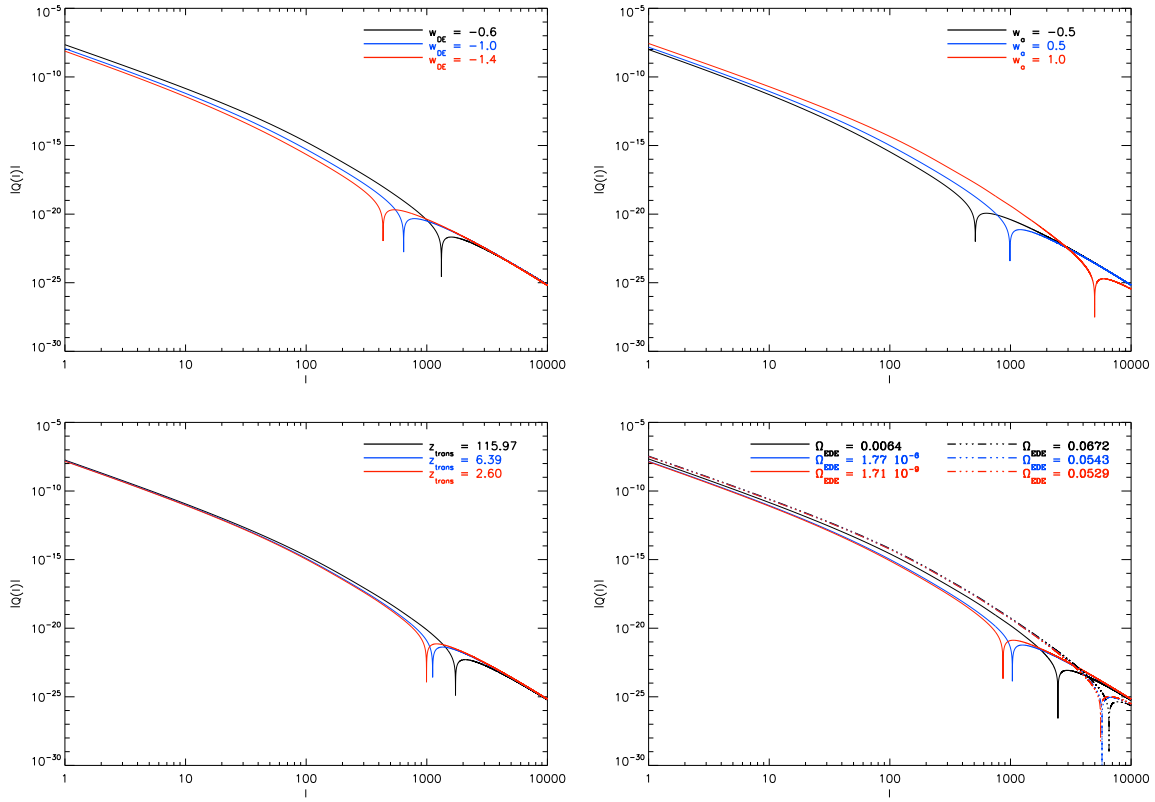

Figure 4.23: The same as Fig. 4.17. Upper left panel: Constant equation of states using $w_{\rm DE} = -0.6$ (blue line), -1 (black line) and -1.4 (red line). Upper right panel: LIND03 using $w_a = -0.5$ (black line), 0.5 (blue line) and 1 (red line). Bottom left panel: KOMAT09 using $z_{\rm trans} = 115.97$ (black line), 6.39 (blue line) and 2.60 (red line). Bottom right panel: WETT04 using $\Omega_{\rm EDE}$ contributions at $z_{\rm lss}$ (solid lines) and $z_{\rm sf}$ (dashed triple dotted lines). see also table 4.2.

of fluctuations (see also 4.3.2) delaying the nonlinear evolution. This is also the case for WETT04 (bottom right panel), where for increasing values of $\Omega_{\rm EDE}$ from $1.71 \cdot 10^{-9}$ to 0.00672 at $z_{\rm lss}$, and 0.0529 to 0.0672 at $z_{\rm sf}$, the sign-change is shifted towards larger l.

A direct comparison of $|Q(l)|$ using the standard cosmological constant with $w_{\rm DE} = -1$ (black line), WETT04 using $\Omega_{\rm EDE} = 0.0064$ (blue line), LIND03 with $w_a = 0.5$ (red line) and KOMAT09 for $z_{\rm trans} = 6.39$ (green line) is shown in Fig. 4.24 (upper panel). WETT04 has the strongest amount of DE, thus the sign change appears at larger l, i.e. $l \sim [2000 - 3000]$ in contrast to the other examples. The weakest contribution of DE is presented by the constant case, with the change being in the range $l \sim [600 - 700]$. In between are the LIND03- and the KOMAT09- example with sign changes at $l \sim [900 - 1000]$ and $l \sim [1000 - 2000]$, respectively. The corresponding bispectra are shown at the bottom panel of Fig. 4.24. (Note that in this plot we show only multipole-moments $l < 1500$, therefore the sign-change for the WETT04 examples does not appear.)

To summarize, the onset of the nonlinear regime is very sensitive to the model of DE (i.e. the amount of DE given by $\Omega_{\rm DE}$) and the corresponding parameters. If the resolution of further CMB observations

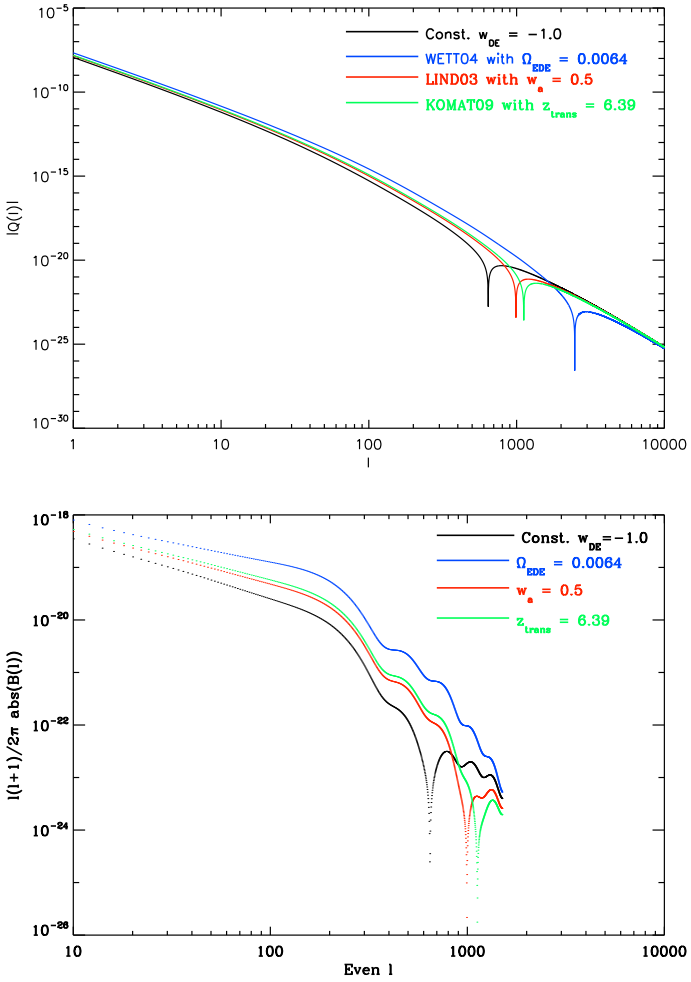

Figure 4.24: Upper panel: The same as Fig. 4.17 but for the constant equation of state with $w_{\rm DE} = -1$ (black solid line), WETT04 using $\Omega_{\rm EDE} = 0.0064$ (blue line), LIND03 with $w_a = 0.5$ (red line), and KOMAT09 using $z_{\rm trans} = 6.39$ (green line). Bottom panel: Evolution of the corresponding angle averaged bispectrum (eq. 4.177), where the multipole-moments are even ($l_1 = l_2 = l_3$)

are strong enough, as expected with PLANCK (see also next section) the theoretically calculated bispectra can be used for comparison with observed CMB bispectra to constrain parameter ranges for DE and to distinguish between different DE models.

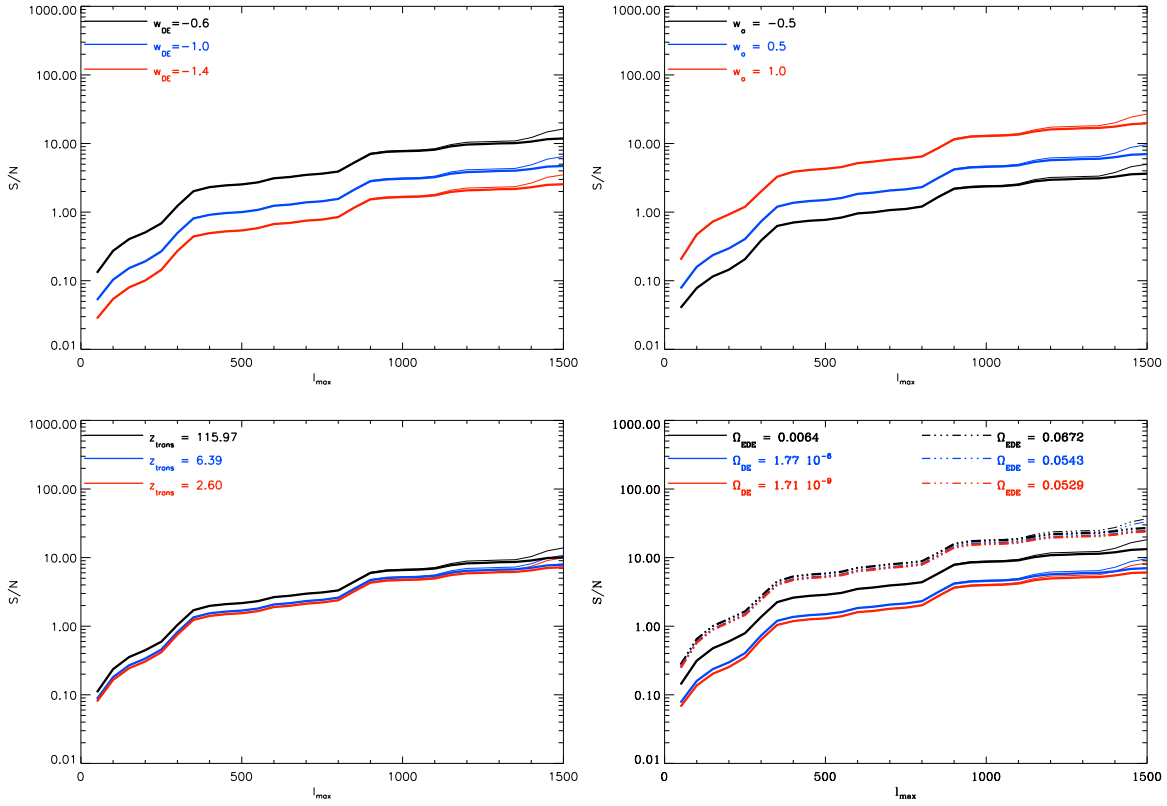

Figure 4.25: Evolution of S/N (eq. (4.202)) with $l_{\max}$ for a cosmic variance limited (thin lines) and PLANCK limited (thick lines) experiment. Upper left panel: Constant equation of states using $w_{\rm DE} = -0.6$ (blue line), -1 (black line) and -1.4 (red line). Upper right panel: WETT04 using $\Omega_{\rm EDE}$ contributions at $z_{\rm lss}$ (solid lines) and $z_{\rm sf}$ (dashed triple dotted lines). see also table 4.2. Bottom left panel: LIND03 using $w_a = -0.5$ (black line), 0.5 (blue line) and 1 (red line). Bottom right panel: KOMAT09 using $z_{\rm trans} = 115.97$ (black line), 6.39 (blue line) and 2.60 (red line).

4.7 Signal-to-Noise Ratio

The signal-to-noise ratio (S/N) can be identified as the ratio of the mean signal to its standard deviation due to noise. In general, it is defined through (Spergel & Goldberg, 1999)

$$\left(\frac{S}{N}\right)^2 = \sum_{2\leq l_1\leq l_2\leq l_3<l_{\max}} \frac{\langle B_{l_1 l_2 l_3}\rangle^2}{\sigma^2_{l_1 l_2 l_3}}, \tag{4.202}$$

where σ^2 expresses the cosmic variance of $B_{l_1 l_2 l_3}$ (Luo, 1994; Spergel & Goldberg, 1999; Gangui & Martin, 2000),

$$\begin{aligned}\sigma^2 = \left\langle a_{l_1 m_1} a_{l_2 m_2} a_{l_3 m_3} a^*_{l_1 m_1} a^*_{l_2 m_2} a^*_{l_3 m_3}\right\rangle &= \left\langle B^2_{l_1 l_2 l_3}\right\rangle - \langle B_{l_1 l_2 l_3}\rangle^2 \\ &\approx N\cdot C_{l_1} C_{l_2} C_{l3}, \end{aligned} \tag{4.203}$$

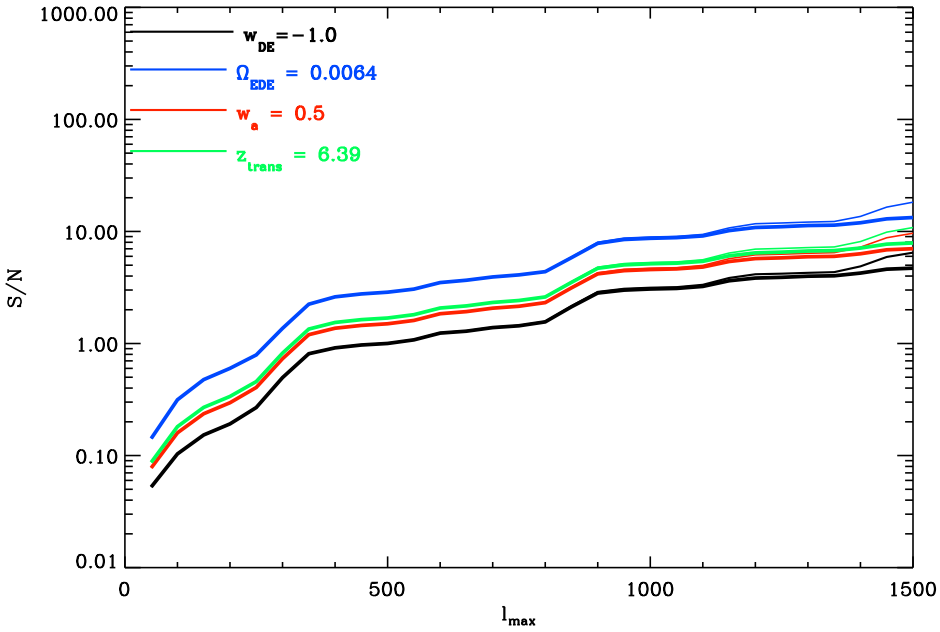

Figure 4.26: The same as Fig. 4.25 but for the constant equation of state with $w_{\rm DE} = -1$ (black solid line), WETT04 using $\Omega_{\rm EDE} = 0.0064$ (blue line), LIND03 with $w_a = 0.5$ (red line), and KOMAT09 using $z_{\rm trans} = 6.39$ (green line).

with $N = 1$ if all l's are different, $N = 2$ if two l's are equal (isosceles configuration) and $N = 6$ if all l's are equal (equilateral configuration). The C_l's denote the power spectrum of temperature fluctuations eq. (4.196), for which the noise contribution is included according to Knox (1995).
Fig. 4.25 shows the evolution of (S/N) with $l_{\rm max}$ (thin lines for a cosmic variance limited-, thick lines for a PLANCK limited experiment, see also appendix B.10 for the WMAP limited case), where $l_1 \leq l_2 \leq l_3 < l_{\rm max}$. (For the comparison using PT and MA99 see also appendix B.10.) We restrict our analysis to multipoles with $l_{\rm max} < 1500$, since for larger values other secondary effects like the OV-effect (Ostriker & Vishniac, 1986) and SZ-effect (Zeldovich & Sunyaev, 1969) become non-negligible. The upper left panel corresponds to constant equation of states, the upper right panel to LIND03, the bottom left panel to KOMAT09 and the bottom right panel to WETT04, respectively. In all cases, the (S/N) increases when $l_{\rm max}$ reaches above a few hundred similar to the findings of Mangilli & Verde (2009) (but which restrict their analysis only to $w_{\rm DE} = -1$). The PLANCK limited case is almost identical to the comsic variance limited one. It begins to differ slightly for $l_{\rm max} > 1400$. Following Fig. 4.25, we see a clear dependence on the strength of $\Omega_{\rm DE}$ as discussed already in section 4.6. For constant $w_{\rm DE}$ the strongest signal corresponds to the example with the largest contribution of $\Omega_{\rm DE}$, i.e. $w_{\rm DE} = -0.6$. The same is for WETT04 using $\Omega_{\rm EDE} = 0.0064$ at $z_{\rm lss}$ and $\Omega_{\rm EDE} = 0.0672$ at $z_{\rm sf}$. The signal is stronger for contributions of EDE at $z_{\rm sf}$, the era of structure formation. For LIND03 the largest (S/N) follows for $w_a = 1$, while for KOMAT09 this is the case for $z_{\rm trans} = 115.97$.
Fig. 4.26 compares all DE-models using the same parameters as in Fig. 4.24. The strongest (S/N) follows for the EDE model with $\Omega_{\rm EDE} = 0.0064$, the lowest is displayed by the standard DE-model

with $w_{\rm DE} = -1$. Both, LIND03 and KOMAT09 lie in between. They evolve similar, which reflects the fact that they are based on a similar parameterization. The strong (S/N) for the EDE model suggests that it should be possible to be distinguished from the standard case. We therefore expect, that PLANCK will be able to answer the question if we live in a universe with EDE, or with the standard cosmological constant.

4.8 Conclusions

We analyzed the L-RS bispectrum (Verde & Spergel, 2002) for different parameterizations of DE with focus on early dark energy. The models incorporate constant equation of states, WETT04 (Wetterich, 2004), LIND03 (Linder, 2003a,b) and KOMAT09 (Komatsu *et al.*, 2009), respectively. To test the dependency of the results on the model of the nonlinear power spectrum, we apply in addition to PT (Bernardeau *et al.*, 2002) the often used descriptions by MA99 (Ma *et al.*, 1999), and HALOFIT (Smith *et al.*, 2003).

We find that the sign-change of the L-RS bispectrum amplitude, which determines the crossing from the linear- to the nonlinear regime depends strongly on the description of the nonlinear power spectrum. Using the standard case with $w_{\rm DE} = -1$, the sign-change appears for MA99 already at multipole-moments in the range $l \sim [200 - 300]$, while for PT and HALOFIT it lies between $l \sim [1000 - 2000]$. Smaller l correspond to larger scales. MA99 enters the nonlinear stage when the fluctuations evolve on larger scales, which is due to the fact that it exhibits a stronger nonlinear power in contrast to PT and HALOFIT (which are quite similar). Yet, PT has slightly more nonlinear power than HALOFIT, resulting in the sign-change shortly before HALOFIT. As already discussed in Mangilli & Verde (2009) an accurate description of the nonlinear evolution is fundamental to obtain unbiased estimates on cosmological parameters. MA99 differs strongly from PT and HALOFIT. Since PT is based on analytical calculations and agrees with numerical simulated spectra (e.g. Jeong & Komatsu, 2006), we use it for our further analysis.

Applying different DE-models, the crossing from the linear to the nonlinear stage shows a strong dependency on $\Omega_{\rm DE}$. A large $\Omega_{\rm DE}$ implies a stronger acceleration of the expansion, thus, the linear growth of structures is damped and the nonlinear evolution delayed. The sign-change shifts therefore with increasing $\Omega_{\rm DE}$ to larger l (smaller scales). For const. $w_{\rm DE}$ the sign-changes lie between $l \sim [300 - 2000]$, where the first one corresponds to $w_{\rm DE} = -0.6$ (which has the largest $\Omega_{\rm DE}$), followed by $w_{\rm DE} = -1.0$ and $w_{\rm DE} = -1.4$, respectively. The same is for WETT04, which has the sign-changes for decreasing $\Omega_{\rm EDE}$ contributions at $z_{\rm lss}$ between $l \sim [700 - 300]$, and for $z_{\rm sf}$ between $l \sim [5000 - 7000]$. The first one corresponds for $z_{\rm lss}$ to the example using $\Omega_{\rm EDE} = 0.0064$ followed by $\Omega_{\rm EDE} = 1.77 \cdot 10^{-6}$ and $\Omega_{\rm EDE} = 1.71 \cdot 10^{-9}$. For $z_{\rm sf}$ they proceed as $\Omega_{\rm EDE} = 0.0672$, $\Omega_{\rm EDE} = 0.0543$ and $\Omega_{\rm EDE} = 0.0529$. The $\Omega_{\rm EDE}$ contributions is stronger for the $z_{\rm sf}$ examples, thus their sign-changes lie at larger l. In the case of LIND03, the first sign-change appears for the example using $w_{\rm a} = -0.5$, followed by $w_{\rm a} = 0.5$ and $w_{\rm a} = 1.0$, respectively. For KOMAT09 this is the case using $z_{\rm trans} = 115.97$, $z_{\rm trans} = 6.39$ and $z_{\rm trans} = 2.60$. Comparing the DE-models, we see that the strongest contribution of $\Omega_{\rm DE}$ arises for early quintessence, the lowest from the standard case with $w_{\rm DE} = -1$. This behavior is also reflected in the evolution of the S/N ratio with l, which corresponds to a resolution achieved with PLANCK. The strongest signal comes from the examples with the largest $\Omega_{\rm EDE}$, and complies with the early quintessence. The comparison shows, that the lowest example follows from the standard case. Thus, PLANCK should be able to distinguish between the DE-models and allows to answer the

question if we live in a universe with a constant $w_{\rm DE}$ or if we are ruled by $w_{\rm DE}(z)$.

Chapter 5

Summary and Outlook

The first part of this thesis was focused on modelling shear flows, in particular the KHI with analytical- and numerical methods. The second part enters the very interesting topic of dark energy and its trace within the CMB. This chapter shortly summarizes the main results and gives an outlook for future perspectives.

5.1 Part I : Modelling Shear Flows with SPH and Grid Based Methods

The numerical study of the KHI uses the SPH models VINE (Wetzstein *et al.*, 2009; Nelson *et al.*, 2009), and the code developed by Price (2008) P08, while the grid based methods rely on FLASH (Fryxell *et al.*, 2000), PROTEUS (e.g. Heitsch *et al.*, 2006), PLUTO (Mignone *et al.*, 2007) and RAMSES (Teyssier, 2002), respectively. The analytic study of the KHI is based on the original work of Chandrasekhar (1961), with the extension of a constant viscosity. We summarize our findings below:

i) SPH-RESULTS, EQUAL DENSITY SHEARING LAYERS:
The viscosity in VINE has been measured via the analytical description of the KHI growth. The effect of AV has been identified, where the usual settings of AV-parameters to $\alpha = 1$, and $\beta = 2$ lead to a strong suppression of the KHI. A corresponding viscosity in the range of $\nu_{\rm SPH} \sim [0.06 - 0.1]$ for $\alpha \sim [0 - 1]$ can be assigned. For the same α regime Reynolds (*Re*) values only up to 12 are reached. The Balsara viscosity reduces artificial dissipation due to AV.

ii) SPH-RESULTS, DIFFERENT DENSITY SHEARING LAYERS:
The results discussed in Agertz *et al.* (2007), where the KHI is completely suppressed for shear flows with different densities (in the case of VINE for $DC \geq 6$) has been confirmed. As an additional test, different mass particles were used for $DC = 10$, yet the KHI remains suppressed. The solution in form of ATC proposed by Price (2008) allows SPH-particles to mix and therefore, the instability to develop. We tested this method using $DC = 10$, and indeed, the KHI evolves and the amplitude growth agrees with the analytical prediction.

iii) GRID CODE-RESULTS, EQUAL DENSITY SHEARING LAYERS:
The non-viscous growth using FLASH, PLUTO and RAMSES is in good agreement with the analytical prediction as well as the viscous evolution with FLASH. However, PROTEUS

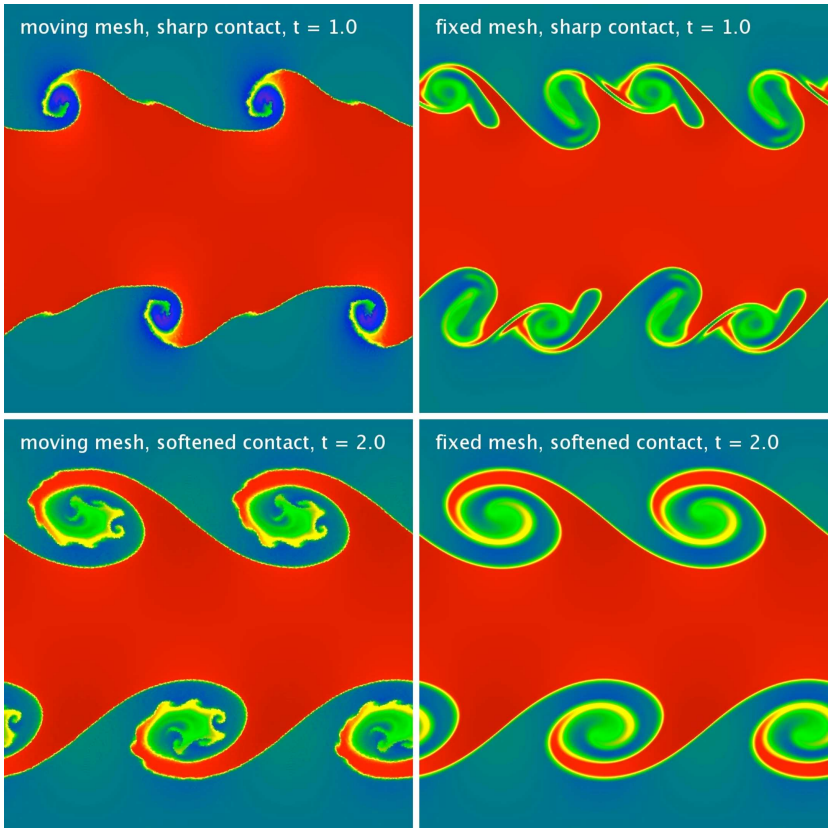

Figure 5.1: Snapshots of the KHI at $t = 1$ (upper panel) and $t = 2$ (bottom panel) using the moving mesh code by Springel (2010) for $DC = 2$ compared to a fixed mesh code.

disagrees and underpredicts the KHI growth dramatically. The comparison with VINE using AV $= 0$ demonstrated that VINE has an intrinsic viscosity ($\nu_{\rm int} = 0.065$).

iv) GRID CODE-RESULTS, DIFFERENT DENSITY SHEARING LAYERS:
Again, FLASH, PLUTO and RAMSES show an consistent non-viscous evolution for $DC = 10$ when compared to the analytical prediction. In the viscous case studied with FLASH we find a slight overprediction. The ramp-function as proposed by Robertson *et al.* (2009) to suppress artificial small scale perturbations does not alter the KHI-growth.

5.1.1 Outlook

Further developments by various groups have been achieved. Recently, Valcke *et al.* (2010) discuss in detail the solutions for the KHI suppression proposed by Read *et al.* (2010). Furthermore, the new developed hybrid code by Springel (2010), that combines the strengths of SPH and GRID codes in form of a moving mesh shows promising results (see Fig. 5.1, courtesy of Volker Springel).
The next important step is to test those solutions on an actual astrophysical system, e.g. the movement of an infalling cold cloud into a hot gaseous halo, most subject to the KHI. Another very important

issue occurs at galactic disk formation and is known as the angular momentum problem (Navarro & Steinmetz, 2000). Simulated disks using N-body hydrodynamical codes (SPH) appear to be too small compared to observations. It seems that the angular momentum of the gas is not conserved and instead transformed to the dark matter particles during gravitational collapse. Yet, another reason for this problem could be related to the incorrect development of hydrodynamical instabilities, such as the KHI. The KHI is artificially suppressed in SPH for shear flows of different densities, if not any further meachnisms like the ATC are invoked. This can be crucial during galaxy evolution, where the gas from infalling satellites is stripped via ram pressure and hydro-instabilities and begins to settle in the disk. If the KHI is suppressed - which is the case in standard SPH formalisms - the clouds are not dispersed and the gas remains within its corresponding subhalo and violates the galactic disk formation. This scenario provides therefore an interesting test example for improved SPH-algorithms.

5.2 Part II : The Trace of Dark Energy captured within the CMB

We analyzed the L-RS bispectrum amplitude and the corresponding S/N ratio for different descriptions of the nonlinear power spectrum, in particular PT (Bernardeau *et al.*, 2002), MA99 (Ma *et al.*, 1999) and HALOFIT (Smith *et al.*, 2003), and for different DE-models with the focus on early quintessence. The Quintessence models correspond to WETT04 (Wetterich, 2004), LIND03 (Linder, 2003a,b) and KOMAT09 (Komatsu *et al.*, 2009), respectively. In addition, we also study DE-models with constant equation of states $(w_{\rm DE} = const.)$. We summarize our findings below:

i) **L-RS bispectrum using PT, MA99 & HALOFIT:**
MA99 exhibits more nonlinear power at larger scales and higher redshifts compared to PT and HALOFIT. It thus enters the nonlinear stage first, as indicated by the sign-change of the L-RS bispectrum amplitude appearing between $l \sim [200-300]$. In contrast to this, PT and HALOFIT have the crossing in the range $l \sim [1000-2000]$. PT and HALOFIT show a similar behavior, yet PT has a slightly enhanced nonlinear power.

ii) **L-RS bispectrum using Quintessence:**
We find a strong dependency on the crossing from the linear to the nonlinear stage with increasing $\Omega_{\rm DE}$. For larger values of $\Omega_{\rm DE}$ the linear growth becomes damped and the nonlinear evolution delayed. The sign-change shifts towards smaller scales. The strongest contributions correspond to early quintessence examples.

iii) **Signal-to-Noise Ratio:**
Again, we find the same behavior as with the L-RS bispectrum amplitude. The S/N evolution increases with increasing $\Omega_{\rm DE}$, with the strongest signal coming from early quintessence. We use cosmic variance limited and PLANCK limited settings and conclude, that with PLANCK it should be possible to distinguish between different DE-models.

5.2.1 Outlook: Polarization-Bispectrum of the CMB

Another very promising source within the CMB is provided by polarization. It contains important information about the statistical properties of the initial conditions and non-Gaussian contributions (e.g. Zaldarriaga, 1997; Hu, 2000; Babich & Zaldarriaga, 2004; Cooray *et al.*, 2004).

The polarization on the sky is described with the so called trace-free symmetric Stokes matrix, see e.g. Hu (2000),

$$\mathbf{P}(\mathbf{l}) =_{+} X(\mathbf{l})\,(\mathbf{m}_{+}\otimes\mathbf{m}_{+}) +_{-} X(\mathbf{l})\,(\mathbf{m}_{-}\otimes\mathbf{m}_{-})\,, \tag{5.1}$$

with

$${}_{\pm}X(\mathbf{l}) = Q(\mathbf{l}) \pm iU(\mathbf{l}), \tag{5.2}$$

being the complex Stokes parameter. Furthermore, ${}_{\pm}X$ is a spin-2 object and can be expanded using the spin-speherical harmonics (Newman & Penrose, 1966; Goldberg *et al.*, 1967),

$${}_{\pm}X(\mathbf{l}) = \sum_{lm} {}_{\pm}X_{lm}Y_{lm}(\mathbf{l}). \tag{5.3}$$

For further definitions see also appendix B.11. The polarization field is divided into the gradient part (E) and curl part (B) due to the parity eigenstates,

$${}_{\pm}X(\mathbf{l}) = E_{lm} \pm iB_{lm}. \tag{5.4}$$

E_{lm} obeys to the $(-1)^l$ parity (electric parity), while B_{lm} corresponds to the $(-1)^{l+1}$ parity (magnetic parity). The density fluctuations in the linear analysis only stimulate the E component of polarization. Therefore, it is coupled to the potential and a cross-correlation between E-polarization, lensing-, and RS-effect results in a non-Gaussian signal. The corrsponding cross-correlation bispectrum can be used, like in the case of the L-RS bispectrum to constrain DE. This will be the focus of our future work. Below we show the calculation to obtain the bispectra, which are required to obtain the S/N-ratios.
For the derivation of the polarization bispectrum we use a similar approach as discussed in section 4.6. The polarization multipoles are given by,

$$\begin{aligned} {}_{\pm}X(\mathbf{l}) &= {}_{\pm}X(\mathbf{l}+\nabla\Theta) && (5.5)\\ &\approx {}_{\pm}X(\mathbf{l}) + \nabla\Theta\nabla\,({}_{\pm}X(\mathbf{l}))\,. && (5.6)\end{aligned}$$

Expanding the ${}_{\pm}X(\mathbf{l})$ using the spin weighted spherical harmonics eq. (B.31), we obtain

$${}_{\pm}X_{lm}(\mathbf{l}) =_{\pm} X_{lm} + \int d^2\mathbf{l}\,({}_{\pm2}Y^{*}_{lm})\,\nabla\Theta(\mathbf{l})\nabla\,({}_{\pm}X(\mathbf{l})). \tag{5.7}$$

With the help of eq. (4.189) and eq. (5.3) it follows,

$${}_{\pm}X_{lm}(\mathbf{l}) =_{\pm} X_{lm} + \sum_{l'm'}\sum_{l''m''}\Theta_{l'm'}\,({}_{\pm}X_{l''m''})\int d^2\mathbf{l}\,({}_{\pm2}Y^{*}_{lm})\,\nabla Y_{l'm'}\nabla\,({}_{\pm2}Y_{l''m''}), \tag{5.8}$$

and applying (Hu, 2000)

$$\nabla^2_{\pm}Y_{lm} = [-l(l+1)+4]_{\pm2}Y_{lm} \tag{5.9}$$

we get the expression for the integral,

$$\begin{aligned}\int d^2\mathbf{l}\,({}_{\pm2}Y^{*}_{lm})\,\nabla Y_{l'm'}\nabla\,({}_{\pm2}Y_{l''m''}) &= \frac{1}{2}\left[l'(l'+1)+l''(l''+1)-l(l+1)\right]\\ &\quad\int d^2\mathbf{l}\,({}_{\pm2}Y^{*}_{lm})\,Y_{l'm'}\,({}_{\pm2}Y_{l''m''}). \end{aligned}\tag{5.10}$$

Using

$$\int d^2\mathbf{l}\left({}_{s_1}Y^*_{l_1m_1}\right)\left({}_{s_2}Y_{l_2m_2}\right)\left({}_{s_3}Y_{l_3m_3}\right) = (-1)^{m_1+s_1}\sqrt{\frac{(2l_1+1)(2l_2+1)(2l_3+1)}{4\pi}}\cdot \begin{pmatrix} l_1 & l_2 & l_3 \\ s_1 & -s_2 & -s_3 \end{pmatrix}\begin{pmatrix} l_1 & l_2 & l_3 \\ -m_1 & m_2 & m_3 \end{pmatrix}, \tag{5.11}$$

we finally get,

$$\begin{aligned} {}_{\pm}X_{lm}(\mathbf{l}) &= {}_{\pm}X_{lm} + \frac{1}{2}\sum_{l'm'}\sum_{l''m''}(-1)^{-(m+m'+m'')\pm 2}\left[l'(l'+1)+l''(l''+1)-l(l+1)\right]\cdot \\ &\quad \sqrt{\frac{(2l+1)(2l'+1)(2l''+1)}{4\pi}}\begin{pmatrix} l & l' & l'' \\ \pm 2 & 0 & \mp 2 \end{pmatrix}\begin{pmatrix} l & l' & l'' \\ -m & m' & m'' \end{pmatrix}\cdot \\ &\quad \left({}_{\pm}X^*_{l'-m'}\right)\Theta^*_{l''-m''}. \end{aligned} \tag{5.12}$$

Cross-correlating the ${}_{\pm}X_{lm}$ with the a_{lm}, eq. (4.193) produces the cross-correlation-polarization bispectra. We concentrate on the E-polarization (${}_{\pm}X_{lm} = E_{lm}$), since only these are stimulated by the linear density perturbations.

- ETT-Bispectrum: $B^{m_1m_2m_3}_{l_1l_2l_3} = \langle E_{l_1m_1}a_{l_2m_2}a_{l_3m_3}\rangle$

$$\begin{aligned} B^{m_1m_2m_3}_{l_1l_2l_3} &= \frac{1}{2}\sum_{l_1m_1}\sum_{l_2m_2}\left[l_1(l_1+1)-l_2(l_2+1)+l_3(l_3+1)\right]\zeta^{m_1m_2m_3}_{l_1l_2l_3}\cdot \\ &\quad C^{TE}_{l_1}\left\langle\Theta^*_{l_3m_3}a^{\mathrm{NL}}_{l_3m_3}\right\rangle + (l_2 \longleftrightarrow l_3) + \frac{1}{2}\sum_{l_2m_2}\sum_{l_3m_3}\sqrt{\frac{(2l_1+1)(2l_2+1)(2l_3+1)}{4\pi}}\cdot \\ &\quad \left[l_2(l_2+1)-l_1(l_1+1)+l_3(l_3+1)\right]\begin{pmatrix} l_1 & l_2 & l_3 \\ \pm 2 & 0 & \pm 2 \end{pmatrix}\begin{pmatrix} l_1 & l_2 & l_3 \\ m_1 & m_2 & m_3 \end{pmatrix}\cdot \\ &\quad C^{TE}_{l_2}\left\langle\Theta^*_{l_3m_3}a^{\mathrm{NL}}_{l_3m_3}\right\rangle + (l_2 \longleftrightarrow l_3). \end{aligned} \tag{5.13}$$

  For the corresponding upper bound on (S/N) follows, see also Hu (2000)

$$\left(\frac{S}{N}\right)^2 \geqslant \sum_{l_1l_2l_3}\frac{\left(B^{m_1m_2m_3}_{l_1l_2l_3}\right)^2}{6C^{EE}_{l_1}C^{TT}_{l_2}C^{TT}_{l_3}}. \tag{5.14}$$

  The C^{TT}_l, C^{TE}_l and C^{EE}_l denote the power spectra shown in Fig. 4.14.

- EET-Bispectrum: $B^{m_1m_2m_3}_{l_1l_2l_3} = \langle E_{l_1m_1}E_{l_2m_2}a_{l_3m_3}\rangle$

$$\begin{aligned} B^{m_1m_2m_3}_{l_1l_2l_3} &= \frac{1}{2}\left[l_1(l_1+1)-l_2(l_2+1)+l_3(l_3+1)\right]\cdot\sqrt{\frac{(2l_1+1)(2l_2+1)(2l_3+1)}{4\pi}}\cdot \\ &\quad \begin{pmatrix} l_2 & l_1 & l_3 \\ \pm 2 & 0 & \pm 2 \end{pmatrix}\begin{pmatrix} l_1 & l_2 & l_3 \\ m_1 & m_2 & m_3 \end{pmatrix}C^{EE}_{l_1}\left\langle\Theta^*_{l_3m_3}a^{\mathrm{NL}}_{l_3m_3}\right\rangle + (l_2 \longleftrightarrow l_1). \end{aligned} \tag{5.15}$$

  And the upper bound on signal-to noise is (Hu, 2000),

$$\left(\frac{S}{N}\right)^2 \geqslant \sum_{l_1l_2l_3}\frac{\left(B^{m_1m_2m_3}_{l_1l_2l_3}\right)^2}{6C^{EE}_{l_1}C^{EE}_{l_2}C^{TT}_{l_3}} \tag{5.16}$$

- EEE-Bispectrum: The EEE spectrum vanishes, since there are not enough correlation-terms.

Our next aim will be to calculate the corresponding S/N ratios in order to determine how well different DE-models can be distinguished using the information encompassed within polarization.

Bibliography

Abazajian, K., Adelman-McCarthy, J. K., Agüeros, M. A., Allam, S. S., Anderson, S. F., Annis, J., Bahcall, N. A., Baldry, I. K., Bastian, S., Berlind, A., Bernardi, M., et al. 2003: *The First Data Release of the Sloan Digital Sky Survey*, AJ, 126, 2081

Abel, T. 2010: *rpSPH: a much improved Smoothed Particle Hydrodynamics Algorithm*, ArXiv e-prints

Agertz, O., Moore, B., Stadel, J., Potter, D., Miniati, F., Read, J., Mayer, L., Gawryszczak, A., Kravtsov, A., Nordlund, Å., Pearce, F., et al. 2007: *Fundamental differences between SPH and grid methods*, MNRAS, 380, 963

Agertz, O., Teyssier, R., & Moore, B. 2009: *Disc formation and the origin of clumpy galaxies at high redshift*, MNRAS, 397, L64

Babich, D. & Zaldarriaga, M. 2004: *Primordial bispectrum information from CMB polarization*, Phys. Rev. D, 70, 083005

Balbi, A., Ade, P., Bock, J., Borrill, J., Boscaleri, A., De Bernardis, P., Ferreira, P. G., Hanany, S., Hristov, V., Jaffe, A. H., Lee, A. T., et al. 2000: *Constraints on Cosmological Parameters from MAXIMA-1*, ApJ, 545, L1

Balbi, A., Ade, P., Bock, J., Borrill, J., Boscaleri, A., De Bernardis, P., Ferreira, P. G., Hanany, S., Hristov, V., Jaffe, A. H., Lee, A. T., et al. 2001: *Erratum: Constraints on Cosmological Parameters from MAXIMA-1*, ApJ, 558, L145

Balsara, D. S. 1995: *von Neumann stability analysis of smooth particle hydrodynamics–suggestions for optimal algorithms*, J. Comp. Phys., 121, 357

Banerjee, R., Klessen, R. S., & Fendt, C. 2007: *Can Protostellar Jets Drive Supersonic Turbulence in Molecular Clouds?*, ApJ, 668, 1028

Bardeen, J. M., Bond, J. R., Kaiser, N., & Szalay, A. S. 1986: *The statistics of peaks of Gaussian random fields*, ApJ, 304, 15

Barreiro, T., Bento, M. C., Santos, N. M., & Sen, A. A. 2003: *WMAP constraints on quintessence*, Phys. Rev. D, 68, 043515

Bartelmann, M., Doran, M., & Wetterich, C. 2006: *Non-linear structure formation in cosmologies with early dark energy*, A&A, 454, 27

Bartelmann, M. & Schneider, P. 2001: *Weak gravitational lensing*, Phys. Rep., 340, 291

Bennett, C. L., Banday, A. J., Gorski, K. M., Hinshaw, G., Jackson, P., Keegstra, P., Kogut, A., Smoot, G. F., Wilkinson, D. T., & Wright, E. L. 1996: *Four-Year COBE DMR Cosmic Microwave Background Observations: Maps and Basic Results*, ApJ, 464, L1+

Benoît, A., Ade, P., Amblard, A., Ansari, R., Aubourg, É., Bargot, S., Bartlett, J. G., Bernard, J.-P., Bhatia, R. S., Blanchard, A., Bock, J. J., et al. 2003a: *The cosmic microwave background anisotropy power spectrum measured by Archeops*, A&A, 399, L19

Benoît, A., Ade, P., Amblard, A., Ansari, R., Aubourg, É., Bargot, S., Bartlett, J. G., Bernard, J.-P., Bhatia, R. S., Blanchard, A., Bock, J. J., et al. 2003b: *Cosmological constraints from Archeops*, A&A, 399, L25

Benz, W. 1990: *Smooth Particle Hydrodynamics - a Review*, in Numerical Modelling of Nonlinear Stellar Pulsations Problems and Prospects, ed. J. R. Buchler, 269–+

Bernardeau, F., Colombi, S., Gaztañaga, E., & Scoccimarro, R. 2002: *Large-scale structure of the Universe and cosmological perturbation theory*, Physics Reports, 367, 1

Bland-Hawthorn, J., Sutherland, R., Agertz, O., & Moore, B. 2007: *The Source of Ionization along the Magellanic Stream*, ApJ, 670, L109

Boubekeur, L., Creminelli, P., D'Amico, G., Noreña, J., & Vernizzi, F. 2009: *Sachs-Wolfe at second order: the CMB bispectrum on large angular scales*, 8, 29

Burkert, A. 2006: *The turbulent interstellar medium*, Comptes Rendus Physique, 7, 433

Burkert, A., Naab, T., Johansson, P. H., & Jesseit, R. 2008: *SAURON's Challenge for the Major Merger Scenario of Elliptical Galaxy Formation*, ApJ, 685, 897

Caldwell, R. R., Dave, R., & Steinhardt, P. J. 1998: *Cosmological Imprint of an Energy Component with General Equation of State*, Physical Review Letters, 80, 1582

Caldwell, R. R. & Doran, M. 2004: *Cosmic microwave background and supernova constraints on quintessence: Concordance regions and target models*, Phys. Rev. D, 69, 103517

Caldwell, R. R., Doran, M., Müller, C. M., Schäfer, G., & Wetterich, C. 2003: *Early Quintessence in Light of the Wilkinson Microwave Anisotropy Probe*, ApJ, 591, L75

Carroll, J. J., Frank, A., Blackman, E. G., Cunningham, A. J., & Quillen, A. C. 2009: *Outflow-Driven Turbulence in Molecular Clouds*, ApJ, 695, 1376

Carroll, S. M. 2001: *The Cosmological Constant*, Living Reviews in Relativity, 4, 1

Chandrasekhar, S. 1961, Hydrodynamic and Hydromagnetic Stability (Dover Publications)

Chevallier, M. & Polarski, D. 2001: *Accelerating Universes with Scaling Dark Matter*, International Journal of Modern Physics D, 10, 213

Coble, K., Dodelson, S., & Frieman, J. A. 1997: *Dynamical Λ models of structure formation*, Phys. Rev. D, 55, 1851

Colagrossi, A. 2004, Dottorato di Ricerca in Meccanica Teorica ed Applicata XVI CICLO, A meshless Lagrangian method for free-surface and interface flows with fragmentation, Phd Thesis (Universita di Roma, La Sapienza)

Colella, P. & Woodward, P. R. 1984: *The Piecewise Parabolic Method (PPM) for Gas-Dynamical Simulations*, Journal of Computational Physics, 54, 174

Colless, M. 1999: *First results from the 2dF Galaxy Redshift Survey*, Royal Society of London Philosophical Transactions Series A, 357, 105

Cooray, A. & Hu, W. 2001: *Weak Gravitational Lensing Bispectrum*, ApJ, 548, 7

Cooray, A., Huterer, D., & Baumann, D. 2004: *Growth rate of large-scale structure as a powerful probe of dark energy*, Phys. Rev. D, 69, 027301

Cooray, A. & Sheth, R. 2002: *Halo models of large scale structure*, Phys. Rep., 372, 1

Couchman, H. M. P., Thomas, P. A., & Pearce, F. R. 1995: *Hydra: an Adaptive-Mesh Implementation of P 3M-SPH*, ApJ, 452, 797

Das, S. & Chattopadhyay, I. 2008: *Computation of mass loss from viscous accretion disc in presence of cooling*, New Astronomy, 13, 549

Davis, M. & Peebles, P. J. E. 1977: *On the integration of the BBGKY equations for the development of strongly nonlinear clustering in an expanding universe*, ApJS, 34, 425

de Bernardis, P., Ade, P. A. R., Bock, J. J., Bond, J. R., Borrill, J., Boscaleri, A., Coble, K., Crill, B. P., De Gasperis, G., Farese, P. C., Ferreira, P. G., et al. 2000: *A flat Universe from high-resolution maps of the cosmic microwave background radiation*, Nat, 404, 955

Dekel, A., Birnboim, Y., Engel, G., Freundlich, J., Goerdt, T., Mumcuoglu, M., Neistein, E., Pichon, C., Teyssier, R., & Zinger, E. 2009: *Cold streams in early massive hot haloes as the main mode of galaxy formation*, Nat, 457, 451

Diemand, J., Kuhlen, M., Madau, P., Zemp, M., Moore, B., Potter, D., & Stadel, J. 2008: *Clumps and streams in the local dark matter distribution*, Nat, 454, 735

Dodelson, S. 2003, Modern cosmology, ed. S. Dodelson

Dodelson, S., Narayanan, V. K., Tegmark, M., Scranton, R., Budavári, T., Connolly, A., Csabai, I., Eisenstein, D., Frieman, J. A., Gunn, J. E., Hui, L., et al. 2002: *The Three-dimensional Power Spectrum from Angular Clustering of Galaxies in Early Sloan Digital Sky Survey Data*, ApJ, 572, 140

Doran, M., Lilley, M., Schwindt, J., & Wetterich, C. 2001a: *Quintessence and the Separation of Cosmic Microwave Background Peaks*, ApJ, 559, 501

Doran, M., Schwindt, J.-M., & Wetterich, C. 2001b: *Structure formation and the time dependence of quintessence*, Phys. Rev. D, 64, 123520

Efstathiou, G., Frenk, C. S., White, S. D. M., & Davis, M. 1988: *Gravitational clustering from scale-free initial conditions*, MNRAS, 235, 715

Einfeld, B. 1988: *On Godunov-type methods for gas dynamics*, SIAM Journal on Numerical Analysis, 25, 294

Einstein, A. 1917: *Kosmologische Betrachtungen zur allgemeinen Relativitätstheorie*, Sitzungsberichte der Königlich Preußischen Akademie der Wissenschaften (Berlin), Seite 142-152., 142

Eisenstein, D. J., Hu, W., & Tegmark, M. 1999: *Cosmic Complementarity: Joint Parameter Estimation from Cosmic Microwave Background Experiments and Redshift Surveys*, ApJ, 518, 2

Español, P. & Revenga, M. 2003: *Smoothed dissipative particle dynamics*, Phys. Rev. E, 67, 026705

Evrard, A. E., Summers, F. J., & Davis, M. 1994: *Two-fluid simulations of galaxy formation*, ApJ, 422, 11

Fehlberg, E. 1974: *Classical seventh-, sixth,- and fith-order Runge-Kutta-Nystroem formulas with stepsize control for general second-order differential equations*, NASA TR R-432

Ferreira, P. G. & Joyce, M. 1998: *Cosmology with a primordial scaling field*, Phys. Rev. D, 58, 023503

Flebbe, O., Muenzel, S., Herold, H., Riffert, H., & Ruder, H. 1994: *Smoothed Particle Hydrodynamics: Physical viscosity and the simulation of accretion disks*, ApJ, 431, 754

Fry, J. N. 1984: *The Galaxy correlation hierarchy in perturbation theory*, ApJ, 279, 499

Fryxell, B., Olson, K., Ricker, P., Timmes, F. X., Zingale, M., Lamb, D. Q., MacNeice, P., Rosner, R., Truran, J. W., & Tufo, H. 2000: *FLASH: An Adaptive Mesh Hydrodynamics Code for Modeling Astrophysical Thermonuclear Flashes*, ApJS, 131, 273

Funada, T. & Joseph, D. D. 2001: *Viscous potential flow analysis of Kelvin Helmholtz instability in a channel*, Journal of Fluid Mechanics, 445, 263

Gangui, A. & Martin, J. 2000: *Best unbiased estimators for the three-point correlators of the cosmic microwave background radiation*, Phys. Rev. D, 62, 103004

Gingold, R. A. & Monaghan, J. J. 1977: *Smoothed particle hydrodynamics - Theory and application to non-spherical stars*, MNRAS, 181, 375

Giovi, F., Baccigalupi, C., & Perrotta, F. 2003: *Constraining the dark energy dynamics with the cosmic microwave background bispectrum*, Phys. Rev. D, 68, 123002

Giovi, F., Baccigalupi, C., & Perrotta, F. 2005: *Cosmic microwave background constraints on dark energy dynamics: Analysis beyond the power spectrum*, Phys. Rev. D, 71, 103009

Godunov, S. K. 1954: *Ph.D. Dissertation: Different Methods for Shock Waves, Moscow State University*

Godunov, S. K. 1959: *A difference scheme for numerical computation of discontinuous solution of hyperbolic equation*, Sbornik: Mathematics, 47, 271

Goldberg, D. M. & Spergel, D. N. 1999: *Microwave background bispectrum. II. A probe of the low redshift universe*, Phys. Rev. D, 59, 103002

Goldberg, J. N., Macfarlane, A. J., Newman, E. T., Rohrlich, F., & Sudarshan, E. C. G. 1967: *Spin-s Spherical Harmonics and ????*, Journal of Mathematical Physics, 8, 2155

Goroff, M. H., Grinstein, B., Rey, S.-J., & Wise, M. B. 1986: *Coupling of modes of cosmological mass density fluctuations*, ApJ, 311, 6

Grcevich, J., Heitsch, F., & Putman, M. 2010: *Simulations of Dwarf Galaxy Gas Loss in a Milky Way-like Halo Medium*, in Bulletin of the American Astronomical Society, Vol. 41, Bulletin of the American Astronomical Society, 480–+

Gritschneder, M., Naab, T., Burkert, A., Walch, S., Heitsch, F., & Wetzstein, M. 2009a: *iVINE - Ionization in the parallel TREE/SPH code VINE: first results on the observed age-spread around O-stars*, MNRAS, 393, 21

Gritschneder, M., Naab, T., Walch, S., Burkert, A., & Heitsch, F. 2009b: *Driving Turbulence and Triggering Star Formation by Ionizing Radiation*, ApJ, 694, L26

Grossi, M. & Springel, V. 2009: *The impact of early dark energy on non-linear structure formation*, MNRAS, 394, 1559

Hamilton, A. J. S. 2001: *Formulae for growth factors in expanding universes containing matter and a cosmological constant*, MNRAS, 322, 419

Hamilton, A. J. S., Kumar, P., Lu, E., & Matthews, A. 1991: *Reconstructing the primordial spectrum of fluctuations of the universe from the observed nonlinear clustering of galaxies*, ApJ, 374, L1

Hanany, S., Ade, P., Balbi, A., Bock, J., Borrill, J., Boscaleri, A., de Bernardis, P., Ferreira, P. G., Hristov, V. V., Jaffe, A. H., Lange, A. E., et al. 2000: *MAXIMA-1: A Measurement of the Cosmic Microwave Background Anisotropy on Angular Scales of* $10' - 5$deg, ApJ, 545, L5

Hanson, D., Smith, K. M., Challinor, A., & Liguori, M. 2009: *CMB lensing and primordial non-Gaussianity*, Phys. Rev. D, 80, 083004

Harten, A., Lax, P., & Van Leer, B. 1983: *On Upstream Differencing and Godunov-Type Schemes for Hyperbolic Conservation Laws*, SIAM Review, 25, 35

Heath, D. J. 1977: *The growth of density perturbations in zero pressure Friedmann-Lemaitre universes*, MNRAS, 179, 351

Heinzeller, D., Duschl, W. J., & Mineshige, S. 2009: *Turbulent viscosity by convection in accretion discs - a self-consistent approach*, MNRAS, 397, 890

Heitsch, F. & Putman, M. E. 2009: *The Fate of High-Velocity Clouds: Warm or Cold Cosmic Rain?*, ApJ, 698, 1485

Heitsch, F., Slyz, A. D., Devriendt, J. E. G., Hartmann, L. W., & Burkert, A. 2006: *The Birth of Molecular Clouds: Formation of Atomic Precursors in Colliding Flows*, ApJ, 648, 1052

Hernquist, L. & Katz, N. 1989: *TREESPH - A unification of SPH with the hierarchical tree method*, ApJS, 70, 419

Hockney, R. W. & Eastwood, J. W. 1988, Computer simulation using particles, ed. Hockney, R. W. & Eastwood, J. W.

Hu, W. 2000: *Weak Lensing of the CMB: A Harmonic Approach*, Phys. Rev. D, 62, 043007

Hu, W. & Dodelson, S. 2002: *Cosmic Microwave Background Anisotropies*, ARA&A, 40, 171

Hu, W., Sugiyama, N., & Silk, J. 1997: *The physics of microwave background anisotropies*, Nat, 386, 37

Hu, W. & White, M. 1997: *CMB anisotropies: Total angular momentum method*, Phys. Rev. D, 56, 596

Jain, B. & Bertschinger, E. 1994: *Second-order power spectrum and nonlinear evolution at high redshift*, ApJ, 431, 495

Jain, B., Mo, H. J., & White, S. D. M. 1995: *The evolution of correlation functions and power spectra in gravitational clustering*, MNRAS, 276, L25

Jeong, D. & Komatsu, E. 2006: *Perturbation Theory Reloaded: Analytical Calculation of Nonlinearity in Baryonic Oscillations in the Real-Space Matter Power Spectrum*, ApJ, 651, 619

Jesseit, R., Naab, T., Peletier, R. F., & Burkert, A. 2007: *2D kinematics of simulated disc merger remnants*, MNRAS, 376, 997

Kaiser, C. R., Pavlovski, G., Pope, E. C. D., & Fangohr, H. 2005: *The stability of buoyant bubbles in the atmospheres of galaxy clusters*, MNRAS, 359, 493

Katz, N., Hernquist, L., & Weinberg, D. H. 1992: *Galaxies and gas in a cold dark matter universe*, ApJ, 399, L109

Knox, L. 1995: *Determination of inflationary observables by cosmic microwave background anisotropy experiments*, Phys. Rev. D, 52, 4307

Kogut, A., Lineweaver, C., Smoot, G. F., Bennett, C. L., Banday, A., Boggess, N. W., Cheng, E. S., de Amici, G., Fixsen, D. J., Hinshaw, G., Jackson, P. D., et al. 1993: *Dipole Anisotropy in the COBE Differential Microwave Radiometers First-Year Sky Maps*, ApJ, 419, 1

Komatsu, E. 2002: *The Pursuit of Non-Gaussian Fluctuations in the Cosmic Microwave Background*, ArXiv Astrophysics e-prints

Komatsu, E., Dunkley, J., Nolta, M. R., Bennett, C. L., Gold, B., Hinshaw, G., Jarosik, N., Larson, D., Limon, M., Page, L., Spergel, D. N., et al. 2009: *Five-Year Wilkinson Microwave Anisotropy Probe Observations: Cosmological Interpretation*, ApJS, 180, 330

Komatsu, E. & Spergel, D. N. 2001: *Acoustic signatures in the primary microwave background bispectrum*, Phys. Rev. D, 63, 063002

Kotarba, H., Lesch, H., Dolag, K., Naab, T., Johansson, P. H., & Stasyszyn, F. A. 2009: *Magnetic field structure due to the global velocity field in spiral galaxies*, MNRAS, 397, 733

Krauss, L. M. & Turner, M. S. 1995: *The cosmological constant is back*, General Relativity and Gravitation, 27, 1137

Landau, L. D. & Lifschitz, E. M. 1991, Hydrodynamik (Deutsch (Harri))

Lanzafame, G., Belvedere, G., & Molteni, D. 2006: *Low compressibility accretion disc formation in close binaries: the role of physical viscosity*, A&A, 453, 1027

Lattanzio, J., Monaghan, J., Pongracic, H., & Schwartz, M. 1986: *Controlling Penetration*, SIAM Journal on Scientific and Statistical Computing, 7, 591

Lattanzio, J. C., Monaghan, J. J., Pongracic, H., & Schwarz, M. P. 1985: *Interstellar Cloud Collisions*, MNRAS, 215, 125

Liddle, A. R. & Scherrer, R. J. 1999: *Classification of scalar field potentials with cosmological scaling solutions*, Phys. Rev. D, 59, 023509

Linder, E. 2003a: *Probing dark energy with SNAP*, in Identification of Dark Matter, ed. N. J. C. Spooner & V. Kudryavtsev, 52–57

Linder, E. V. 2003b: *Exploring the Expansion History of the Universe*, Physical Review Letters, 90, 091301

Linder, E. V. 2008: *The dynamics of quintessence, the quintessence of dynamics*, General Relativity and Gravitation, 40, 329

Linder, E. V. & Jenkins, A. 2003: *Cosmic structure growth and dark energy*, MNRAS, 346, 573

Lucy, L. B. 1977: *A numerical approach to the testing of the fission hypothesis*, AJ, 82, 1013

Luo, X. 1994: *The angular bispectrum of the cosmic microwave background*, ApJ, 427, L71

Ma, C. 1998: *Analytical Approximation to the Nonlinear Power Spectrum of Gravitational Clustering*, ApJ, 508, L5

Ma, C., Caldwell, R. R., Bode, P., & Wang, L. 1999: *The Mass Power Spectrum in Quintessence Cosmological Models*, ApJ, 521, L1

Ma, C. & Fry, J. N. 2000: *Deriving the Nonlinear Cosmological Power Spectrum and Bispectrum from Analytic Dark Matter Halo Profiles and Mass Functions*, ApJ, 543, 503

MacNeice, P., Olson, K. M., Mobarry, C., de Fainchtein, R., & Packer, C. 2000: *PARAMESH: A parallel adaptive mesh refinement community toolkit*, Computer Physics Communications, 126, 330

Makino, N., Sasaki, M., & Suto, Y. 1992: *Analytic approach to the perturbative expansion of nonlinear gravitational fluctuations in cosmological density and velocity fields*, Phys. Rev. D, 46, 585

Mangilli, A. & Verde, L. 2009: *Non-Gaussianity and the CMB bispectrum: Confusion between primordial and lensing-Rees-Sciama contribution?*, Phys. Rev. D, 80, 123007

Marri, S. & White, S. D. M. 2003: *Smoothed particle hydrodynamics for galaxy-formation simulations: improved treatments of multiphase gas, of star formation and of supernovae feedback*, MNRAS, 345, 561

Masiero, A., Pietroni, M., & Rosati, F. 2000: *SUSY QCD and quintessence*, Phys. Rev. D, 61, 023504

McClelland, J. & Silk, J. 1977: *The correlation function for density perturbations in an expanding universe. I - Linear theory*, ApJ, 216, 665

Mignone, A., Bodo, G., Massaglia, S., Matsakos, T., Tesileanu, O., Zanni, C., & Ferrari, A. 2007: *PLUTO: A Numerical Code for Computational Astrophysics*, ApJS, 170, 228

Miller, A. D., Caldwell, R., Devlin, M. J., Dorwart, W. B., Herbig, T., Nolta, M. R., Page, L. A., Puchalla, J., Torbet, E., & Tran, H. T. 2000: *A Measurement of the Angular Power Spectrum of the CMB from l = 100 to 400*, in Bulletin of the American Astronomical Society, Vol. 31, Bulletin of the American Astronomical Society, 1458–+

Monaghan, J. J. 1992: *Smoothed particle hydrodynamics*, ARA&A, 30, 543

Monaghan, J. J. 1997: *SPH and Riemann Solvers*, J. Comp. Phys., 136, 298

Monaghan, J. J. 2005: *Smoothed particle hydrodynamics*, Reports of Progress in Physics, 68, 1703

Monaghan, J. J. & Gingold, R. A. 1983: *Shock Simulation by the Particle Method SPH*, J. Comp. Phys., 52, 374

Monaghan, J. J. & Lattanzio, J. C. 1985: *A refined particle method for astrophysical problems*, A&A, 149, 135

Morris, J. 1997: *A Switch to Reduce SPH Viscosity*, J. Comp. Phys., 136, 41

Mukhanov, V. 2005, Physical foundations of cosmology (Physical foundations of cosmology, by V. Mukhanov. Cambridge, UK: Cambridge University Press, 2005)

Murray, S. D., White, S. D. M., Blondin, J. M., & Lin, D. N. C. 1993: *Dynamical instabilities in two-phase media and the minimum masses of stellar systems*, ApJ, 407, 588

Naab, T., Jesseit, R., & Burkert, A. 2006: *The influence of gas on the structure of merger remnants*, MNRAS, 372, 839

Navarro, J. F., Frenk, C. S., & White, S. D. M. 1995: *The assembly of galaxies in a hierarchically clustering universe*, MNRAS, 275, 56

Navarro, J. F. & Steinmetz, M. 2000: *Dark Halo and Disk Galaxy Scaling Laws in Hierarchical Universes*, apj, 538, 477

Nelson, A. F., Wetzstein, M., & Naab, T. 2009: *Vine A Numerical Code for Simulating Astrophysical Systems Using Particles. II. Implementation and Performance Characteristics*, ApJS, 184, 326

Netterfield, C. B., Ade, P. A. R., Bock, J. J., Bond, J. R., Borrill, J., Boscaleri, A., Coble, K., Contaldi, C. R., Crill, B. P., de Bernardis, P., Farese, P., et al. 2002: *A Measurement by BOOMERANG of Multiple Peaks in the Angular Power Spectrum of the Cosmic Microwave Background*, ApJ, 571, 604

Newman, E. T. & Penrose, R. 1966: *Note on the Bondi-Metzner-Sachs Group*, Journal of Mathematical Physics, 7, 863

Neyman, J. & Scott, E. L. 1952: *A Theory of the Spatial Distribution of Galaxies.*, ApJ, 116, 144

Nishikawa, H. & Kitamura, K. 2008: *Very simple, carbuncle-free, boundary-layer-resolving, rotated-hybrid Riemann solvers*, J. Comp. Phys., 227, 2560

Ostriker, J. P. & Steinhardt, P. J. 1995: *The Observational Case for a Low Density Universe with a Non-Zero Cosmological Constant*, Nat, 377, 600

Ostriker, J. P. & Vishniac, E. T. 1986: *Generation of microwave background fluctuations from nonlinear perturbations at the ERA of galaxy formation*, ApJ, 306, L51

Padmanabhan, T. 1993, Structure Formation in the Universe (Structure Formation in the Universe, by T. Padmanabhan, pp. 499. ISBN 0521424860. Cambridge, UK: Cambridge University Press, June 1993.)

Padmanabhan, T. 2003: *Cosmological constant-the weight of the vacuum*, Phys. Rep., 380, 235

Park, M. 2009: *Mass Accretion Rate of Rotating Viscous Accretion Flow*, ApJ, 706, 637

Peacock, J. A. & Dodds, S. J. 1994: *Reconstructing the Linear Power Spectrum of Cosmological Mass Fluctuations*, MNRAS, 267, 1020

Peacock, J. A. & Dodds, S. J. 1996: *Non-linear evolution of cosmological power spectra*, MNRAS, 280, L19

Peacock, J. A. & Smith, R. E. 2000: *Halo occupation numbers and galaxy bias*, MNRAS, 318, 1144

Peebles, P. J. E. 1974a: *The Gravitational-Instability Picture and the Nature of the Distribution of Galaxies*, ApJ, 189, L51+

Peebles, P. J. E. 1974b: *The Nature of the Distribution of Galaxies*, A&A, 32, 197

Peebles, P. J. E. 1980, The large-scale structure of the universe (Research supported by the National Science Foundation. Princeton, N.J., Princeton University Press, 1980. 435 p.)

Peebles, P. J. E. 1984: *Tests of cosmological models constrained by inflation*, ApJ, 284, 439

Peebles, P. J. E. & Ratra, B. 1988: *Cosmology with a time-variable cosmological 'constant'*, ApJ, 325, L17

Penzias, A. A. & Wilson, R. W. 1965: *A Measurement of Excess Antenna Temperature at 4080 Mc/s.*, ApJ, 142, 419

Perlmutter, S., Aldering, G., Goldhaber, G., Knop, R. A., Nugent, P., Castro, P. G., Deustua, S., Fabbro, S., Goobar, A., Groom, D. E., Hook, I. M., et al. 1999: *Measurements of Omega and Lambda from 42 High-Redshift Supernovae*, ApJ, 517, 565

Pitrou, C., Uzan, J., & Bernardeau, F. 2010: *The cosmic microwave background bispectrum from the non-linear evolution of the cosmological perturbations*, 7, 3

Price, D. J. 2008: *Modelling discontinuities and Kelvin Helmholtz instabilities in SPH*, J. Comp. Phys., 227, 10040

Quilis, V. & Moore, B. 2001: *Where Are the High-Velocity Clouds?*, ApJ, 555, L95

Ratra, B. & Peebles, P. J. E. 1988: *Cosmological consequences of a rolling homogeneous scalar field*, Phys. Rev. D, 37, 3406

Read, J. I., Hayfield, T., & Agertz, O. 2010: *Resolving mixing in smoothed particle hydrodynamics*, MNRAS, 767

Rees, M. J. & Sciama, D. W. 1968: *Larger scale Density Inhomogeneities in the Universe*, Nat, 217, 511

Riess, A. G., Filippenko, A. V., Challis, P., Clocchiatti, A., Diercks, A., Garnavich, P. M., Gilliland, R. L., Hogan, C. J., Jha, S., Kirshner, R. P., Leibundgut, B., et al. 1998: *Observational Evidence from Supernovae for an Accelerating Universe and a Cosmological Constant*, AJ, 116, 1009

Ritchie, B. W. & Thomas, P. A. 2001: *Multiphase smoothed-particle hydrodynamics*, MNRAS, 323, 743

Robertson, B. E., Kravtsov, A. V., Gnedin, N. Y., Abel, T., & Rudd, D. H. 2009: *Computational Eulerian hydrodynamics and Galilean invariance*, MNRAS, 1774

Roe, P. L. 1981: *Approximate Riemann Solvers, Parameter Vectors, and Difference Schemes*, J. Comp. Phys., 43, 357

Sachs, R. K. & Wolfe, A. M. 1967: *Perturbations of a Cosmological Model and Angular Variations of the Microwave Background*, ApJ, 147, 73

Scherrer, R. J. & Bertschinger, E. 1991: *Statistics of primordial density perturbations from discrete seed masses*, ApJ, 381, 349

Schneider, P. 2006, Einführung in die extragalaktische Astronomie und Kosmologie (Einführung in die extragalaktische Astronomie und Kosmologie / Peter Schneider. Berlin: Springer, ISBN 3-540-25832-9, ISBN 978-3-540-25832-2, 2006, XV+452 pp.)

Schuessler, I. & Schmitt, D. 1981: *Comments on smoothed particle hydrodynamics*, A&A, 97, 373

Scoccimarro, R. & Frieman, J. A. 1996: *Loop Corrections in Nonlinear Cosmological Perturbation Theory. II. Two-Point Statistics and Self-Similarity*, ApJ, 473, 620

Scoccimarro, R., Sheth, R. K., Hui, L., & Jain, B. 2001: *How Many Galaxies Fit in a Halo? Constraints on Galaxy Formation Efficiency from Spatial Clustering*, ApJ, 546, 20

Seljak, U. 2000: *Analytic model for galaxy and dark matter clustering*, MNRAS, 318, 203

Seljak, U. & Zaldarriaga, M. 1996: *A Line-of-Sight Integration Approach to Cosmic Microwave Background Anisotropies*, ApJ, 469, 437

Serna, A., Domínguez-Tenreiro, R., & Sáiz, A. 2003: *Conservation Laws in Smooth Particle Hydrodynamics: The DEVA Code*, ApJ, 597, 878

Serra, P. & Cooray, A. 2008: *Impact of secondary non-Gaussianities on the search for primordial non-Gaussianity with CMB maps*, Phys. Rev. D, 77, 107305

Sheth, R. K. & Jain, B. 1997: *The non-linear correlation function and density profiles of virialized haloes*, MNRAS, 285, 231

Sijacki, D. & Springel, V. 2006: *Physical viscosity in smoothed particle hydrodynamics simulations of galaxy clusters*, MNRAS, 371, 1025

Smith, R. E., Peacock, J. A., Jenkins, A., White, S. D. M., Frenk, C. S., Pearce, F. R., Thomas, P. A., Efstathiou, G., & Couchman, H. M. P. 2003: *Stable clustering, the halo model and non-linear cosmological power spectra*, MNRAS, 341, 1311

Sod, G. A. 1978: *A survey of several finite difference methods for systems of nonlinear hyperbolic conservation laws*, Journal of Computational Physics, 27, 1

Spergel, D. N., Bean, R., Doré, O., Nolta, M. R., Bennett, C. L., Dunkley, J., Hinshaw, G., Jarosik, N., Komatsu, E., Page, L., Peiris, H. V., et al. 2007: *Three-Year Wilkinson Microwave Anisotropy Probe (WMAP) Observations: Implications for Cosmology*, ApJS, 170, 377

Spergel, D. N. & Goldberg, D. M. 1999: *Microwave background bispectrum. I. Basic formalism*, Phys. Rev. D, 59, 103001

Spergel, D. N., Verde, L., Peiris, H. V., Komatsu, E., Nolta, M. R., Bennett, C. L., Halpern, M., Hinshaw, G., Jarosik, N., Kogut, A., Limon, M., et al. 2003: *First-Year Wilkinson Microwave Anisotropy Probe (WMAP) Observations: Determination of Cosmological Parameters*, ApJS, 148, 175

Springel, V. 2010: *E pur si muove: Galilean-invariant cosmological hydrodynamical simulations on a moving mesh*, MNRAS, 401, 791

Springel, V. & Hernquist, L. 2002: *Cosmological smoothed particle hydrodynamics simulations: the entropy equation*, MNRAS, 333, 649

Steinhardt, P. J., Wang, L., & Zlatev, I. 1999: *Cosmological tracking solutions*, Phys. Rev. D, 59, 123504

Steinmetz, M. & Navarro, J. F. 1999: *The Cosmological Origin of the Tully-Fisher Relation*, ApJ, 513, 555

Steinmetz, M. & Navarro, J. F. 2002: *The hierarchical origin of galaxy morphologies*, New Astronomy, 7, 155

Suto, Y. & Sasaki, M. 1991: *Quasinonlinear theory of cosmological self-gravitating systems*, Physical Review Letters, 66, 264

Takeda, H., Miyama, S. M., & Sekiya, M. 1994: *Numerical Simulation of Viscous Flow by Smoothed Particle Hydrodynamics*, Progress of Theoretical Physics, 92, 939

Teyssier, R. 2002: *Cosmological hydrodynamics with adaptive mesh refinement. A new high resolution code called RAMSES*, A&A, 385, 337

Thacker, R. J. & Couchman, H. M. P. 2000: *Implementing Feedback in Simulations of Galaxy Formation: A Survey of Methods*, ApJ, 545, 728

Thacker, R. J., Tittley, E. R., Pearce, F. R., Couchman, H. M. P., & Thomas, P. A. 2000: *Smoothed Particle Hydrodynamics in cosmology: a comparative study of implementations*, MNRAS, 319, 619

Thomas, P. A. & Couchman, H. M. P. 1992: *Simulating the formation of a cluster of galaxies*, MNRAS, 257, 11

Valcke, S., De Rijcke, S., Roediger, E., & Dejonghe, H. 2010: *Kelvin-Helmholtz instabilities in Smoothed Particle Hydrodynamics*, ArXiv e-prints

Verde, L. & Spergel, D. N. 2002: *Dark energy and cosmic microwave background bispectrum*, Phys. Rev. D, 65, 043007

Vietri, M., Ferrara, A., & Miniati, F. 1997: *The Survival of Interstellar Clouds against Kelvin-Helmholtz Instabilities*, ApJ, 483, 262

Vishniac, E. T. 1983: *Why weakly non-linear effects are small in a zero-pressure cosmology*, MNRAS, 203, 345

Wadsley, J. W., Veeravalli, G., & Couchman, H. M. P. 2008: *On the treatment of entropy mixing in numerical cosmology*, MNRAS, 387, 427

Walch, S., Naab, T., Whitworth, A., Burkert, A., & Gritschneder, M. 2010: *Protostellar discs formed from turbulent cores*, MNRAS, 402, 2253

Wang, L. & Steinhardt, P. J. 1998: *Cluster Abundance Constraints for Cosmological Models with a Time-varying, Spatially Inhomogeneous Energy Component with Negative Pressure*, ApJ, 508, 483

Wang, Y. & Tegmark, M. 2004: *New Dark Energy Constraints from Supernovae, Microwave Background, and Galaxy Clustering*, Physical Review Letters, 92, 241302

Weinberg, S. 1989: *The cosmological constant problem*, Reviews of Modern Physics, 61, 1

Wetterich, C. 1988: *Cosmology and the fate of dilatation symmetry.*, Nuclear Physics B, 302, 668

Wetterich, C. 2004: *Phenomenological parameterization of quintessence*, Physics Letters B, 594, 17

Wetzstein, M., Nelson, A. F., Naab, T., & Burkert, A. 2009: *Vine A Numerical Code for Simulating Astrophysical Systems Using Particles. I. Description of the Physics and the Numerical Methods*, ApJS, 184, 298

Xia, J. & Viel, M. 2009: *Early dark energy at high redshifts: status and perspectives*, Journal of Cosmology and Astro-Particle Physics, 4, 2

Zaldarriaga, M. 1997: *Polarization of the microwave background in reionized models*, Phys. Rev. D, 55, 1822

Zaldarriaga, M. 2000: *Lensing of the CMB: Non-Gaussian aspects*, Phys. Rev. D, 62, 063510

Zeldovich, Y. B. & Sunyaev, R. A. 1969: *The Interaction of Matter and Radiation in a Hot-Model Universe*, Ap&SS, 4, 301

Appendix A

Modelling Shear Flows with SPH and Grid Based Methods

A.1 Analysis methods - cloud in cell

In order to make a detailed comparison of SPH data with data from GRID simulations, it is fundamental to have a similiar scheme applied to the SPH output. Therefore, a grid has to be superimposed over the SPH-particles (left side of Fig. 3.3), and the corresponding physical quantities have to be derived by weighing the SPH-particles to the grid-points (right side of Fig. 3.3). For example, the weight, velocity and mass for the grid-points (x_i, y_i), (x_i, y_{i+1}), (x_{i+1}, y_i) and (x_{i+1}, y_{i+1}) deduced from the neighboring SPH-particles, (those SPH-particles which lie within the bordering cells) is as follows,

$$w_{x_i}(i_{SPH}) = -\left(\frac{x_{i_{SPH}} - x_i}{\Delta x}\right), \quad w_{x_{i+1}}(i_{SPH}) = -w_{x_i}(i_{SPH}) + 1 \tag{A.1}$$

$$w_{y_i}(i_{SPH}) = -\left(\frac{y_{i_{SPH}} - y_i}{\Delta y}\right), \quad w_{y_{i+1}}(i_{SPH}) = -w_{y_i}(i_{SPH}) + 1, \tag{A.2}$$

Δx and Δy are the corresponding sizes of the cell. The x-velocity components of the grid-points are determined by,

$$(i,i) : v_x = \frac{\sum_{i_{SPH}=1}^{n_{SPH}} w_{x_i}(i_{SPH}) w_{y_i}(i_{SPH}) v_x(i_{SPH}) m(i_{SPH})}{\sum_{i_{SPH}=1}^{n_{SPH}} w_{x_i}(i_{SPH}) w_{y_i}(i_{SPH})}, \tag{A.3}$$

$$(i,i+1) : v_x = \frac{\sum_{i_{SPH}=1}^{n_{SPH}} w_{x_i}(i_{SPH}) w_{y_{i+1}}(i_{SPH}) v_x(i_{SPH}) m(i_{SPH})}{\sum_{i_{SPH}=1}^{n_{SPH}} w_{x_i}(i_{SPH}) w_{y_{i+1}}(i_{SPH})}, \tag{A.4}$$

$$(i+1,i) : v_x = \frac{\sum_{i_{SPH}=1}^{n_{SPH}} w_{x_{i+1}}(i_{SPH}) w_{y_i}(i_{SPH}) v_x(i_{SPH}) m(i_{SPH})}{\sum_{i_{SPH}=1}^{n_{SPH}} w_{x_{i+1}}(i_{SPH}) w_{y_i}(i_{SPH})}, \tag{A.5}$$

$$(i+1,i+1) : v_x = \frac{\sum_{i_{SPH}=1}^{n_{SPH}} w_{x_{i+1}}(i_{SPH}) w_{y_{i+1}}(i_{SPH}) v_x(i_{SPH}) m(i_{SPH})}{\sum_{i_{SPH}=1}^{n_{SPH}} w_{x_{i+1}}(i_{SPH}) w_{y_{i+1}}(i_{SPH})}, \tag{A.6}$$

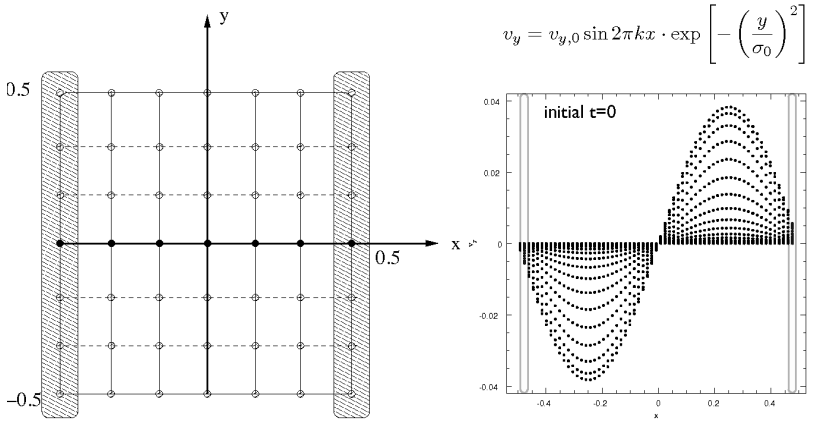

Figure A.1: Measure of the KHI-amplitudes: The v_y-velocity of the particles within the shaded region are subject to the Fourier-Transformation. The maximum of the Back-Transformation gives the maximal amplitude.

where the *y*-velocity components are obtained replacing $v_x(i_{SPH})$ with $v_y(i_{SPH})$ and $m(i_{SPH})$ denotes the mass of the SPH-particle. The same scheme gives the gridpoint masses,

$$(i,i) : m = \frac{\sum_{i_{SPH}=1}^{n_{SPH}} w_{x_i}(i_{SPH}) w_{y_i}(i_{SPH}) m(i_{SPH})}{\sum_{i_{SPH}=1}^{n_{SPH}} w_{x_i}(i_{SPH}) w_{y_i}(i_{SPH})}, \tag{A.7}$$

$$(i,i+1) : m = \frac{\sum_{i_{SPH}=1}^{n_{SPH}} w_{x_i}(i_{SPH}) w_{y_{i+1}}(i_{SPH}) m(i_{SPH})}{\sum_{i_{SPH}=1}^{n_{SPH}} w_{x_i}(i_{SPH}) w_{y_{i+1}}(i_{SPH})}, \tag{A.8}$$

$$(i+1,i) : m = \frac{\sum_{i_{SPH}=1}^{n_{SPH}} w_{x_{i+1}}(i_{SPH}) w_{y_i}(i_{SPH}) m(i_{SPH})}{\sum_{i_{SPH}=1}^{n_{SPH}} w_{x_{i+1}}(i_{SPH}) w_{y_i}(i_{SPH})}, \tag{A.9}$$

$$(i+1,i+1) : m = \frac{\sum_{i_{SPH}=1}^{n_{SPH}} w_{x_{i+1}}(i_{SPH}) w_{y_{i+1}}(i_{SPH}) m(i_{SPH})}{\sum_{i_{SPH}=1}^{n_{SPH}} w_{x_{i+1}}(i_{SPH}) w_{y_{i+1}}(i_{SPH})}. \tag{A.10}$$

This procedure is called 'cloud in cell method' (Hockney & Eastwood, 1988) and allows to transform the SPH particle distribution into an ordered grid distribution with its corresponding physical quantities. We use this approach to compare our SPH- and GRID results. Of course, other methods for the weighing (e.g. cubic weighing) exist, but for our purposes the linear scheme as discussed above is sufficient.

A.2 Measuring the KHI-amplitudes

To measure the amplitude growth of the KHI, we apply a Fourier-Transformation (FT) to the v_y-velocity component of the grid points. The FT allows to select the desired modes reducing the numerical noise.

The region of our focus, $x = [-0.5, 0.5]$ and $y = [-0.5, 0.5]$ containts one mode of the v_y-perturbation (eq. (3.36)) triggering the instability, see Fig. A.1. The shaded regions comprise the particles sub-

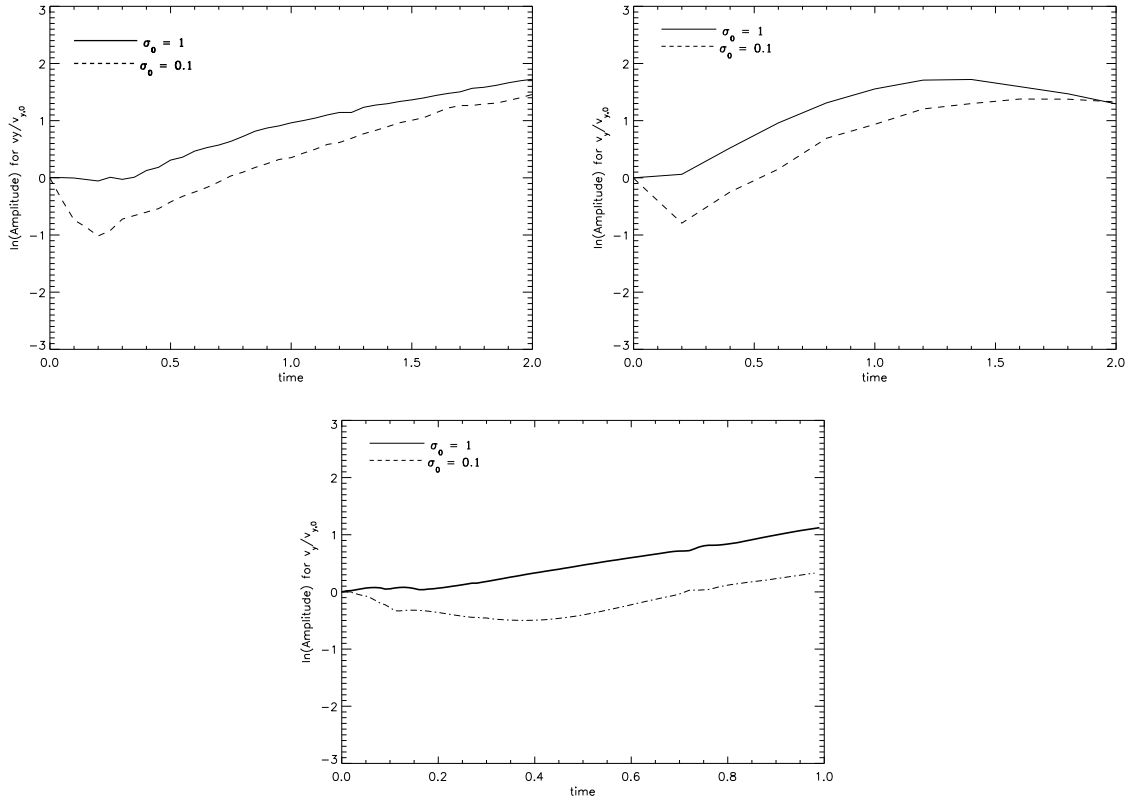

Figure A.2: Variation of KHI-amplitude in the case of equal density layers using VINE (upper left panel) and FLASH (upper right panel) for different values of σ_0. For the different density case with $DC = 10$ we show RAMSES (bottom panel).

ject to the FT. The maximum of the FT gives the dominant mode k and its corresponding velocity amplitude, which we compare wit the analytical model.

A.3 Dependence of KHI-amplitudes on σ_0

DEPENDENCE OF KHI ON σ_0:
This parameter determines the strength of the initial v_y-perturbation (eq. (3.36)). In Fig. 3.4 we show the time evolution of the vy-amplitude, which describes the growth of the KHI. For $t \leq 0.2$ the amplitudes decrease since the SPH particles lose kinetic energy by moving along the y-direction into the area of the opposite stream. If the magnitude of the initial perturbation is low (i.e. small σ_0), then the decrease in the amplitude is stronger than for e.g. $\sigma_0 = 1$, where the initial perturbation is large and the decrease less prominent. But independently of the value of σ_0 the subsequent growth of the instability is similar, and we obtain comparable results neglecting the decreasing initial part. Fig. A.2 shows the dependency of the KHI-amplitudes using different values of σ_0, for VINE (upper left panel) and FLASH (upper right panel). For both examples we use equal density layers, where for FLASH

a viscosity of $\nu = 0.3$ has been taken. The bottom panel of Fig. A.2 shows the different density case using RAMSES with $DC = 10$. Clearly visible is the initial drop caused by a low value of σ_0. This is the case for all codes, and arises due to the transformation of energy to build up the KHI. The fitted slopes do not vary much with σ_0. To extract the slopes, we concentrate on the time evolution after this initial drop.

Appendix B

The trace of dark energy captured within the CMB

B.1 Numerical Calculation of the Growth Suppression Factor

To solve eq. (4.61), we have to deal with an differential equation of the form,

$$\ddot{y} = f(x, y, \dot{y}). \tag{B.1}$$

The numerical approach to solve this kind of differential equation is called the *Runge-Kutta-Nystroem-method* (RKN-method). It is described in detail in Fehlberg (1974). We will give a short motivation. The initial conditions for the values $x, y, \dot{y}$ are given by $x_0, y_0, \dot{y}_0$, and it follows,

$$\begin{aligned}
f_0 &= f(x_0, y_0, \dot{y}_0), \\
f_1 &= f\left(x_0 + \alpha_1 h, y_0 + \dot{y}_0 \alpha_1 h + \frac{1}{2} f_0 \alpha_1^2 h^2, \dot{y}_0 + f_0 \alpha_1 h\right), \\
f_2 &= f\left(x_0 + \alpha_2 h, y_0 + \dot{y}_0 \alpha_2 h + \frac{1}{2} f_0 \alpha_2^2 h^2 + \gamma_{21}(f_1 - f_0) h^2, \dot{y}_0 + f_0 \alpha_2 h + \beta_{21}(f_1 - f_0) h\right) \\
f_3 &= f\left(x_0 + \alpha_3 h, y_0 + \dot{y}_0 \alpha_3 h + \frac{1}{2} f_0 \alpha_3^2 h^2 + \gamma_{32}(f_2 - f_0) h^2, \dot{y}_0 + f_0 \alpha_3 h + \beta_{32}(f_2 - f_0) h\right) \\
&\vdots \\
f_\kappa &= f\left(x_0 + \alpha_\kappa h, y_0 + \dot{y}_0 \alpha_\kappa h + h^2 \cdot \sum_{\lambda=0}^{\kappa=1} \gamma_{\kappa\lambda} \cdot f_\lambda, \dot{y}_0 + h \cdot \sum_{\lambda=0}^{\kappa-1} \beta_{\kappa\lambda} \cdot f_\lambda\right),
\end{aligned}$$

where h denotes the integration stepsize, and the α's, β's and γ's are the Runge-Kutta-Nystroem coefficients which need to be calculated. κ depends on the desired order of the integration, e.g. $\kappa = 1, 2, 3, ..., 13$ for the seventh order. We use the 5th-order RKN-formulae. Its evaluations lead to,

$$\begin{aligned}
y(x_0 + h) &= y_0 + \dot{y}_0 h + (c_0 f_0 + c_1 f_1 + c_2 f_2 + c_3 f_3 + \\
&\quad c_4 f_4 + c_5 f_5 + c_6 f_6 + c_7 f_7) h^2, \qquad \text{(B.2)} \\
\dot{y}(x_0 + h) &= \dot{y}_0 + (\dot{c}_0 f_0 + \dot{c}_1 f_1 + \dot{c}_2 f_2 + \dot{c}_3 f_3 + \\
&\quad \dot{c}_4 f_4 + \dot{c}_5 f_5 + \dot{c}_6 f_6 + \dot{c}_7 f_7) h. \qquad \text{(B.3)}
\end{aligned}$$

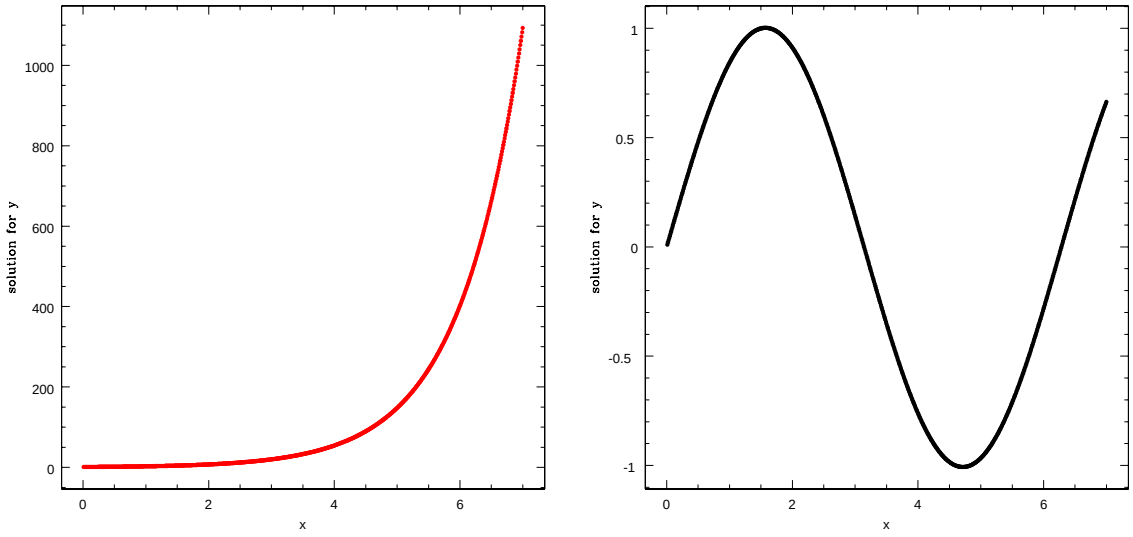

Figure B.1: On the left side the numerical solution of the differential equation $\ddot{y} - \dot{y} = 0$ is shown, with the analytical solution being $y(x) \sim \exp x$. On the right side the numerical solution for $\ddot{y} + y = 0$ is presented. The analytical solution is $y \sim \sin x$.

The corresponding weight factors, c_κ and $\dot{c}_\kappa$ need to be computed following the derivation in Fehlberg (1974), where a complete table of all coefficients is given.

Fig. B.1 presents the solutions of two simple test cases. The first test case, the differential equation $\ddot{y} - \dot{y} = 0$ has the analytical solution $y(x) \sim \exp(x)$. As can be seen from Fig. B.1, the numerical solution reproduces this functional behavior. The same holds for the second case, the differential equation $\ddot{y} + y = 0$ with the analytical solution being $y(x) \sim \sin x$. The numerical result reproduces the analytical solution very well.

B.2 Transfer Function

The behavior of the transfer function depends on the scale L of the fluctuation and the moment it enters the horizon, characterized through $z_{\text{enter}}(L)$. If this happens at the era of radiation (i.e. before $\rho_{\text{M}} = \rho_{\text{Rad}}$ denoted by $z_{\text{RM-eq}}$) the expansion of the universe is too strong and any growth is prevented. It starts only when matter begins to dominate, after $z < z_{\text{MR-eq}}$. This leads to a special scale, where

$$z_{\text{RM-eq}} = z_{\text{enter}}(L_0), \tag{B.4}$$

with L_0 being the comoving distance (eq. (4.26)) to matter radiation equality. Therefore, fluctuations with $L > L_0$ will enter the horizon at matter domination and hence grow. In the case of $L < L_0$ radiation dominates and the growth is suppressed until $z < z_{\text{RM-eq}}$. A quantitative description of those effects allows to determine the transfer function (e.g. Schneider, 2006). For example, the transfer function of

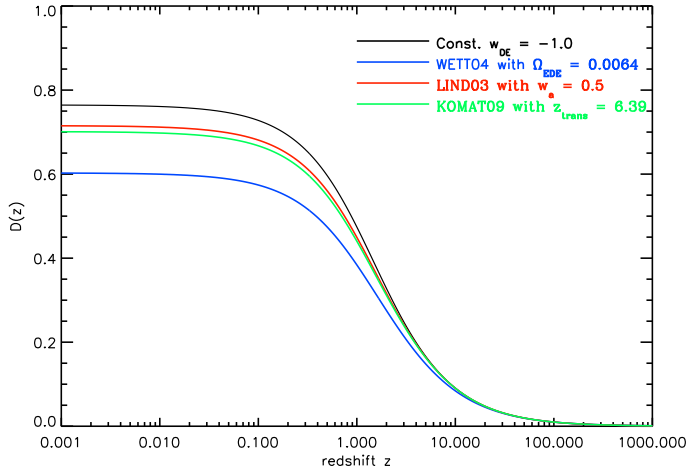

Figure B.2: Comparison of $D(z)$ (eq. 4.63) for all DE parameterizations: Cosmological constant (black line) using $w_{\rm DE} = -1$, WETT04 parameterization with $\Omega_{\rm EDE} = 0.0064$ (blue line), LIND03 parameterization using $w_a = 0.5$ (red line) and KOMAT09 parameterization with $z_{\rm trans} = 6.39$ (green line).

Bardeen *et al.* (1986) is determined through

$$T(q) = \frac{\ln(1+2.34q)}{2.34q} \cdot \left[1+3.89q+(16.1q)^2+(5.4q)^3+(6.71q)^4\right]^{-1/4} \tag{B.5}$$

$$q = \frac{k}{\Gamma h}. \tag{B.6}$$

q is given by,

$$q(k) = \frac{k}{\mathrm{Mpc}^{-1}} \cdot \alpha^{-1/2}(\Omega_0 h^2)^{-1}\Theta_{2,7}^2, \tag{B.7}$$

with

$$\alpha = a_1^{-\Omega_b/\Omega_0} \cdot a_2^{-(\Omega_b/\Omega_0)^2}, \tag{B.8}$$

and $\Theta_{2,7}^2 \sim 1$. Ω_0 is the total matter content of the universe today and $\Omega_b \sim 0.046$ the amount of baryons. a_1 and a_2 are determined by,

$$a_1 = (46.9\Omega_0 h^2)^{0.670}[1+(32.1\Omega_0 h^2)^{-0.532}], \tag{B.9}$$

$$a_2 = (12.0\Omega_0 h^2)^{0.424}[1+(45.0\Omega_0 h^2)^{-0.582}]. \tag{B.10}$$

B.3 Comoving Distances for different DE Models

Fig. B.3 presents the comoving distances (eq. (4.26)) for constant equation of states (upper left panel), LIND03 (upper right panel), KOMAT09 (bottom left panel) and WETT04 (bottom right panel).

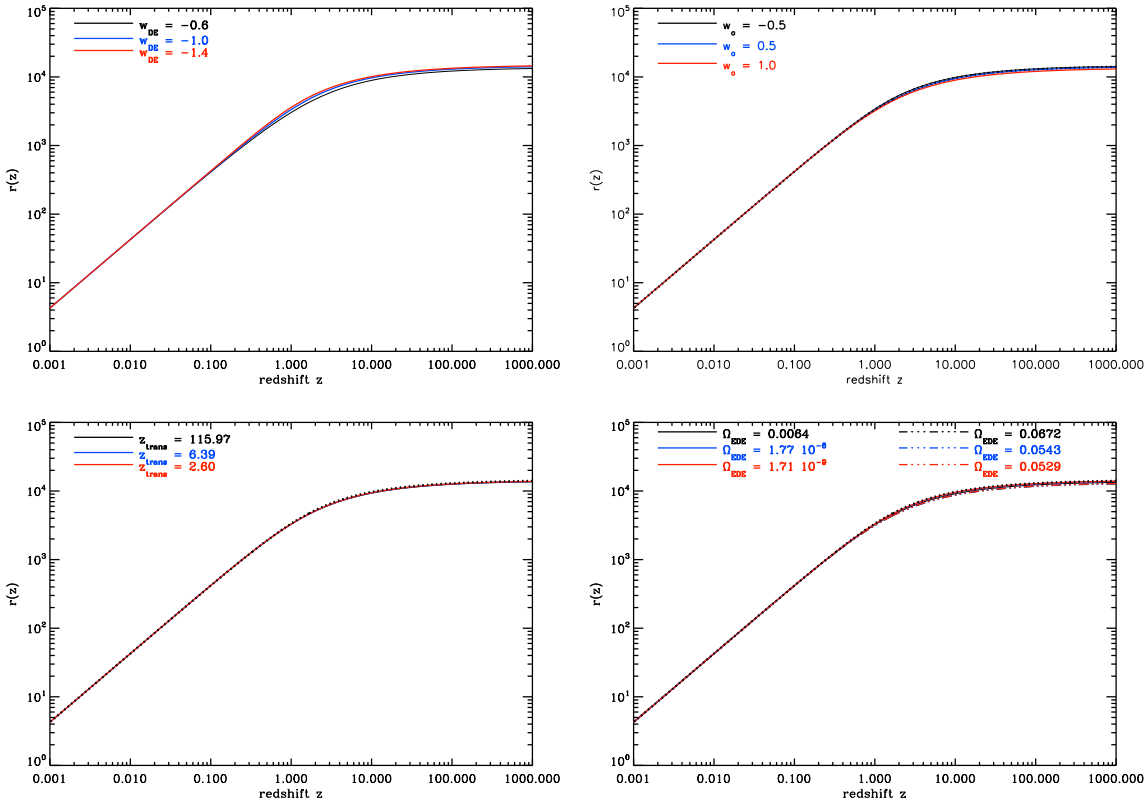

Figure B.3: Evolution of the comoving distances (eq. (4.26)) for $w_{\rm DE} = const.$ (upper left panel), LIND03 (upper right panel), KOMAT09 (bottom left panel) and WETT04 (bottom right panel), respectively.

B.4 Comparison of Growth Factors for different DE Models

Fig. B.2 shows the various growth factors $D(z)$ (eq. 4.63) with z for the case of the standard cosmological constant using $w_{\rm DE} = -1$ (black line), WETT04 using $\Omega_{\rm EDE} = 0.0064$ (blue line), LIND03 with $w_a = 0.5$ (red line) and KOMAT09 with $z_{\rm trans} = 6.39$ (green line). The strongest growth of $D(z)$ is for $w_{\rm DE} = -1$, since the DE density is the lowest in this case. WETT04 yields the most reduced $D(z)$, because DE plays a role already at early times and dampens the growth of structures most effectively. LIND03 with $w_a = 0.5$ (close to the value proposed by SUGRA, see 4.3.2) and KOMAT09 with $z_{\rm trans} = 6.39$ are also lower compared to the standard case.

B.5 Summary of Models for the Nonlinear Power Spectrum

- HKLM FORMALISM:
  This method is based on the stable clustering hypothesis (Peebles, 1974a, 1980; Davis & Peebles, 1977), which claims that clustering in a very non-linear regime leads to virialized regions with fixed proper density, thereby retaining some memory of its initial configurations. Assum-

ing the stable clustering hypothesis on small scales, Hamilton *et al.* (1991) (HKLM) introduced a scaling Ansatz, which interpolates between the linear regime on large scales and the non-linear regime on small scales in terms of a fitting function to N-body simulations. Further corrections were made by Peacock & Dodds (1994) and Peacock & Dodds (1996) (PD96), respectively. An accuracy test was provided by Jain *et al.* (1995).

- SCALE-FREE MODELS:
  This description is independent on any characteristic physical length scales, and requires two conditions (Efstathiou *et al.*, 1988),

  i) Initial power spectrum resembles a power law, $P(k) = A \cdot k^n$ for $1 < n < -3$,

  ii) The scalefactor evolution follows a power law too, $a(t) \propto t^\alpha$. A nonlinear wavenumber k_{NL} needs to be identified, constrained by the presumed cosmological model. The statistics of gravitational clustering are expressed by a similarity solution, see Smith *et al.* (2003),

  $$P(k,a) = \tilde{P}(k/k_{NL}). \tag{B.11}$$

  (Davis & Peebles, 1977; Peebles, 1980)

B.6 HALOFIT-Coefficients

Smith *et al.* (2003) obtained the following coefficients,

$$\log_{10} a_n = 1.4861 + 1.8369n + 1.6762n^2 + 0.7940n^3 + 0.1670n^4 - 0.6206C, \tag{B.12}$$
$$\log_{10} b_n = 0.9463 + 0.9466n + 0.3084n^2 - 0.9400C, \tag{B.13}$$
$$\log_{10} c_n = -0.2807 + 0.6669n + 0.3214n^2 - 0.0793C, \tag{B.14}$$
$$\gamma_n = 0.8649 + 0.2989n + 0.1631C, \tag{B.15}$$
$$\alpha_n = 1.3884 + 0.3700n - 0.1452n^2, \tag{B.16}$$
$$\beta_n = 0.8291 + 0.9854n + 0.3401n^2, \tag{B.17}$$
$$\log_{10} \mu_n = -3.5442 + 0.1908n, \tag{B.18}$$
$$\log_{10} \nu_n = 0.9589 + 1.2857n, \tag{B.19}$$

where the Ω dependent functions for $\Omega = \Omega_{\rm M} \leq 1$ are

$$f_{1a}(\Omega) = \Omega^{-0.0732}, \tag{B.20}$$
$$f_{2a}(\Omega) = \Omega^{-0.1423}, \tag{B.21}$$
$$f_{3a}(\Omega) = \Omega^{0.0725}, \tag{B.22}$$

while for $\Omega = \Omega_{\rm M} + \Omega_{\rm DE} = 1$ it follows

$$f_{1b}(\Omega) = \Omega^{-0.0307}, \tag{B.23}$$
$$f_{2b}(\Omega) = \Omega^{-0.0585}, \tag{B.24}$$
$$f_{3b}(\Omega) = \Omega^{0.0743}. \tag{B.25}$$

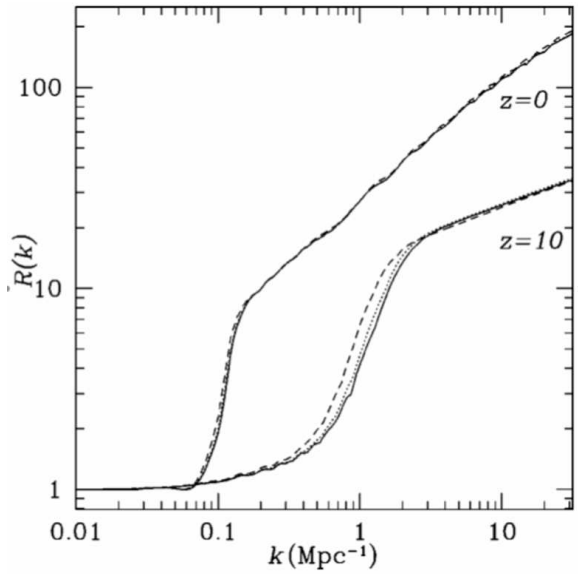

Figure B.4: The ratio of nonlinear to linear power spectra as discussed in Giovi *et al.* (2003), for different dark energy models.

B.7 Ratio of Power Spectra

Giovi *et al.* (2003) uses the MA99 approach but assuming an implicit dependence on k_{nl}, see eq. (4.164). Their result for the ratio of nonlinear to linear power spectra for different dark energy models is shown in Fig. B.4. Interestingly, they get a very large contribution of nonlinear effects at high redshifts, as seen by the $z = 10$ example. This is unexpected, since for larger redshifts the nonlinear effects should be less dominant (see e.g. bottom panel of Fig. 4.12). We too tested their approach, and did not find such an behavior.

B.8 Derivative of the MA99 Power Spectrum

This section shortly discusses the derivative of the Ma *et al.* (1999) power spectrum, which is needed for the calculation of $|Q(l)|$ (eq. (4.198)), and the corresponding comparison with PT and HALOFIT. The derivative of eq. (4.148) results in,

$$\frac{\partial \Delta_{nl}(k_{nl},z)}{\partial z} = \frac{\partial \Delta_l(k_l,z)}{\partial z} \cdot G\left(\frac{\Delta_l(k_l,z)}{g_0^{3/2}\sigma_8^{\beta}}\right) + \Delta_l(k_l,z) \cdot \frac{\partial G}{\partial z}, \tag{B.26}$$

where for the various components (eq. (4.149), eq. (4.152) and eq. (4.150)) it follows:

$$\frac{\partial x}{\partial z} = x\left\{\Delta_l(k_l,z)^{-1}\frac{\partial \Delta_l(k_l,z)}{\partial z} - \left(\frac{3}{2}g_0^{1/3}\frac{\partial g_0}{\partial z} + \frac{\beta}{\sigma_8}\frac{\partial \sigma_8}{\partial z}\right)\right\}, \tag{B.27}$$

$$\frac{\partial \sigma_8}{\partial z} = \sigma_8(z)\cdot\left\{\frac{1}{g_Q}\frac{\partial g_Q}{\partial z} - \frac{1}{g_\Lambda}\frac{\partial g_\Lambda}{\partial z} - \frac{1}{(1+z)}\right\}, \tag{B.28}$$

$$\begin{aligned}\frac{\partial G(x)}{\partial z} &= G(x)\cdot\left\{\frac{0.5}{(1+0.5x)\cdot[1+\ln(1+0.5x)]}\cdot\frac{\partial x}{\partial z}\right\} + \\ &\quad G(x)\cdot\left\{\frac{0.024x^3\partial x/\partial z + 8c_1x^7/g^3\partial x/\partial z - 3c_1x^8/g^4\partial g/\partial z}{(1+0.02x^4+c_1x^8/g^3)}\right\} - \\ &\quad G(x)\cdot\left\{\frac{c_2 7.5x^{6.5}\partial x/\partial z}{(1+c_2x^{7.5})}\right\}.\end{aligned} \tag{B.29}$$

The derivative of g_0 vanishes, since $w_{\rm DE} = -1$ is constant. We use these equations to calculate eq. (4.200). Note: Using the approach by Giovi *et al.* (2003), the only thing that changes is the dependence of G on k_{nl} instead of k_l.

B.9 Evolution of $\partial P_\Phi(z)/\partial z$ for different DE Models

Fig. B.5 shows dP_Φ/dz with redshift for $k = 4$ Mpc^{-1}, where the regime is completely nonlinear. The upper left panel shows the examples for constant equation of states using $w_{\rm DE} = -0.6$ (black lines), -1 (blue lines) and -1.4 (red lines). The upper right panel shows the WETT04 examples for $\Omega_{\rm EDE}$ contributions at $z_{\rm lss}$ (solid lines) and $z_{\rm sf}$ (dashed triple dotted lines), see also table 4.2. The bottom right panel presents LIND03 for $w_a = -0.5$ (black lines), 0.5 (blue lines) and 1 (red lines), while the bottom right panel shows KOMAT09 for $z_{\rm trans} = 115.97$ (black lines), 6.39 (blue lines) and 2.60 (red lines).

B.10 Signal to Noise

Fig. B.6 shows the S/N evolution with $l_{\rm max}$ for a cosmic variance limited experiment using PT and MA99. Both approaches are similar.
Fig. B.7 and Fig. B.8 present the S/N evolution with $l_{\rm max}$ for a WMAP limited experiment. Compared to Fig. 4.25 and Fig. 4.26 the signal is much lower. Future measurements as PLANCK will provide more insight into the nature of DE.

B.11 Spin Weighted Spherical Harmonics

The so called spin weighted spherical harmonics introduced by Newman & Penrose (1966) present a generalization from the usual spherical harmonics and are written as, ${}_sY_l^m$, where s denotes the spin weight and l, m correspond to their normal description. The ${}_sY_l^m$ are obtained by using spin raising and lowering operators, where the standard form for the spherical harmonics refers to the weight $s = 0$,

$${}_0Y_l^m = Y_l^m. \tag{B.30}$$

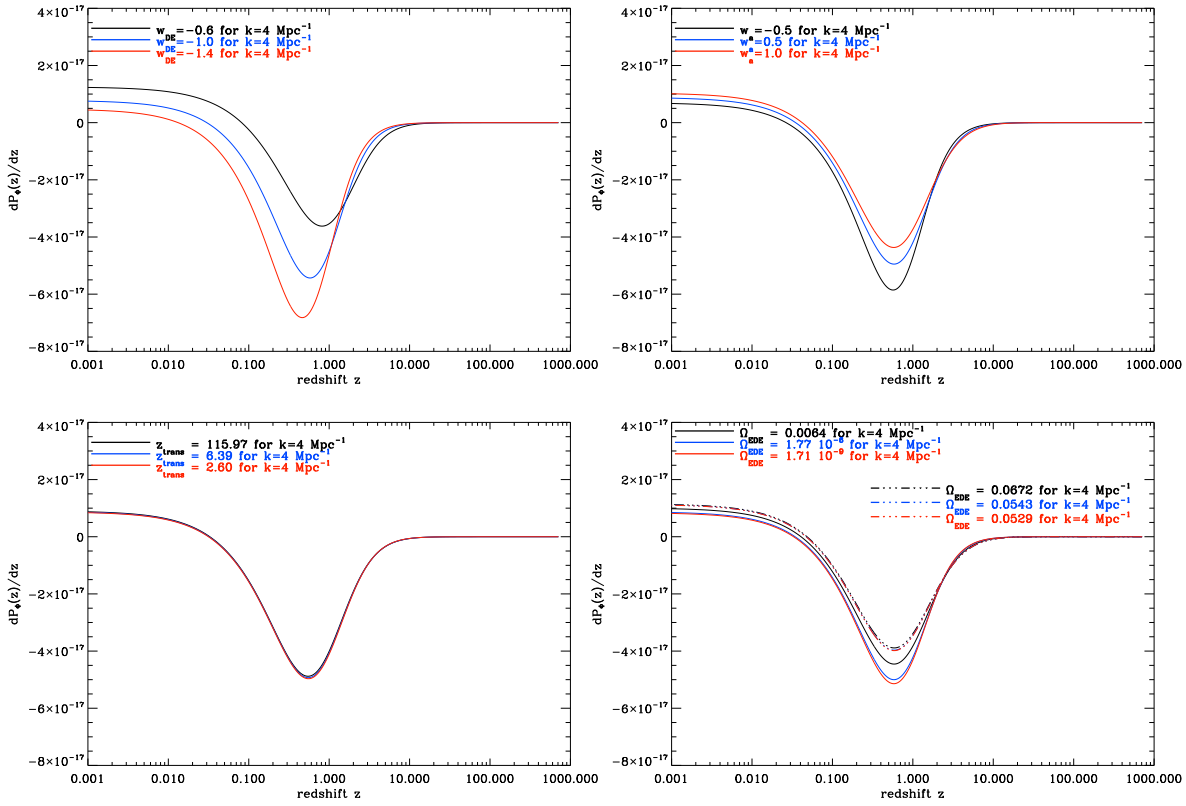

Figure B.5: The same as in Fig. 4.18 but for $k = 4$ Mpc^{-1}.

The spin weighted harmonics can be recursively calculated by applying the raising or lowering operators and it follows from Goldberg *et al.* (1967),

$$
\begin{aligned}
{}_sY_{lm}(\Theta,\phi) \quad = \quad & \left[\frac{(l+m)!(l-m)!}{(l+s)!(l-s)!}\frac{(2l+1)}{4\pi}\right]^{\frac{1}{2}}(\sin\Theta/2)^{2l}\,\cdot \\
& \sum_{r=0}^{l-s}\binom{l-s}{r}\binom{l+s}{r+s-m}(-1)^{l-r-s}e^{im\phi}\,(\cot\Theta/2)^{2r+s-m}\,. \qquad \text{(B.31)}
\end{aligned}
$$

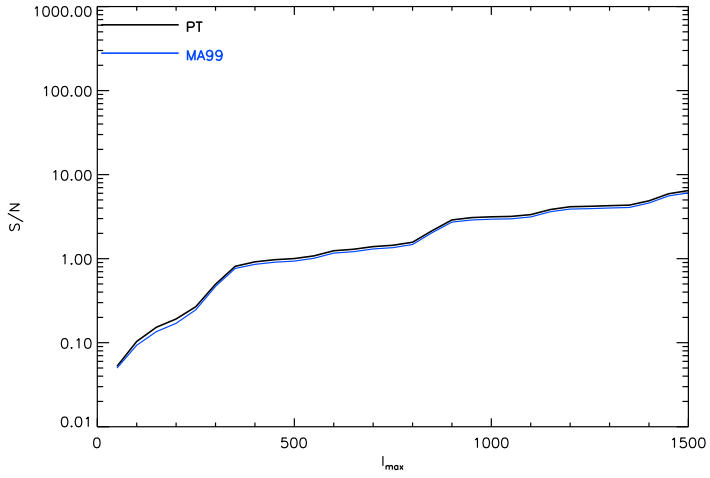

Figure B.6: The same as Fig. 4.25 using PT (black line) and MA99 (blue line).

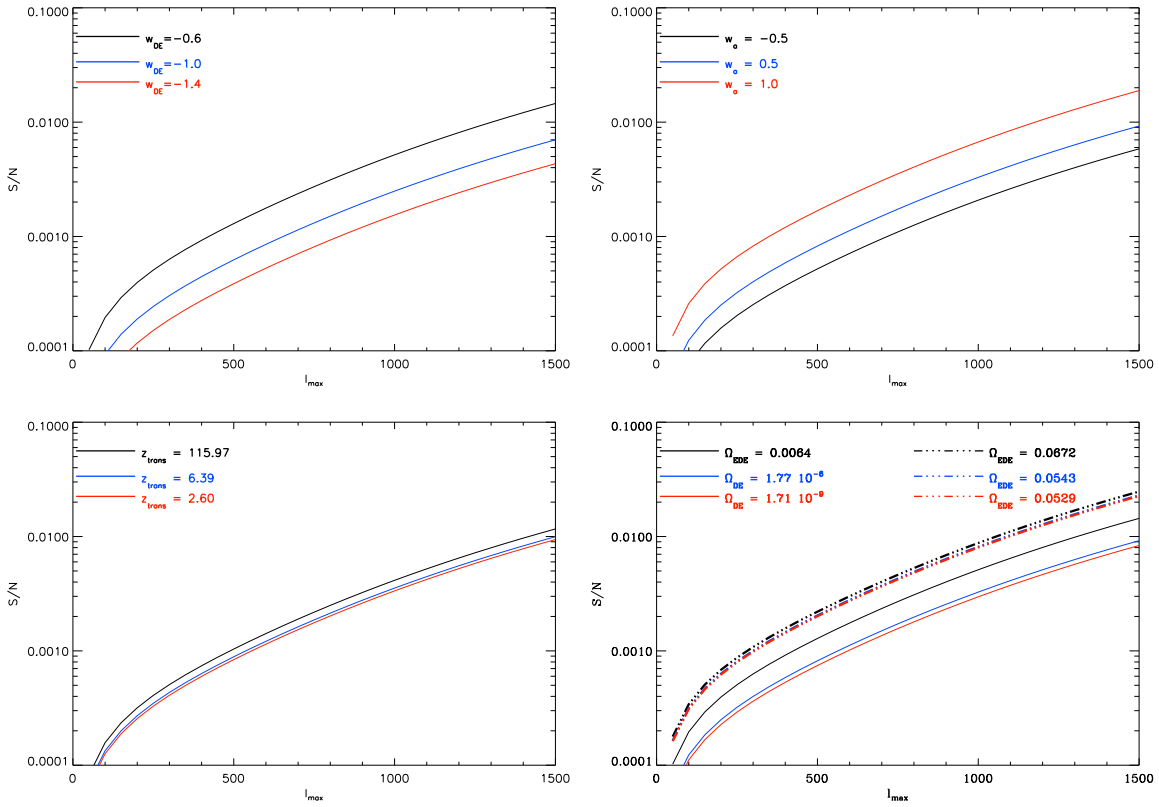

Figure B.7: The same as Fig. 4.25 but for a WMAP limited experiment.

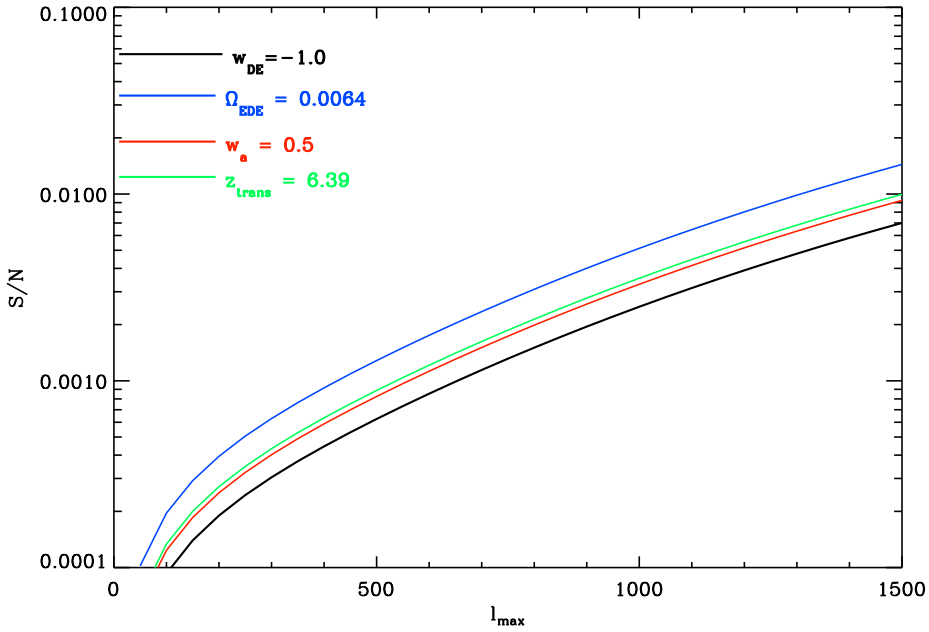

Figure B.8: The same as Fig. 4.25 but for the constant equation of state with $w_{\rm DE} = -1$ (black solid line), WETT04 using $\Omega_{\rm EDE} = 0.0064$ (blue line), LIND03 with $w_a = 0.5$ (red line), and KOMAT09 using $z_{\rm trans} = 6.39$ (green line).

Acknowledgements

Mein Dank gilt der gesamten Universitäts-Sternwarte München, im besonderen der Computational Group. Allen voran möchte ich mich bei Prof. Dr. Andreas Burkert bedanken, für die Möglichkeit meine Dissertation bei ihm machen zu dürfen und bei Prof. Dr. Jochen Weller für die vielen wertvollen Diskussionen und Hilfen. Ebenfalls zu grossem Dank verplichtet bin ich Prof. Dr. David Spergel (Universität Princeton) und Prof. Dr. Eiichiro Komatsu (Universität Texas) für ihre Unerstützung, sowie Prof. Dr. Harald Lesch. Ein lieben Dank auch an Peter Johansson für die vielen gut organisierten Gruppen- und Astroph-Treffen.

Ein grosser Dank geht natürlich an meine Freunde, allen voran meinen besten Freund Oliver Binder, der mein ganzes Leben für mich da war und ist, ebenso wie Elena D'Onghia und Andrea Gehr. Die vielen unvergesslichen Jio-Abende verdanke ich Christine Botzler und Jan Snigula, die lustigen Wii-Abende Armin Gabasch, die vielen schönen Museums-Kino-Besuche Inge Burkert und die vielen erleuchteten Mittagessen Florian Lang, Claus Gössel, Ulrich Hopp und Judith Ngoumou. Ganz besonderer Dank geht an meine Frustschwester Christina Kraus, ohne unsere Mails hätte ich es nicht geschafft und an Christine Muschik für die vielen hilfreichen Telefonate.
Nicht vergessen will ich Frank Packschies für einen wirklich besonders lustigen Einstieg in das Bergwandern.

Am meisten schulde ich jedoch meiner Familie, ohne deren Untersützung ich es nie geschafft hätte. Vor allem Dank schulde ich meiner Mutter für ihr Vertrauen und ihrer Stärke. Danke auch an meinen Vater für seine Hilfe und an meinen kleinen Bruder, der mich immer wieder auf den Boden der Tatsachen zurückgebracht hat. Und letztendlich an meinen allerliebsten Buben, unserem Altdeutschen-Schäferhund Eddy.